



City Research Online

City, University of London Institutional Repository

Citation: Xu(Xiong), X.Y. (1992). Numerical analysis of blood flow in 3-D arterial bifurcations. (Unpublished Doctoral thesis, City, University of London)

This is the accepted version of the paper.

This version of the publication may differ from the final published version.

Permanent repository link: <https://openaccess.city.ac.uk/id/eprint/28575/>

Link to published version:

Copyright: City Research Online aims to make research outputs of City, University of London available to a wider audience. Copyright and Moral Rights remain with the author(s) and/or copyright holders. URLs from City Research Online may be freely distributed and linked to.

Reuse: Copies of full items can be used for personal research or study, educational, or not-for-profit purposes without prior permission or charge. Provided that the authors, title and full bibliographic details are credited, a hyperlink and/or URL is given for the original metadata page and the content is not changed in any way.

NUMERICAL ANALYSIS OF BLOOD FLOW
IN 3-D ARTERIAL BIFURCATIONS

by

XIAO YUN XU(XIONG)

A dissertation submitted to
The City University
in fulfilment of the requirement
for the degree of
Doctor of philosophy

MARCH 1992

Department of Mechanical Engineering & Aeronautics
The City University
London

020217398

TABLE OF CONTENTS

	<u>PAGE</u>
TABLE OF CONTENTS	1
LIST OF TABLES	7
LIST OF FIGURES	8
ACKNOWLEDGEMENTS	15
DECLARATION	16
ABSTRACT	17
NOMENCLATURE	18
<u>CHAPTER 1: INTRODUCTION</u>	21
1.1 HEMODYNAMICS AND ATHEROSCLEROSIS	22
1.2 GENERAL FEATURES OF ARTERIAL BIFURCATION FLOW	27
1.3 MODEL DESCRIPTION AND ITS VALIDITY	29
1.4 OBJECTS OF RESEARCH	32
1.5 METHODOLOGY AND STRATEGY EMPLOYED	33
<u>CHAPTER 2: NUMERICAL METHODS FOR THE SOLUTION OF 3D</u> <u> TIME DEPENDENT NAVIER – STOKES EQUATIONS</u>	36
2.1 INTRODUCTION	36
2.2 GOVERNING EQUATIONS	36
2.3 DISCRETIZATION METHODS	38
2.3.1 Spatial Discretisation	38
2.3.2 Treatment of Advection	41
2.3.3 Time Differencing Scheme	43
2.4 COMPUTATION ALGORITHMS	43
2.5 AVAILABLE COMPUTER CODES	46
2.5.1 Introduction	46
2.5.2 Comparison of CFD Codes	46

	<u>PAGE</u>
2.5.3 Details of ASTEC	50
2.5.3.1 General Features and Capabilities of the Code	50
2.5.3.2 The Mesh and Discretisation	52
2.5.3.3 Calculation Procedure	54
<u>CHAPTER 3: LITERATURE SURVEY</u>	57
3.1 INTRODUCTION	57
3.2 GEOMETRY OF ARTERIAL BIFURCATIONS	57
3.2.1 Structure and Physiology of Arteries	58
3.2.2 Bifurcation Geometry	62
3.2.3 Geometric Effects on Flow in Bifurcations	65
3.3 GRID GENERATION TECHNIQUES	66
3.3.1 Introduction	66
3.3.2 Algebraic Methods	68
3.3.3 Partial Differential Equation Methods	69
3.3.4 Special Techniques for Irregular Geometries	72
3.3.4.1 Multi-block Grids	74
3.3.4.2 Unstructured Grids	75
3.3.5 Adaptive Gridding	76
3.4 BLOOD FLOW IN ARTERIES	78
3.4.1 Introduction	78
3.4.2 Arterial Wave Propagation	80
3.4.3 Flow at Arterial Bifurcations	84
3.5 RHEOLOGICAL PROPERTIES OF BLOOD	87
3.5.1 Introduction	87
3.5.2 An Outline of Blood Rheology	87
3.5.3 The Constitutive Equation	90
3.5.4 The Effects of Non-Newtonian Characteristics on Bifurcation Flows	95

	<u>PAGE</u>
3.6 THE MECHANICAL PROPERTIES OF BLOOD VESSELS	98
3.6.1 Introduction	98
3.6.2 The Structure and Composition of the Blood Vessel Wall	98
3.6.3 Mathematical Representations of the Stress – Strain Relationship	100
3.6.4 The Effects of Wall Distensibility on Bifurcation Flow	104
3.7 EXPERIMENTAL TECHNIQUES FOR MEASUREMENTS OF BLOOD FLOW IN ARTERIES	105
3.7.1 Introduction	105
3.7.2 Velocity Measurement	105
3.7.2.1 Doppler Ultrasound Techniques	107
3.7.2.1.1 Principles of Doppler Ultrasound	107
3.7.2.1.2 Development and Applications of Doppler Ultrasound	108
3.7.2.2 Laser-Doppler Anemometry	110
3.7.3 Wall Shear Stress Measurement	112
 <u>CHAPTER 4: CODE IMPROVEMENT</u>	 114
4.1 INTRODUCTION	114
4.2 GRID GENERATION FOR GENERAL 3-D BIFURCATION GEOMETRIES	114
4.2.1 Mesh Generation Procedure in SOPHIA (old)	114
4.2.2 Definition of General Bifurcation Geometries	117
4.2.3 The Purpose-built Routine	120
4.2.4 Applications	122
4.3 IMPLEMENTATION OF NON-NEWTONIAN MODEL	126
4.4 INCORPORATION OF THE COMPLIANT WALL	129
4.4.1 Mathematical Model of The Arterial Wall	131

	<u>PAGE</u>
4.4.2 Treatment of Moving Wall	134
<u>CHAPTER 5: CODE VALIDATION</u>	137
5.1 INTRODUCTION	137
5.2 FLOW IN TUBES	138
5.2.1 Three-Dimensional Steady Flow in a Rigid Circular Tube with (a) Newtonian, and (b) Non-Newtonian Fluid	138
5.2.2 Three-Dimensional Pulsatile Flow in a Rigid Circular Tube with Newtonian Fluid	141
5.2.3 Three-Dimensional Pulsatile Flow in an Elastic Circular Tube with Newtonian Fluid	143
5.3 FLOW IN BIFURCATIONS	146
5.3.1 Two-Dimensional Steady Flow in a T-bifurcation	146
5.3.1.1 Problem Definition and Grid Resolution Tests	146
5.3.1.2 Comparison of Calculated and Measured Velocity Profiles	147
5.3.1.3 Wall Shear Stress	150
5.3.2 Two-Dimensional Pulsatile Flow in a T-bifurcation	158
5.3.2.1 Problem Definition	158
5.3.2.2 Comparison of Calculated and Measured Velocity Profiles	160
5.3.2.3 Wall Shear Stress	163
5.3.2.4 Effects of Pulsation	166
5.3.3 Three-Dimensional Pulsatile Flow in a T-bifurcation	169
5.3.3.1 Problem Definition	169
5.3.3.2 Description of Velocity Field	171
5.3.3.3 Description of Wall Shear Stress	179
5.3.3.4 Effects of Three-Dimensionality	184
5.3.3.5 Effects of Non-Newtonian Viscosity	185
5.3.3.6 Comparison with LDA Measurements of Ku and Liepsch	193

	<u>PAGE</u>
5.4 SUMMARY	195
<u>CHAPTER 6: PREDICTIONS OF FLOW IN 3D CANINE FEMORAL</u> <u>ARTERY BIFURCATIONS</u>	 196
6.1 INTRODUCTION	196
6.2 PROBLEM DEFINITION	196
6.2.1 Bifurcation Geometry	196
6.2.2 Boundary Conditions	197
6.2.3 Grid Resolution Tests	202
6.3 NUMERICAL RESULTS	202
6.3.1 Velocity Field	203
6.3.2 Wall Shear Stress	217
6.4 INFLUENCES OF VARIOUS FACTORS	222
6.4.1 Bifurcation Geometry	222
6.4.2 Upstream Flow Conditions	224
6.4.3 Non-Newtonian Viscosity	227
6.5 COMPARISON WITH IN VIVO MEASUREMENTS	234
6.6 SUMMARY	239
<u>CHAPTER 7: CONCLUSIONS</u>	241
<u>REFERENCES AND BIBLIOGRAPHY</u>	244
<u>APPENDICES</u>	
A GENERAL FORM OF THE STRESS TENSOR EQUATION FOR INCOMPRESSIBLE NON-NEWTONIAN FLUIDS	 261
B FINITE NONLINEAR ELASTIC ANALYSIS	263
C FORTRAN SUBROUTINE FOR THE NON-NEWTONIAN MODEL	265

	<u>PAGE</u>
D RELATIONSHIP OF VELOCITY, FLOW RATE AND WALL SHEAR STRESS TO AN OSCILLATORY PRESSURE GRADIENT	267
E PRESSURE DISTRIBUTIONS IN A 3D T-BIFURCATION	271
F PUBLISHED PAPERS	274

LIST OF TABLES

- Table 2.1 Suppliers of CFD codes.
- Table 2.2 Comparison of codes' capabilities.
- Table 2.3 Comparison of codes' numerical treatment.
- Table 2.4 Main features and capabilities of ASTEC.
- Table 2.5 Numerical methods employed in ASTEC.
- Table 3.1 Normal value for canine cardiovascular parameters.
- Table 3.2 Summary of advantages and disadvantages of the three types of partial differential equation grid generation methods.
- Table 3.3 Summary of numerical research on blood flow in bifurcations.
- Table 3.4 Summary of experimental techniques for study of flow patterns in arteries.
- Table 4.1 Summary of material constants for the polynomial strain energy function.
- Table 5.1 Flow parameters investigated.
- Table 5.2 Location and size of the separation region.
- Table 5.3 Location of separation zone for steady flow (Khodadadi et al, 1986).
- Table 5.4 Comparison of Newtonian and non-Newtonian flow: maximum forward flow velocity and maximum reversed flow velocity at site D (2.5mm behind the flow divider).
- Table 5.5 Comparison of Newtonian and non-Newtonian flow: maximum, minimum and time-averaged shear stresses on the outer and divider walls at sites A, D and F.
- Table 6.1 Maximum forward flow velocity, maximum reversed flow velocity and maximum secondary flow velocity at the level of the flow divider in models A and B during a cardiac cycle.
- Table 6.2 Maximum, minimum and time averaged wall shear stress at sites 1-7 of models A and B over a cardiac cycle.

LIST OF FIGURES

- Figure 1.1 Particle paths in the median plane of a rounded T-junction at $Re_o=245$ and $Q_1/Q_2=0.25$.
- Figure 2.1 Relationship between ASTEC, associated data files, and the pre- and post-processor.
- Figure 2.2 Mesh used in ASTEC.
- Figure 2.3 The iterative scheme within a cycle.
- Figure 3.1 Major organs in the circulation.
- Figure 3.2 Major branches of the canine arterial tree.
- Figure 3.3 Idealised geometry of human carotid artery bifurcations.
- Figure 3.4 Casts of (a) human renal artery and (b) aortic arch.
- Figure 3.5 Tracings of canine ilio-femoral bifurcations.
- Figure 3.6 Geometric parameters of a bifurcation.
- Figure 3.7 Logic breakdown of grid generation methods.
- Figure 3.8 Generation of a curvilinear coordinate system in 2D.
- Figure 3.9 Block structure for an H (Cartesian) mesh topology.
- Figure 3.10 Point correspondence at block interfaces.
- Figure 3.11 Unstructured mesh (a) triangle mesh, (b) quadrilateral mesh.
- Figure 3.12 Pressure and velocity waveforms in various arteries of a dog:
A – Ascending aorta, B – Thoracic aorta, C – Abdominal Aorta,
D – Femoral artery, E – Saphenous artery.
- Figure 3.13 Models of arterial elements from which a conduit is formed :
(a) segment with a continuous outflow (no or only small side branches), (b) bifurcation segment, (c) pathological segment.
- Figure 3.14 Variation of apparent viscosity of human blood with rate of shear.
- Figure 3.15 Relationship between viscosity and rate of shear for human

blood cell suspended in their own anticoagulated plasma at 25°C for various hematocrit.

- Figure 3.16 Rheogram for different types of flow behaviour, assuming constant pressure and temperature.
- Figure 3.17 Comparison of a Newtonian and a viscoelastic fluid for pulsatile flow over a whole cycle at 2.5mm behind a 90°-T-junction of a glass model with rounded corners. The entrance Reynolds number 250 and the flow rate ratio $Q_2/Q_o=0.5$.
- Figure 3.18 Comparison of a Newtonian and a viscoelastic fluid for pulsatile flow over a whole cycle at 2.5mm behind a 90°-T-junction of an elastic silicon rubber model with sharp corners. The flow conditions the same as those in Fig.3.17.
- Figure 3.19 Schematic illustration of the structure of arterial wall.
- Figure 3.20 Principle of Doppler ultrasound.
- Figure 3.21 Principle of Laser-Doppler anemometer.
- Figure 4.1 3-D structural block.
- Figure 4.2 Grid generation procedure in SOPHIA.
- Figure 4.3 Definition of general bifurcation geometry.
- Figure 4.4 Grid generation procedure for a general 3-D bifurcation.
- Figure 4.5 Flow chart of the grid generation routine.
- Figure 4.6 Grid configuration of a T-Bifurcation.
- Figure 4.7 Grid configuration of a curved branch.
- Figure 4.8 Grid configuration of a canine femoral bifurcation.
- Figure 4.9 Grid configuration of a human carotid bifurcation model.
- Figure 4.10 Dynamic non-Newtonian viscosity of human blood with a hematocrit of 45% at 23°C.
- Figure 4.11 A feedback system of two functional units.
- Figure 4.12 Comparison of computed pressure-diameter curve for an 0.34mm

thick graft (—) and measured values (+) of How and Clarke (1984).

- Figure 4.13 Illustration of the moving wall treatment.
- Figure 5.1 Comparison between theoretical solution (—) and calculation (o o o) for fully developed flow in a straight tube with (a) Newtonian, and (b) non-Newtonian fluid.
- Figure 5.2 Comparison of shear rate between a Newtonian (—) and a non-Newtonian (o o o) fluid.
- Figure 5.3 Pressure gradient boundary condition.
- Figure 5.4 Comparison between theoretical solution (—) and calculation (o o o) for pulsatile flow in a rigid tube over a whole cycle.
- Figure 5.5 Relation of flow (Q) and wall shear rate (S) to the pressure gradient (P).
- Figure 5.6 Diameter–pressure curve for the silicone model.
- Figure 5.7 Comparison between calculation (—) and experiment (o o o) for unsteady flow in an elastic tube over the whole cycle.
- Figure 5.8 Comparison of wall shear stress for a rigid tube (—) and an elastic tube (o o o).
- Figure 5.9 Bifurcation geometry.
- Figure 5.10 Axial velocity profiles in the main tube for cases 1–5.
- Figure 5.11 Axial velocity profiles in the branch tube for cases 1–5.
- Figure 5.12 Comparison of axial velocity profiles with the LDA measurements.
- Figure 5.13 Comparison of axial velocity profiles between ASTEC and FLOW3D.
- Figure 5.14 Wall shear stress along the bottom wall of the main tube.
- Figure 5.15 Wall shear stress along the divider wall of the main tube.
- Figure 5.16 Wall shear stress along the upstream wall of the branch.
- Figure 5.17 Wall shear stress along the divider wall of the branch.
- Figure 5.18 Pulsating pressure gradient at the inlet.
- Figure 5.19 Comparison of axial velocity profiles in the main tube

(— calculation, ●●● measurement).

Figure 5.20 Comparison of axial velocity profiles in the branch tube

(— calculation, ●●● measurement).

Figure 5.21 Wall shear stress along the bottom wall W1, the upstream side wall W2, and the divider wall W3 at three phase angles (90° , 225° and 315°).

Figure 5.22 Temporal variation of the size of the separation zones in (a) main tube and (b) branch tube.

Figure 5.23 Finite element subdivision of the 3D T-bifurcation.

Figure 5.24 Fully developed velocity profiles calculated using Womersley's solution.

Figure 5.25 Definition of cross sectional positions where numerical results are presented.

Figure 5.26 Axial velocity profiles in the plane of symmetry and planes through the axis of the main tube at 45° and 90° to the bifurcation plane at specified phase angles.

Figure 5.27 Secondary velocity vector field at different cross-sections for the maximum and minimum flow rates.

Figure 5.28 Secondary velocity profiles at different cross-sections for the maximum and minimum flow rates.

Figure 5.29 Wall shear stress along the outer wall (W1) and the divider wall (W2) at specified phase angles.

Figure 5.30 Wall shear stress vs phase angle at the outer wall and the divider wall at different cross-sections of the bifurcation.

Figure 5.31 Comparison of axial velocity profiles between Newtonian and non-Newtonian fluid in (a) symmetry plane and (b) perpendicular plane.

Figure 5.32 Comparison of wall shear stress between Newtonian and non-

Newtonian fluid at specified phase angles.

- Figure 5.33 Comparison of time varying wall shear stress between Newtonian and non-Newtonian fluid.
- Figure 5.34 Comparison between calculations and measurements: axial velocity profiles in the bifurcation plane 25mm upstream and 2.5mm downstream of the flow divider for (a) the Newtonian fluid, and (b) the non-Newtonian fluid.
- Figure 6.1 Schematic illustration and three-dimensional representation of the two canine ilio-femoral bifurcation models.
- Figure 6.2 Average canine velocity pulse waveform under normal conditions.
- Figure 6.3 Calculated axial velocity profiles at the exit of a straight tube 10 diameters long.
- Figure 6.4 Measured average velocity waveforms and instantaneous upstream axial velocity profiles in models A and B.
- Figure 6.5 Definition of pulse phases where numerical results are presented.
- Figure 6.6 Axial velocity profiles in the bifurcation plane of model A at four different phases A_p , B_p , C_p and D_p during a cardiac cycle.
- Figure 6.7 Axial velocity profiles in the bifurcation plane of model B at four different phases A_p , B_p , C_p and D_p during a cardiac cycle.
- Figure 6.8 Three-dimensional representation of axial velocity at cross-sections perpendicular to the bifurcation plane at sites 1-5 of model A during a cardiac cycle.
- Figure 6.9 Three-dimensional representation of axial velocity at cross-sections perpendicular to the bifurcation plane at sites 1-5 of model B during a cardiac cycle.
- Figure 6.10 Secondary velocity vector field at different cross-sections of bifurcation model A during a cardiac cycle.
- Figure 6.11 Secondary velocity vector field at different cross-sections of

bifurcation model B during a cardiac cycle.

- Figure 6.12 Wall shear stress vs phase at selected sites in model A.
- Figure 6.13 Wall shear stress vs phase at selected sites in model B.
- Figure 6.14 Wall shear stress along the outer wall (ooo) and the divider wall (+++) of model B at specified phases.
- Figure 6.15 Duration of flow reversal in the outer corner region at defined points over a cardiac cycle.
- Figure 6.16 Comparison of axial velocity profiles in the bifurcation plane of model A between type 1 (—) and type 2 (ooo) upstream flow conditions.
- Figure 6.17 Comparison of time varying wall shear stress between type 1 (—) and type 2 (ooo) upstream boundary conditions.
- Figure 6.18 Comparison of axial velocity profiles in the bifurcation plane of model A between Newtonian (—) and non-Newtonian (ooo) fluid.
- Figure 6.19 Comparison of axial velocity profiles in the bifurcation plane of model B between Newtonian (—) and non-Newtonian (ooo) fluid.
- Figure 6.20 Comparison of time varying wall shear stress between Newtonian (—) and non-Newtonian (●●●) fluid at selected sites in model A.
- Figure 6.21 Comparison of time varying wall shear stress between Newtonian (—) and non-Newtonian (●●●) fluid at selected sites in model B.
- Figure 6.22 Comparison between calculations (—) and measurements (ooo): axial velocity profiles at sites 1–5 over a cardiac cycle for model A. The right hand side is the outer wall and the left hand side is the flow divider side.

Figure 6.23 Comparison between calculations (—) and measurements (o o o): axial velocity profiles at sites 1–5 over a cardiac cycle for model B. The right hand side is the outer wall and the left hand side is the flow divider side.

Figure 6.24 Comparison between calculations (—) and measurements (o o o): secondary velocity profiles in the bifurcation plane at the level of the flow divider (site 6) over a cardiac cycle for model B. The right hand side is the outer wall and the left hand side is the flow divider side.

Figure E.1 Pressure contours in the bifurcation plane at (a) maximum, and (b) minimum flow rates.

Figure E.2 Distribution of pressure on the wall at different cross-sections for the (a) maximum, and (b) minimum flow rates.

ACKNOWLEDGEMENTS

I wish to acknowledge with grateful thanks the sponsorship of British Heart Foundation for this project, and the support of the U.K. Medical Research Council for a supercomputer grant.

My special thanks are due to my supervisor Prof. M.W. Collins, for all his help, advice and encouragement generously given throughout the course of this project.

My sincere thanks also go to Dr. C.J.H. Jones and Dr. K.H. Parker for their much valued suggestions and discussions during the course of the work, and especially for supplying detailed experimental data.

Also, special thanks are due to Dr. A. Burns who has given valuable advice on programming and computing, and Dr. R.D. Lonsdale who loaded the computer software ASTEC and provided much help on using the code.

I appreciate very much the helpful suggestions given by Prof. P.D. Richardson, Brown University, and the interesting discussions with him during his visits in London.

Finally, I would like to express my special thanks to my husband Zhi-guo for his understanding, patience and various support, and my parents for their persistent encouragement and support throughout the years of my study.

DECLARATION

I grant powers of discretion to the University Librarian to allow this thesis to be copied in whole or in part without further reference to me. This permission covers only single copies made for study purposes, subject to normal conditions of acknowledgement.

ABSTRACT

A major medical problem in the circulatory system is the frequent occurrence of atherosclerosis and thrombosis in arterial bends and bifurcations. Although the exact mechanism remains unclear, it has been suggested that the local fluid dynamics plays an important role. Therefore, detailed analysis of flow phenomena and hemodynamic stresses in arterial bifurcations is of immediate interest.

In addition to *in vivo* and *in vitro* experiments, numerical simulations of blood flow in arterial bifurcation models also contribute to a better understanding of the flow patterns and shear stress distributions in these bifurcations, and thereby help to clarify the link between fluid dynamics and atherogenesis.

The problem of blood flow in an arterial bifurcation involves many complicating factors, four of them are considered to be important, namely (i) the three-dimensional geometry of the bifurcation, (ii) the pulsatile nature of the flow, (iii) the non-Newtonian character of the blood, and (iv) the distensibility of the arterial wall. In this dissertation, a full analytical treatment of blood flow in 3-D arterial bifurcations is presented. The incompressible 3-D time-dependent Navier-Stokes equations are employed to describe the flow, and a finite volume code ASTEC, which has an unstructured finite element mesh, is adopted to solve the equations. In the predictions, the non-Newtonian characteristics of the blood are taken into account and their effects on bifurcation flow fields investigated. Possibilities of accommodating the vessel wall compliance are also explored, and a simplified approach is proposed, in which the flow equations and wall displacements are solved separately within a time step, but are coupled in the sense that the boundary conditions of the former are updated through the solution of the later. This approach is valid provided that the wall movement is much slower than the motion of fluid and the flow is generally parallel to the wall. It has been applied to a straight circular tube. For bifurcation predictions, however, the vessel wall is assumed to be rigid.

A comprehensive range of code validation exercises are carried out, especially for T-bifurcations. The predictions are proved reliable by comparison with published laboratory measurements.

Finally, numerical predictions for physiological flow in canine femoral bifurcations are performed, in which the true bifurcation geometries are used. Results are validated against the best available *in vivo* measurements so far obtained. It is demonstrated that the presented numerical modelling scheme in conjunction with the new generation of super-computers can be used as an efficient and reliable tool for detailed analysis of blood flow in arterial bifurcations. Incorporation of the distensibility of the arterial wall in the bifurcation prediction will complete such an analysis.

Some of the material published during the course of the project is included in Appendix F.

NOMENCLATURE

A	Cross-sectional area
c	Wave speed
Cr	Courant number ($Cr = \frac{c}{\Delta x/\Delta t}$)
D_i	Undeformed vessel diameter
d	Vessel diameter
dA	Control surface area
dV	Control volume
E	Young's modulus
F	Longitudinal force
f	Frequency
F_i	Body force
H_i	Undeformed vessel wall thickness
h	Vessel wall thickness
J_2	Second invariant of strain rate tensor (S_{ij})
k	Turbulent energy
L_i	Undeformed vessel length
l	Vessel length
\dot{m}	Mass flow rate
p	Static pressure
Pc	Cell Peclet number ($Pc = \frac{\rho u \Delta x}{\Gamma}$)
Q	Volume flow rate
r	radius
Re	Reynolds number ($Re = \frac{\rho \bar{u} d}{\mu}$)
S_{ij}	Strain rate tensor
t	Time
tp	Pulse time
u_i	Velocity

u,v,w	Velocity components in 3-D flows
x_i	Coordinates
x,y,z	Cartesian coordinates in 3-D flows

Greek Symbols

α	Womersley number ($\alpha = \frac{d}{2} \sqrt{\frac{\rho\omega}{\mu}}$)
α_1	Parent to larger daughter vessel angle
α_2	Parent to smaller daughter vessel angle
$\dot{\gamma}$	Shear rate
δ_{ij}	Kronecker delta
Δt	Time step
ϵ_{ijk}	Alternating unit tensor
ϵ	Turbulent dissipation rate
λ	Wave length
μ	Dynamic viscosity
∇	Vector differential operator
ν	Kinematic viscosity
ξ,η,ζ	Curvilinear coordinates
ρ	Density
σ_{ij}	Stress tensor
τ	Shear stress
Ψ	Generic scalar
ω	Angular frequency

Subscripts

1	Parent vessel of bifurcation models
2	Larger daughter vessel of bifurcation models

3	Smaller daughter vessel of bifurcation models
Ao	Bifurcation apex
eff	Effective
i,j,k	Generic components
L	Laminar
N	Newtonian
n-N	Non-Newtonian
ost	Oscillatory
st	Steady
T	Turbulent
w	Wall

Superscripts

n	Generic time step
–	Time-averaged or cross-sectional averaged

CHAPTER 1

INTRODUCTION

Atherosclerosis is a widespread disease accounting for almost half of the deaths in the industrialised world. It causes much disabling morbidity, including chest pain, fainting spells, leg cramps, heart attacks, stroke, and aortic aneurysms. This complicated disease affects only specific arteries and is highly localised within these vessels. The selective localisation of atherosclerotic lesions strongly suggests that there is an important relationship between the disease and the characteristics of the blood flowing through the arteries. Furthermore, it is the detailed flow characteristics in those most commonly diseased regions which are of particular interest.

Atherosclerotic plaques have been found to occur predominately in certain large and medium-sized arteries, such as, the abdominal aorta as well as the iliac, femoral, coronary and carotid arteries, but to be more specific, they are particularly prevalent in regions of branching and sharp curvature where unusual flow patterns are expected. Blood flow in such regions remains, nevertheless, beyond fully detailed understanding at present. This is in part due to its complexity; the flow is highly unsteady and passes through vessels which are complicated both in geometry and in their visco-elastic nature; furthermore, blood is a very complex fluid. An additional important factor is a lack of techniques for accurate and detailed investigation of arterial blood flow *in vivo*. Although substantial progress has been made through laboratory model studies using Laser Doppler anemometry or flow visualisation techniques, these usually involve some degree of simplification, such as idealised geometry, steady flow, rigid wall and Newtonian fluid, which may well be questionable in arterial bifurcation flow. Similar limitations have also applied to most previous numerical simulations. However, the latest computational dynamics techniques and a new generation of supercomputers have provided the possibility

to investigate this flow problem more realistically. The goal of this dissertation is, by making use of these tools, to model more closely the actual flow field at arterial bifurcations, and thus to provide comparable numerical results to *in vivo* measurements as well as those unobtainable *in vivo*. In doing so, it would help to reduce the need for *in vivo* experiments. Moreover, the detailed numerical results obtained may contribute to a better understanding of the role of hemodynamics in the process of atherosclerosis.

1.1 HEMODYNAMICS AND ATHEROSCLEROSIS

Cardiovascular disease remains the major cause of death in western societies. According to statistics, more people in the UK die from this than from any other cause. The disease itself is most frequently caused by atherosclerosis. The complex process of the development of atherosclerotic lesions is characterised by the accumulation of materials in the intimal layer of arteries, and changes in both cellular and connective tissue components of the vessel wall. The basic lesion, the atheroma, is usually seen microscopically as a fibrous plaque with accumulations of smooth muscle cells, large amounts of connective tissue like a cap around a deeper pool of tissue debris, foam cells, and spaces from lipid crystals. These atheromatous lesions may lead to narrowing (stenoses) and hardening of the arterial wall, and can progress to more complex plaques which result in further complications such as media thinning, elastic tissue loss and fragmentation.

Atherosclerosis is a highly localised disease which generally affects the major central arteries, including the aorta, the coronary arteries, carotid arteries and the large arteries of the upper leg, rather than the peripheral circulation. It is not normally seen in certain other arteries, e.g. the pulmonary, renal, mesenteric, mammary, and intercostal arteries. Furthermore, the distribution of the lesions within the affected vessels is also very focal. Within the aorta, the abdominal

aorta is severely affected, whereas the thoracic aorta is relatively free of plaque (Clarkson, 1963). In the coronary arteries, lesions are usually found at the outer walls of the bifurcation site, while the inner walls downstream from the bifurcation are left free (Svindland and Walloe, 1983). Such a distinct spatial pattern of the atherosclerotic lesions can also be noticed in the human carotid arteries. At the outer wall of the internal carotid sinus, intimal plaques are thickest, while the inner walls of the bifurcation as well as the apex of the flow divider are well protected regions (Ku and Giddens, 1985).

The selective localisation of atherosclerotic lesions and the involvement of bifurcations and geometrical contorted regions as their preferential sites, have provided a primary motivation for the resurgence of interest in arterial fluid dynamics. Besides biochemical and cytological factors, various hemodynamic characteristics have been proposed to correlate the development of atherosclerosis with local flow conditions in the arterial system. A list of these includes hypotheses concerned with senescence, arterial hypertension, turbulence, wall shear stresses, and flow separation.

Aging is associated with the arterial hardening. It is generally agreed that atherosclerosis is ubiquitous and increases in severity with age. This results from the fact that in man and probably in most animals the size of the arterial vessel increases with age while at the same time elastic wall components are replaced by the much stiffer collagen. According to the fundamental laws of fluid dynamics, it is inevitable that the pulsatile arterial flow in the aging vessel undergoes pronounced changes, such as, the well known augmentation of pulse pressure difference between peak systolic and end diastolic arterial pressure. However, evidence to date does not point to aging as a necessary determinant, but rather as a time factor in atherosclerosis.

Hypertension has been related to clinical complications of atherosclerosis (Wilens, 1951), particularly in coronary artery disease (Dawber et al, 1957). However, the role of blood pressure from a fluid mechanics viewpoint is not yet clear. At one time it was thought that blood-arterial wall lipid transport was due to a pressure driven, bulk flow process, but later experimental data tend to refute any major importance of such a pressure effect. The increased pressure pulse and the associated alteration of velocity waveform, and increase of peak velocity were also hypothesised to be important. A stronger suggestion made recently was that the mean blood pressure plays a major role due to its effect on arterial geometry — a potential risk factor (Nerem and Levesgue, 1983). It has been reported that gross elevation of aortic pressure distorts the geometry of the aortic tree to the point where angles of branching are markedly changed (Fry, 1976). This could have the effect of changing a relatively well-behaved flow field into a considerably more tortuous one which would result in a significant alteration in the local detailed fluid dynamics characteristics.

Turbulence has also been postulated as a possible atherogenic factor (Mitchell and Schwartz, 1965; Wesolowski et al, 1965). However, both *in vitro* studies in model bifurcations and *in vivo* monkey coarctation experiments fail to support this suggestion. First, measurements in several arterial branch models give no indication of turbulent flow over a physiological range of Reynolds numbers and flow division ratios (Bharadvaj et al, 1982(a)). Furthermore, *in vitro* pulsatile flow experiments using laser Doppler anemometry and *in vivo* pulsed Doppler ultrasound studies of carotid arteries in normal human subjects do not exhibit turbulence (Ku and Giddens et al, 1985). Findings show that strong secondary flow patterns at normal carotid bifurcations exist, while turbulence does not. Consequently, it has been suggested by several authors that turbulence is not a prominent feature at sites of early plaque formation.

Flow separation has been regarded as a primary hemodynamic factor associated with lesion development (Fox and Hugh, 1966). It is suggested that regions of local flow separation at arterial branch points and along curved segments cause zones of stasis to form. The bloodstream stagnates locally and allows platelets and fibrin to form a mesh at the wall in which lipid particles become trapped and eventually coalesce to form atheromatous plaques. Nevertheless, the configurations chosen in this study were not representative of typical configurations in the arterial system. Consequently, severe adverse pressure gradients were generated locally in these experiments which excessively accentuated flow separation behaviour compared with anticipated behaviour in the vascular tree. Although zones of flow separation may well influence lesion development within the arterial system, the results of this study should not be interpreted as being representative of typical arterial flow conditions (Gessner, 1973).

Wall shear stresses have received most attention and have long been considered as an important factor in the pathogenesis of atherosclerosis. Different hypotheses have been postulated from this point of view, those of (i) high wall shear stress, (ii) low wall shear stress, and (iii) wall shear stresses which change direction over time. Fry (1969, 1972) demonstrated that extremely high shear stresses can result in actual mechanical damage to the endothelial lining of the arterial wall and increase permeability to lipid, thus he suggested that this can foster the onset of early atheroma. This view was supported by observations in hyper-cholesterolemic diet animals. However, subsequent experiments found that these very high rates of shear required for mechanical damage to the arterial wall do not exist in the actual circulation. Caro and co-workers (1971, 1981) studied the distribution of early atheroma in a large number of human and canine subjects and showed that early lesions occur preferentially in regions where arterial wall shear rate is expected to be relatively low, while the development of lesions is inhibited or retarded in those regions where wall shear rate is expected to be high. This hypothesis has gained

much support from other laboratory and theoretical investigations (Friedman et al, 1981; Kjaernes et al, 1981). It suggests that the development of atheroma is associated with shear dependent mass transport phenomena rather than wall damage due to the motion of blood. The explanation of this concept is that accumulation of material in the wall is in part due to alteration of material entering the wall and inadequate efflux of material from the wall to blood.

The low shear stress hypothesis is also supported by experimental studies of flow in a scale model of the human carotid bifurcation (Ku and Giddens et al, 1985). These studies not only confirmed earlier findings that atherosclerotic plaques tend to form in area of low, rather than high wall shear stress, but also indicated that marked oscillation in the direction of wall shear stress may enhance atherogenesis. This proposal has now been generally accepted, although the underlying mechanisms are not yet clearly established.

The mechanisms by which hemodynamic factors influence the development of atherosclerosis have been studied in a number of laboratories. Two of the major theories of atherogenesis are : (i) endothelial injury; and (ii) insufficient efflux of endogenous cholesterol. Although some form of injury to arterial endothelial cells may result in traumatic aneurysm, dissection and thrombosis; and insufficient rate of mass transfer from arterial wall to blood may account for the buildup of plaques in regions with constant low wall shear stress, neither of these hypotheses adequately explains the complex set of experimental and observed data encompassing atherosclerosis. However, parts of each of these theories in conjunction with another factor which is constantly present in the artery may have the potential to account for such complicated phenomena. Evidence to date indicates that this factor is the hemodynamic stress associated with arterial blood flow. Thus, a detailed study of flow patterns and shear stress distributions at arterial bifurcations becomes highly desirable.

1.2 GENERAL FEATURES OF ARTERIAL BIFURCATION FLOW

Flows at bifurcations have been studied by numerous investigators both experimentally and numerically (e.g. O'Brien, 1976 and 1977; Bharadvaj, 1982(a,b); Ku and Giddens, 1983 and 1987; Perktold et al, 1990 and 1991). The general features of bifurcation flow which are relevant to flow in arteries can be summarised as follows :

- (a) highly unsteady flows;
- (b) substantially three-dimensional with secondary flows in the branches;
- (c) flow separation in the branch with lower mean velocity;
- (d) increasingly disturbed flow as branch angle increases;
- (e) considerably higher wall shear stress at the apex in comparison with the outer wall.

Figure 1.1 illustrates the flow distribution, separation-reattachments and vortices in the median plane of a 90° glass model T-junction with uniform diameter. For an upstream Reynolds number (Re_o) of 245 and a flow division of $Q_1/Q_2 = 0.25$, paired spiral secondary flows and separation zones are clearly present: a large separation zone in the main tube at the entry of the daughter tube; and a small secondary corner separation zone at the entry of the side branch. Such patterns may also occur in the arterial circulation.

The flow patterns at the bifurcation and the formation and sizes of the separation regions are strongly influenced by the detailed bifurcation geometry including vessel diameters, branching angle and the shape of the apex; upstream flow rate as manifested through the Reynolds number; flow division between branches; and the pulsatile nature of the flow, i.e., the shape of the flow waveform, as well as the amplitude and frequency of the pulsation. It is, therefore, very important to model the bifurcation geometry, pulse waveform, upstream boundary conditions and down-

stream resistances physiologically accurately. It should also be emphasised that a fully three-dimensional modelling of the flow under pulsatile conditions is virtually essential, due to the presence of the non-negligible three-dimensional phenomena, such as secondary flow in the bifurcating and curved regions, and the highly unsteady nature of the arterial flow. In addition, there are two relatively minor factors which may have influences on the flow at bifurcations, i.e., the distensibility of the blood vessel wall and the non-Newtonian viscosity of the blood. In most of the previous studies, they were regarded as “second-order” factors and were generally neglected. However, recent experimental results (Moravec and Liepsch, 1983; Ku and Liepsch, 1986) tend to indicate that wall compliance and non-Newtonian flow behaviour may well be important factors in the understanding of arterial bifurcation flows. To explore their effects further, the distensibility of the vessel wall and the non-Newtonian effects of the blood must be accommodated in numerical modelling of these flows.

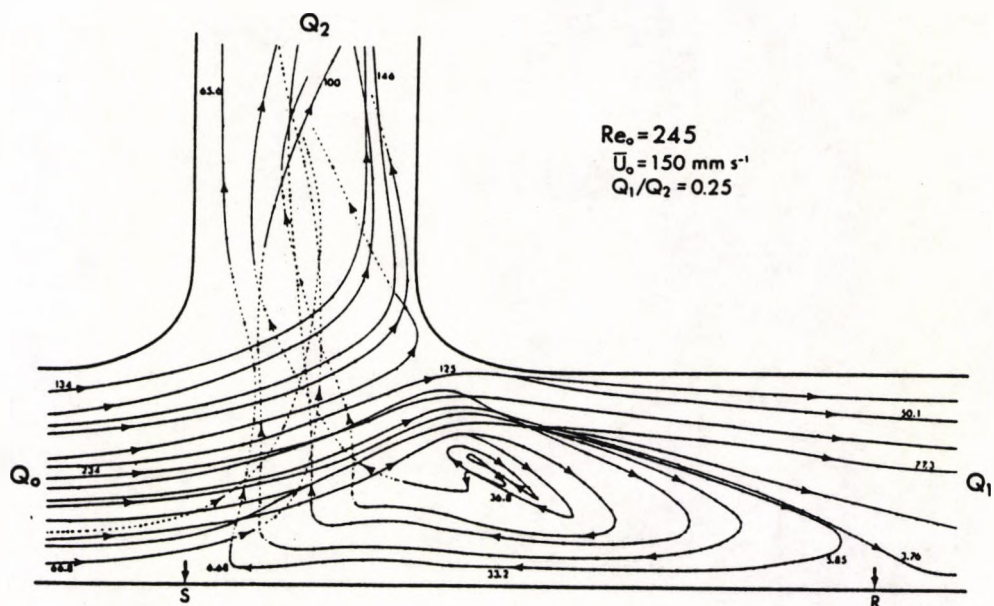


Fig. 1.1 Partial paths in the median plane of a rounded T-junction at

$Re_0=245$ and $Q_1/Q_2 = 0.25$. (From Karino *et al*, 1979)

1.3 MODEL DESCRIPTION AND ITS VALIDITY

The basic equations required for modelling fluid flow are the equations of conservation of mass and momentum, the constitutive equations specifying the mechanical properties of the material, and if heat transfer and chemical reactions are involved, the energy and reaction rate equations. These coupled with the boundary conditions are all that are needed for a numerical simulation. To construct a mathematical model for a specific problem, the equations can be simplified accordingly.

Focusing upon the problem of blood flow in arterial bifurcations, the general features of the flow have been described in the preceding section. It should be noted that despite the existence of such complex phenomena as separated and secondary flow; blood flow in arterial bifurcations can be regarded as laminar, since in the human circulatory system the duration of a heartbeat is too short to develop a full turbulent flow (Liesch, 1986).

Also emphasised in the previous section is the necessity of accommodating the three-dimensional nature of the bifurcation geometry and the pulsatility of the flow. This demands the treatment of the full three-dimensional time-dependent Navier-Stokes equations. As for the bifurcation geometry, an idealised 90° T-bifurcation was adopted first for code validation purpose, since a complete set of experimental data for such a bifurcation was available. As presented in chapter 5, the T-bifurcation geometries used in this study were the same as those employed in the experiment. For the modelling of physiological flow in canine femoral bifurcations, geometries of the two bifurcation models adopted here were based upon data from the *in vivo* measurements (Jones et al, 1990), in which branching angles, B-mode ultrasound images of the cross-sections of the upstream parent and both daughter vessels, and the origin of both vessels were all photographed. True geometrical data measured from photographs were used in the predictions. Details of

these are described in chapter 6.

Blood flow in arteries is pulsatile with instantaneous blood velocity and pressure varying during a cardiac cycle according to the pumping action of the heart. When dealing with flows in idealised T-bifurcations, a sinusoidal oscillating pressure gradient was superimposed on a steady flow to generate the pulsatile flow. When canine femoral bifurcation flows were treated, two types of physiological velocity waveform were employed. One was an averaged velocity waveform in canine arteries, another was the *in vivo* waveform measured upstream of each bifurcation models.

Two dimensionless parameters have been consistently used in this dissertation to characterise the flow, they are defined as follows:

$$\text{Reynolds number} = \frac{\text{inertial force}}{\text{viscous force}} = \frac{\rho \bar{U} d}{\mu} \quad (1.1)$$

$$\text{Womersley number} = \sqrt{\frac{\text{transient inertial force}}{\text{viscous force}}} = \frac{d}{2} \sqrt{\frac{\rho \omega}{\mu}} \quad (1.2)$$

d being the parent vessel diameter, \bar{U} the time-averaged velocity in the parent vessel, ρ the fluid density, μ the dynamic viscosity, and ω the angular frequency of the pulsating flow. In the canine femoral bifurcations studies, the mean Reynolds number was about 100 and the Womersley number around 2.2.

Blood is a suspension of a variety of cells in an aqueous solution called plasma. In large blood vessels, it is reasonable to consider blood as a homogeneous incompressible fluid. But blood is not generally Newtonian, its viscosity varying with shear rate. While at very high shear rates ($> 1000 S^{-1}$) blood can be assumed as

Newtonian, but at low shear rates the viscosity of blood decreases with the increase of shear rate. Actually in large arteries such high shear rates occur only during a relative short part of the cycle period, and in addition, predominantly close to the wall. Consequently, it is more appropriate to treat blood as a non-Newtonian fluid. Several functional forms for constitutive equations have been developed to model the non-Newtonian behaviour of blood (Walburn and Schneck, 1976; Nakamura and Sawada, 1988; Rodkiewicz et al, 1990). Among these the general power law was considered to be more appropriate and was therefore adopted in this study .

The arterial wall is anisotropic and viscoelastic. In the actual circulation the radial dilatation of large arteries is up to 2–15%, while the longitudinal movement is very small because of the tethering of vessels to the surrounding tissues. A large variety of mathematical models for the mechanical properties of the arterial wall have been derived under various assumptions. Among these models the pseudo strain energy functions derived from finite nonlinear elastic deformation analysis were claimed to be one of the simplest and most accurate forms. In this model the arterial wall is assumed to be homogeneous, incompressible and non-linearly elastic. These assumptions have been proven valid within the normal physiological pressure range (Fung et al, 1979; How and Clarke, 1984). Hence, a polynomial form of strain energy function was adopted in this study. A simplified coupled approach to incorporate this in the fluid flow modelling was developed, i.e., fluid flow equations and wall displacement equation are solved separately within a time step, but are connected in terms of pressure and boundary conditions. The essential procedures of this approach can be summarised as follows: at each time step (i) solve the flow equations as if the wall is rigid, (ii) apply the pressure obtained from (i) as loading on the wall and solve the stress-strain function to evaluate radial displacement of the wall. (iii) the result of (ii) is then used to determine the new boundary position for (i). This approach is valid provided that the wall movement is much slower than that of the fluid and the flow is generally parallel to

the wall. At the present stage, however, this approach has only been applied to a straight circular tube. Due to the insufficient memory capacity of ULCC's CRAY X-MP/28 (which has been replaced by CONVEX) and the time constraints of this study, applications to bifurcation geometry will be carried out in future studies.

1.4 OBJECTS OF RESEARCH

Due to the potential importance of arterial blood flow related hemodynamic stress in atherogenesis, this research focuses on gaining and analysing detailed information on flow field and wall shear stress distribution in physiologically valid arterial bifurcation models, by means of computational fluid dynamics techniques. The main purposes of the research may then be stated as follows:

- (a) to construct a purpose-built module to be able to generate grids for arbitrary three-dimensional arterial bifurcations with the minimum user input.
- (b) to incorporate the non-Newtonian viscosity of blood in the existing code and to investigate its effects on a bifurcation flow field.
- (c) to explore the possibility of incorporating wall compliance in the existing fluid flow modelling code.
- (d) to carry out a wide range of code validation exercises for flow in idealised T-bifurcations under various flow conditions by comparison with reliable LDA measurements.
- (e) to provide predictive data for *in vivo* canine femoral bifurcation measurements of Jones et al, and hence to validate the numerical results against the experimental ones.

and in addition

- (f) to provide wall shear stress distributions which were unobtainable *in vivo*.

In doing so, it would help

- (g) to reduce the need for *in vivo* measurements.
- (h) to acquire a better understanding of the role of hemodynamics in the formation of atherosclerosis.

1.5 METHODOLOGY AND STRATEGY EMPLOYED

The problem of blood flow in arterial bifurcation involves many complicating factors, such as, complex 3D geometry, pulsatility, wall distensibility and non-Newtonian viscosity. Full incorporation of all these features in one prediction is a tedious computational task and no one has yet achieved this so far. However, in numerical studies it is possible to isolate each one of these and to investigate their individual and combined influence on the flow field of interest, and consequently to make the model more close to reality. This is the rationale followed in this research.

From the numerical simulation point of view, several methods are available for the solution of flow equations, of which the finite difference/ finite volume (FV) method and the finite element (FE) method are the most important ones. The major advantage of FE methods is their ability to cope with complex geometries and highly non-uniform grids. Therefore, the application of finite element methods to flow problems of complex 3D geometries with high velocity gradients seems to be more appropriate. Nevertheless, the cost of inverting the global matrices that they introduce in time-dependent flows is quite prohibitive. On the other hand, FV methods are more efficient in their use of computer storage and time, but are less amenable to irregularly shaped geometries. Although coordinate transformation can be used to good effect on some simple problems, accurate representation of complex geometries is far more difficult. To make a compromise between computational economy and geometrical flexibility, it would be ideal to combine the

features of both FE and FV methods in one. The newly released CFD code ASTEC, developed at UKAEA, provided such a unique combination. While retaining the efficiency of FV solution methods, it has an unstructured mesh giving it the flexibility of a FE system. This unusual feature has made it the most suitable code for the current application, although it does not have adaptive or transient gridding capability.

An alternative code is FLOW3D from AERE, Harwell. It is a FV code using non-orthogonal body-fitted coordinates. Although its latest version is capable of accommodating almost all the features of the flow problem under consideration, its earlier version (at the time this research started) could not tackle 3D bifurcation geometries unless highly idealised. Yet, since FLOW3D has become one of the market leaders in FV codes, and especially in our research center (Thermo-Fluids Engineering Research Center, City University) Collins et al have about 11 years' experience of using this code for various problems including transient laminar flows as well as turbulent flows (eg. Ciofalo and Collins, 1988; Ciofalo and Collins, 1990), it would be of interest for validation purposes to provide an extra set of predictive data using FLOW3D as a basis for code to code comparison. Hence, in this research ASTEC was used for solving the flow problem, while FLOW3D was solely used at the initial stage of code validation (see chapter 5).

The strategy of the analysis followed a logical progression. First of all, a comprehensive range of code validation exercises was performed. This was started with predictions of fully developed flow in a straight circular tube with (i) non-Newtonian viscosity, (ii) pulsatility of flow, and (iii) wall elasticity being taken into account in turn, in order to test the code's capability of dealing with these cases, and the accuracy of predictions checked through quantitative comparison with established analytical solutions and laboratory measurements. This was followed by investigations of both steady and pulsatile flows in an idealised plane 90°

T-bifurcation under various flow conditions, and the predictions were validated against published LDA measurements. These results would not only demonstrate the reliability of the numerical predictions, but also give a clear indication of how the bifurcation flow field and wall shear stress distribution were influenced by the basic flow parameters. Then the investigation proceeded to study flow in a 3D T-bifurcation of circular cross-section with (i) Newtonian and (ii) non-Newtonian fluid; these results would reveal the importance of three-dimensional modelling and the effects of flow pulsatility and non-Newtonian viscosity. Having done these, true physiological flows in canine femoral bifurcations were studied and detailed information on flow field and wall shear stress were obtained. Finally, predicted velocity profiles were validated by means of quantitative comparison with the *in vivo* measurements obtained by Jones et al (1990).

All calculations presented in this dissertation were carried out on ULCC's CRAY X-MP/28, while pre- and post-processing were performed on Sun workstations at the City University.

CHAPTER 2

NUMERICAL METHODS FOR THE SOLUTION OF 3D TIME-DEPENDENT NAVIER-STOKES EQUATIONS

2.1 INTRODUCTION

The flow of blood through an arterial bifurcation segment can be considered as a time-dependent three-dimensional incompressible laminar flow. In this chapter, the basic equations are introduced, and the currently employed numerical methods for solving these equations, including discretisation methods, advective term schemes, time differencing schemes and pressure-velocity coupling algorithms, are summarised. This is followed by an introduction and comparison of commercially available CFD (computational fluid dynamics) software packages; among them ASTEC is described in detail.

2.2 GOVERNING EQUATIONS

Modelling fluid flow requires the simultaneous satisfaction of two conservation principles, namely those of continuity and momentum. Expressed in compact tensor notation, with summation over repeated indices, the basic continuity and momentum equations may be expressed as:

$$\frac{\partial \rho}{\partial t} + \frac{\partial}{\partial x_i}(\rho u_i) = 0 \quad (2.1)$$

and

$$\frac{\partial}{\partial t}(\rho u_i) + \frac{\partial}{\partial x_j}(\rho u_j u_i) = \frac{\partial}{\partial x_j} \sigma_{ij} + F_i \quad (2.2)$$

Since no heat transfer is involved in this particular problem, the energy equation can be omitted. In these equations, u_i is the velocity of the fluid, x_i the Cartesian coordinates, ρ the fluid's density, σ_{ij} the stress tensor and F_i the body force which consists mainly of inertial force due to gravitational acceleration and is usually

negligible in analysing blood flow in arteries.

For a Newtonian fluid with a constant viscosity of μ , the stress tensor σ_{ij} is given by:

$$\sigma_{ij} = -p\delta_{ij} + \lambda S_{kk}\delta_{ij} + 2\mu S_{ij} \quad (2.3)$$

where δ_{ij} is the Kronecker delta, S_{ij} the strain rate tensor defined as:

$$S_{ij} = \frac{1}{2} \left(\frac{\partial u_i}{\partial x_j} + \frac{\partial u_j}{\partial x_i} \right) \quad (2.4)$$

and λ the material constant. Since the fluid is assumed to be incompressible, the condition of incompressibility $\partial u_i/\partial x_i = 0$ reduces Eqn.(2.3) to the form:

$$\sigma_{ij} = -p\delta_{ij} + 2\mu S_{ij} \quad (2.5)$$

substituting these into Eqn.(2.2), the governing equations for an incompressible Newtonian fluid are obtained:

$$\frac{\partial u_i}{\partial x_i} = 0 \quad (2.6)$$

and

$$\frac{\partial u_i}{\partial t} + u_j \frac{\partial u_i}{\partial x_j} = -\frac{1}{\rho} \frac{\partial p}{\partial x_i} + \frac{\mu}{\rho} \frac{\partial^2 u_i}{\partial x_j \partial x_j} \quad (2.7)$$

For 3-D flows, Eqns (2.6) and (2.7) comprise four equations for four flow variables, i.e., three velocity components and pressure. Together with appropriate initial and boundary conditions these equations are solvable.

As mentioned in Chapter 1, blood is not a Newtonian fluid. Its viscosity is not a constant, but varies with the strain rate. To accommodate the non-Newtonian

behaviour of blood the Newtonian equation (2.5) can be generalised as (for details, see Appendix A):

$$\sigma_{ij} = -p\delta_{ij} + 2\mu(J_2)S_{ij} \quad (2.8)$$

where μ is a function of J_2 — the second invariant of the strain rate tensor:

$$J_2 = \frac{1}{2}S_{ij} S_{ji} \quad (2.9)$$

Substituting Eqn.(2.8) into Eqn.(2.2), we obtain a set of governing equations for an incompressible non-Newtonian fluid:

$$\frac{\partial u_i}{\partial x_i} = 0 \quad (2.10)$$

and

$$\frac{\partial u_i}{\partial t} + u_j \frac{\partial u_i}{\partial x_j} = -\frac{1}{\rho} \frac{\partial p}{\partial x_i} + \frac{1}{\rho} \frac{\partial}{\partial x_j} \left[\mu(J_2) \left(\frac{\partial u_i}{\partial x_j} + \frac{\partial u_j}{\partial x_i} \right) \right] \quad (2.11)$$

To solve Eqns (2.10) and (2.11), the constitutive equation for the non-Newtonian behaviour of the blood must be specified. Details about the constitutive equations of the blood and its incorporation in the flow equations are covered in Chapter 3 and 4 respectively.

These governing equations are complex non-linear partial-differential equations. The numerical approaches for solving these equations are discussed in the succeeding sections.

2.3 DISCRETISATION METHODS

2.3.1 Spatial Discretisation

Methods used to discretise the flow governing equations can be roughly divided into three categories: (a) finite difference/finite volume methods; (b) finite element methods; and (c) spectral methods.

Finite difference and finite volume methods have the similar appearance, but differ slightly in the methodology used. The usual procedure used in finite difference methods is to approximate the derivatives in Eqns. (2.1)–(2.2) via a truncated Taylor series. Thus the unknowns of the resulting algebraic equations contain only the values of the flow variables at discrete points. The same view is adopted in finite volume methods, in which the computational domain is split up into a number of non-overlapping control volumes, and the differential equations are integrated over each control volume, ensuring discrete conservation of mass, momentum and energy. To evaluate the required integrals in the formulation, interpolation procedures or profile assumptions expressing the variation of flow variables between the grid points are needed. The resulting discrete equation is a system of nonlinear algebraic equations containing the values of flow variables at grid points.

One of the most attractive features of the finite difference or finite volume methods is that they are easy to understand and lend themselves to direct physical interpretations. For this reason and their relatively less computer cost, they are now by far the most popular methods in CFD. However, the significant drawback of the finite difference methods (on a regular coordinate grid) is that they are less amenable to irregular-shaped geometries, as the representation of curved or inclined boundaries on a Cartesian grid is not convenient. This problem has been partially overcome by the introduction of body-fitted curvilinear coordinates, but even so, accurate representation of complex geometries is still problematical.

Finite element methods subdivide the computational domain into a set of elements, which could be triangles or quadrilaterals in 2D and tetrahedra or hexahedra in 3D. Each flow variable is approximated by a 'shape function' or profile assumption and the discretised equations are usually derived by the use of a variational principle or the Galerkin method, which is a special case of the method of weighted residuals.

Finite element methods were originally developed for stress and strain analysis in structural mechanics, but were rapidly expanded into many other areas, particularly they are receiving increased attention in CFD (Cuvelier et al, 1986). The major advantage of finite element methods is their more general geometric capabilities, so that irregular geometries can be treated with relative ease. However, these methods are computationally very expensive for the time-dependent flows due to the global matrices introduced. Although Gresho (1984) and others have modified the finite element algorithm for solving the time-dependent incompressible Navier-Stokes equations, the computer code produced was still more expensive than the standard finite difference codes. Moreover, high-order differencing schemes and model changes can be cumbersome to implement.

Spectral methods are characterised by the expansion of each flow variables in a truncated series of global polynomials. An essential aspect of spectral methods is the choice of expansion functions which must be appropriate to the boundary conditions of the problem. For example, Fourier series are only appropriate for problems with periodic boundary conditions; while in the general, nonperiodic case, normalised to $[-1, 1]$, the appropriate class of functions is the polynomials, such as Chebyshev and Legendre functions.

Numerical spectral methods for partial differential equations were originally developed by meteorologists. These methods used in fluid mechanics prior to 1970 are now termed spectral Galerkin methods, in which the equations are derived by the techniques used in classical analysis, and the fundamental unknowns are the expansion coefficients. With the advent of computers, an alternative discretisation method — spectral collocation technique — has been developed (Kreiss and Olinger, 1971; Orszag, 1972), in which the unknowns are the values at selected collocation points, and the series expansion is used solely for the purpose of approximating

derivatives.

Spectral methods have become the prevailing tool for large-scale calculations. They are more accurate than comparably resolved finite difference and finite volume algorithms, but prove correspondingly more difficult in handling general boundary conditions and usually require more operations per mesh point. Thus, by the present time their applications have been mostly restricted to simple problems.

2.3.2 Treatment of Advection

The main consideration in the derivation of the discretisation equations is the formulation of the advection and diffusion terms. It has been recognised that the advection-diffusion discretisation scheme has a direct consequence on the accuracy of the solution, and the convergence of the problem is also dependent on the scheme. Thus, it is essential to choose an appropriate advection diffusion formulation that leads to stable and accurate results with grids of modest fineness.

The established methods, such as the central-differencing scheme, upwind scheme, hybrid scheme (Spalding, 1972), and the power-law scheme (Patankar, 1980), have their own drawbacks in terms of accuracy and stability. The central-differencing scheme is likely to give a physically unrealistic solution ('wiggles') when the cell Peclet number ($P_c = \frac{\rho u \delta x}{\Gamma}$) exceeds 2. Although it is, in principle, possible to refine the grid until P_c is small enough (< 2), this strategy is not feasible in most practical problems. A remedy for this is the upwind scheme, but it is well known that this scheme causes severe false diffusion. An alternative is the hybrid scheme which is a combination of the central-differencing and upwind scheme (use central-differencing scheme when $|Pc| < 2$, and upwind scheme when $|Pc| \geq 2$), but still can not eliminate false diffusion errors. Thus, a number of new formulations have been proposed for preventing 'wiggles' while minimising numerical diffusion. These may be summarised as follows:

(a) 'Skew upwind' schemes based on the concept of Raithby (1976), that the direction of the velocity vector is used in obtaining the convective influence from upstream. Similar techniques are 'mass-flow-weighted skew upwind' (Hassan, 1983), 'vector upstream' (Lillington, 1981) and 'bounded skew upwind' (Syed and Chiappetta).

(b) Higher-order schemes, such as the second-order upwind, the third-order upwind based on the quadratic upstream interpolation 'QUICK' (Leonard, 1979), the 'Hermitian polynomial' scheme (Glass and Rodi, 1982) and the 'spline' methods (Rubin and Graves, 1975; Kumar, 1981).

(c) Methods based on a locally exact solution of the differential equations, such as the 'locally analytical method' (Wong and Raithby, 1979; Stubble et al, 1980), and the 'finite analytical method' (Chen et al, 1981).

(d) Modified-central differencing schemes, such as CONDIF (Runchal, 1987), and NONDIF (Hedberg, 1989).

A large number of comparative studies has been conducted and their major results are summarised by Patankar (1988). He concluded that the formulation of a satisfactory advection-diffusion scheme still remains an unresolved question. Lower-order schemes such as upwind or hybrid are stable and monotonic but involve severe false diffusion. Higher-order schemes such as QUICK eliminate false diffusion but produce nonphysical overshoots and undershoots, and lead to oscillations and divergence. Also, higher-order schemes imply a significant increase in computational complexity — one way of handling this is the 'deferred correction approach' employed by Burns and Wilkes (1987), where the extra terms are absorbed into the source term on the right hand side of the equations.

2.3.3 Time Differencing Schemes

For transient problems, the time derivative of the flow variable in the differential equations can be approximated in many ways. If the equation for a flow variable ϕ is written in the form:

$$\frac{\partial \phi}{\partial t} = F(\phi) \quad (2.12)$$

then the discretised form can be generalised as:

$$\frac{\phi^{n+1} - \phi^n}{\Delta t} = xF(\phi^{n+1}) + (1 - x)F(\phi^n) \quad (2.13)$$

The quantity of x is used to denote the level of implicitness, for example, $x = 1.0$ gives the fully implicit scheme; $x = 0.5$ gives a Crank–Nicolson scheme and $x = 0.0$ reduces to the fully explicit scheme. It is known that the fully implicit and the Crank–Nicolson schemes are usually considered as unconditionally stable in a mathematical sense, while the explicit scheme is subject to the Courant stability criterion, which can be expressed as:

$$C_r = \frac{c}{\Delta x / \Delta t} \leq 1 \quad (2.14)$$

where C_r is the Courant number, c the celerity of propagation in the analytical solution, Δx the width of the smallest mesh, and Δt the time step.

2.4 COMPUTATION ALGORITHMS

The available methods for solving flow equations can be roughly divided as being based on primitive variables or vorticity. The methods based on vorticity–stream function have been rather popular in two–dimensional simulations for a long time. The essential feature of this approach is that the pressure makes no appearance, thus, instead of dealing with the continuity equation and the momentum equations, only two equations need to be solved to obtain the stream function and vorticity. However, this method has difficulties for the specification of the

vorticity boundary conditions at sharp corners, and is not easy to extend to three-dimensional situations, for which a stream function does not exist. Therefore, attention has turned to formulations based on the primitive variables, namely the velocity components and pressure.

A number of currently employed velocity/pressure coupling methods originate from the SIMPLE procedure which was first introduced by Patankar and Spalding (1972). Essentially, the SIMPLE method is based on a two-step iterative cycle, in which a guessed pressure field is introduced in the momentum equations to evaluate velocities, and then a pressure-correction equation derived by enforcing continuity under certain simplifications, is solved to obtain an improved guess. However, the original SIMPLE method is rather slow to converge and needs heavy under-relaxation. Thus, a number of more efficient variants of SIMPLE have been developed, and are outlined as following:

(a) SIMPLER method (Patanekar, 1980; 1981), in which an extra equation is solved for the evaluation of pressure. It has been found to give faster convergence than SIMPLE.

(b) SIMPLEST method (Spalding, 1980), which is based on an explicit treatment of convective and implicit treatment of diffusive terms in the momentum equations.

(c) SIMPLEC method (Van Doormaal and Raithby, 1984), which uses consistent under-relaxation for the momentum and pressure corrections. It has been shown to allow faster convergence for problems dominated by pressure gradients and drag forces. For a number of model problems, it has proved less sensitive than SIMPLE to selection of under-relaxation factors (Burns et al, 1987).

(d) PISO method (Issa, 1985), in which an additional pressure-correction step is performed at each iteration to improve the solution of the momentum equations while maintaining continuity. For transient problems, it may be used as a non-iterative algorithm, but requires an accurate solution of the linearised equations.

On the whole, it has proved to be faster than SIMPLE for transient problems in which the flow field varies markedly at each step, but not for 'smooth' time-dependent flows (Ciofalo and Collins, 1988).

(e) PISOC method, in which the similar modifications of SIMPLEC are applied to PISO.

To solve the linearised momentum equations and pressure-correction equations, the Gauss-Seidel point-by-point or line-by-line methods have been commonly used. However, these methods converge very slowly, especially when a large number of grid points are involved. An alternative method for solving multidimensional discretisation equations is the Strongly Implicit Procedure (SIP) described by Stone (1968) which has been found more reliable for large three-dimensional problems, especially those with many internal blockages (Burns, et al, 1987). Experience has also shown that it is best to solve the pressure-correction equation to a higher degree of accuracy than the other equations. Since the matrix representing the pressure-correction equation is symmetric, the preconditioned conjugate gradient (PCG) method may be applied. Kightley and Jones (1985) have found that a simple incomplete Cholesky preconditioning is a good compromise between efficiency and reliability on both scalar and vector computers.

A number of new techniques have recently been proposed, some of them being extensions of the Stone's method. Lin (1985) has proposed the use of three free parameters to accelerate the convergence of Stone's method. In the methods formulated by Schneider and Zedan (1981) and Peric (1987), the five-diagonal matrix in Stone's method is replaced by a nine-diagonal matrix. As a result, these modified methods are applicable to the discretisation formulations that lead to nine-diagonal matrices; they are also shown to be more efficient when applied to five-diagonal systems as well. In a series of papers, the use of multigrid techniques has been introduced. Phillips and Schmidt (1984) described the use of this technique for

solving the diffusion equations. One useful aspect of the multigrid technique is that it allows local grid refinement in the regions of large gradients. The introduction of local grid refinement in the solution of convection–diffusion equation is demonstrated by Phillips and Schmidt (1985a). They also presented a multilevel–multigrid technique for recirculating flows (Phillips and Schmidt, 1985b).

2.5 AVAILABLE COMPUTER CODES

2.5.1 Introduction

Computational fluid dynamics (CFD) has been used for flow predictions since about 1965. With the rapid development of computer hardware, it has grown into a major technique area. Up to now, a number of CFD computer programs have been produced based on either finite difference/finite volume or finite element methods with various numerical features and varying degrees of modelling capabilities. In this section a comparison of some of the most popular CFD packages that are commercially available is presented. Particular emphasis is laid on ASTEC, which was used throughout this research.

2.5.2 Comparison of CFD Codes

A list of some of the most popularly available CFD codes includes: PHOENICS, FLOW3D, FLUENT, ASTEC, STARCD, FIRE, FIDAP, P/FLOTRAN and FEAT, all having three dimensional capability. Table 2.1 lists the suppliers of the computer programs. The modelling capabilities and numerical features of all the programs are compared in Table 2.2 and Table 2.3 respectively. Note that solving incompressible laminar flows with a Newtonian fluid for steady state conditions is generally regarded as a very basic requirement for a CFD code, and is ready to be treated by almost all these codes. Hence, only the additional modelling capabilities, such as transient, non-Newtonian, multi-phase flow *et al*, and the numerical

features of the codes are compared.

CODE	TYPE*	SUPPLIER	COUNTRY
PHOENICS	FV	CHAM	UK
FLOW3D	FV	CFDS Harwell	UK
FLUENT	FV	CREARE Inc.	USA
ASTEC	Hybrid	CFDS Harwell	UK
STAR-CD	Hybrid	Computational Dynamics	UK
FIRE	FV	AVL LIST	AUSTRIA
FIDAP	FE	Fluid Dynamics Int.	USA
P/FLOTRAN	FE	PDA Engineering	USA
FEAT	FE	Nuclear Electric	UK

*FE : Finite element code

FV : Finite volume code

Hybrid : Essentially FV but offering unstructured mesh

Table 2.1 Suppliers of CFD Codes.

In both finite element and finite difference methods, the accuracy of the solution depends not only on the formulation of the convection and diffusion terms, but also on the fineness of the mesh and the mesh distribution. Thus, the accuracy of different program is hard to quantify, and in Table 2.3 it is given as the order of accuracy of the advection schemes employed. The cost of each program is even more difficult to quantify, as it tends to be problem-dependent and machine-dependent. Generally, finite element codes using direct solution methods are more expensive.

The advent of supercomputers with their vector processing and parallel processing capabilities has made some impact on how computer programs and numerical algorithms are designed. To obtain the best performance from current supercomputers, some of the codes have been specifically tailored and designed to achieve a high degree of vectorisation. This information is also included in Table 2.3.

CODE	PHOENICS	FLOW3D	FLUENT	ASTEC	STARCD	FIRE	FIDAP	P/FLOTRAN	FEAT
(1) Physical model									
Turbulent	✓	✓	✓	✓	✓	✓	✓	✓	✓
Transient	✓	✓	✓	✓	✓	✓	✓	×	✓
Compressible	✓	✓	✓	✓	✓	✓	×	×	×
Non-Newtonain	✓	×	✓	×	×	✓	✓	×	×
Two-phase	✓	✓	×	×	×		×	×	×
Buoyant	✓	✓	✓	✓	✓		✓	✓	✓
Porous media	✓	✓	✓	✓	✓		✓	×	
Combustion	✓	✓	✓	✓	✓		✓		
Chemical reaction	✓	✓	✓	×	✓		×		
Free surface	✓	✓	✓	×	×			×	
Extra scalars	✓	✓	✓	✓		✓	×	×	
(2) Grid									
Type of grid	FV S	FV S	FV S	FV US	FV US	FV US	FE US	FE US	FE US
Body-fitted coordinates	✓	✓	✓	N/A	N/A	N/A	N/A	N/A	N/A
Local grid refinement	×	×	×	✓	✓	✓	✓	✓	✓
adaptive gridding	×	✓	×	×	×				

*FV : Finite volume
FE : Finte element

S : Structured
US : Unstructured

Table 2.2 Comparison of codes' capabilities.

Apart from the flow solvers themselves, their pre- and post-processing facilities are also important. All the codes listed here have their own grid generation capability and graphics package, but their ease of use varies from code to code.

CODE	ADVECTION* SCHEME	ACCURACY	SOLUTION METHODS
PHOENICS	Hybrid Upwind	1st	Iterative
FLOW3D	Hybrid Upwind HUW QUICK CONDIF	1st/2nd	Iterative
FLUENT	QUICK	1st/2nd	Iterative
ASTECC	Hybrid Upwind SU HSU CONDIF	1st	Iterative
STAR-CD		1st/2nd	Iterative
FIRE			Iterative
FIDAP	Galerkin	1st	
P/FLOTRAN		equal	
FEAT			Iterative

*CONDIF : modified central differencing scheme
 HSU : hybrid skew upwind scheme
 HUW : second-order upwind scheme
 QUICK :: third-order upwind scheme
 SU : skew upwind scheme

Table 2.3 Comparison of codes' numerical treatment.

2.5.3 Details of ASTEC

2.5.3.1 General features and capabilities of the code

The ASTEC code was developed for modelling fluid dynamics and associated physical phenomena in complex geometries. The equations for three-dimensional, single phase flow are solved on a finite element mesh, which allows great geometrical flexibility. However, the discrete equations are derived using a finite volume approach, so that the code avoids the heavy usage of computing resources which characterises classical three-dimensional finite element flow codes. Its main features and capabilities are summarised in Table 2.4. Numerical methods employed in the code are outlined in Table 2.5.

Physical Models:	(a) Laminar flow Turbulent flow ($k-\epsilon$ model) (b) Incompressible Compressible for Mach numbers < 0.2 (c) Steady Transient (d) Buoyant (Boussinesq approximation or fully compressible) (e) Conduction in solids (f) User-defined equations for scalars
Geometry :	(a) 2D or 3D (b) Unstructured mesh consists of arbitrarily shaped 8-node elements (c) Boundaries : Solid region Inlet Outlet Thin surface Symmetry plane (d) Porous media

Table 2.4 Main features and capabilities of ASTEC.

(a) Finite volume discretisation	non-staggered grid except for pressure
(b) Treatment of advection:	Hybrid Upwind CONDIF Hybrid skew upwind
(c) Pressure-correction eqn. solver:	Conjugate gradients Algebraic multigrid
(d) Other transport eqns solver:	Algebraic multigrid Gauss-seidel
(e) Time-differencing:	Fully implicit
(f) Velocity/pressure coupling:	SIMPLE

Table 2.5 Numerical methods employed in ASTEC.

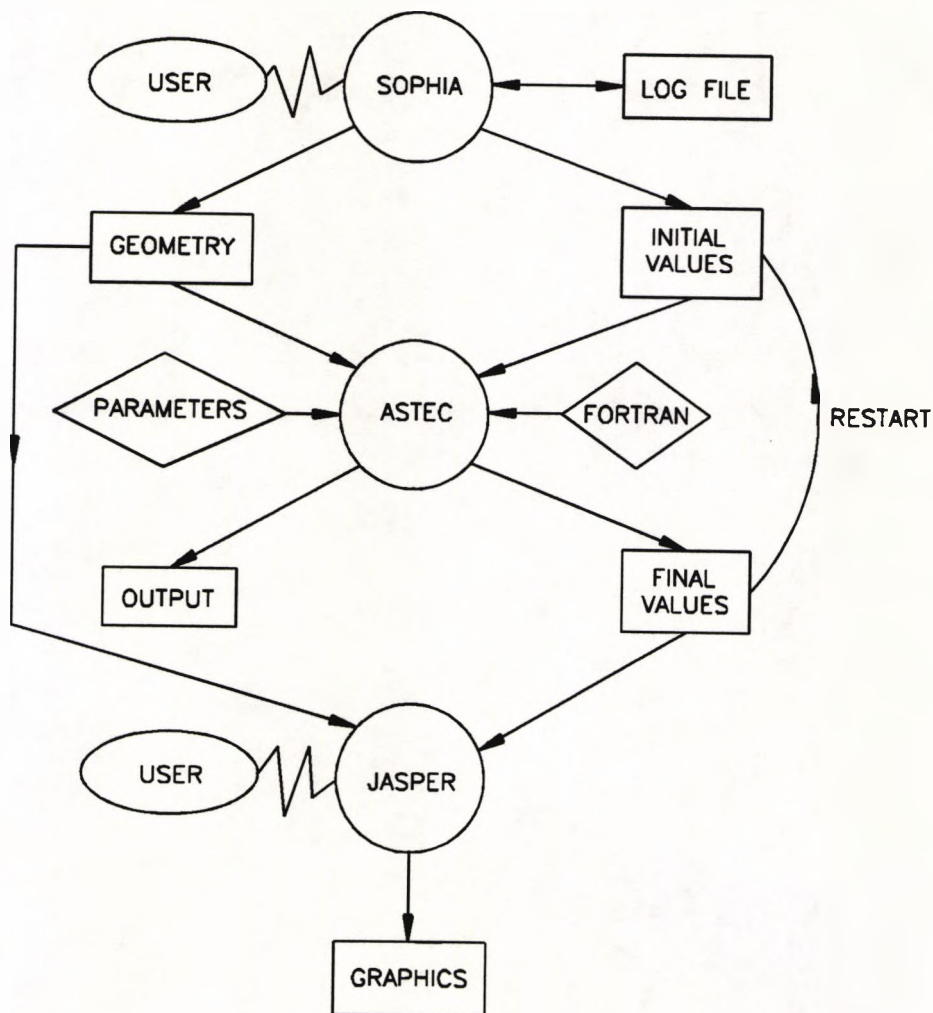


Fig. 2.1 Relationship between ASTEC, associated data files, and the pre- and post-processor.

ASTECC itself is a flow solver, and it is supported by a pre-processor SOPHIA and a post-processor JASPER (all developed in UKAEA). As illustrated in Fig.2.1, to use the package involves firstly running the mesh generator to produce a mesh file specifying the geometry, together with an initial values file containing the starting guess for the solution. To run ASTEC, an additional parameter data file is required for choosing options and generally directing the calculation. For some problems, user-supplied Fortran subroutines may be required for specifying non-standard additions to the model. After running ASTEC, an output file is produced which provide diagnostic messages from the code, including error messages. In addition, a dump file is generated which contains final values for the variables in the same format as the initial values file. Thus this dump file may also be used to restart the code. Once a solution is obtained, pictures of the results can be plotted by running the post-processor using the mesh and final dump files as input.

2.5.3.2 The mesh and discretisation

ASTECC has an unstructured mesh, which consists of arbitrary quadrilaterals in 2-D and 8-node blocks in 3-D. As shown in Fig.2.2, in 2-D situations a control volume around each node is defined by joining the midpoint of opposite sides in every element. Moving to 3-D, the region is split into eight node elements. Within each element, the points at the midpoint of each edge, and at the centre of gravity of the four nodes on each face, and at the centre of gravity of the eight nodes forming the element, are joined to construct a control surface around each node, which encloses the nodal control volume. The four points that define each face of the control surface need not be coplanar; the face is constructed from two triangles when the surface is not planar. Although each element must have eight nodes, note that there is no restriction regarding the number of elements to which a particular node belongs.

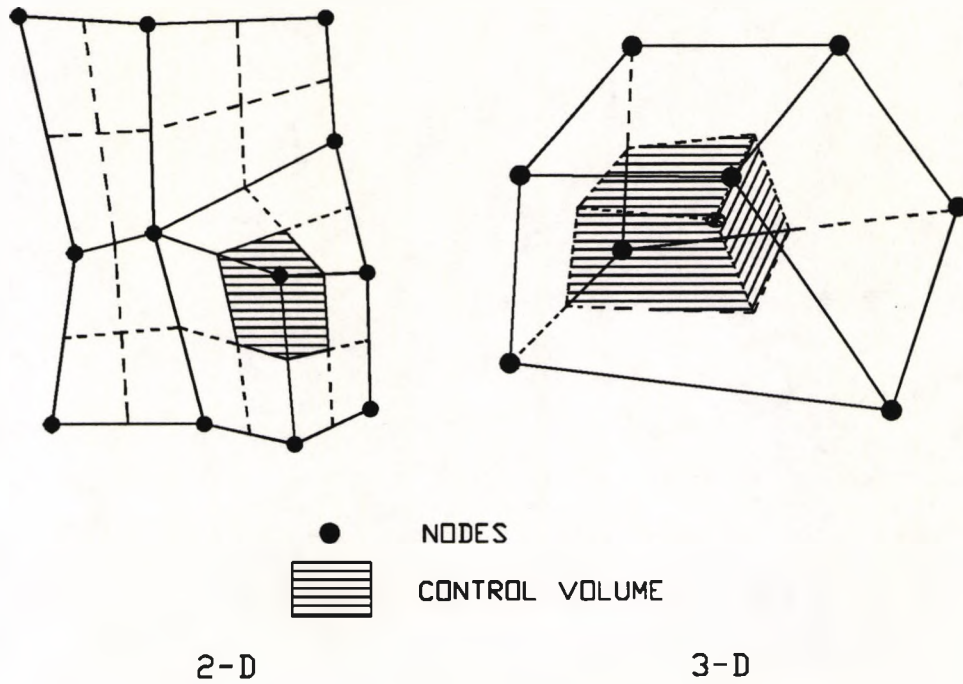


Fig. 2.2 Mesh used in ASTEC.

In ASTEC the Navier-Stokes equations are written in integral form, in which volume integrals are approximated by assuming that the mean value of the variable over the control volume equals the nodal value. However, the pressure gradient term is converted to a surface integral of pressure using Gauss's divergence theorem. The surface integrals are evaluated by summing over the faces of the control surface shown in Fig.2.2. On each face, the pressure is assumed to be the mean of the pressures at the two nodes whose control volumes are separated by the face. When calculating fluxes through each face, only nodes belonging to the element in which the face lies are used. For the diffusive flux, the gradient of the variables is estimated from the nodal values around the element containing that face. When calculating the advective flux through a face, central differencing is used for low cell Peclet number (< 2), with a proportion of upwinding employed when cell Peclet numbers exceed two. A form of streamline upwinding is used to reduce false diffusion when the flow lies at an angle to the mesh. The flow through the face is estimated from the adjacent nodal velocities by employing the interpolation procedure of Rhie and Chow (1983).

2.5.3.3 Calculation procedure

In ASTEC, the procedure for solving the discrete equations is iterative and based on the SIMPLE method. As shown in Fig.2.3, each cycle consists of several outer iterations, each of which contains the following steps:

STEP 1 Solve the linearised momentum equations to obtain an improved estimation of u , v , w , reducing the errors in these equations by a specified proportion.

STEP 2 Reduce the maximum continuity error by a specified proportion. Simultaneously, update the pressure p according to the changes in velocity that are required to ensure mass conservation.

STEP 3 Solve the temperature and turbulence equations (if turbulent) to improve estimates of T , k and ε , again reducing the errors by a specified proportion. Also solve the scalar equations to improve estimates of any other scalars being calculated.

These iterations will cease if one of the following occurs:

(a) The maximum velocity change δu from one iteration to the next becomes smaller than C_v — a small fraction (default 10^{-3}) of a typical velocity for the problem, and the maximum continuity error smaller than d — the divergence of the velocity field and can be set as a small fraction (default 2×10^{-3}) of the inverse of a typical time scale for the problem.

(b) The maximum velocity change δu from one iteration to the next becomes smaller than a user-specified proportion of the velocity change in the first iteration.

(c) The number of iterations reaches the maximum number allowed — which can also be specified by the user.

Convergence of temperature and other scalar variables are controlled in the same way. Once velocities and these other scalar variables satisfy either (a) or (b), or once the maximum number of iterations have been performed, a cycle is complete

and the code then proceeds to the next cycle in transient calculations until a specified finishing time is achieved, or to the stop in a steady state calculation.

Within each of the above described steps there are inner iterations, or sweeps. Convergence within iterations is also monitored. For the continuity equation which is solved by a diagonally preconditioned conjugate gradient method, the code determines the maximum value of $\nabla \cdot \mathbf{u}$ over the mesh following the momentum equation solution, and then performs conjugate gradient sweeps until the maximum divergence is a specified fraction (default 0.02) of the original. There is also a maximum number of sweeps (default 10000) which can be performed before the continuity procedure ceases. The same approach is adopted for solving the linearised momentum and scalar equations, but here the scheme consists of one Jacobi sweep followed by several sweeps of SOR*. These sweeps aims to reduce the maximum residual by a specified factor (default 0.02) from its original value. Again, there is a maximum number of sweeps that can be performed by the SOR solver (default 20). These values can also be determined by the user.

* Successive Over-Relaxation

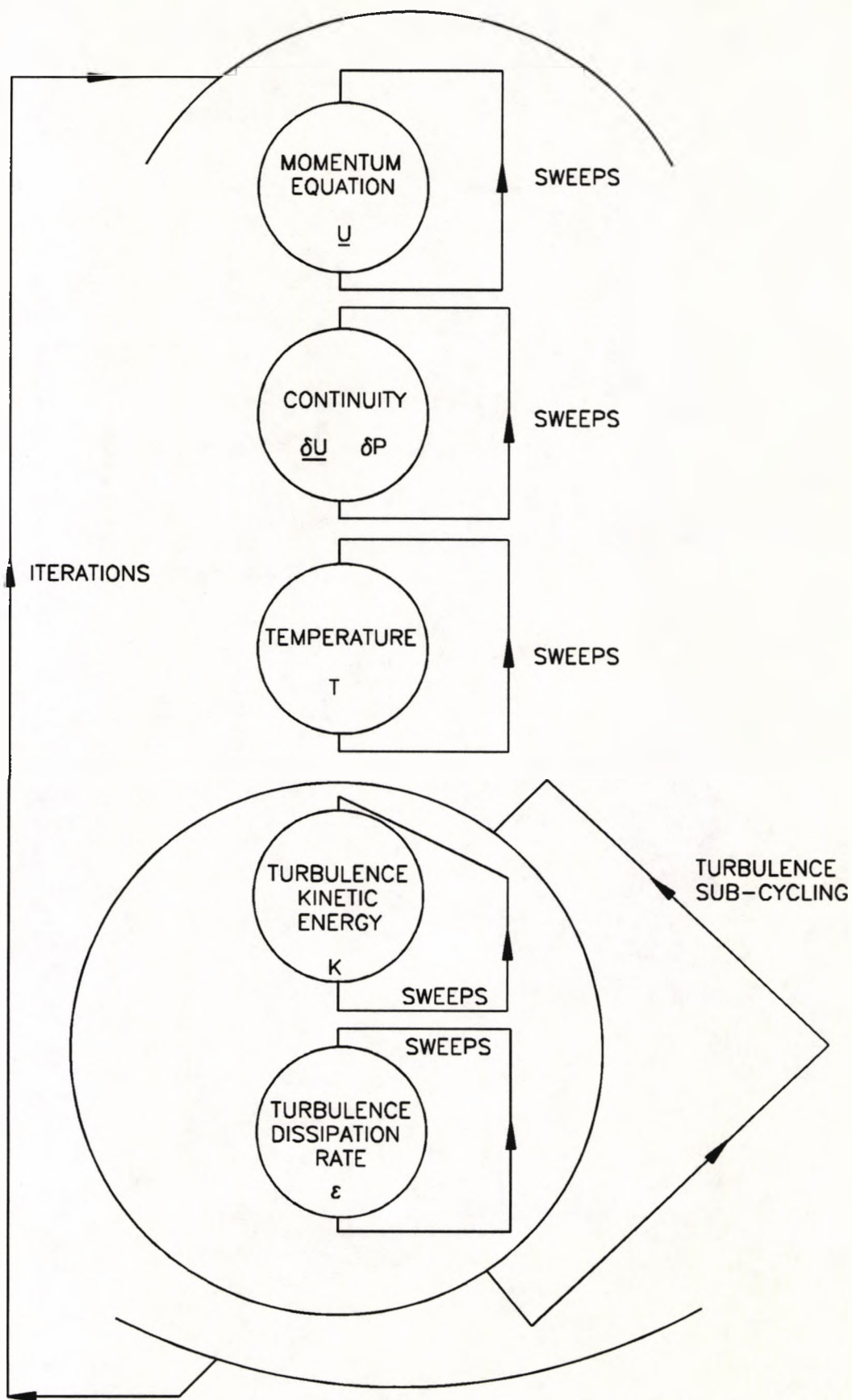


Fig. 2.3 The iterative scheme within a cycle.

CHAPTER 3

LITERATURE SURVEY

3.1 INTRODUCTION

It was pointed out in chapter 1 that to investigate arterial bifurcation flow analytically, there are four major factors which need to be accommodated — the three-dimensionality of the bifurcation; the pulsatile nature of the (laminar) flow; the distensibility of the arterial wall; and the non-Newtonian character of the blood. In this chapter, both engineering and medical aspects of each factor are carefully surveyed. It includes description of geometries of arteries obtained from anatomical and/or ultrasonic Doppler and radiological investigations; recent developments in numerical grid generation, particularly for irregular geometries; and an overview of current understanding of blood flow in arteries, especially at bifurcations. In addition, the viscous behaviour of blood and the mechanical properties of blood vessels, as well as their mathematical models are included. For the sake of completeness, a brief description of experimental techniques for measurement of blood flow in arteries is given in the last section.

3.2 GEOMETRY OF ARTERIAL BIFURCATIONS

In order to simulate hemodynamic phenomena in an arterial bifurcation numerically, the geometry chosen becomes the first consideration. Studies of geometry of arteries by means of anatomical, surgery, ultrasonic Doppler and radiological techniques are discussed in this section. Elements of physiology of the circulatory system are summarised at the beginning of the section with the intention of supplying the required background for understanding the various systems described in the dissertation. Finally, the importance of modelling accurately the bifurcation geometry and its influences on local detailed flow properties are addressed.

3.2.1 Structure and Physiology of Arteries

The circulatory system of the human body consists of the heart muscle and two components: the pulmonary and systemic circulation. Major organs in the circulation are shown in Fig.3.1. The heart, composed of two atria (right and left atrium) and two ventricles (right and left ventricle), is a combination of two synchronised pulsatile pumps in series. The pulmonary circulation is initiated at the right ventricle and transmits blood only to lungs, where filtration of CO_2 and supply of fresh oxygen take place. The systemic circulation, which is initiated at the left ventricle, is responsible for the supply of fresh blood to all the organs and tissues of the body, and thus can be considered as the feeding line of all the elements of the body. The transmission of blood through arteries is one of the most important parts of this circulation.

A striking characteristic of the circulatory system is its geometric complexity. Blood must flow through many bends, bifurcations, taperings, and stenoses during its journey. The arterial tree comprises of vessels of various length and diameter which successively branch into smaller vessels. The anatomy of the canine aorta and its main branches is illustrated in Fig.3.2, and the relevant dimensions are given in Table 3.1. The aorta originates in the left ventricle at the aortic valve. Its initial part is relatively straight for about 3cm and is called the ascending aorta. It then curves about 180° (the 'aortic arch'), branching off to the head and upper limbs. The aortic arch is tapered, curved, and twisted (i.e., it does not lie in plane). The aorta then pursues a fairly straight course down through the diaphragm to the abdomen and legs, giving off further branches. All other larger arteries, similarly, are curved and branched in a complicated three-dimensional way. There are relatively few straight segments of artery without branches where the fluid mechanics of long straight tubes can be applied.

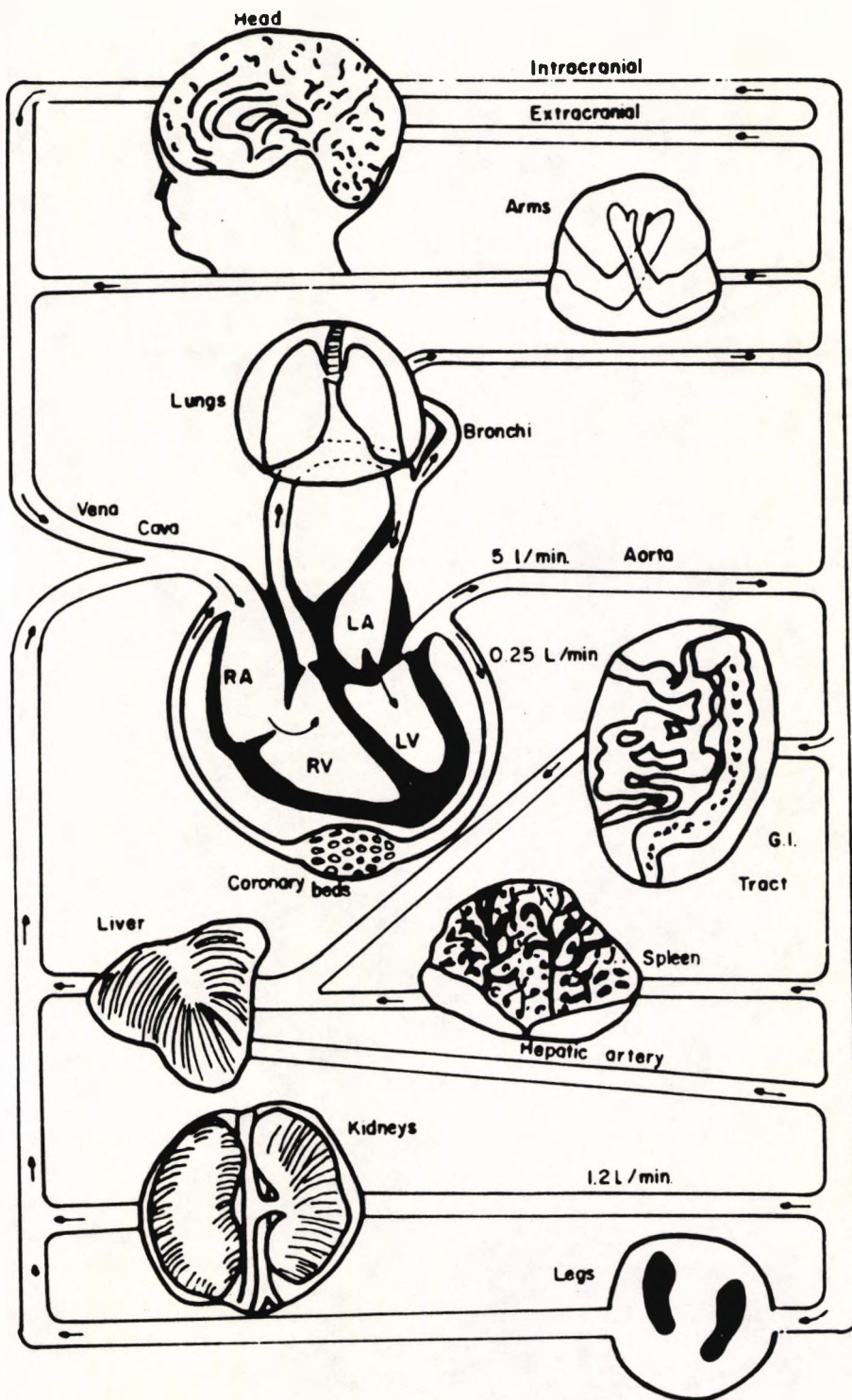


Fig. 3.1 Major organs in the circulation.

(From Dinnar, 1981)

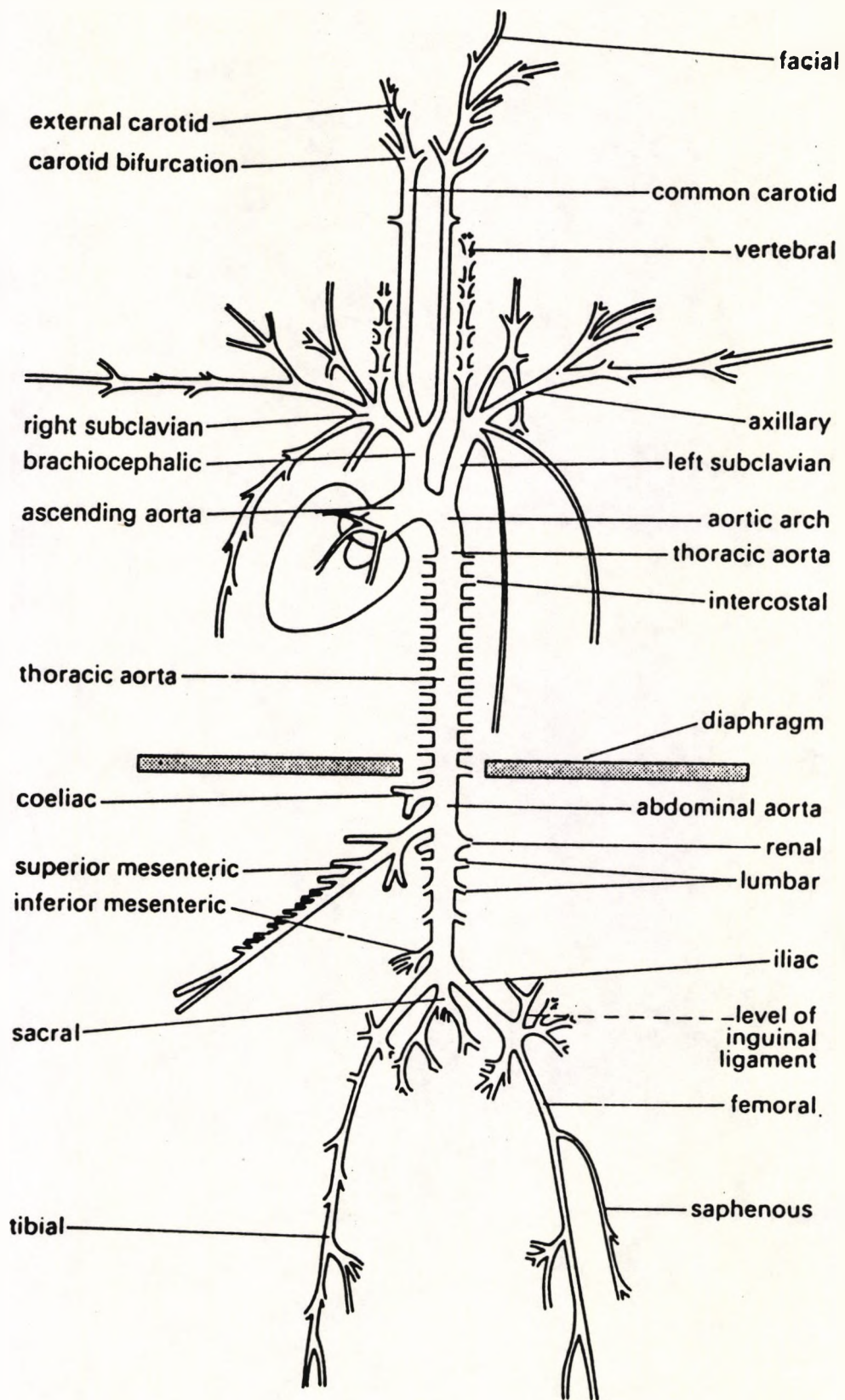


Fig. 3.2 Major branches of the canine arterial tree.
 (From McDonald, 1974)

Site		Ascending aorta	Descending aorta	Abdominal aorta	Femoral artery	Carotid artery	Arteriole	Capillary	Venule	Inferior vena cava	Main pulmonary artery			
Internal diameter d_i	cm	1.5 1.0-2.4	1.3 0.8-1.8	0.9 0.5-1.2	0.4 0.2-0.8	0.5 0.2-0.8	0.005 0.001-0.008	0.0006 0.0004-0.0008	0.004 0.001-0.0075	1.0 0.6-1.5	1.7 1.0-2.0			
Wall thickness h	cm			0.05 0.04-0.06	0.04 0.02-0.06	0.03 0.02-0.04	0.002	0.0001	0.0002	0.015 0.01-0.02	0.02 0.01-0.03			
h/d_i		0.05-0.08 0.07 0.055-0.084		0.06 0.04-0.09	0.07 0.055-0.11	0.08 0.053-0.095	0.4	0.17	0.05	0.015	0.01			
Length	cm	5	20	15	10	15	0.15	0.06	0.15	30	3.5			
Approximate cross-sectional area	cm ²	2	1.3	0.6	0.2	0.2	10-20	0.1-0.2	0.02-0.1	0.1-0.2	20-40			
Total vascular cross-sectional area at each level	cm ²	2	2	2	3	3	2×10^{-5}	3×10^{-7}	2×10^{-5}	0.8	2.3			
Peak blood velocity	cm s ⁻¹	120 40-290	105 25-250	55 50-60	100 100-120		0.75 0.5-1.0	0.07 0.02-0.17	0.35 0.2-0.5	25	70			
Mean blood velocity	cm s ⁻¹	20 10-40	20 10-40	15 8-20	10 10-15								15-40	15
Reynolds number (peak)		4500	3400	1250	1000					0.09	0.001	0.035	700	3000
α (heart rate 2 Hz)		13.2	11.5	8	3.5	4.4	0.04	0.005	0.035	8.8	15			
Calculated wave-speed c_0	cm s ⁻¹		580	770	840	850				100	350			
Measured wave-speed c	cm s ⁻¹		500	700	900	800				400	250			
Young's modulus E	Nm ⁻² $\times 10^5$		400-600	600-750	800-1030	600-1100				100-700	200-330			
			3-6	9-11	9-12	7-11				0.4-1.0	2-10			

(From C. G. Caro, T. J. Pedley, and W. A. Seed (1974). 'Mechanics of the circulation', Chapter 1 of *Cardiovascular physiology* (ed. A. C. Guyton). Medical and Technical Publishers, London.)

Table 3.1 Normal values for canine cardiovascular parameters. (From Caro *et al.*, 1978)

3.2.2 Bifurcation Geometry

The human circulatory system consists of many anatomically different arterial branches, with various branch angles, diameter ratios of the daughters to parent vessel, and parent and daughter vessel curvature. The geometries of arterial bifurcations have been studied by a number of investigators. Because of its clinical importance, much of the work has been devoted to the carotid bifurcation. Based upon a study of biplanar angiograms, Bharadvaj et al (1982a,b) developed an 'average' geometry of the human adult carotid bifurcation and constructed both glass and plexiglas models. As depicted in Fig.3.3, the carotid artery bifurcation consists of a main branch, namely the common carotid artery, which asymmetrically divides into two branches, the internal and external carotid arteries. The internal carotid artery is characterised by a widening in its most proximal part, the sinus or the bulb. Two assumptions were made in this model : (a) the arteries and the carotid sinus are circular in cross-section; (b) the parent and the daughter vessels are in the same plane at the bifurcation. Reneman et al (1985, 1986) used a multi-gate pulsed Doppler system to measure the relative diameter changes of the arteries during the cardiac cycle in young and old presumed healthy subjects; also the angle between the internal and common carotid artery was determined by means of a B-mode imagery. A more exhaustive study was undertaken by Forster et al (1985). In this study, a complete set of the common, internal and external arteries at various locations, the bifurcation angles and information on the tortuosity of the vessel is given in terms of mean values and standard deviations for a normal population. These data are valuable in constructing a three-dimensional model of the carotid bifurcation for both experimental and numerical studies.

Bifurcation geometries at other sites have been much less extensively studied than the carotid artery bifurcation. Casts of the human renal artery and the aortic arch are shown in Fig.3.4(a,b). It is important to emphasize that apart from the

geometrical differences between the bifurcations at different sites, there are also rather large individual variations both in human and other mammalian species. Jones et al (1990) studied the geometry of and flow in the ilio-femoral bifurcations of eight mongrel dogs weighing from 15–25Kg. In this study, branching angles were measured from photographs; B-mode ultrasound images of the cross-section of the upstream parent and both downstream daughter vessels, and the origin of both vessels at the bifurcation were also photographed, as illustrated in Fig.3.5. All photographs were synchronised to the time of peak upstream pressure. From photographic prints, it was found that the parent to large daughter angle ranged from 7–46°, and the parent to smaller daughter angle from 5–50°. Diameters of the parent vessels varied from 2.3 to 4.6mm, and the ratio of the larger to smaller daughter vessel diameters from 1.47 to 2.37. These demonstrated that individual variations in branching angles and superficial geometry are significant. The detailed geometries shown in Fig.3.5 were adopted in the flow predictions described later in Chapter 6.

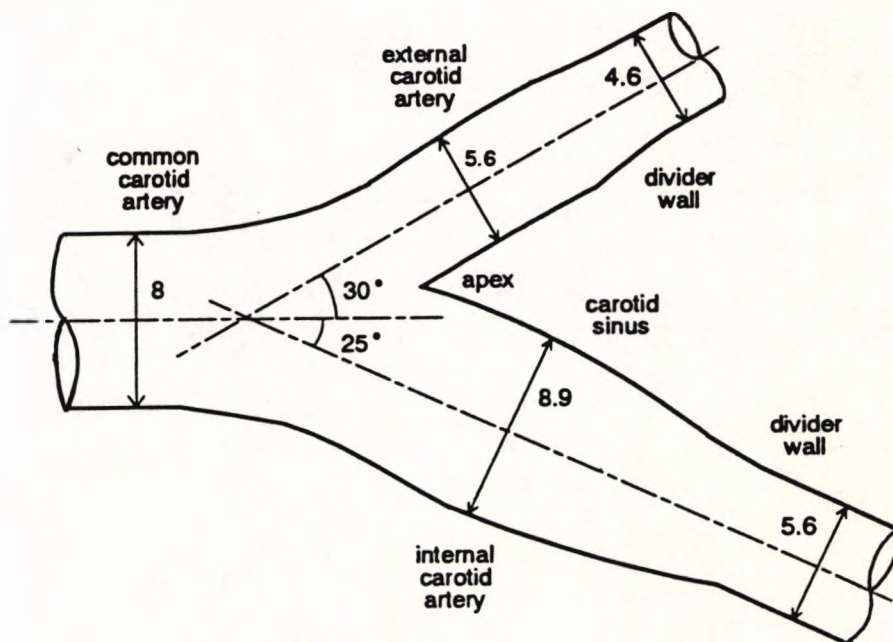
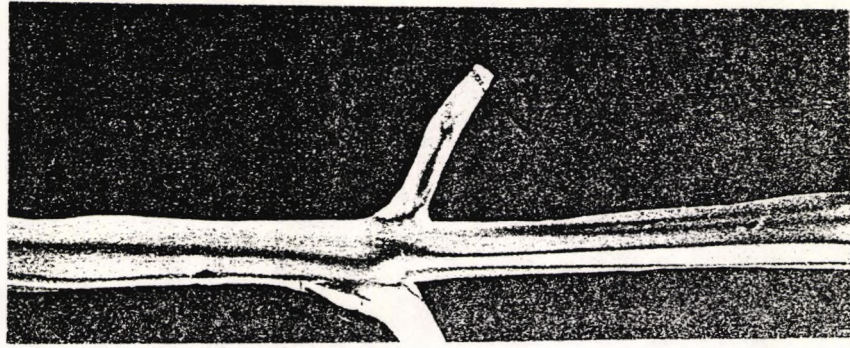
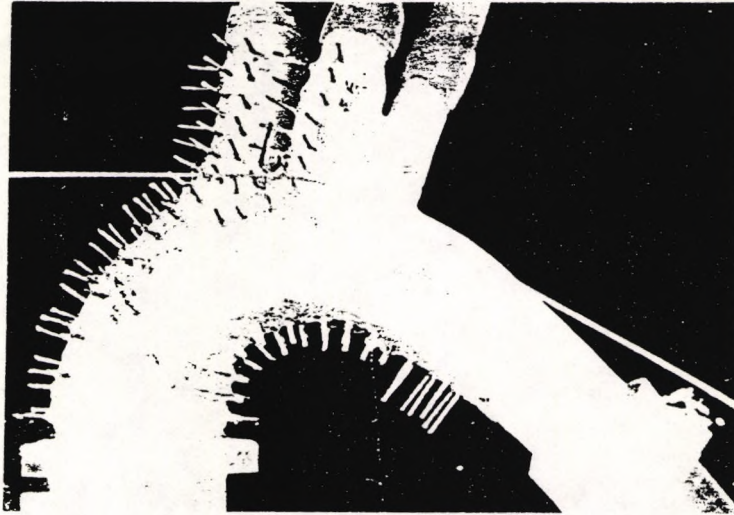


Fig. 3.3 Idealised geometry of human carotid artery bifurcations.



(a)



(b)

Fig. 3.4 Casts of (a) human renal artery and (b) aortic arch.

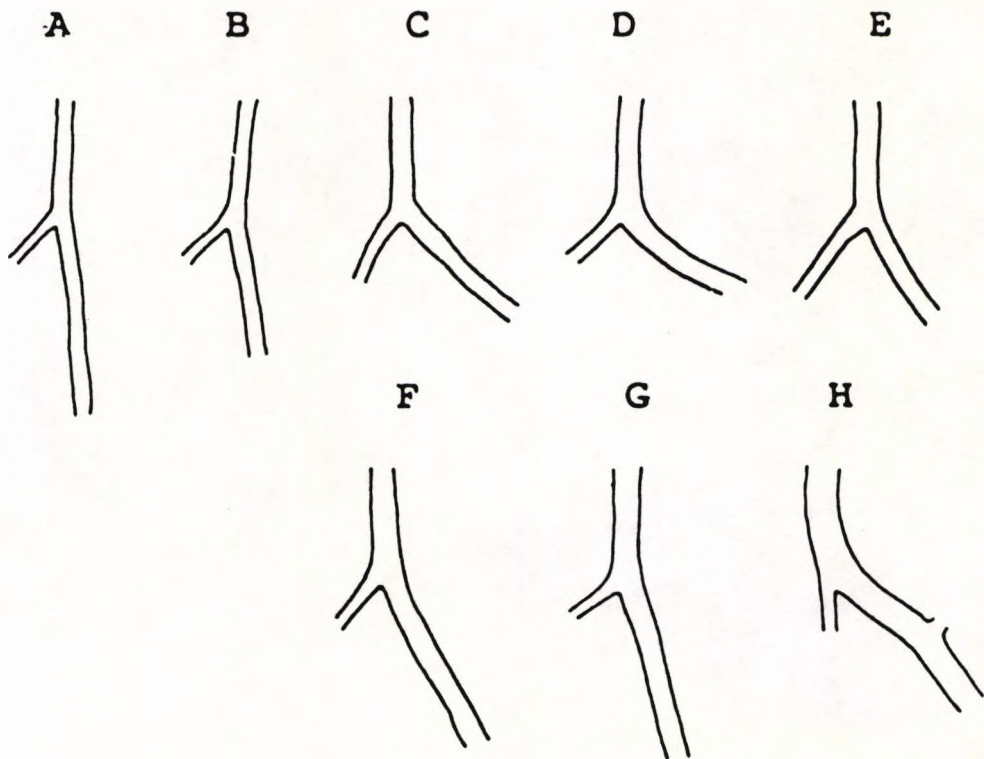


Fig. 3.5 Tracings of canine ilio-femoral bifurcations.

(From Jones *et al.*, 1990)

3.2.3 Geometric Effects On Flow In Bifurcations

The dependence of flow patterns and pressure on local arterial geometry has been examined by several authors. Four specific geometric parameters of the bifurcation were found to influence the detailed flow field. These variables, illustrated in Fig.3.6, are described below:

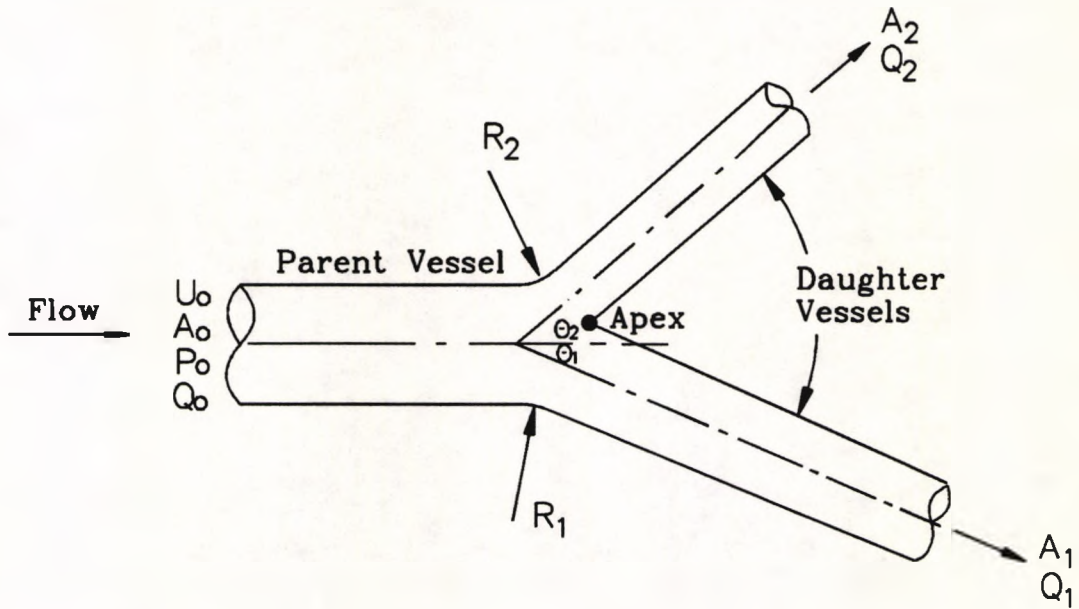


Fig. 3.6 Geometric parameters of a bifurcation.

(1) $\frac{A_1}{A_0}, \frac{A_2}{A_0}$. At given downstream boundary conditions and given state of vasoconstriction or vasodilation, the area ratios of daughter to parent vessels directly influence the flow partition between two branches $\frac{Q_1}{Q_2}$, which is known to have a significant effect on the existence of flow separation in the branch vicinity (Richardson, 1990), as well as the local pressure changes (Cho et al, 1985). Richardson proposed that for a given Reynolds number, there is a critical value of $\frac{Q_1}{Q_2}$ given by:

$$\left\{ \left(1 + \frac{Q_2}{Q_1} \right)^{\frac{1}{2}} - 1 \right\} = \frac{\Lambda}{Re} \quad (3.1)$$

where Λ is an empirical constant. Eqn.(3.1) serves as a demarcation between flows with and without separation.

(2) θ_1, θ_2 . At a given branch flow rate ratio $\frac{Q_1}{Q_2}$ and upstream Reynolds num-

ber, pressure change coefficient $\left(\frac{P-P_0}{\frac{1}{2}\rho u_1^2}\right)$ in the parent vessel in the branch region rises with the increase of branch angle $\theta(\theta = \theta_1 + \theta_2)$ (Cho *et al*, 1985).

(3) Apex. Some bifurcations, such as the aorto-iliac, appear to have sharp apices whereas others have more rounded ones. Greater apical sharpness is probably associated with less reflection of axial and periaxial streamlines into the saddle zone and the outer walls opposite the apex (Malcolm *et al*, 1979). In addition, an apex which is offset from the axis of the parent vessel induces considerable asymmetry in the flow field and promotes increased secondary flows.

(4) R_1, R_2 . Sharp curvatures of the outer walls may encourage boundary layer separation and cause large secondary velocities.

3.3 GRID GENERATION TECHNIQUES

3.3.1 Introduction

For the application to modelling of a bifurcation the grid generation problem is crucial, since the complex boundary shapes of the bifurcation have to be represented as accurately as possible, ensuring that no unnecessary errors are introduced. Numerical grid generation has now become a fairly common tool for use in the numerical solution of partial differential equations on arbitrarily shaped regions. Very substantial progress has been witnessed in this area in the past decade or so. A comprehensive survey of procedures and applications has been given by Thompson *et al.* (1982), and a number of conferences specifically in the area of numerical grid generation have been held (Thompson, 1982; Hauser, 1986). Recent general surveys have been given by Thompson (1984) and Eiseman and Eriebacher (1987).

With the introduction of boundary-fitted curvilinear coordinate systems generated to maintain coordinate lines coincident with the boundaries, finite difference

codes can be written that are applicable to general configurations without the need of special procedures at the boundaries. However, this is achieved at the expense of making the computational domain more complicated due to the non-linear coordinate transformation. Broadly speaking, numerical grid generation falls into two primary categories : algebraic methods and partial differential equation methods. A logic breakdown of these approaches is illustrated in Fig.3.7. Detailed discussion of these methods is given in the following sections.

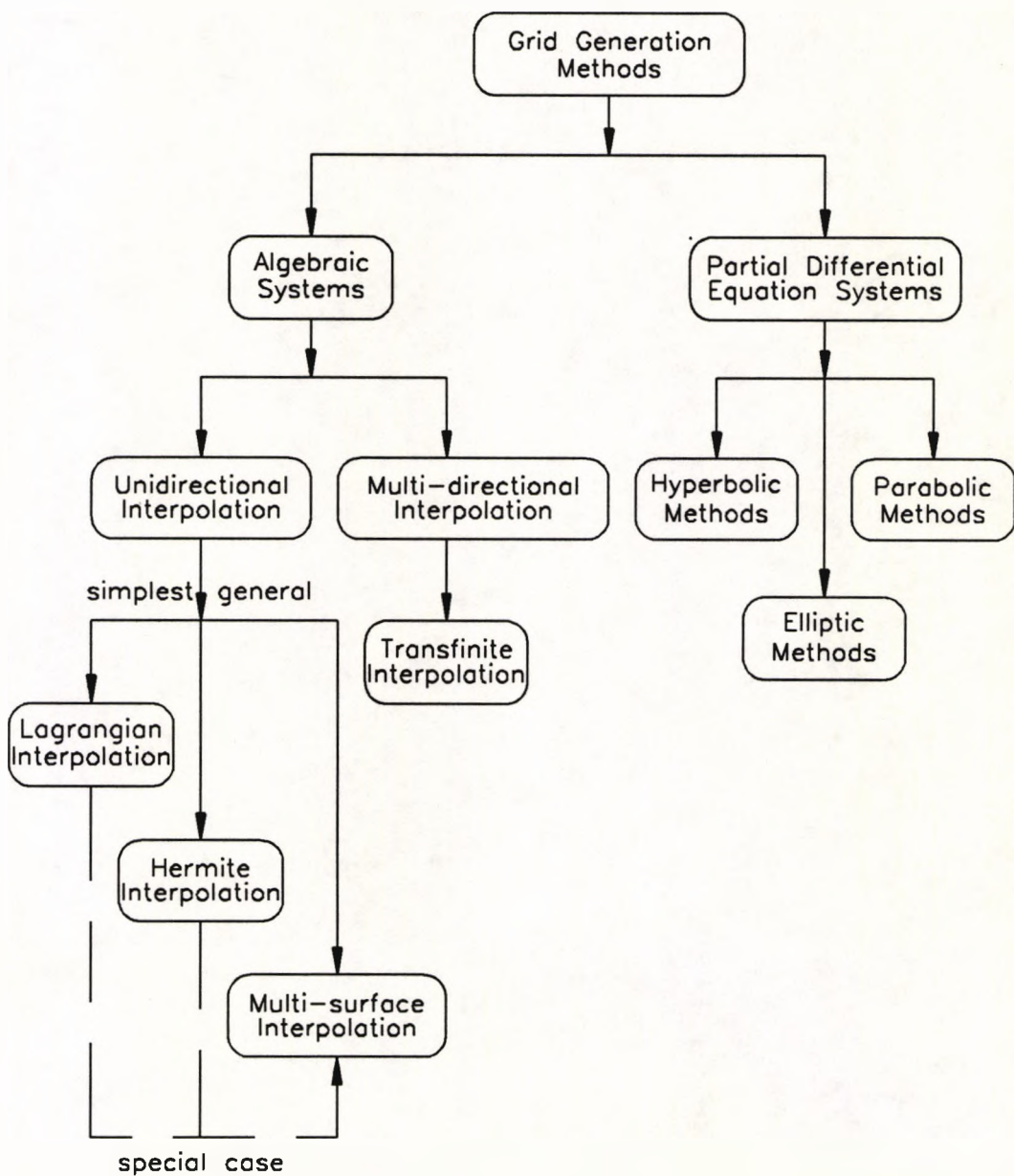


Fig. 3.7 Logic breakdown of grid generation methods.

3.3.2 Algebraic Methods

Algebraic mesh generation methods are those in which the coordinates are determined by interpolation among boundaries and/or intermediate surfaces. Algebraic grid generation distinguishes itself from other grid generation methodologies by the ability to provide a direct functional description of the coordinate transformation between the computational and physical domains. The various interpolation methods used in algebraic grid generation can be classified as : (a) uni-directional and (b) multi-directional.

Uni-directional interpolation means that the interpolation is in one curvilinear coordinate direction only, therefore it is fundamentally between points. The simplest one is Lagrangian interpolation, which matches only function values. The Hermite method is another type of uni-directional interpolation, which is capable of matching both function and first derivative values. The more general uni-directional construction is the multi-surface procedure. This procedure is constructed from an interpolation of a specified vector field followed by vector normalisation at each interpolation point in order to cause a desired telescopic collapse so that the boundaries are matched. The chief characteristic of the multi-surface procedure is the introduction of intermediate surfaces between the inner and the outer boundaries. The Hermite and Lagrangian interpolations are two special cases of the multi-surface procedure.

Multi-directional interpolation involves interpolation among functions defined along curves or surfaces, rather than among point values. The most general one is transfinite interpolation, which is generated by combining uni-directional interpolation with Boolean sums. Transfinite interpolation matches the function at any number of points. It was introduced by Gordon and Thiel (1982) and has been used in several papers for both two-dimensional (Usab and Murman, 1983) and

three-dimensional (Eriksson, 1982) grid generation.

One of the major advantages of algebraic methods is that the generation of a mesh is performed directly and is computationally very fast. Also these techniques allow the explicit control of grid point spacing. Unfortunately, since the methods do not possess inherent smoothing properties, discontinuities can arise in the mesh.

3.3.3 Partial Differential Equation Methods

Partial differential equation systems are grid generation procedures in which the grids are the solution of a set of partial differential equations. These are further split into sub-categories entitled hyperbolic, elliptic and parabolic methods to reflect the type of partial differential equation used to generate the grids.

When only one boundary is specified, hyperbolic partial differential equations may be used to obtain a grid by spatially marching from the given boundary. The inherent efficiency of the method is due to the use of a single sweep through physical space. In two dimensions, the primary system is given by:

$$\begin{cases} x_{\xi}x_{\eta} + y_{\xi}y_{\eta} = 0 \\ x_{\xi}y_{\eta} - x_{\eta}y_{\xi} = V(\xi, \eta) \end{cases} \quad (3.2)$$

where $V(\xi, \eta)$ is the specified Jacobian which comes from the cell areas of the reference grid. The numerical solution of Eqn.(3.2) is relatively easy since marching tridiagonal solutions can be used if an appropriate linearisation is carried out, which makes the hyperbolic grid generation faster than the elliptic system (discussed later) by one or two orders of magnitude. A fundamental development of the hyperbolic system was made by Starius (1977), and the application to general orthogonal grids was presented by Steger and Sorenson (1980). The hyperbolic methods, however, are applicable only to certain cases in which the inner boundary is specified, but the surrounding outer boundary is arbitrary.

Elliptic methods produce a grid by the solution of an elliptic partial differential equation. These methods have certain advantages as a mesh generator. First of all, elliptic methods treat the general case of a completely specified boundary rather than the case of only one specified boundary. Secondly, the basic solution of these methods is smooth in the sense of derivative continuity, and boundary slope discontinuities are not propagated into the field. Finally, some elliptic methods can guarantee a one-to-one mapping between the physical and computational domains.

The elliptic generation system is more popular than any other system due to the previously described merits and its flexible grid control property. Various different types of equations have been considered, as discussed in Thompson et al (1982), but the most widely used is the Poisson equation. In three dimensions the system of Poisson equations is:

$$\begin{cases} \xi_{xx} + \xi_{yy} + \xi_{zz} = P(\xi, \eta, \zeta) \\ \eta_{xx} + \eta_{yy} + \eta_{zz} = Q(\xi, \eta, \zeta) \\ \zeta_{xx} + \zeta_{yy} + \zeta_{zz} = R(\xi, \eta, \zeta) \end{cases} \quad (3.3)$$

where P, Q and R are prescribed functions that are employed to control the grid.

There are several ways to determine these control functions:

- (a) Attraction to coordinate lines/points.
- (b) Attraction to lines/points in space.
- (c) Evaluation along a coordinate line.
- (d) Evaluation on a coordinate surface.
- (e) Evaluation from boundary point distribution.
- (f) Iterative determination.

These approaches are discussed in detail in Thompson (1982).

To solve Eqn.(3.3) together with the control function equations, a number of numerical algorithms have been used, including point and line successive over-relaxation (SOR), approximate factorisation and alternating direction implicit (ADI)

schemes. The convergence can be accelerated by using multiple grid iteration (Forsey and Billing, 1988). For general configurations, point SOR is the most convenient to code and has been found to be rapid and dependable. Applications of elliptic generation systems have been made by many researchers (e.g. Thompson et al, 1974; Mastin and Thompson, 1978; Hauser and Taylor, 1986). In addition, an elliptic system can also be applied as a smoother to a grid generated by other means.

Parabolic mesh generation equations are usually derived from a suitable parabolisation of elliptic equations. While attempting to retain some of the desirable properties of the elliptic approach, this method incorporates the single sweep procedure of the hyperbolic methods. In contrast to the latter methods, the outer boundary can be specified. In comparison with elliptic methods, the grid controls are generally weak and difficult. The parabolic approach has proved useful for a limited range of relatively simple geometries (Nakamura, 1982; Edwards, 1985).

The partial differential equation grid generation methods discussed above can be summarised as in Table 3.2. It should be stressed here that orthogonality is one of the most highly desirable properties in regard to mesh generation. An orthogonal coordinate system makes the application of boundary conditions more straightforward, enables much more efficient techniques to be adopted and permits a greater degree of vectorisation on supercomputers. On the other hand, severe departure from orthogonality will introduce truncation errors in difference expressions and thus reduce the accuracy of a numerical approximation. Orthogonal systems are generally applicable to any two-dimensional domain, but are difficult, or indeed impossible, to achieve in three dimensions. Therefore, it is of interest to generate grids which are nearly orthogonal, with the conditions for orthogonality being at least partially satisfied.

Methods Properties	Hyperbolic	Elliptic	Parabolic
Numbers of boundaries specified	one	all	two
Continuity	no guarantee, propagate discontinuity	guarantee	no guarantee, propagate discontinuity
Orthogonality	guarantee	near Orthogonality	near Orthogonality
One-to-one mapping	no guarantee	some guarantee	no guarantee
Solution algorithm	no iteration, tridiagonal solution, fast	iteration SOR, ADI et al slow	no iteration, tridiagonal solution, fast
Grid control	weakest	strongest	weaker

Table 3.2 Summary of advantages and disadvantages of the three types of partial differential equation grid generation methods.

3.3.4 Special Techniques For Irregular Geometries

In the above sections, the main approaches to the generation of structured meshes have been discussed. It is clear that structured meshes, whether derived from algebraic methods or partial differential equations, result in a set of curvilinear coordinates. One way of viewing this is that, in two dimensions, the physical domain is mapped on to a rectangle in the computational domain, as shown in Fig.3.8. However, for realistic geometries, particularly for the three-dimensional bifurcations concerned here, it is very difficult to obtain a reasonable grid with the entire physical domain transferred to a single rectangular domain. Therefore, special techniques are required for gridding three-dimensional complex configurations. Two methods are now popular for this purpose: (a) multi-block and (b) unstructured mesh generation.

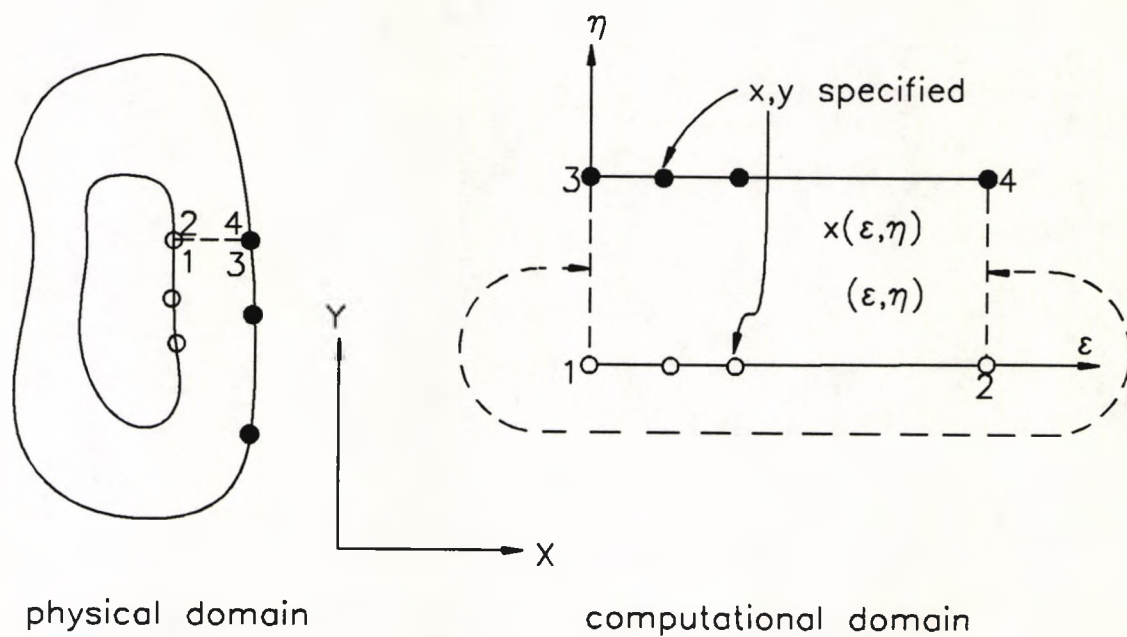


Fig. 3.8 Generation of a curvilinear coordinate system in 2D.

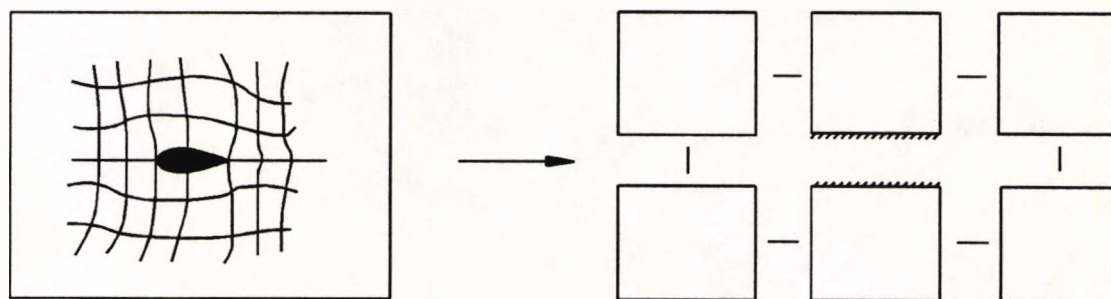


Fig. 3.9 Block structure for an H (Cartesian) mesh topology.

3.3.4.1 Multi-block grids

The multi-block concept is to segment the physical domain into contiguous blocks, with grids being generated in each block (Fig.3.9). Thus, instead of utilising one global curvilinear coordinate system, several local curvilinear systems are constructed and connected together. This concept in mesh generation is very powerful. The arrangement of blocks defines how the local curvilinear systems connect and the resulting connectivities between the local curvilinear systems define the grid topology. It is possible to construct a wide range of mesh topologies for any given configuration. In particular, it is possible to construct mesh topologies which are ideally suited for each component of the configuration, and different coordinate systems are allowed in each block. This is an important aspect of the design and construction of high quality methods. Moreover, the multi-block concept is not restricted to any particular grid generation technique. The generation of grid points can be performed using either algebraic or elliptic partial differential equation methods.

One of the major concerns in generating multi-block grids is the treatment of grid points at block interfaces. It is important to state a necessary condition which block interfaces must satisfy, i.e., the grid points at the common edge of any two adjacent blocks must be continuous (see Fig.3.10). More continuity¹ can also be enforced at the block interfaces, such as, (i) slope continuity and (ii) complete continuity. Slope continuity at block interfaces can be achieved directly by using either transfinite interpolation or an elliptic system with proper control functions. However, to achieve complete continuity at block interfaces, the position of grid points on boundaries must evolve as part of the solution procedure for interior mesh points. It is, therefore, not possible to solve for grid points on a block-by-block basis, but rather meshes in all blocks must be generated simultaneously.

¹'Continuity' is used here in the sense of correspondence rather than mass conservation

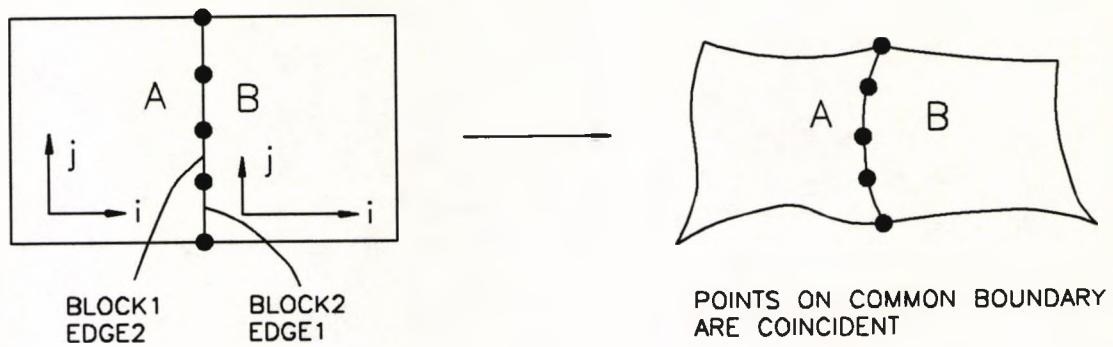


Fig. 3.10 Point correspondence at block interface.

The multi-block approach is a very popular method of applying structured grids to complex geometrical shapes. It has been applied on a variety of complex three-dimensional geometries (e.g. Miki and Tagagi, 1984; Weatherill and Forsey, 1985; Weatherill and Shaw, 1988). It has also been implemented in the latest version of FLOW3D (discussed in 2.5.2). Although the concept of multi-block mesh is attractive from a mesh generation view point, it is clear that additional complexities are introduced in the data handling and solution procedure for the mesh points. This added complexity is also carried over to the solution routine for the flow equations.

3.3.4.2 Unstructured grids

An alternative approach to complex geometries is to divide the computational domain into an unstructured assembly of computational cells. The notable feature of an unstructured mesh is that the number of cells surrounding a typical interior node of the mesh is not constant. As shown in Fig.3.11, unstructured meshes are generally composed of triangles or arbitrary quadrilaterals in two dimensions (and tetrahedra or eight-node bricks in three dimensions). The techniques which are normally adopted to generate unstructured triangular meshes are either the Delaunay or the advancing front approaches, as discussed in detail by Peraire et al (1990).

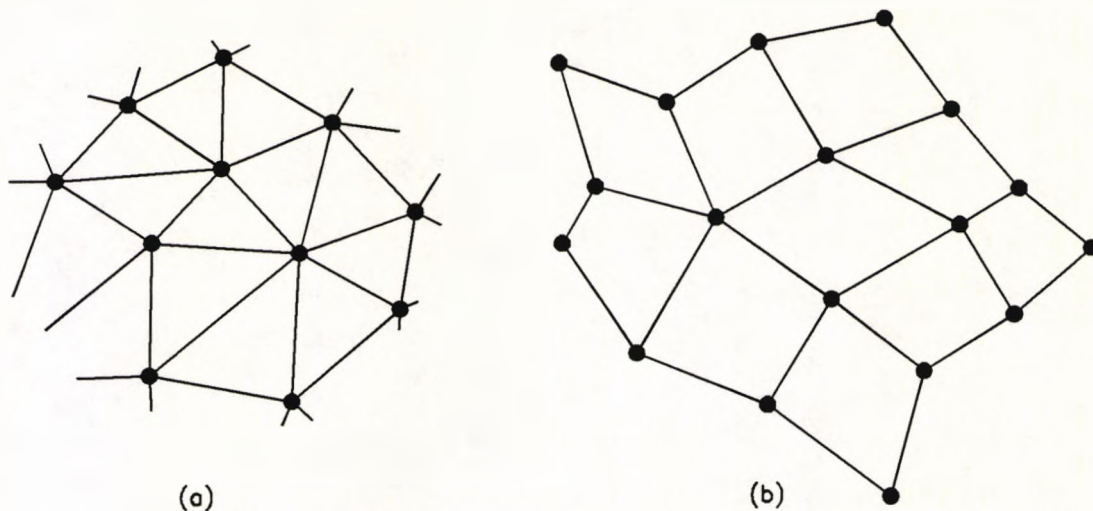


Fig. 3.11 Unstructured mesh (a) triangle mesh, (b) quadrilateral mesh.

The principal advantage of the unstructured mesh is that it provides a very powerful tool for discretising domains of complex shape, and naturally offers the possibility of incorporating adaptivity (discussed in the next section). However, such a mesh is poorly ordered and is therefore less amenable to the use of certain algorithms and vectorised computers. In addition, it requires considerably more computer time and storage, as well as much more involved data handling procedure than does the structured mesh.

3.3.5 Adaptive Gridding

In various important physical phenomena, there is some distinctive attribute which is changing rapidly at some unpredictable locations in space and possibly in time as well. With fixed grids, such phenomena are often not adequately captured in numerical simulations. There are also cases in which the boundaries are not fixed, but are time dependent and move in response to influences of the flow field or solution. This is an important issue here since the arterial vessel wall is distensible during the cardiac cycle by the pressure and shear stress exerted on the wall by the blood. In these circumstances, there is a requirement for mesh generation techniques capable of moving or positioning points to resolve adequately

the features of the physical field. This requirement has led to the development of adaptive mesh generation in which the mesh generator and flow algorithm interact.

From a simplistic viewpoint mesh adaptivity involves two distinct problems. One is to set up adaptivity criteria, i.e., to choose a feature of the flow field or solution to which mesh points should be concentrated. Another is a system of strategies employed to move or adapt the mesh. Adaptivity criteria are either based on an assessment of the error in the solution of the flow equations or are constructed to detect features of the flow field. These estimators are intimately connected to the flow equations to be solved. Hence, the choice of criteria is extensive. Once adaptivity criteria have been formulated, it is necessary to move points around the domain so as to achieve a better resolution of the flow and, in turn, reduce the error in the solution. There are three basic strategies that may be employed:

- (1) redistribution of a fixed number of points,
- (2) local refinement of a fixed set of points,
- (3) local increase in algorithm order.

The development and application of adaptive grids have been surveyed by Eiseman and Eribacher (1987). The above described adaptive grid schemes are dynamically coupled with the solution. For a problem with a merely moving boundary, adaptive meshing is desirable but not necessary. For the problem of moving boundaries, then, a simpler treatment can be made. Instead of choosing an adaptivity criterion, equations for the movement of the coordinate system are required. The simplest procedure is to regenerate the coordinate system at each time step using the new boundary locations, which are either merely time dependent or functions of parameters of the physical problem. The solution for the new coordinates at each time step thus is done separately from the physical solution at that step. Alternatively, the equations for the coordinate system can be added to the system of physical solution equations and the entire set of equations solved simultaneously

at each time step. The incorporation of the moving grid into the solution algorithm, in general, is the same regardless of the reason for grid movement. Several examples of grids following boundary motions are cited by Thompson et al (1982). Since the time derivative of the Jacobian for the coordinate transformation from physical to computational domain is introduced, more computations are necessary.

Having reviewed the geometry of arterial bifurcations and the relevant numerical grid generation techniques, the remainder of the chapter will concentrate on the fluid dynamics aspect of the arterial bifurcation flow problem.

3.4 BLOOD FLOW IN ARTERIES

3.4.1 Introduction

Blood is pumped from the left ventricle into the circulatory system by the rhythmic contractions of the heart. This added blood creates a change in pressure and results in flow of blood along the aorta and throughout the circulatory system. At any given point the pressure and velocity change periodically, and hence the flow is pulsatile and associated with the propagation of a pressure wave. Fig.3.12 shows typical pressure and flow velocities at various locations along the arterial system of a dog; the complicated waveforms and their changes are quite striking. The complete cardiovascular system is far too complicated to be amenable to a comprehensive analytical treatment, and the purpose of any analysis is always to investigate specific aspects of interest.

An extensive account of the historical development of ideas concerning the circulation of blood is given by Fishman and Richards (1964). The most remarkable achievement in modern conception of the circulation of blood is attributed to William Harvey (1579–1657). In his book published in 1628, he formulated the principle of blood circulation based on quantitative measurements and

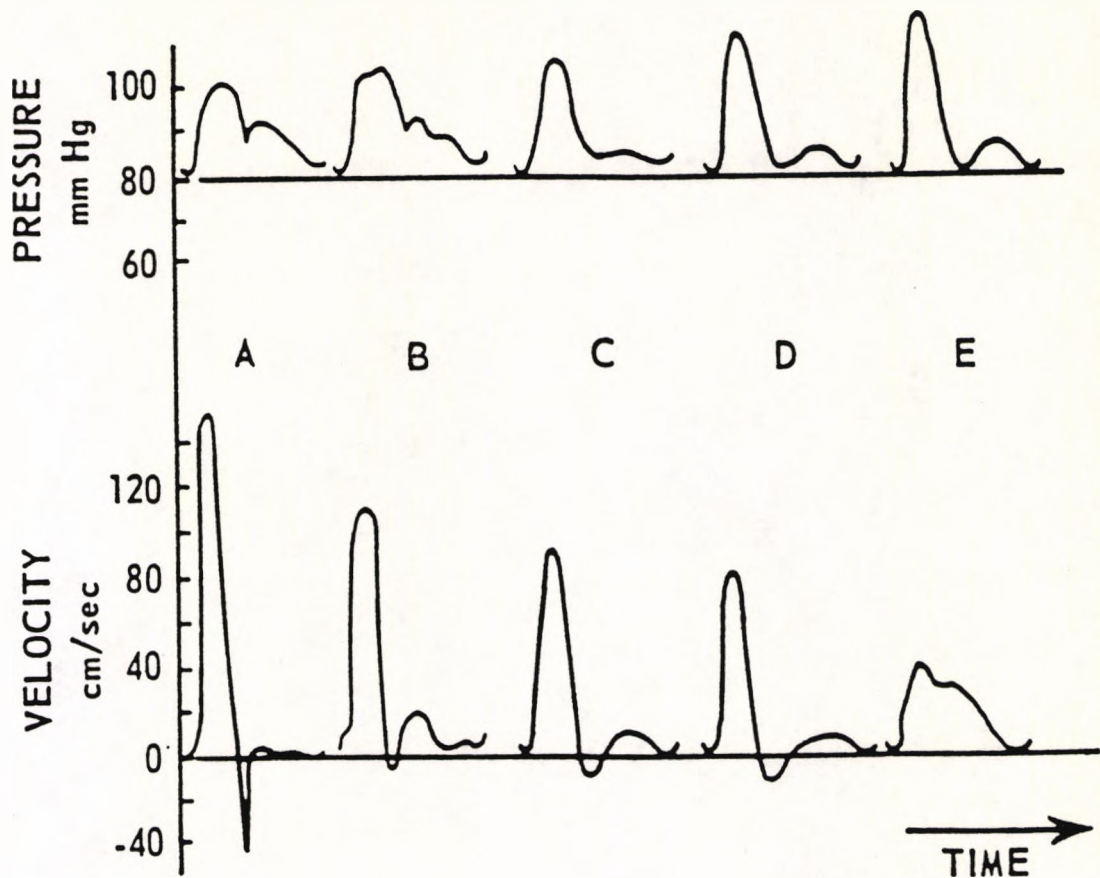


Fig. 3.12 Pressure and velocity waveforms in various arteries of a dog:

A - Ascending aorta, B - Thoracic aorta, C - Abdominal aorta,
 D - Femoral artery, E - Saphenous artery. (From McDonald, 1960)

extrapolations. Another landmark was the first measurement of blood pressure made by Hales (1733), who also developed quantitative measurements of the output of the heart, arterial dimensions and flow velocities. Although the work of Harvey and Hales was partly quantitative, it did not contain any computations which would be now regarded as fluid or solid mechanics. The first mathematical paper on blood flow was by Euler (1775). He developed the one-dimensional equations for inviscid flow of an incompressible fluid in an elastic tube. His equations included both the conservation of mass and the equations of motion. In addition, he postulated a nonlinear law relating the pressure at any point inside a blood vessel to its cross-sectional area. However, he was not able to develop any solution then, since the method of characteristics which is well suited to the solution of those equations was not known in Euler's time. The velocity of propagation of the pulse wave in arteries

was first derived by Young (1808), and was further developed and applied by many others. However, only recently have the details of arterial blood flow begun to attract attention. Starting from the work of Womersley (1955) and McDonald (1960), the pulse wave propagation calculations have been steadily improved and given more complete and precise understanding. In the last two decades or so, the numerical predictions of blood flow through bifurcations have been extensively developed by solving numerically the Navier–Stokes equations. A review of the development of these numerical methods and the recent numerical researches on this subject will be given in the sections below. Finally, experimental achievements in the measurement of blood flow in arteries will be covered in section 3.7.

3.4.2 Arterial Wave Propagation

In the earlier theoretical studies, two major methods were extensively used in the mathematical analysis of wave propagation in arterial blood flow. One is based on the linearised Navier–Stokes equations for incompressible flow, and the other on the method of characteristics.

In the first case, the principle assumptions are: (a) the mean flow velocities are small compared to the wave speed, (b) the strains in the arteries are small, (c) blood is a Newtonian incompressible fluid, (d) the convective acceleration terms of the Navier–Stokes equations may be neglected, and (e) the arterial wall behaviour is linear. Under these assumptions, the Navier–Stokes and continuity equations for one–dimensional flow can be linearised, the resulting equations being analogous to those for electric transmission lines. Pressure p and volume flow rate Q are analogous to voltage and current respectively.

$$\begin{cases} -\frac{\partial p}{\partial x} = \mathbf{R}Q + \frac{\rho}{A} \frac{\partial Q}{\partial t} \\ -\frac{\partial Q}{\partial x} = Gp + \frac{dA}{dp} \frac{\partial p}{\partial t} \end{cases} \quad (3.4)$$

where A represents the cross–sectional area, x the axial coordinate, and \mathbf{R} the flow resistance per unit length of the artery; Gp approximates the leakage per unit

length and results from outflow through small branches of the vessel. The linearisation theory originated from the late 1950's (e.g. McDonald, 1960), and has been developed and applied by many researchers.

In the second case, the flow is treated as quasi-one-dimensional but the non-linear terms of the equations are retained. The basic equations for the method of characteristics are:

The continuity equation

$$\frac{\partial A}{\partial t} + \frac{\partial}{\partial x}(uA) + \psi = 0 \quad (3.5)$$

The momentum equation

$$\frac{\partial u}{\partial t} + u \frac{\partial u}{\partial x} = -\frac{1}{\rho} \frac{\partial p}{\partial x} + f \quad (3.6)$$

and the third equation

$$A = A(p, z, t) \quad (3.7)$$

where A is the cross-sectional area, x the axial coordinate, u the average flow velocity of blood, ψ the seepage through the wall per unit length, and f represents the resultant of all longitudinal body and dissipative forces. In the method of characteristics, Eqns.(3.5) and (3.6) are written as a pair of ordinary differential equations along families of characteristics $x(t)$ with slopes $dx/dt = u \pm c$, where c is the local Young's velocity, $c = \sqrt{hE/2r\rho}$. These equations are suitable for numerical integration by computer. Lambert (1958) was the first to apply this method to blood flow. A significant development of the method of characteristics was made by Anliker et al (1971), in which a major canine arterial pathway was modelled by a tapered elastic tube with branches simulated by a distributed leakage which depends on both pressure and flow; also the effects of viscosity were taken into account.

Many advantages are associated with the use of the linearised equations. Superposition of partial solutions immediately yields periodic solutions in the form

of Fourier series, and the analogy of the mathematical treatment with that of electric transmission line makes available the rich experience accumulated in that field. However, the assumptions required for linearisation are rather far reaching and may well introduce errors. The theory based on the nonlinear equations is extremely versatile, and non-uniformities of cross-sectional area, elastic properties of the blood vessel, or the effects of external forces introduce no additional difficulties. One of the problems is that the calculations must be continued until a periodic state has been reached, which might make the calculations very lengthy, but it must be admitted that this can be easily overcome with the aid of present-day computers.

It can be seen from the above discussion that the two techniques — one based on linearisation of the equations and the other on the method of characteristics — complement each other. They are not only applicable to a segment of the arterial tree, but can also be applied, either separately or in combination, to the entire arterial system. One of the best currently available approaches is that presented by Stettler et al (1981). This model was developed for the prediction of pressure and flow pulses propagating in the arterial system, based on the assumption that each arterial conduit could be represented by a combination of three types of segment. These types are (a) segments with no or only small side branches, (b) bifurcation segments, and (c) pathological segment, as shown in Fig.3.13. Along segments of the first type, the pulse propagation was calculated by means of the method of characteristics and a first order integration. For the other two types the linearised theory was utilised. The standard case for the human arterial pathway extending from the heart to the foot, with eight major branches, was defined using published data and prescribing the ejection pattern from the heart. Therefore, this model permitted a more realistic simulation of bifurcations and stenoses than was possible previously.

Applications of both linear and nonlinear theories to characterise and interpret the arterial system have been numerous (e.g. McDonald, 1960; Lighthill, 1975; Caro *et al*, 1978). Comparisons with experiments have shown that many of the characteristic features of the propagation of the pressure and flow waves in a particular arterial system can be explained either quantitatively or qualitatively by these theories. However, it should be born in mind that in these models, the flow was treated as one-dimensional. This implies that only spatial averages of the pressure and velocity at a given cross section are calculated. Therefore, detailed local flow information is not obtainable.

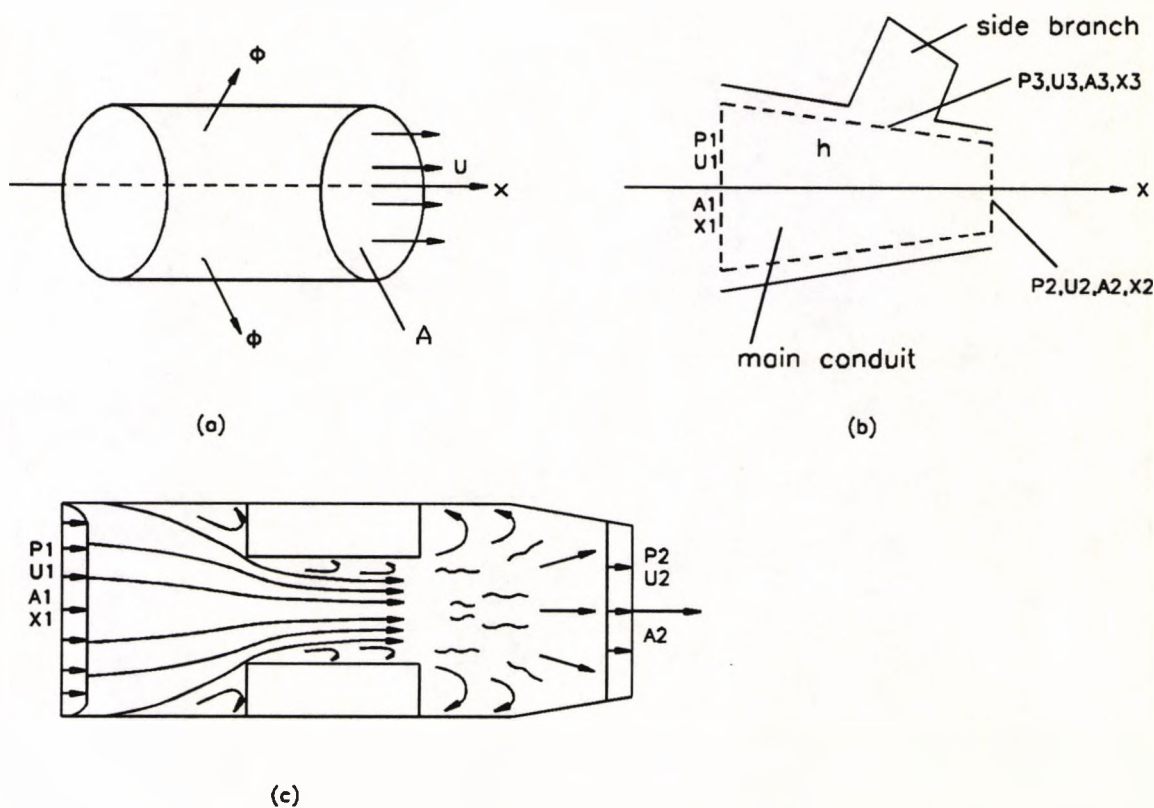


Fig. 3.13 Models of arterial elements from which a conduit is formed: (a) segment with a continuous outflow (no or only small side branches), (b) bifurcation segment, (c) pathological segment.

3.4.3 Flow At Arterial Bifurcations

In the analysis of wave propagation in an arterial system, the local flow pattern is not of specific interest. However, other physiological phenomena are strongly dependent on the local flow behaviour in the vicinity of geometric transitions. For example many studies have suggested that local fluid mechanical factors, such as the distribution of wall shear stress or pressure, play an important role in atherosclerosis and thrombosis. This has led to a number of theoretical and experimental investigations of the local flow patterns in regions of bends, stenoses and bifurcations.

Over the past decade, considerable progress has been made in numerical simulation of blood flow through arterial bifurcations. Some of the most important research is summarised in Table 3.3. In these studies the following assumptions are made: the blood is homogeneous, incompressible and Newtonian, and the flow is laminar, stationary and isothermal, the vessel wall being rigid.

Preliminary numerical studies were performed by O'Brien *et al* (1976, 1977) on two-dimensional unsteady flow through symmetric bifurcations using a vorticity stream function method. This algorithm has some attractive features and as discussed previously has been rather popular for two-dimensional simulations for some time. As was pointed out, the pressure makes no appearance, and, only two equations need to be solved to obtain the stream function and vorticity. However, the major shortcoming of the method is its inappropriateness for three-dimensional situations, for which a stream function does not exist. Thus, attention has turned to methods that use the so-called primitive variables, namely the velocity components and pressure. These procedures were adopted in most of the research in Table 3.3, in which the flow patterns, velocities, pressures and wall shear stresses for steady and/or unsteady flow were computed using finite difference or finite

Reference	Geometry	Type of Flow	Numerical Methods
O'Brien et al (1976)	2-D Y-type	Unsteady	Vorticity Stream Function
O'Brien & Ehrlich (1977)	2-D T-type	Unsteady	Vorticity Stream Function
Liepsch & Moravec (1982)	2-D T-type	Steady	Finite Difference
Perktold & Hilberit (1986)	2-D Carotid	Unsteady	Finite Element
Rindt <i>et al</i> (1987)	2-D Carotid	S&U	Finite element
Khodadadi et al (1988)	2-D T-type	Unsteady	Finite Difference
Wille(1984)	3-D Symmetric	Steady	Finite Element
Dinnar <i>et al</i> (1988)	3-D T-type	Unsteady	Finite Difference
Rindt <i>et al</i> (1989)	3-D Carotid	Steady	Finite Element
Perktold & Peter (1990)	3-D T-type	Unsteady	Finite Element
Perktold <i>et al</i> (1990)	3-D Carotid	Unsteady	Finite Element
Perktold <i>et al</i> (1991)	3-D Carotid	Unsteady	Finite Element

Table 3.3 Summary of numerical research on blood flow in bifurcations.

element techniques. These investigations have served to identify regions of separation and vortex motion and have provided numerical estimates of the distributions of wall shear stress and pressure which may qualitatively represent those found *in vivo*.

It should be noted that most of the previous numerical simulations are restricted to two dimensions. Three-dimensional modelling is virtually essential, due to the absence of non-negligible three-dimensional phenomena, such as secondary flows, in a two-dimensional case. Only in the recent few years, have three-dimensional simulations become possible. As an initial step, Wille (1984) developed a three-dimensional mathematical model of steady flow in a symmetrical bifurcation by using the finite element method. Nevertheless, this method required too long a computational time, thus prohibiting for the time being further simulation development. Another computation scheme based on finite difference methods was presented by Dinnar et al (1988). In an application to a 90-degree T-bifurcation of rectangular cross-section, the suggested scheme proved to be extremely efficient compared with the finite element method. This method, however, is confined to rather simple geometries. The modelling of pulsatile flow in an asymmetric three-dimensional bifurcation with a complex geometry has been rarely performed. This is mainly because the complexity of the geometry combined with the pulsatile nature of the flow not only creates difficulties in generating efficiently an appropriate mesh but also results in a large demand in computer storage and time. Only with a highly vectorised fluid dynamics code and a dedicated computer can the solution of such a problem become practicable. However, the very great computational power have permitted finite element methods to be used again. In the last couple of years, three-dimensional simulations have been performed by Rindt et al (1989) for steady flow in a carotid bifurcation (using the penalty function finite element method), Perktold and Peter (1990) for pulsatile flow in an arterial T-bifurcation, and Perktold and Resch (1990) for pulsatile flow in a human carotid bifurcation,

by using the newly developed pressure correction finite element method with supercomputers. To the author's knowledge, no bifurcation flow simulation has been carried out with the non-Newtonian character of the blood and the vessel wall distensibility taken into account.

3.5 RHEOLOGICAL PROPERTIES OF BLOOD

3.5.1 Introduction

The rheological properties of blood and its constituents play an important role in the physiology of the blood circulation. Extensive work has been done on determination of the mechanical properties of blood and its role in the cardiovascular system of human and animals. Yet even now, with the most modern sophisticated equipment and methods available, there is still much that is not known about this extremely complicated fluid.

3.5.2 An Outline of Blood Rheology

Human blood is a suspension of a variety of cells in an aqueous solution called plasma, which contains about 90% water by weight, 7% plasma protein, 1% inorganic substances, and 1% other organic substances. The cellular contents are essentially all red cells (erythrocytes), with white cells of various categories (leukocytes) and platelets making up less than 3% of the total cellular volume. The red cells are small, numbering about 5 million/mm³, and they normally occupy about 45% of the blood volume. Human red cells have a biconcave discoid shape at rest with a diameter of 7.6 μm (Evens and Fung, 1972), but they are flexible enough to pass easily through capillaries of about one-half this dimension. Other cells (white cells and platelets) are normally not numerous enough to affect the fluid dynamics behaviour of blood, but platelets play a significant role in the formation of blood clots, as well as being involved in the later stages of the development of

atherosclerosis.

The mechanical properties of blood are determined by those of plasma, the rheological properties of the red cells, and the distribution and interaction of individual cells in the circulation. Plasma is a pale yellow transparent fluid, and is incompressible. The density of plasma is $1.03 \times 10^3 \text{Kg/m}^3$ and that of red cells $1.10 \times 10^3 \text{Kg/m}^3$; while whole blood has a density between 1.05 and $1.06 \times 10^3 \text{Kg/m}^3$. Normal plasma behaves like a homogeneous Newtonian fluid with viscosity of $0.0012 - 0.0016 \text{Kg/(ms)}$ at body temperature (37°C) (Chien et al, 1966). Its viscosity varies with temperature in the same way as does that of water. Whole blood however can not be assumed as Newtonian, due to the presence of suspended cells. The experimental results in Fig.3.14 (Whitmore, 1968), which are based on several studies with human blood, show the variation of the apparent viscosity with rate of shear. It is found that the non-Newtonian behaviour becomes insignificant when the shear rate is greater than 1000S^{-1} , and the apparent viscosity approaches an asymptotic value ($4 \times 10^{-3} \text{Kg/ms}$). However, as the shear rate decreases the apparent viscosity increases slowly, until at a shear rate less than 1S^{-1} it rises extremely steeply.

The viscosity of blood also depends strongly on the volumetric fraction of red cells (hematocrit), as shown in Fig.3.15. At hematocrit up to about 12% suspensions of red cells in plasma behave like a Newtonian fluid at all shear rates, although they have a higher viscosity than plasma. As the hematocrit increases, not only does the viscosity of the suspensions increase, but also non-Newtonian behaviour is revealed.

As outlined in the foregoing, blood is a very complex fluid. Its viscosity varies with shear rates, hematocrit, as well as temperature, vessel diameter and disease state if any. In large blood vessels, it is reasonable to consider blood as a homo-

geneous incompressible fluid. It is universally agreed that at very high shear rate ($> 1000\text{S}^{-1}$) blood can be assumed as Newtonian, but at low shear rate the viscosity of blood decreases with the increase of shear rate. Actually in large arteries such high shear rates occur only during a relatively short part of the cycle period, and in addition, predominantly close to the wall. Consequently, while for convenience blood has been assumed to be Newtonian, it is more valid to accept the converse postulation that blood behaves comprehensively as a non-Newtonian fluid, and only for a part of the time period and in a part of flow cross-section area as a Newtonian fluid (Rodkiewicz et al, 1990). Thus, an appropriate constitutive equation for the viscous behaviour of whole blood is necessary for a realistic modelling of blood flow in large arteries. Various proposed models and their validity will be discussed in the next section.

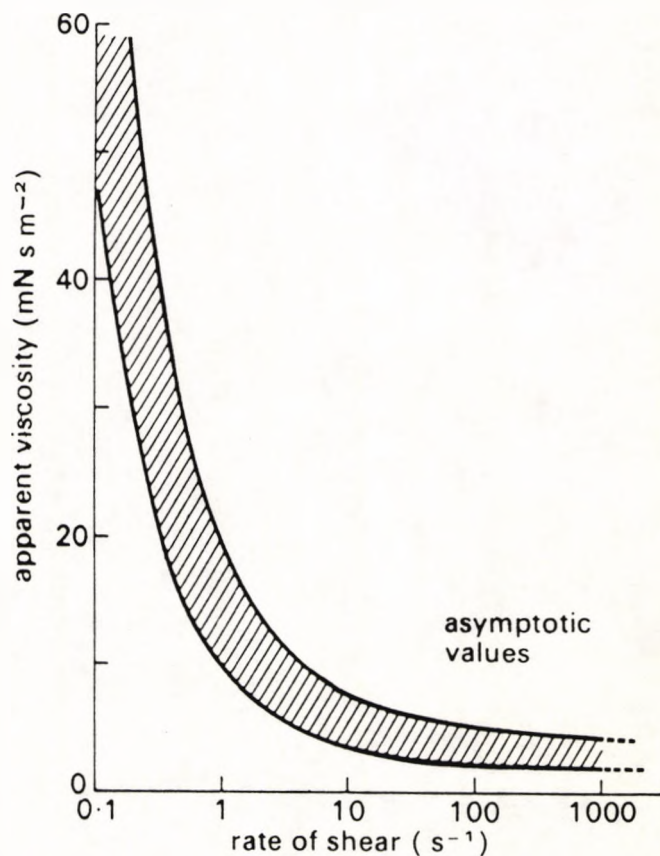


Fig. 3.14 Variation of apparent viscosity of human blood with rate of shear. (From Whitmore, 1968)

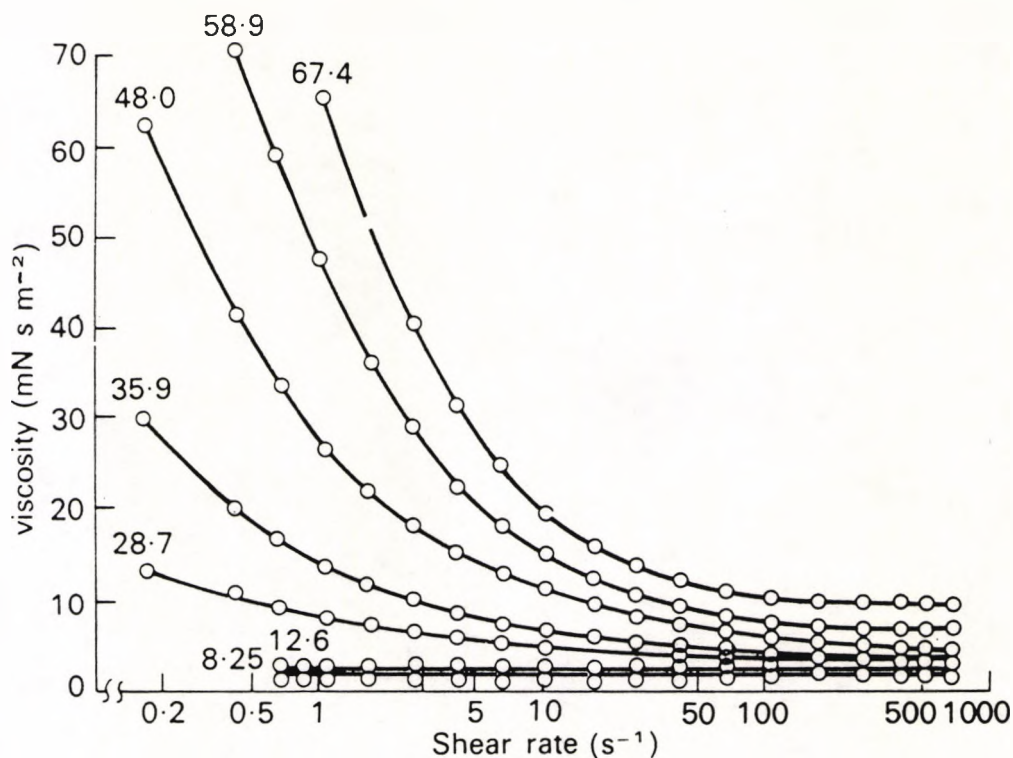


Fig. 3.15 Relationship between viscosity and rate of shear for human blood cell suspended in their own anticoagulated plasma at 25°C for various hematocrit. (From Brooks *et al*, 1970)

3.5.3 The Constitutive Equation

As was described in the last section, the behaviour of blood is essentially non-Newtonian, its viscosity decreasing with an increase in the shear rate. This behaviour is typical of a pseudoplastic fluid. Moreover, it was observed under static loading conditions that whole blood exhibits a yield stress, i.e., a certain minimum force is necessary in order to initiate flow (Cokelet *et al*, 1963). This suggests a Bingham plastic behaviour. However, it should be pointed out that the yield stress for blood is extremely small, only of the order of $0.05 \text{ dyn/cm}^2 (0.005 \text{ N/m}^2)$.

Several functional forms for constitutive equations have been used to model the non-Newtonian behaviour of blood, such as the general power law, Bingham model, Casson model, biviscosity model, and Walburn and Schneck model.

(a) Power law

A general power law can be expressed in the form :

$$\tau = m\dot{\gamma}^n \quad (3.8)$$

where τ : shear stress

$\dot{\gamma}$: shear rate

m : consistency index

n : non-Newtonian index.

Parameters m and n are assumed to be constant for a given hematocrit and a given chemical composition. To allow for the presence of a yield stress, the power law equation can easily be modified:

$$\tau = \tau_y + m\dot{\gamma}^n \quad (3.9)$$

where τ_y is the yield stress.

(b) Bingham model

In this case the relation between shear stress and shear rate is given by:

$$\begin{cases} \tau = \tau_y + \eta\dot{\gamma} & |\tau| \geq \tau_y \\ \dot{\gamma} = 0 & |\tau| < \tau_y \end{cases} \quad (3.10)$$

where η is a constant. This relationship is linear, the line not passing through the origin.

(c) Casson model

This model attempts to describe both the yield stress property of Bingham plastic fluid and the pseudoplastic behaviour, as shown in Fig.3.16. The analytical relation for Casson's fluid has the form:

$$\begin{cases} \sqrt{\tau} = \sqrt{\tau_y} + \eta\sqrt{\dot{\gamma}} & |\tau| \geq \tau_y \\ \dot{\gamma} = 0 & |\tau| < \tau_y \end{cases} \quad (3.11)$$

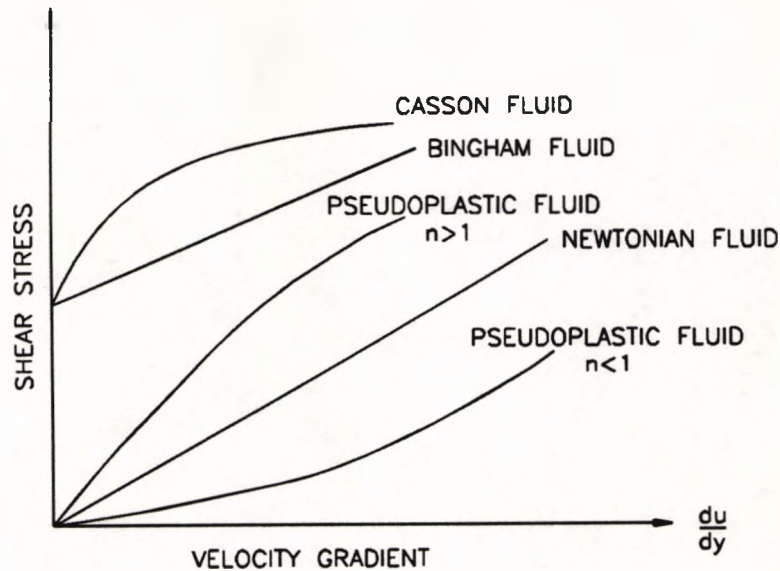


Fig. 3.16 Rheogram for different types of flow behaviour, assuming constant pressure and temperature.

It was derived for pigment-oil suspension of printing ink (Casson, 1959). Eqn.(3.11) can be written in the following way:

$$\begin{cases} \tau = (\tau_y - \eta^2 \dot{\gamma}) + 2\eta \sqrt{\tau_y} \sqrt{\dot{\gamma}} & |\tau| \geq \tau_y \\ \dot{\gamma} = 0 & |\tau| < \tau_y \end{cases} \quad (3.12)$$

The first part is a Bingham's fluid behaviour, the second part has a power law relation between shear stress and shear rate. It is a special case of a general power law with a yield stress.

(d) Biviscosity model

This is a modified Bingham model developed for modelling the pulsatile flow behaviour for slurries (Nakamura and Sawada, 1987). The constitutive equation of

the biviscosity model is written as follows:

$$\begin{cases} \tau_{ij} = 2(\mu_B + \tau_y \sqrt{2\pi}) e_{ij} & \pi \geq \pi_c \\ \tau_{ij} = 2(\mu_B + \tau_y \sqrt{2\pi_c}) e_{ij} & \pi < \pi_c \end{cases} \quad (3.13)$$

where τ_{ij} : (i,j) component of the deviatoric stress tensor

e_{ij} : (i,j) component of the deformation rate tensor

μ_B : plastic viscosity

$\pi : \pi = e_{ij} e_{ji}$

π_c : a constant, which is chosen such as to satisfy the relation:

$$\mu_B \sqrt{2\pi_c} \ll 1.0.$$

The difference between Bingham model and biviscosity models is that when the velocity gradient tends to zero, the apparent viscosity coefficient tends to be infinite in a Bingham, but has a finite value in a biviscosity model.

(e) Walburn and Schneck model

This is a modified general power law to account for various factors that would influence blood flow behaviour. By performing a multiple regression analysis on the viscometric data obtained from anticoagulated blood samples, Walburn and Schneck (1976) found an empirical constitutive equation for whole blood which depends upon shear rate, hematocrit, and total protein minus albumin (TPMA).

$$\tau = C_1 e^{C_2 H} [e^{C_4 (TPMA/H^2)}] \dot{\gamma}^{1-C_3 H} \quad (3.14)$$

where C_1 : constant, $C_1 = 0.00797 Pa \cdot s^{-1}$

C_2 : constant, $C_2 = 0.0608$

C_3 : constant, $C_3 = 0.00499$

C_4 : constant, $C_4 = 14585 \text{ l/Kg}$

H : hematocrit (%)

TPMA : the total protein minus albumin (g/l)

Among the five rheological models of blood, Casson's equation has been the most popular one in the past. Many investigators (e.g. Merrill et al, 1965 and 1967; Chien et al, 1965) have used this equation with a reasonable degree of success. Casson model is valid for steady flow and simple problems in which the strain rate tensor can be calculated in prior. Nevertheless, it is well known that the form of basic equation of Casson model is changed very much by the stress distribution in a fluid, and the shear stress can not be written explicitly for very low shear rates. So, efforts have to be made to find a more appropriate form especially for the low shear rate region. The biviscosity model is one of this type, in which the shear stress can be written explicitly. It was demonstrated that at a mean shear rates of about $20 - 150 \text{ s}^{-1}$, the calculated velocity profiles based on the biviscosity model agree with the measured one very well (Nakamura and Sawada, 1988).

However, in either Casson or biviscosity model, a yield stress exists. It should be pointed out that the yield stress for whole blood has been observed and measured only under static loading conditions. This behaviour is mainly attributed to the interactions between the protein fibrinogen and the erythrocytes. Doubts have been raised regarding the existence of the yield stress in dynamic situations. That is, although fluid velocities and velocity gradients pass routinely through zero in an oscillating flow, there is probably not enough time for static phenomena to appear. In addition to this, as mentioned earlier, the yield stress for blood is very small and virtually constant. Thus, on balance a more appropriate form of the constitutive equation would be the general power law.

Based on a power law functional form containing two parameters, a consistency index and a non-Newtonian index, the Walburn and Schneck model has been developed. Instead of having only one independent variable — shear rate, the W and S model includes two additional independent variables, namely, hematocrit and TPMA. Application to the pulsatile flow in a conduit has shown that results

based on the W and S model are not only in conformity with some experimental results, but are also closer to the actual situation as compared with the other models. Nevertheless, it should be stressed that this model may not be valid in some parts of the flow field where the shear rates are very high, because it was developed at the low shear rate experimental facility. Therefore, further improvement in the constitutive equations of blood is still needed.

3.5.4 The Effects of Non-Newtonian Characteristics on Bifurcation Flows

In most of the previous studies pure Newtonian behaviour of blood was assumed, since the non-Newtonian behaviour of blood has been regarded widely as a 'second-order' effect on arterial bifurcation flow. The non-Newtonian effects have been much less extensively studied than the other factors. Currently, however, attention is being paid to them, and they may have some significance in the parts of the bifurcation of greatest interest.

Moravec and Liepsch (1983) studied the differences in flow behaviour of Newtonian and non-Newtonian fluids in a simplified three-dimensional model of the human renal artery bifurcation under both steady and unsteady states. In this study, aqueous glycerine was used as the Newtonian fluid and the aqueous solution of polyacrylamide as the non-Newtonian. The velocity distribution proximal and distal to (i.e. upstream and downstream of) the bifurcations was measured using a Laser-Doppler anemometer. It was found that differences between the flow patterns in Newtonian and non-Newtonian fluids occurred mainly in zones of flow separation and reverse flow; and for vessel diameters exceeding 1mm, the influence of non-Newtonian behaviour upon velocity distributions distal to bifurcations was significant.

Non-Newtonian effects on arterial bifurcation flows have also been investigated by Ku and Liepsch (1986). The model used for this study was a simple 90° T-bifurcation with rigid and elastic walls. Aqueous glycerine solution and a viscoelastic separan mixture were used as Newtonian and non-Newtonian fluids respectively. Flow visualisation studies were done with a sheet of laser light in the plane of the bifurcation; and the velocity distribution was measured for both steady and pulsatile flows with a LDA. This study further revealed the substantial differences in the flow behaviour of the Newtonian and non-Newtonian fluids, especially behind the bifurcation in the main tube, where secondary flow and flow separation started (see Fig.3.17). What is more, another separation zone at the flow divider was observed when using a non-Newtonian fluid in an elastic silicone rubber model, as shown in Fig.3.18. All these results tend to indicate that non-Newtonian flow behaviour cannot be neglected, even in large blood vessels. It is concluded, therefore, that it is necessary to accommodate this factor in numerical studies.

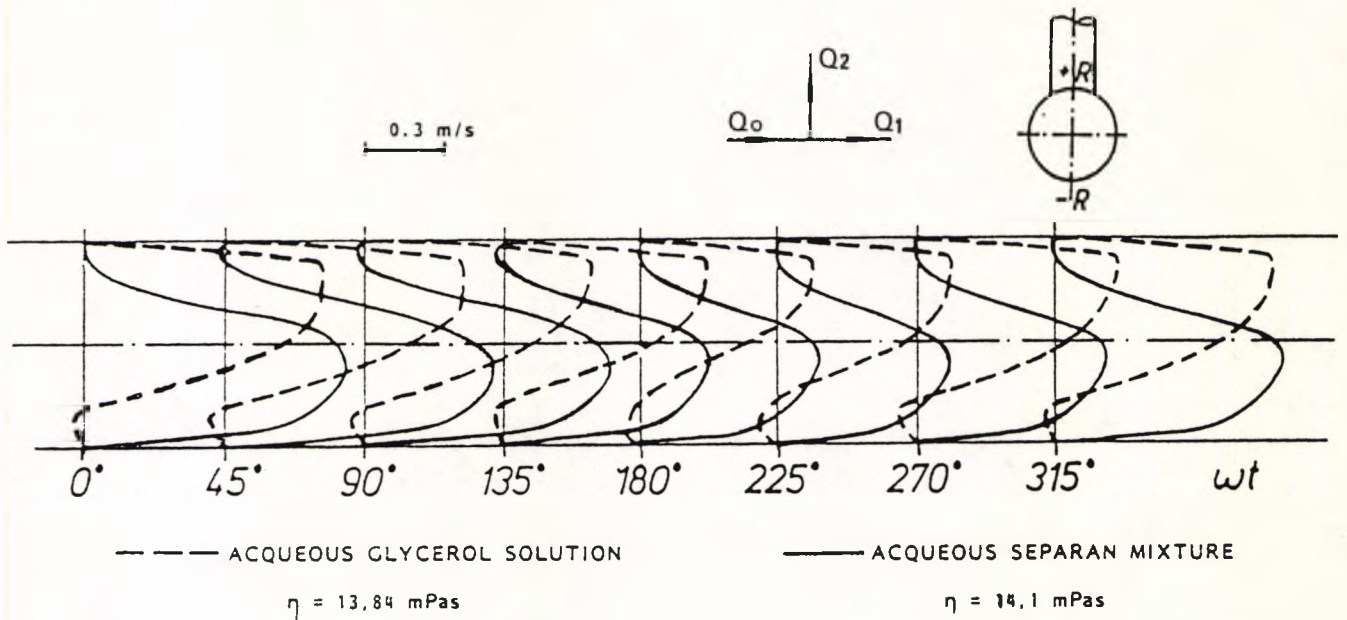


Fig. 3.17 Comparison of a Newtonian and a viscoelastic fluid at pulsatile flow over a whole cycle at 2.5mm behind a 90° T-junction of a glass model with rounded corners. The entrance Reynolds number 250 and the flow rate ratio $Q_2/Q_0 = 0.5$. (From Liesch, 1986)

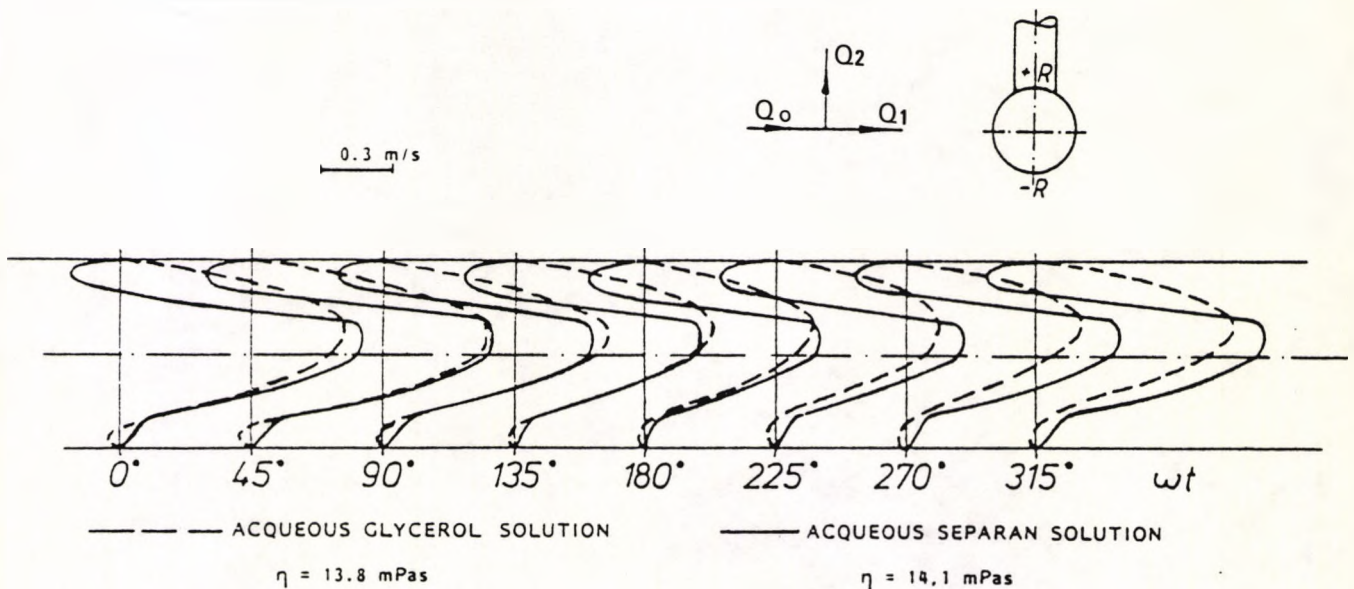


Fig. 3.18 Comparison of a Newtonian and a viscoelastic fluid at pulsatile flow over a whole cycle at 2.5mm behind a 90° T-junction of an elastic silicon rubber model with sharp corners. The flow conditions the same as those in Fig.3.17.

(From Liesch, 1986)

3.6 THE MECHANICAL PROPERTIES OF BLOOD VESSELS

3.6.1 Introduction

For the purpose of blood flow analysis, it is essential to know the elasticity² and viscoelasticity³ of the blood vessels, as well as the interfacial conditions between the blood and the blood vessel. The mechanical properties of blood vessels have been extensively studied for many years. Experimental results have demonstrated the nonlinearity of the stress–strain relationship and the existence of viscoelastic time–dependent behaviour, such as hysteresis, creep and stress relaxation. These mechanical properties must have a structural basis. In this section, the structure of the blood vessel and its correlation with the mechanical properties are discussed; various mathematical expressions of the stress–strain relationship are summarised and assessed. The effects of wall distensibility on arterial bifurcation flows are also addressed.

3.6.2 The Structure and Composition of the Blood Vessel Wall

Blood vessels are viscoelastic inhomogeneous multi–layered tissues. They are mainly composed of four types of tissue in various proportions: endothelial lining, elastin and collagen fibres, and smooth muscles (as illustrated in Fig.3.19). The endothelial lining is the innermost layer of the vessel wall that comes in contact with the flowing blood. It provides a smooth surface and offers a selective permeability to various substances carried in the blood stream but is too soft to contribute to the elastic properties of the wall. Hence, the mechanical properties of this monocyte layer can be omitted from the discussion on overall elastic per-

²Elasticity: A reversible stress/strain behaviour.

³Viscoelasticity: Having both viscous and elastic properties.

formance. Elastin fibres are protein substances, rubbery in constitution and very extensible. In stretching of up to about 60% their original length the elastic fibres follow Hooke's law. However, for extensions beyond this value they will become highly nonlinear. The range of Young's modulus of the elastin fibres is 3×10^5 to $6 \times 10^5 N/m^2$. Collagen fibres are also protein substances, but they are much stiffer having an elastic modulus of the order of 3×10^5 to $1 \times 10^7 N/m^2$. The behaviour of collagen is non-Hookean, and exhibits some plastic deformation. The collagen fibres are arranged in the wall with a degree of slackness so that they do not contribute to the elastic behaviour until some stretching has taken place. It can be concluded that at small displacement of the vessel wall the elastin plays a major role, while the collagen fibres do not interfere. When this displacement becomes large the performance of the wall is dominated by the collagen fibre behaviour. The primary function of the muscles is to provide active tension by contraction under physiological control and thereby change the diameter of the vessel; their elastic modulus varies from $6 \times 10^3 N/m^2$ in the passive state to $5 \times 10^7 N/m^2$ in the active state.

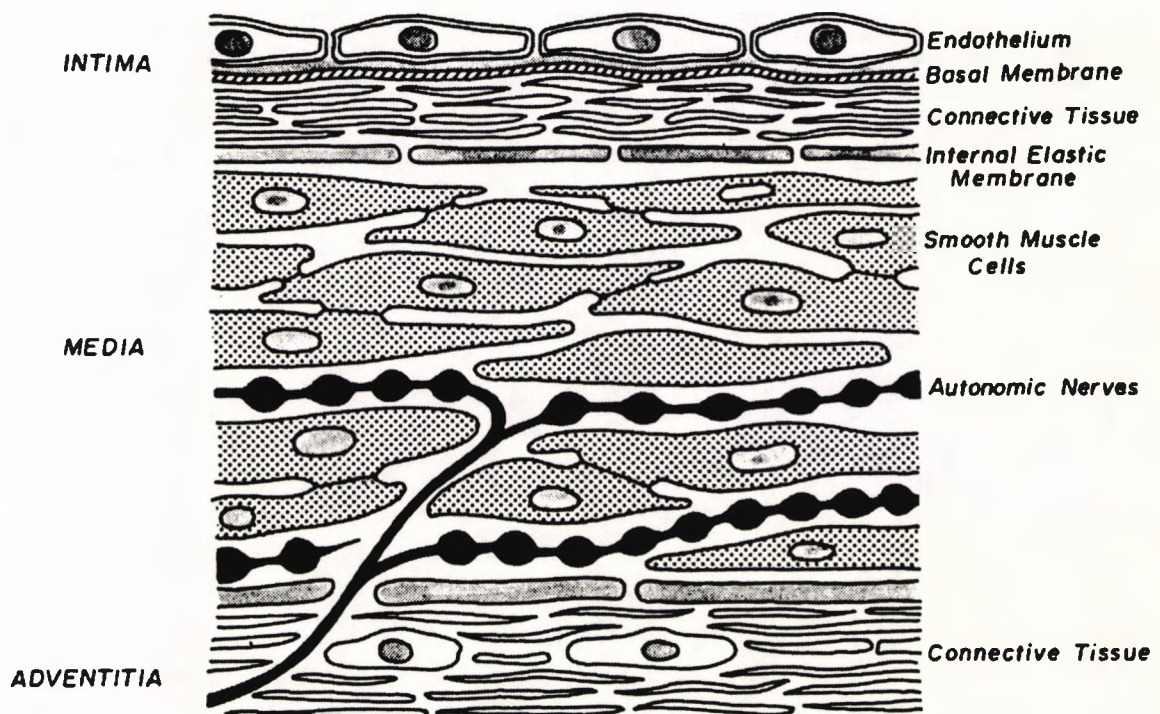


Fig. 3.19 Schematic illustration of the structure of arterial wall.

These components are arranged in three concentric layers, namely, the intima, the media and the adventitia (see Fig.3.19). The intima consists of a single layer of endothelium with a thin layer of elastin and collagen fibres. The media, which forms the large part of the vessel, consists of tight helix fibres with the smooth muscle cells lying between them. The mechanical properties of the wall are determined mainly by the connective tissue and the smooth muscle of the media. The adventitia consists of elastin and collagen fibres that merge with the surrounding tissues. The adventitia and the outer part of the media of large arteries contain small blood vessels (*vasa Vasorum*), lymphatics and nerves.

The forces which deform the elastic walls of arteries include the pressure and shear stress exerted by the blood, the tension developed by the wall smooth muscle and tethering imposed by surrounding tissue. The mechanical properties of the constituents vary with many factors, but mainly with age (Abramson, 1962).

3.6.3 Mathematical Representations of the Stress–Strain Relationship

A proper mathematical description of the mechanical behaviour of the arterial wall is essential to the investigation of their effects on arterial flow. A large variety of mathematical expressions has been derived with various assumptions of arterial wall behaviour, such as, membrane, thick shell, elastic, viscoelastic, linear and nonlinear. These various descriptions can also be classified as uniaxial, biaxial and triaxial models according to the number of modes of wall motion defined in the expression. If a uniaxial model is postulated, the wall motion will usually be in the radial rather than the longitudinal direction, because the tethering inhibits longitudinal wall motions more than radial movement. For this reason the mechanical properties of arteries are commonly defined in terms of a distensibility, which is the fractional change of luminal cross-sectional area A divided by the distending

pressure.

$$D = \frac{1}{A} \left(\frac{dA}{dp} \right) \quad (3.15)$$

The Young's modulus for circumferential stretch is calculated from the equation

$$E = \frac{\Delta p_i}{\Delta d_e} \frac{2d_e d_i^2 (1 - \sigma^2)}{d_e^2 - d_i^2} \quad (3.16)$$

where Δp_i is the change in internal pressure of the vessel, Δd_e is the corresponding change in the external vessel diameter d_e , d_i is the internal diameter, and σ is the Poisson's ratio known to have the value of 0.5. If the vessel is assumed to be thin-walled, its wall thickness $h = 0.5 \times (d_e - d_i)$ is small compared with d_i , and d_i and d_e are approximately equal. In these circumstances, Eqn.(3.16) can be reduced to

$$\frac{2\Delta d}{d\Delta p} = \frac{d(1 - \sigma^2)}{Eh} \quad (3.17)$$

By substituting Eqn.(3.15) into Eqn.(3.17) and note that

$$\frac{1}{A} \frac{dA}{dp} = \frac{2d\Delta d}{d^2\Delta p} = \frac{2\Delta d}{d\Delta p} \quad (3.18)$$

In the case of a material for which σ^2 is negligible compared with 1, Eqn.(3.16) is approximately equivalent to

$$D = \frac{1}{E(h/d)} \quad (3.19)$$

These equations have been extensively applied in both linear and nonlinear theories of arterial wave propagation (McDonald, 1960; Gordon and Scala, 1970). For the investigation of blood flow in a three-dimensional arterial bifurcation segment, however, such a uniaxial elastic model is not adequate.

The wall motion of blood vessels is not one-dimensional. It has been found that when subjected to physiological loads an arterial segment deforms circumferentially by 2–15%; when an artery is excised it shortens by up to 60%. However, during the heartbeat the longitudinal deformation is small. Various models used to describe the biaxial and triaxial deformations of an arterial segment may be

classified as: small strain analysis⁴, incremental analysis⁵, and finite deformation analysis⁶.

In the small strain and incremental analysis the stress components are directly expressed as a function of strains. A different approach based on a strain–energy function is used for finite nonlinear elastic deformation analysis. Although a large variety of forms of the strain energy functions have been postulated, there are essentially only two schools of thought: one uses polynomials (Patel and Vaishnav, 1972; Wesley, 1975), while the other uses exponential functions (Ayorinde et al, 1975; Demiray, 1972; Fung, 1973, 1975, 1979). In the two–dimensional (circumferential and longitudinal) case the strain energy function $\rho_o W^{(2)}$ is a function of the strains $E_{\theta\theta}$ and E_{zz} . A form of $\rho_o W^{(2)}$ advocated by the polynomial hypothesis is

$$\rho_o W^{(2)} = Aa^2 + Bab + Cb^2 + Da^3 + Ea^2b + Fab^2 + Gb^3 \quad (3.20)$$

where $a = E_{\theta\theta}$, $b = E_{zz}$, and A, B, ..., G are material constants. The seven–constants form shown in Eqn.(3.20) is the simplest polynomial function for the nonlinear theory. If the fourth degree terms are introduced the number of constants increases to 12. Patel and Vaishnav (1972) have shown that the accuracy of the function is not much improved by the inclusion of the fourth degree terms.

The form of exponential function preferred by most authors adopting the second approach is the following:

$$\begin{aligned} \rho_o W^{(2)} = & \frac{C}{2} \exp \left[a_1 (E_{\theta\theta}^2 - E_{\theta\theta}^{*2}) + a_2 (E_{zz}^2 - E_{zz}^{*2}) \right. \\ & \left. + 2a_4 (E_{\theta\theta} E_{zz} - E_{\theta\theta}^* E_{zz}^*) \right] \end{aligned} \quad (3.21)$$

where C (N/m^2) and a_1, a_2, a_3, a_4 (dimensionless) are material constants, and

⁴Assume the material is isotropic and linearly elastic.

⁵Based on the use of the linear small strain theory to describe nonlinear stress–strain behaviour.

⁶Assume the work done in deforming an elastic is stored as strain energy which is then expressed as a function of strains only.

$E_{\theta\theta}^*$, E_{zz}^* are strains corresponding to a pair of arbitrarily selected stresses $S_{\theta\theta}$, S_{zz} .

Both these functions can be used. If the seven-constant polynomial form is chosen, by utilising the equilibrium equations for a thin-walled cylinder of mid-wall radius r , and wall thickness h , subjected to an inner wall pressure p and a longitudinal force \mathbf{f} , together with the assumption of incompressibility⁷, the following expressions can be derived (for detail see Appendix B):

$$\left\{ \begin{array}{l} \mathbf{p} = \frac{h}{r} [6Da^3 + (4A + 3D + 4Eb)a^2 + 2(A + Eb + Bb + Fb^2)a + Bb + Fb^2] \\ \mathbf{f} = 2\pi rh [6Gb^3 + (4C + 3G + 4Fa)b^2 + 2(C + Ba + Fa + Ea^2)b \\ \quad + Ba + Ea^2 - \frac{Pr}{2h}] \end{array} \right. \quad (3.22)$$

The Green's strains are defined as:

$$\left\{ \begin{array}{l} a = E_{\theta\theta} = \frac{1}{2} \left[\left(\frac{r}{R} \right)^2 - 1 \right] \\ b = E_{zz} = \frac{1}{2} \left[\left(\frac{l}{L} \right)^2 - 1 \right] \end{array} \right. \quad (3.23)$$

where r , l are deformed mid-wall radius and length, and R , L are undeformed mid-wall radius and length. Once the material constants are obtained, Eqns.(3.22-3.23) can be used to predict the stresses and the principal strains for any combination of pressure and longitudinal force.

These models based on either polynomial or exponential functions have been applied to the study of the mechanical properties of various subjects, such as, the dog aorta (Patel and Vaishnav, 1972), rabbit arteries (Fung *et al*, 1979), and arterial prostheses (How and Clarke, 1984). For the exponential strain energy function, the constants C , a_1 , a_2 , a_4 are determined by a modified Marquart's

⁷Volume of the material does not change under all states of stress.

nonlinear least squares algorithm — by minimising the sum of the squares of the differences between the experimental and theoretical data. For the polynomial, the ordinary least square procedure is sufficient. These studies have shown that the third order polynomial function is adequate to give a satisfactory fit to the experimental data; it is simpler but can be applied to a wider range of materials. The exponential form has the overall smaller coefficients of variations, hence it is preferred if one wishes to study the systematic changes in the arterial segment due to some other factors.

3.6.4 The Effects of Wall Distensibility on Bifurcation Flow

Among the four major factors which influence the flow fields at arterial bifurcations, distensibility of the arterial wall has been regarded as a ‘second-order’ effect in most of the previous work. Even so, it is well known that distensibility is an important factor in pulsed-wave propagation. Some recent experimental studies have shown the differences between rigid and elastic wall behaviour during pulsatile flow. Liepsch (1985) investigated the pulsatile flow in a straight thin-walled elastic tube both theoretically and experimentally. Comparisons of axial velocity profiles in a rigid and an elastic tube showed that the maximum velocity was reduced in the elastic model. Investigations on bifurcations have been performed by Liepsch et al (1983, 1988) for human renal arteries, and Ku and Liepsch (1986) for a 90 degree T-junction model. It was observed that there were obvious reductions in negative velocities and the size of secondary flow region in the elastic models; and the shear stresses were reduced by up to 25% depending on the elasticity of the wall. All these demonstrated the fact that wall elasticity may well be an important factor in the understanding of bifurcation flows.

3.7 EXPERIMENTAL TECHNIQUES FOR MEASUREMENT OF BLOOD FLOW IN ARTERIES

3.7.1 Introduction

The study of blood flow through arterial bifurcations has two primary purposes. One is to give a quantitative description of local flow and velocity distribution. The other, of great potential importance for the understanding of arterial disease, is to obtain detailed distribution of wall shear stress, which is relevant to the early onset of atherosclerosis. In this section, experimental techniques currently used for such purposes are surveyed. These include optical instruments such as Laser-Doppler anemometry and Doppler ultrasound techniques for velocity measurement. Devices for measuring wall shear stress in models and difficulties in measuring it accurately *in vivo* are also discussed.

3.7.2 Velocity Measurement

Many measurement systems have been developed to obtain information on flow and velocity distribution. For a long time mechanical probes have provided the principal means of measuring fluid velocity. For instance, total-pressure probes in conjunction with static-probes have been used in measuring mean velocity and hot-wire or hot-film devices in measuring instantaneous velocity. Although hot-wire and hot-film anemometry has provided much quantitative information on fluid velocity, its application has been substantially limited to constant property flows of low temperature, low speed and low turbulence intensity, outside regions of recirculation. New measuring techniques — ultrasound and optical techniques — can overcome all of these limitations, because unlike mechanical probes, they do not disturb the flow (this quality is described in engineering terms as ‘non-invasive’). An optical method — Laser-Doppler anemometry (LDA) — has found a wide application in measuring velocity profiles in arteries both *in vitro* and in

model studies. Various Doppler Ultrasound techniques have also been developed and extensively applied to *in vivo* studies and clinical diagnoses.

In addition to velocity measurement techniques, flow visualisation methods have also played an important role in obtaining a clear picture of the flow field of interest. The methods normally used are: colouring streamlines, adding particles and hydrogen bubble techniques. A summary of experimental techniques used currently for the study of flow patterns in bifurcations is given in Table 3.4.

Flow Visualisation		Velocity Measurement	
Methods	Authors and References	Methods	Authors and References
Hydrogen Bubble	Bharadvaj <i>et al</i> (1982a) Ku and Giddens (1983)	LDA	Khodadadi <i>et al</i> (1988) Ku and Giddens (1987) Bharadvaj <i>et al</i> (1982b)
Colouring Streamline	Stehbens (1975) Malcolm and Roach (1979)	Doppler Ultrasound	Ku <i>et al</i> (1985) Reneman <i>et al</i> (1986) Jones <i>et al</i> (1991)
Adding Particles	Feuerstein <i>et al</i> (1976) Karino <i>et al</i> (1979)	Hot-film Hot-wire Anemometer	Schultz <i>et al</i> (1969) Olson (1971) Nerem <i>et al</i> (1974)

Table 3.4 Summary of experimental techniques for study of flow patterns in arteries.

3.7.2.1 Doppler ultrasound techniques

Doppler ultrasound technique has shown fundamental application both in research animals and for diagnosis in human subjects (Reneman, 1974; Taylor et al, 1988). Its main advantages are as following:

(a) It is non-invasive with no surgery, no catheterisation, and little or no trauma to disturb the system being measured.

(b) It provides relatively accurate *in vivo* measurement of blood pressure, blood flow velocity and dynamic changes of vessel diameter.

(c) It enables diagnosis of arterial occlusive disease.

(d) It is relatively inexpensive and reliable, and measurements are repeatable.

3.7.2.1.1 Principles of Doppler ultrasound

Historically, the Doppler effect was first observed by Christian Doppler (1843). He found that the apparent frequency of a constant frequency source is dependent on the motion of both the source and the receiver. If the effective path length is being reduced with time, the received frequency is greater than that of the source, and vice versa.

The use of transcutaneous Doppler ultrasound for the measurement of blood velocity was first reported by Satomura (1959) and subsequently by many others (e.g. Baker et al, 1964; Stegall et al, 1966). The principle on which a Doppler ultrasound system is based is shown in Fig.3.20. In its simplest form a pencil probe which houses co-planar emitting and receiving crystals is used. The transmitter crystal T sends a beam of ultrasound which is backscattered in all directions by the blood cells moving within the vessel. The receiver crystal R picks up part of this scattered ultrasonic power with a shift in frequency. This effect, called the Doppler shift Δf , is given by:

$$\Delta f = \frac{2fu \cos \psi}{c} \quad (3.24)$$

Where f is the transmitter frequency, u is the velocity of blood cells, and c is the velocity of sound in blood. When ultrasound is incident on a vessel a range of Doppler shift frequencies is generated corresponding to the velocity profile across the vessel. To measure u from this spectrum, specially designed Doppler spectrum processors are used.

3.7.2.1.2 Development and applications of Doppler ultrasound

The first Doppler technique used to detect blood velocity was continuous wave (CW) ultrasound, which is still widely used in the clinical environment. In a CW Doppler the transmitting and receiving crystals are mounted side by side on a probe placed on the subject's skin (as shown in Fig.3.20), and the transmission and reception of ultrasound signals are continuous. Because the target volume is large and blood cells travel at different velocities within the blood vessel, a spectrum of Doppler frequencies is produced. The problem is then to detect u from this spectrum. Three techniques have been used for this purpose. These are the zero crossing detector, the average frequency meter and the spectrum analyser.

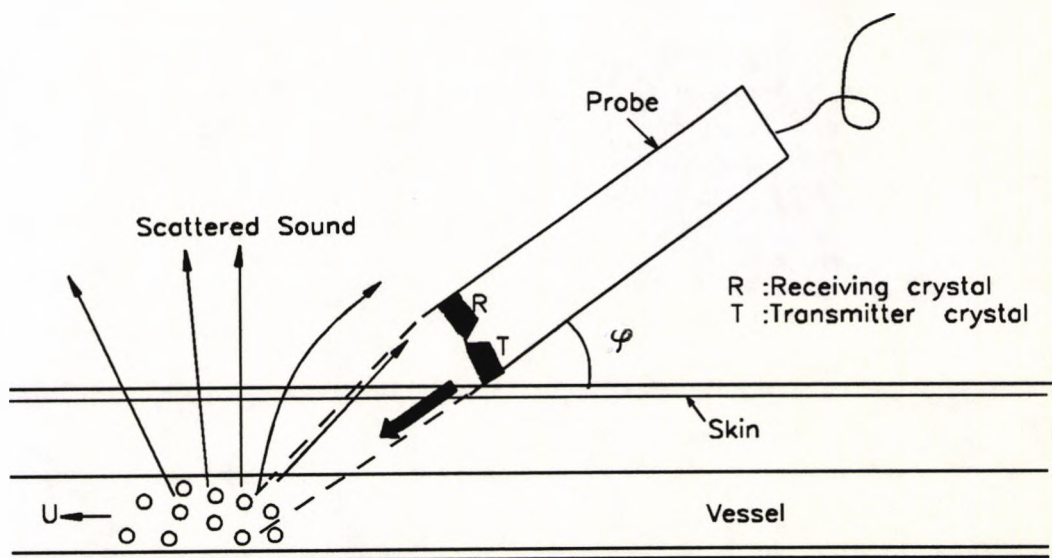


Fig. 3.20 Principle of Doppler ultrasound.

The first application of Doppler ultrasound techniques in the evaluation of arterial disease was performed by Strandness *et al* (1967). The principle was simple: the course of an artery was traced along the limb whilst the operator listened for sudden changes in the characteristics of the signal. It was soon found that compression of the limb produced changes in the distal flow patterns, and that these changes were different in normal and in occluded vessels (Rittenhouse and Brockenbrough, 1969). The next step was the discovery that pressure changes in the leg (measured with a Doppler detector in conjunction with a sphygmomanometer) seems to correlate with the level of disease (Lewis *et al*, 1972). They observed that the blood pressure at the ankle did not alter greatly following exercise in a healthy state, but in disease it fell substantially (up to 50% of the resting pressure) immediately after exercise.

Of the organs that require examination for vascular function, the heart is perhaps the most inaccessible, while at the same time being one of the most important. Kalmanson *et al* (1970, 1972) have extensively exploited the use of the Doppler velocimeter for the diagnosis of right ventricular disease using both transcutaneous and catheterised probes. Further, Tunstall Pedoe (1972) has successfully exploited pattern recognition techniques. By making directional measurements of subclavian artery flow patterns, he achieved an 85% accuracy in the diagnosis of aortic incompetence. Subsequently, Fitzgerald and his colleagues (1976) have applied sonogram pattern recognition methods to the study of coronary artery blood flow.

However, simple CW Doppler systems are unable to measure the distance between the probe and the moving target. This has severely restricted their application to measuring velocity profiles especially in multidirectional flows. A series of more sophisticated techniques has been developed to allow velocity and position of the target to be measured simultaneously. The first of these was the pulsed wave (PW) Doppler developed independently by Flaherty and Strauts (1969), Peron-

neau and Leger (1969), and Wells (1969). In a PW Doppler, pulses of ultrasound are transmitted at a regular frequency and received by the same crystal. By only receiving returning signals within a limited time span (range-gating), the instrument could investigate flow in a narrow spatial range. PW Doppler has been used in measurement of the instantaneous velocity profile in a vessel and its variation through the cardiac cycle. (eg. Peronneau *et al*, 1972; Reneman *et al*, 1985; Vieli *et al*, 1986). It has also been added to a B-mode ultrasound imager to provide combined anatomical imaging and flow data (Phillips *et al*, 1980). An important limitation of the PW Doppler method is that the maximum velocity which may be measured at any particular range is restricted by ambiguity with the pulse repetition frequency. Therefore, it is often combined with CW Doppler to detect high frequencies.

3.7.2.2 Laser-Doppler anemometry (LDA)

LDA has undergone considerable development since the technique was first introduced by Yeh and Cummins (1964) for velocity measurements of small tracer particles suspended in a flowing fluid. Although a number of different optical systems and different fringe modes have been used in LDA, its main components, as shown in Fig.3.21, consists of a laser light source, optical systems to transmit and collect light, a photodetector and a signal processor.

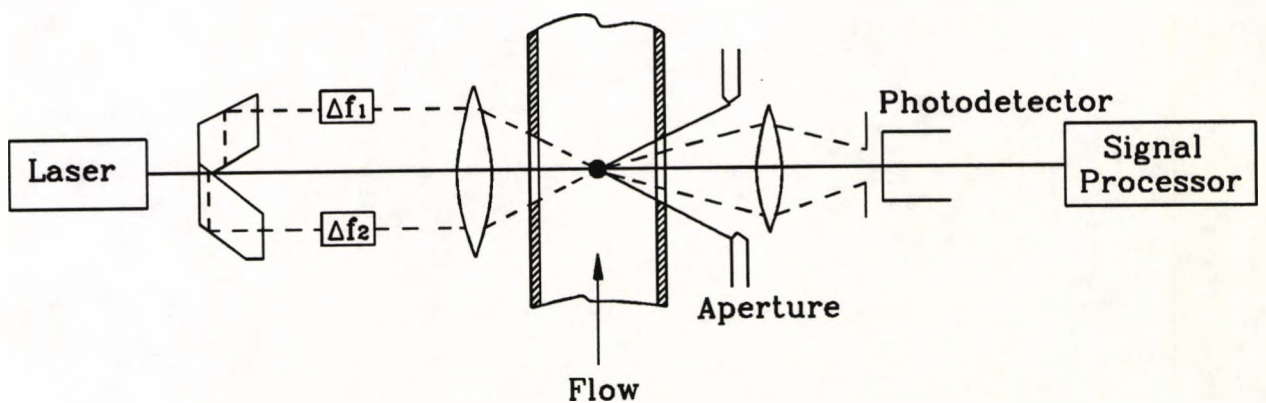


Fig. 3.21 Principle of Laser-Doppler anemometer.

The laser is a source of coherent light of appropriate intensity, its beam is split into two parts which cross to form a fringe grid in the local region of the flow where velocity measurements are required. Tracer particles in the fluid passing through the fringe grid send out a different frequency. From the Doppler shift of scattered radiation, or from fringe considerations, a linear relationship between the frequency difference of the two scattered beams and the velocity of the particles can be derived as follows:

$$f_D = \frac{2U_x}{\lambda} \sin \frac{\psi}{2} \quad (3.25)$$

where ψ is the angle between the incident beams, λ the wave length of the laser beams, and U_x is the measured velocity component. The photodetector measures the frequency difference and converts the optical signal to an electronic signal which is processed by an appropriate signal-processing arrangement.

The advantage of the LDA lies in its high temporal and spatial resolution. The measuring volume can be smaller than $10^{-4}mm^3$, depending on the focal and beam distances. This optical method is linear and has a fast response time. No calibration is necessary and the flow is not disturbed. Up to now, a number of 3-D LDA systems have been developed which allow the three orthogonal velocity components to be measured simultaneously. Therefore, LDA is being used more and more in the place of hot wires for quantitative measurement of instantaneous velocity, especially for complex flows involving high turbulence intensities and recirculation.

The accuracy of the LDA depends mainly on the accuracy of one's knowledge of the illuminating light frequency, the design of the optics and the accuracy of measurement of the Doppler shift frequency.

Many attempts have been made with LDA to investigate the complicated flow field in arterial bifurcations. It has shown great advantages in obtaining detailed velocity profiles in model and *in vitro* studies, but is not applicable to *in vivo* measurement (Durst et al, 1982). This is because one of the necessary conditions for the operation of LDA is a transparent medium with a suitable concentration of tracer particles. Although it was demonstrated that Doppler signals could be obtained from the laser light scattered by red cells, it was also shown that the quality of the signal diminished with increasing hematocrit and that with whole blood, i.e. a hematocrit of 45%, measurable signals could not be obtained from vessels of inside diameter greater than around $250\mu m$. Therefore, it can be concluded that in general LDA is unlikely to be of any value in the study of local velocity *in vivo* or in whole blood flowing in glass tubes.

3.7.3 Wall Shear Stress Measurement

Accurate measurements of wall shear stress at the boundaries of a three-dimensional flow field are indeed difficult. So far, no method has yet been proved possible to measure wall shear stress accurately as a function of time either *in vivo* or *in vitro*. This is because: (i) the velocity gradient varies rapidly across a thin boundary layer ($< 2mm$) near the arterial wall, so any probe must be accurately embedded in the wall; any protuberance can significantly affect the local distribution of shear stress; (ii) the wall shear probe must respond accurately to higher frequencies than a velocity probe; and (iii) the wall shear stress may reverse its direction when the average and centre-line velocity do not; furthermore, it always has a phase lead over those velocities, thus the problems associated with reversal are more pronounced than in velocity measurement.

In general, wall shear stress is measured in two ways: (i) to measure it directly with a hot-film shear probe (Ling et al, 1968) or an electrochemical technique (Lutz, 1975); (ii) to estimate it by measuring the velocity profile near the wall

and extrapolating it to zero at the wall. The former methods assume a boundary layer type flow exists in the neighbourhood of the sensor; they have poor frequency response (this issue is discussed in detail by Pedley (1980)) and are confined to steady flow studies. For the latter approach, sample volume resolution problems arise and even when the velocity profile is known quite accurately, extrapolation to estimate wall shear is notoriously inaccurate. The inaccuracy comes from both errors in the location of the exact wall position, and in that velocity measurements can not be made as close to the wall as desired because of having to retain an adequate Doppler signal.

A previous study of steady flow in a carotid bifurcation model (Bharadvaj et al, 1982b) showed that the method for estimating wall shear stress from the measured velocity profiles gave values within 15% of the theoretical Poiseuille result in the common carotid artery proximal to the bifurcation. More recently, several attempts have been made to derive unsteady wall shear from LDV measurements of near wall velocities. Ku et al (1985) studied the instantaneous wall shear stress in a rigid carotid bifurcation under pulsatile flow conditions. Deters et al (1986) obtained the time-varying wall shear rate in a compliant cast of a human aortic bifurcation. Since the cast wall is in motion through the pulsatile cycle, the time variation of the distance from the velocimeter sampling volume to the cast wall was obtained from LDV measurements of the velocity of the wall itself.

CHAPTER 4

CODE IMPROVEMENT

4.1 INTRODUCTION

The employed computer code ASTEC has three-dimensional, time-dependent capabilities and an unstructured finite element mesh which provides the possibility of coping with the three-dimensional bifurcation geometry. However, to make the code more suited and robotic for the current application, there are several aspects that need to be improved. Firstly, the pre-processor — mesh generator SOPHIA is not very straightforward in use, especially for complex bifurcation geometries. It needs a great deal of input data, for which careful preparation and calculation (sometimes necessary) have to be done beforehand. Secondly, at the beginning of this research ASTEC did not have non-Newtonian modelling capability, although possibilities of implementing this in the code do exist. Finally, the code could not treat problems with moving boundaries. In this chapter, improvements on the forgoing aspects are described. It contains the development of a purpose-built automatic grid generation routine for general bifurcation geometries, the implementation of non-Newtonian model, and a preliminary scheme to incorporate the arterial wall compliance.

4.2 GRID GENERATION FOR GENERAL 3-D BIFURCATION GEOMETRIES

4.2.1 Mesh Generation Procedure in SOPHIA (old)

SOPHIA is a semi-automatic interactive mesh generator which produces 3-D finite element mesh for use with the ASTEC. Before using the routine, the outline of the structure to be modelled should be divided into a few structural blocks, each of these must have six sides which can be a plane or a curved surface. The

geometry of each block is defined by twenty points. As shown in Fig.4.1, these structural points are the eight "corners" and the twelve "mid-face" points. Note that although the term "corner" is used here these could be points on a curve. The grid generation procedure is illustrated in Fig.4.2. First of all, coordinates of the structural points are read into the routine to locate the block, then the topology of the block is requested to generate the block structure. To describe the topology, each block has its own local node numbering system. It lists the corners first working anti-clockwise from bottom to top, then the mid-points starting between the first two corners.

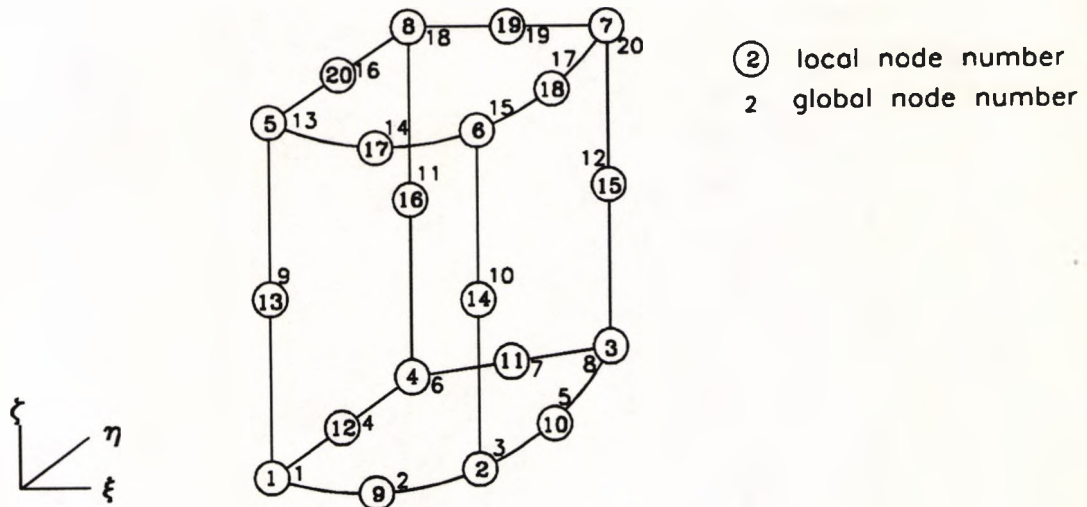


Fig. 4.1 3-D structural block.

Fig.4.1 also shows the $\xi - \eta - \zeta$ axes for the local node system. These do not have to be the same as the global $x - y - z$ axes. The sub-division of the block is based on the number of elements required in the ξ , η , and ζ directions, which are specified by the user. Note that where two blocks are adjacent the numbers of elements at the common edge must be the same in order to keep the mesh lines continuous. The edge of each block is subdivided either equally or non-uniformly under the control of a weighting factor. Boundary condition patches are requested to specify boundary conditions in the mesh. In ASTEC code, each patch has a

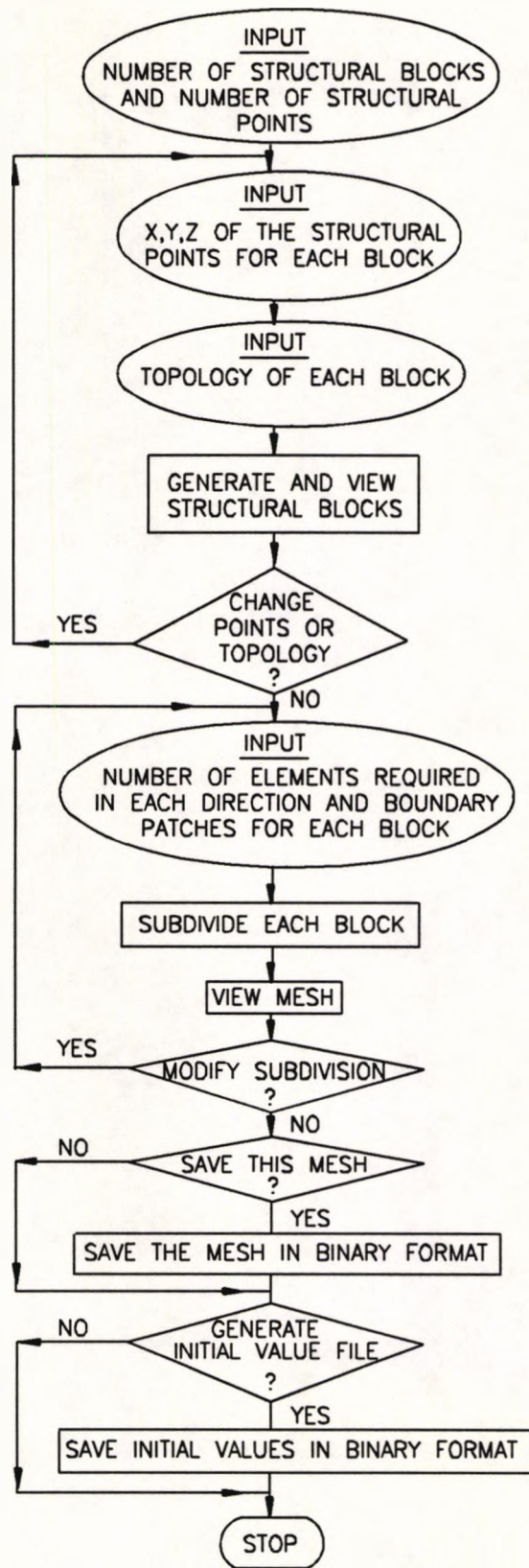


Fig. 4.2 Grid generation procedure in SOPHIA.

unique name and a corresponding NOB* number. Listed in descending order of priority, the standard boundary condition patches are: walls, solid regions, inlets, outlet, symmetry lines and symmetry planes. Having generated the mesh, all data which specify the complete mesh geometry are saved in a data file in binary format. An initial values file is also produced after the completion of mesh generation.

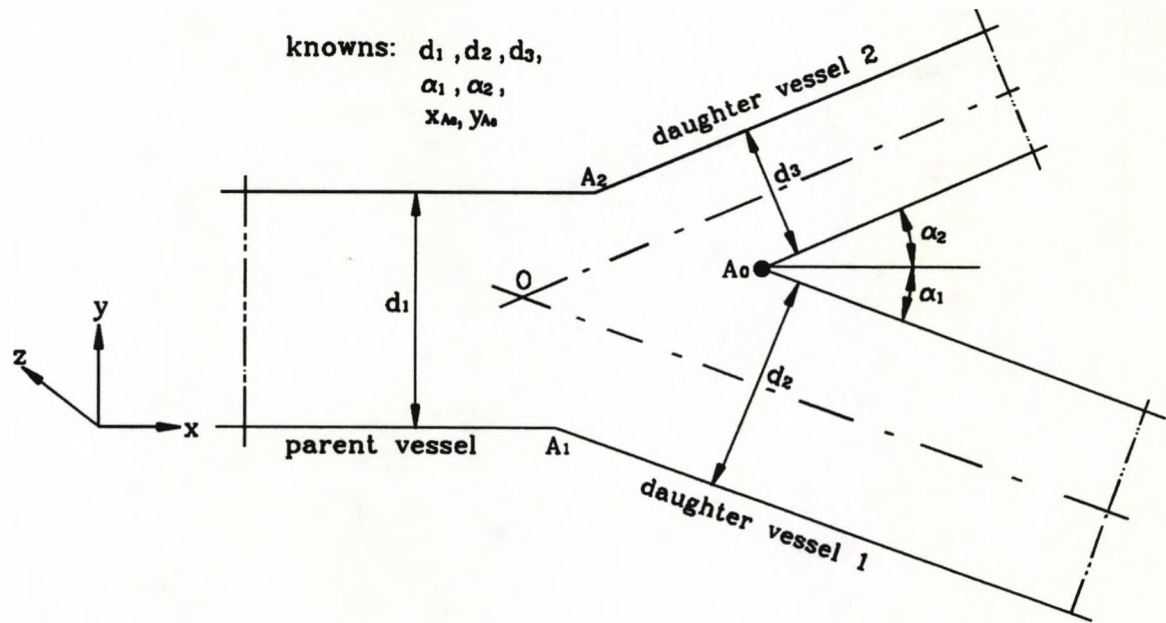


Fig. 4.3 Definition of general bifurcation geometry.

4.2.2 Definition of General Bifurcation Geometries

A bifurcation consists of three vessels which intersect each other. Before defining the geometry for a general bifurcation, two assumptions are made: (i) all vessels are circular in cross section; and (ii) intersection areas between parent and daughter vessels are not smoothed. If the bifurcation is planar, i.e., parent and daughter vessels are in the same plane, a local view of the bifurcation geometry in the symmetry plane can be illustrated as Fig.4.3. In such a case, the geometry of the bifurcation is defined by the vessel diameters at the branching (d_1, d_2, d_3), the branch angles (α_1, α_2), and the relative position of the apex (x_{A_0}, y_{A_0}). Let $O(x_o, y_o)$ be the intersection of the two daughter vessels' axes, and $x - y - z$ be the global axes. Since the vessels are assumed to be circular, using the general analytical geometry

equation of a cylinder and the formulae for coordinate transformation, their geometries in the bifurcation area can be mathematically expressed as:

parent vessel

$$(y - r_1)^2 + z^2 = r_1^2 \quad (4.1)$$

daughter vessel No.1

$$[(y - y_o) \cos \alpha_1 + (x - x_o) \sin \alpha_1]^2 + z^2 = r_2^2 \quad (4.2)$$

daughter vessel No.2

$$[(y - y_o) \cos \alpha_2 + (x - x_o) \sin \alpha_2]^2 + z^2 = r_3^2 \quad (4.3)$$

where r_1 , r_2 and r_3 being the radius of each vessel. Intersection between parent vessel and daughter vessel No.1 can be described by satisfying Eqns.(4.1) and (4.2) simultaneously. Solving the coupled equations, two roots are obtained:

$$x = x_o + \left[(y_o - y) \cos \alpha_1 \pm \sqrt{(y - r_1)^2 - (r_1^2 - r_2^2)} \right] / \sin \alpha_1 \quad (4.4)$$

Since the intersection area of interest is on the left hand side of the daughter vessel, the smaller root is then chosen. Hence, points at the intersection between parent and daughter vessel No.1 are given by:

$$\begin{cases} x = x_o + \left[(y_o - y) \cos \alpha_1 - \sqrt{(y - r_1)^2 - (r_1^2 - r_2^2)} \right] / \sin \alpha_1 \\ z = \pm \sqrt{r_1^2 - (y - r_1)^2} \end{cases} \quad (4.5)$$

Similarly, points at the intersection between parent and daughter vessel No.2 are obtained:

$$\begin{cases} x = x_o + \left[(y - y_o) \cos \alpha_2 - \sqrt{(y - r_1)^2 - (r_1^2 - r_3^2)} \right] / \sin \alpha_2 \\ z = \pm \sqrt{r_1^2 - (y - r_1)^2} \end{cases} \quad (4.6)$$

Points at the intersection between two daughter vessels are given by:

$$\begin{cases} x = x_o + \frac{1}{C_3} \sqrt{C_2^2 (y - y_o)^2 - C_3 [C_1 (y - y_o)^2 - (r_2^2 - r_3^2)]} - C_2 (y - y_o) \\ z = \pm \sqrt{r_2^2 - [(y - y_o) \cos \alpha_1 + (x - x_o) \sin \alpha_1]^2} \end{cases} \quad (4.7)$$

where

$$\begin{cases} C_1 = \cos^2 \alpha_1 - \cos^2 \alpha_2 \\ C_2 = \sin \alpha_1 \cos \alpha_1 + \sin \alpha_2 \cos \alpha_2 \\ C_3 = \sin^2 \alpha_1 - \sin^2 \alpha_2 \end{cases} \quad (4.8)$$

From Fig.4.3 relationships between x_o , y_o and the basic known geometric data can be derived:

$$x_o = x_{A_o} - \overline{OA_o} \cdot \cos \beta \quad (4.9)$$

$$y_o = y_{A_o} - \overline{OA_o} \cdot \sin \beta \quad (4.10)$$

where

$$\beta = \arctan \frac{(d_2/d_3) \sin \alpha_2 - \sin \alpha_1}{\cos \alpha_1 - (d_2/d_3) \cos \alpha_2} \quad (4.11)$$

$$\overline{OA_o} = \frac{d_2}{2 \sin(\alpha_1 + \beta)} \quad (4.12)$$

Positions of the two shoulder points A_1 and A_2 may also be determined:

$$x_{A_1} = x_{A_o} - \overline{OA_o} \cdot \cos \beta + [\cos \alpha_1 (y_{A_o} - \overline{OA_o} \cdot \sin \beta) - d_2/2] / \sin \alpha_1 \quad (4.13)$$

$$x_{A_2} = x_{A_o} - \overline{OA_o} \cdot \cos \beta + [\cos \alpha_2 (d_1 - y_{A_o} + \overline{OA_o} \cdot \sin \beta) - d_3/2] / \sin \alpha_2 \quad (4.14)$$

Note that the bifurcation is assumed to be planar when deriving the above relations. If the bifurcation is non-planar, i.e., there is an off-plane angle for

one of the daughter vessels, then the plane shown in Fig.4.3 can be considered as the plane where the parent and one of the daughter vessels sit, while the other daughter vessel is drawn as its projection on the defined plane. In that case, an extra coordinate transformation should be performed for the daughter vessel lying an angle to the bifurcation plane.

4.2.3 The Purpose-built Routine

In the previous section, bifurcation geometry at the local branching area is described mathematically. A complete definition of a general bifurcation geometry should also include information on variation of diameters of each vessel, as well as their length. In this section, a purpose-built routine which aims at minimising the user input for the mesh generator SOPHIA is presented. The preparation procedure for a bifurcation with constant parent and daughter vessel diameters is presented first; it is then extended to the case where vessel diameters are allowed to change.

Fig.4.4(a) shows the symmetry plane of a bifurcation with constant vessel diameters. Positions of A_1 , A_2 and other points at intersections can be determined using relations derived in the last section. First of all, the bifurcation is divided into six parts, each of which can be represented as part of a cylinder. For each part, the following two steps are performed:

Step 1 Split each part into three blocks as illustrated in Fig.4.4(b). Each block satisfies the requirement for a structural block used in SOPHIA, i.e., it has eight corners, the geometry being defined by twenty points.

Step 2 Specify subdivision requirements for each block, ensuring that (i) numbers of elements at block interfaces are well-matched, and (ii) at cross-sections, distribute finer grids near the wall; in the axial direction, distribute finer grids near the branching.

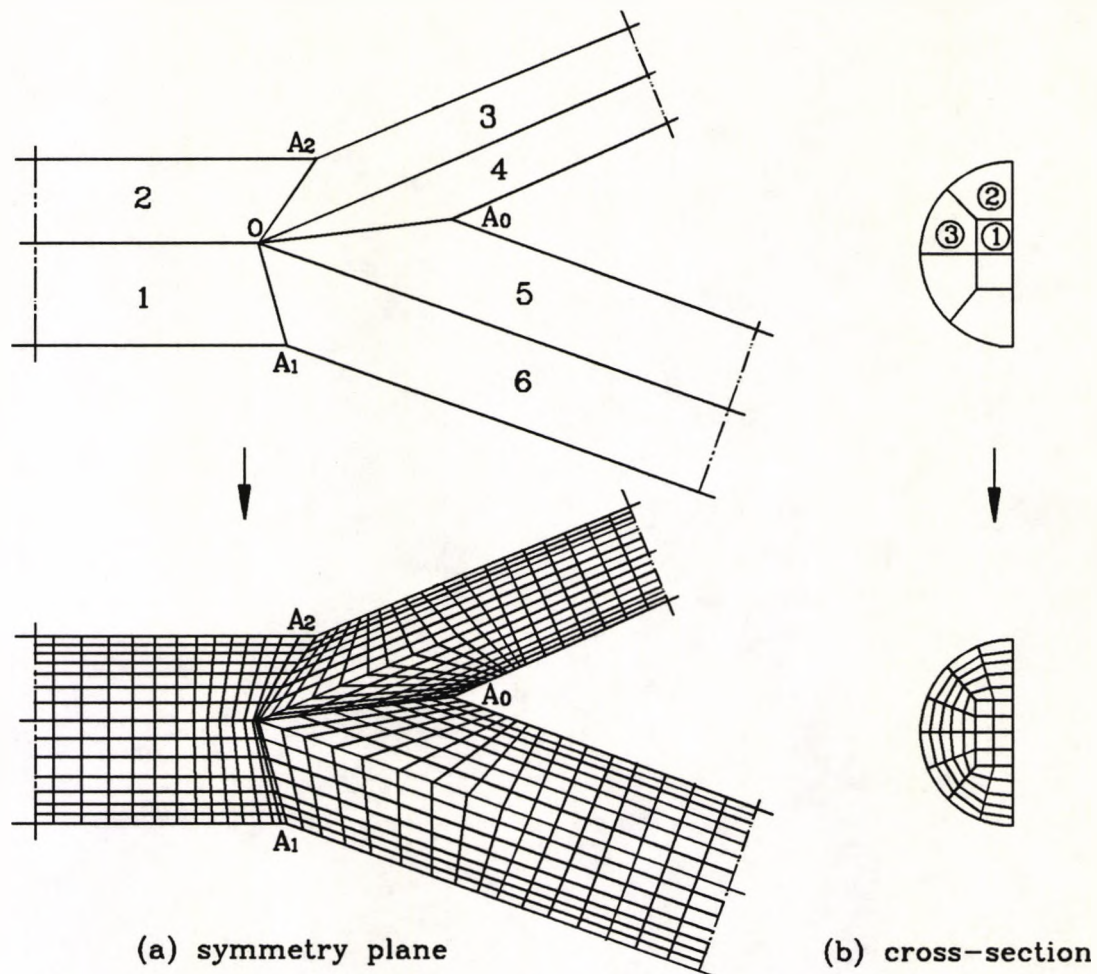


Fig. 4.4 Grid generation procedure for a general 3D bifurcation.

Since these two steps have to be repeated for each block, a standard subroutine was written to perform these automatically and is called once for each block. This subroutine allows vessel diameter to change linearly. For those cases where the variations of vessel diameters are non-linear, the vessel should be further split into smaller parts, within which a linear variation applies. This treatment is rather crude for bifurcations having curved branches or non-linear vessel profiles. Therefore, a standard subroutine to generate grid for a curved tube was designed, this can be called wherever a curved segment exists. A further improvement is to consider the use of a polynomial function for the description of vessel profiles.

Boundary condition patches for each block follow their own rules, for example, block 1 in Fig.4.4(b) has a maximum of two types of patches: (i) a symmetry plane, and (ii) a symmetry plane and an inlet or outlet, depending upon whether it is a

internal segment or includes any inlets or outlets. To designate boundary condition patches more conveniently, a special numbering system was adopted so that blocks having the same types of boundary condition patches can be easily identified.

The flow chart of the routine is illustrated in Fig.4.5. It requires only basic geometric data and produces all necessary informations required by the mesh generator SOPHIA. By using this routine together with the SOPHIA, the amount of user input is significantly reduced. Applications to various bifurcation geometries are presented in the following section.

4.2.4 Applications

In order to demonstrate the applicability of the grid generation routine developed, applications to a variety of bifurcation geometries were carried out. These include idealised 90° T-bifurcations, curved branches, canine femoral bifurcation, and human carotid bifurcation models. Fig.4.6 shows the grid configuration for a 90° T-bifurcation, in which diameters of the main and branch tubes are the same and kept constant. Fig.4.7 illustrates the grid configuration for a curved branch having a curved angle of 45° . Fig.4.8 shows the grid configuration for a canine femoral bifurcation, which has a 1.47 diameter ratio between the daughter vessels and 7° and 40° bifurcation angles from parent to larger daughter vessels and parent to smaller daughter vessels respectively. Again the cross-sectional area of each vessel is constant. Fig.4.9 shows the grid configuration for a human carotid bifurcation model with variable diameters for the larger daughter vessel.

In all these applications, only the basic defined geometrical data, such as vessel diameters and bifurcation angles were supplied by the user. The generated grids are suitable for use with finite volume and finite element based fluid flow solvers. It is demonstrated that the mesh generation routine developed is a convenient and efficient tool in the grid generation of a considerably complicated bifurcation

geometry. However, a further study concerning the smoothing of bifurcation corner areas still needs to be done.

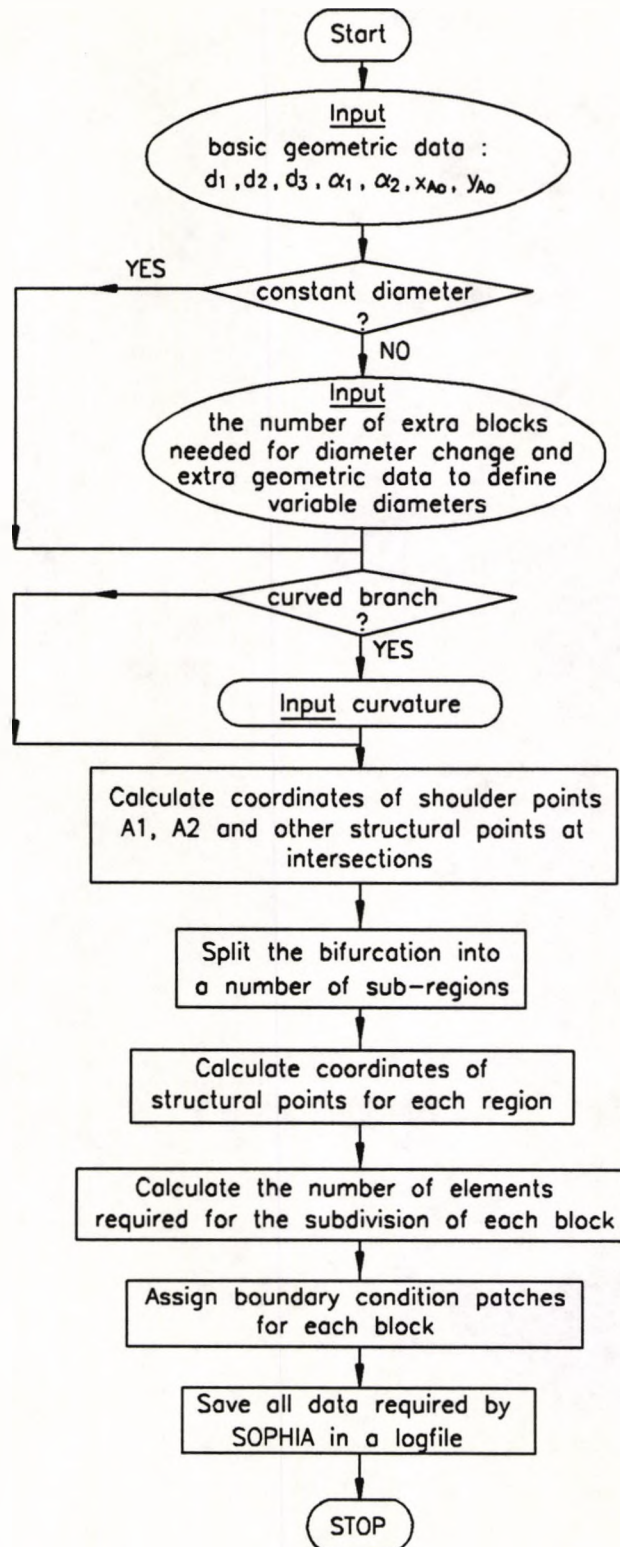


Fig. 4.5 Flow chart of the grid generation routine.

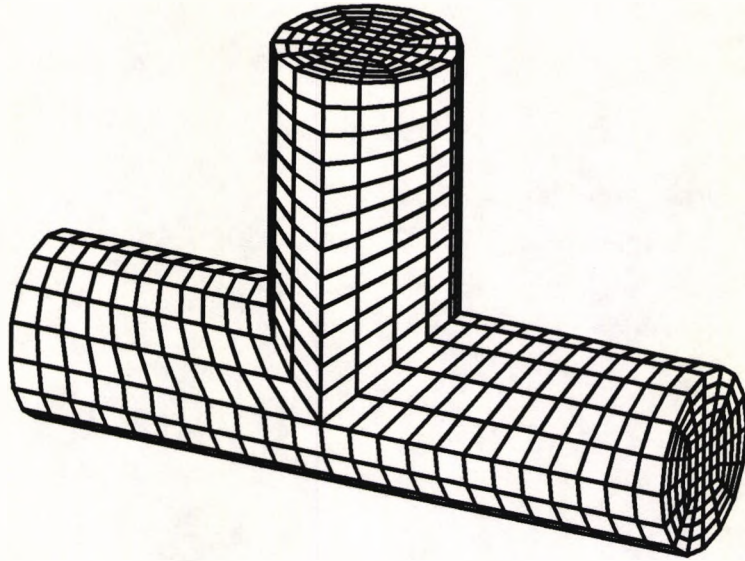


Fig. 4.6 Grid configuration of a T-bifurcation.

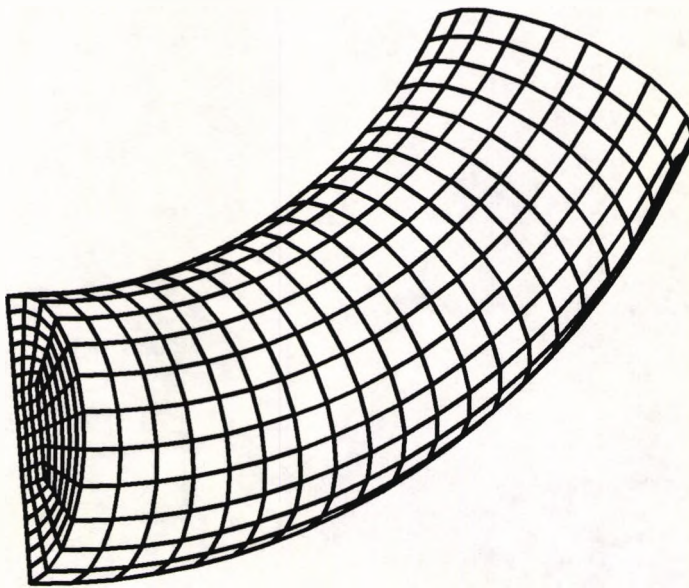


Fig. 4.7 Grid configuration of a curved branch.

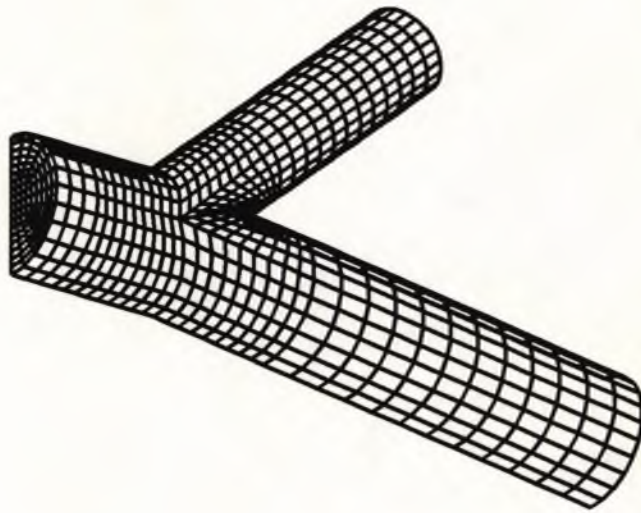


Fig. 4.8 Grid configuration of a canine femoral bifurcation.

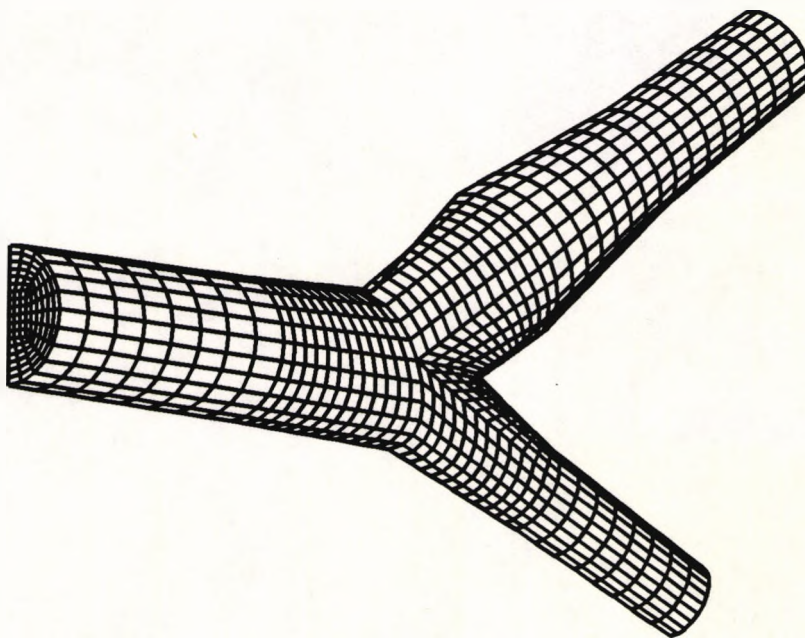


Fig. 4.9 Grid configuration of a human carotid bifurcation model.

4.3 IMPLEMENTATION OF NON-NEWTONIAN MODEL

The momentum equations for an incompressible non-Newtonian fluid was introduced in chapter 2 (Eqn.(2.11)), where the viscosity is considered as a function of the second invariant of the strain rate tensor. In the ASTEC code, the conservation equations are written in the integral form and are solved numerically by applying them to individual control volumes. The integral form of the momentum equations can be expressed as:

$$\rho \frac{\partial}{\partial t} \int \mathbf{u} dV = -\rho \int \mathbf{u} \mathbf{u} \cdot d\mathbf{A} - \int \nabla P dV + \int \mu_{eff} (\nabla \mathbf{u}) \cdot d\mathbf{A} \quad (4.15)$$

where \mathbf{u} is the velocity vector, $d\mathbf{A}$ and dV the elements of control surface area and control volume respectively, and μ_{eff} the effective viscosity. Since ASTEC employs the $k - \varepsilon$ turbulence model, it is more general to define the effective viscosity as:

$$\mu_{eff} = \mu_L + \mu_T \quad (4.16)$$

where μ_L being the laminar viscosity which is constant, and μ_T the turbulent viscosity which is calculated from:

$$\mu_T = C_\mu \rho \frac{k^2}{\varepsilon} \quad (4.17)$$

with C_μ a constant, k and ε the turbulent energy and dissipation rate. Although turbulent modelling is of no interest here, note that in ASTEC whether the flow is laminar or turbulent, μ_T is set and used from the local values of k and ε . Thus by setting non-zero values of k in the initial values file or user supplied subroutine, the local turbulent viscosity can be prescribed even for a laminar calculation. This feature has been utilised to accommodate the non-Newtonian viscosity. The detailed procedures are as follows:

- (a) Set $\mu_L = 0$, thus $\mu_{eff} = \mu_T$;

- (b) Set $\varepsilon = C_\mu = \text{constant}$ (by default $C_\mu = 0.09$), thus $\mu_T = \rho k^2$;
- (c) Use the constitutive equation of $\mu(J_2)$ to calculate the local nodal viscosity μ_{n-N} , and set $\mu_T = \mu_{n-N}$;
- (d) Set $k = \sqrt{\mu_T/\rho}$.

Steps (b)–(d) are implemented in a user supplied subroutine, which is called every iteration immediately after the scalar variables are updated. By doing so, the non-Newtonian viscosity is specified and calculated from the local values of shear rate.

One question arises here is that of the constitutive equation, i.e., what form of $\mu(J_2)$ should be used? This question has been addressed in chapter 3, where five rheological models of blood were discussed in detail, among them a general power law expression was considered to be more appropriate. Take the general power law for instance, the relationship between shear stress τ and shear rate $\dot{\gamma}$ is given by:

$$\tau = m|\dot{\gamma}|^n \quad (4.18)$$

with m and n being constants. Hence the non-Newtonian viscosity can be written as:

$$\mu_{n-N} = \mu_{n-N}(|\dot{\gamma}|) = m|\dot{\gamma}|^{n-1} \quad (4.19)$$

For a simple shear flow, the shear rate is:

$$\dot{\gamma} = 2S_{12} \quad (4.20)$$

In this case, all other components of S_{ij} vanish and the second invariant of the shear rate tensor J_2 depends only on S_{12} :

$$J_2 = S_{12}^2 \quad (4.21)$$

So that from Eqn.(4.20), we have:

$$|\dot{\gamma}| = 2\sqrt{J_2} \quad (4.22)$$

Thus, for general 2D or 3D flows Eqn.(4.19) may be modified as:

$$\mu_{n-N} = \mu(J_2) = m(2\sqrt{J_2})^{n-1} \quad (4.23)$$

where J_2 , expressed in a 3D Cartesian coordinate system, is:

$$J_2 = \frac{1}{2} \left\{ \left(\frac{\partial u}{\partial x} \right)^2 + \left(\frac{\partial v}{\partial y} \right)^2 + \left(\frac{\partial w}{\partial z} \right)^2 \right\} + \frac{1}{4} \left\{ \left(\frac{\partial u}{\partial y} + \frac{\partial v}{\partial x} \right)^2 + \left(\frac{\partial w}{\partial y} + \frac{\partial v}{\partial z} \right)^2 + \left(\frac{\partial u}{\partial z} + \frac{\partial w}{\partial x} \right)^2 \right\} \quad (4.24)$$

Note that the similar approach can also be applied to other non-Newtonian models, e.g., the general form of the Casson relation may be derived as:

$$\mu(J_2) = \frac{1}{2\sqrt{J_2}} \left(\sqrt{\tau_y} + \eta\sqrt{2\sqrt{J_2}} \right)^2 \quad (4.25)$$

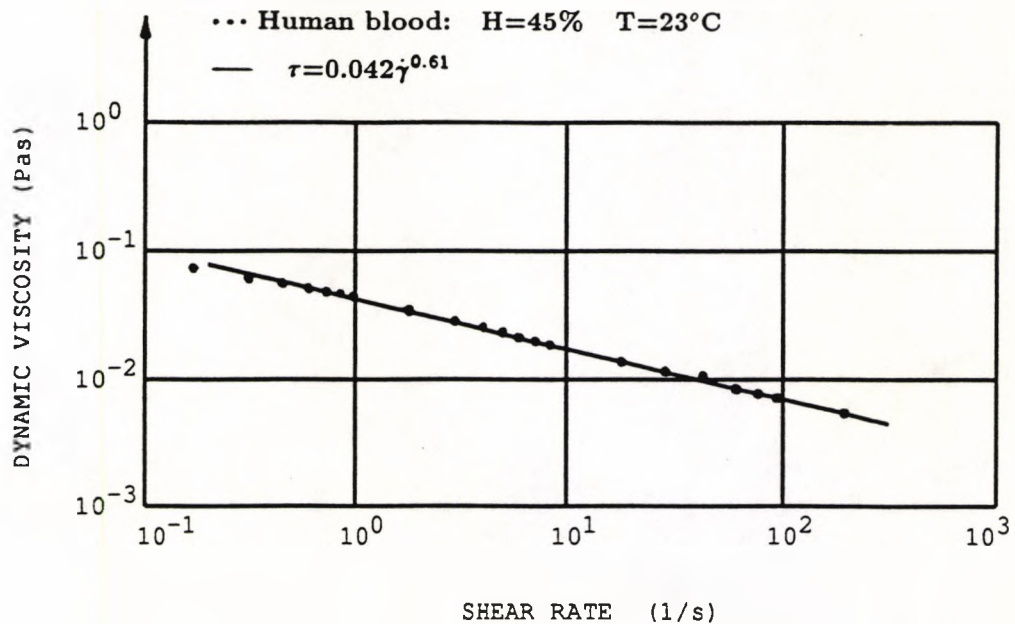


Fig. 4.10 Dynamic non-Newtonian viscosity of human blood with a hematocrit of 45% at 23°C.

Fig.4.10 shows the dynamic flow curve of human blood with hematocrit of 45% at 23°C (Liepsch and Moravec, 1984). The experimental data were fitted using a power law relation of Eqn.(4.18), and the two constants were obtained: $m = 0.042$, $n = 0.61$. Substituting these into Eqn.(4.23) yields the constitutive equation for blood:

$$\mu(J_2) = 0.042(2\sqrt{J_2})^{-0.39} \quad (\text{Pa}\cdot\text{s}) \quad (4.26)$$

Eqn.(4.26) is valid when $J_2 \neq 0$ and rather small. On the other hand, when J_2 is sufficiently large, the blood viscosity is constant. The point of transition from Eqn.(4.26) to the Newtonian equation, $\mu = \text{constant}$, depends on the hematocrit H . For normal blood with a normal hematocrit, $H = 45\%$, experimental results showed that the transition point was around $\dot{\gamma} \simeq 700\text{S}^{-1}$, and the dynamic viscosity approached an asymptotic value of 0.004 Pa·s. The Fortran subroutine for the specification of non-Newtonian viscosity is listed in Appendix C.

4.4 INCORPORATION OF THE COMPLIANT WALL

To solve the flow field in an arterial bifurcation with a distensible wall is a rather complex problem, since it couples the modelling of mechanical behaviour of the arterial wall and the modelling of fluid flow. This problem may be analyzed as a feedback system of two functional components as illustrated in Fig.4.11. In the lower block, arterial wall is regarded as a conduit for fluid flow with a specified shape. For a given upstream flow condition the fluid flow equations can be solved and velocities and stresses including normal stress (pressure) and shear stress are obtained. This stress distribution may then be applied as loading on the arterial wall which can be regarded as an elastic or a viscoelastic body as represented by

the upper block. Using the theory of solid mechanics, the stress-strain equations for the arterial wall can be derived and wall displacements are evaluated. These results are then used to determine the boundary conditions for the fluid flow problem represented by the lower block. This cycle should be carried out until a consistent solution is achieved. Then the calculation can proceed to the next time step.

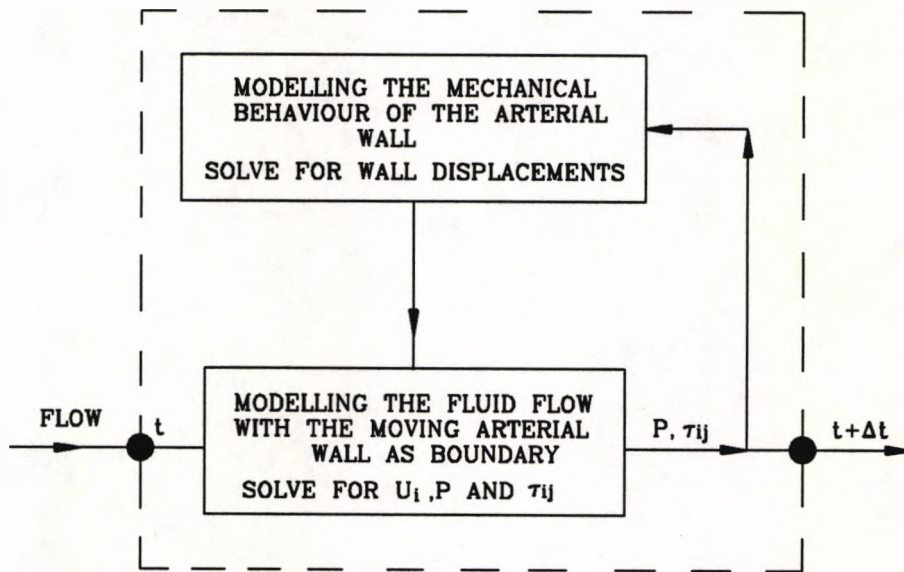


Fig. 4.11 A feedback system of two functional units.

Such a fully coupled treatment is an ideal way to accommodate the distensible wall in the fluid flow modelling and has been applied to one-dimensional flow analysis. However, when applied to three-dimensional flow modelling, it brings about great computational difficulties. A fully coupled simulation demands the merger of a solid mechanics code and a fluid dynamics code into a single one. Although the importance of this merge has been realised recently, no such a code has been developed so far. Since the effect of wall compliance on flow at arterial bifurcations has drawn researchers' attention only recently, very little has been learned on this even from experimental studies, it is thought reasonable to accommodate this factor in a rather simplified way before a comprehensive approach is practicable. Up to now, the only numerical study on arterial bifurcation flow with the wall distensibility being taken into account is that of Reuderink (1991), in which an decoupled approach

was used for flow analysis in a distensible model of the carotid arterial bifurcation. The calculation was performed in three sequential steps: (i) calculate the pressure distribution using a one-dimensional model for wave propagation; (ii) calculate the wall motion due to this pressure distribution; and (iii) solve the flow equations with the wall motion prescribed as boundary conditions. This approach was claimed to be valid if the pressure distribution is mainly dependent upon wave phenomena but not on local fluid flow effects. This point is difficult to justify as the pressure distribution from the three-dimensional flow equations were not calculated and compared with the one from the one-dimensional analysis. In this dissertation, a simplified coupled scheme is proposed for the incorporation of the distensible wall. Details of this approach are described in the following two subsections.

4.4.1 Mathematical Model of the Arterial Wall

The arterial wall is assumed to be isotropic, incompressible and non-linearly elastic and can be modelled as a thin walled cylinder undergoing finite deformation. As discussed in chapter 3, the third-order polynomial strain-energy function can be applied to describe the stress-strain relationship for an artery under these assumptions, and two expressions which relate the Green's strains (circumferential and longitudinal) with inner wall pressure (P) and longitudinal force (F) were also derived (see Eqn.(3.22)). Considering the fact that in actual circulation, longitudinal movement of the vessel wall in large arteries is very small, except for the pulmonary artery and the ascending aorta (Petal et al, 1964). it is therefore assumed here that the longitudinal wall motion is negligible. This assumption leads to a simplified form of Eqn.(3.22):

$$\begin{cases} P = \frac{h}{r} [6Da^3 + (4A + 3D)a^2 + 2Aa] \\ F = 2\pi r h \left(Ba + Ea^2 - \frac{Pr}{2h} \right) \end{cases} \quad (4.27)$$

where A, B, D, E are material constants which are derived from experimental data,

h and r are deformed mid-wall radius and wall thickness, and a is the circumferential Green's strain defined as:

$$a = \frac{1}{2} \left[\left(\frac{r}{R_i} \right)^2 - 1 \right] \quad (4.28)$$

Let R_i and H_i denote the original (undeformed) mid-wall radius and wall thickness. From the assumption of incompressibility, the volume of the artery remains constant when stressed:

$$\pi h r = \pi H_i R_i \quad (4.29)$$

$$\frac{h}{r} = \frac{H_i R_i}{r^2} = \frac{1}{2a + 1} \frac{H_i}{R_i} \quad (4.30)$$

Substituting Eqn.(4.30) into Eqn.(4.27) yields:

$$P = \frac{1}{2a + 1} \frac{H_i}{R_i} \left[6Da^3 + (4A + 3D)a^2 + 2Aa \right] \quad (4.31)$$

Eqn.(4.31) gives a nonlinear relationship between pressure and the circumferential strain. Once the material constants and the undeformed dimension are known, it may be solved for a at any given pressure P . Subsequently, the longitudinal force F at the same pressure can be obtained. For convenience of use, Eqn.(4.31) can be converted into a polynomial functional form between pressure and diameter within the physiological pressure range:

$$\frac{d}{D_o} = f \left(\frac{P}{P_o} \right) \quad (4.32)$$

where P_o is the mean systemic pressure of 100 mmHg and D_o is the diameter at P_o . This relation is used to approximate vessel dilation under a distending pressure.

To obtain the polynomial function of Eqn.(4.32), the material constants have to be known. For this purpose a number of experimental works have been done, their

major results are summarised in Table 4.1. Using the material constants obtained by How and Clarke (1982), a third order polynomial function is derived:

$$\frac{d}{D_o} = 0.10676 \left(\frac{P}{P_o}\right)^3 - 0.18182 \left(\frac{P}{P_o}\right)^2 + 0.27130 \left(\frac{P}{P_o}\right) + 0.80151 \quad (4.33)$$

This is compared with their experimental data as shown in Fig.4.12.

Model*	A	B	C ($\times 10^8 \text{ N/m}^2$)	D	E	F	G	Reference
R.C.A	-7.1889	3.1255	0.1911	1.3711	10.2775	-3.3677	0.0787	Fung et al (1979)
R.L.I.	-16.3871	-0.3854	2.9122	16.0463	29.6790	1.1872	-2.2552	—
R.L.A.	-14.7220	-4.1606	4.4821	16.5753	29.9390	6.2093	-1.8999	—
R.U.A.	-12.0062	5.1405	-1.5938	-2.1292	23.5706	-7.3431	2.2089	—
A.P.	3.0231	2.9227	4.1104	-1.6959	-1.8700	-2.8331	-1.9322	How & Clarke(1984)

R.C.A. Rabbit carotid artery

R.L.I. Rabbit left iliac

R.L.A. Rabbit lower aorta

R.U.A. Rabbit upper aorta

A.P. Arterial prostheses with internal diameter between 3 and 6mm

Table 4.1 Summary of material constants for the polynomial strain energy function.

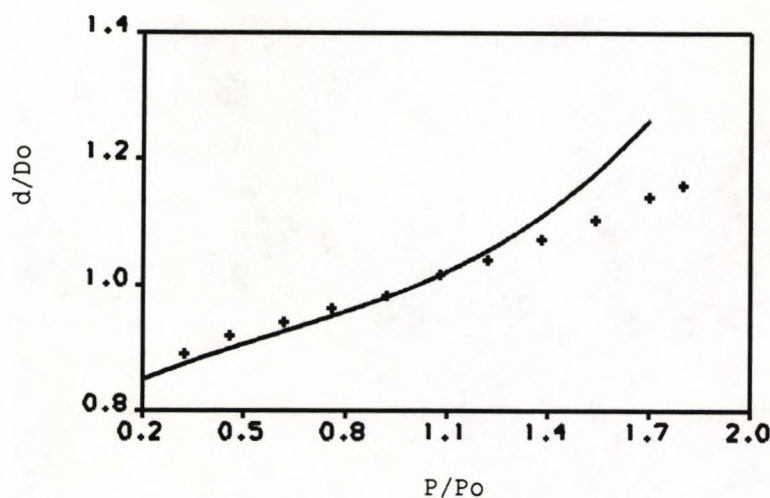


Fig. 4.12 Comparison of computed pressure-diameter curve for an 0.34mm thick graft (—) and measured values (+) of How and Clarke.

4.4.2 Treatment of Moving Wall

Over a pulsatile cycle, the motion of arterial wall due to the pulsating pressure is predicted using the pressure–diameter relationship described in the last section. This is only one aspect of the problem, the remainder of the problem is how to accommodate the wall movement in the flow modelling.

Solving the flow field with a distensible wall requires the grid to be time dependent because of the wall moves. There are two basic strategies that may be employed:

- (a) Redistribution of a fixed number of grid points at each time step using new wall locations.
- (b) Local grid enhancement according to wall movement.

In approach (a), near wall points are redistributed to account for the contraction and dilation of the arterial wall. As a consequence, the space between these grid points are reduced or increased. This approach has the advantage of not increasing the computer storage and time during the solution, and of being straightforward in data structure. The disadvantage is the possibility of the grid becoming too skewed. In approach (b), grid points are added locally in near wall regions. The practical advantage of this method is that the original grid structure is preserved. But the computer storage and time increase with the grid enhancement, and the coding and data structure are difficult.

Now turning to the fluid flow solver ASTEC, it is separated from the grid generator and the geometry data are read and processed only at the beginning of flow calculation. Such a code structure does not allow either approach (a) or (b) to be fully implemented within a practical time scale. However, the idea of (b) that the original grid structure is unchanged is quite useful. Thus, an adapted version of (b) was used for ASTEC. Rather than adding grid points as vessel dilates, it moves

the wall boundary on a pre-generated mesh according to the new wall position. Therefore, the boundary points on the wall are time dependent, i.e., points on the wall at this time step may be either inside or outside the wall at the next time step. Those points inside the wall are treated as free-nodes, and those outside are treated as solid region.

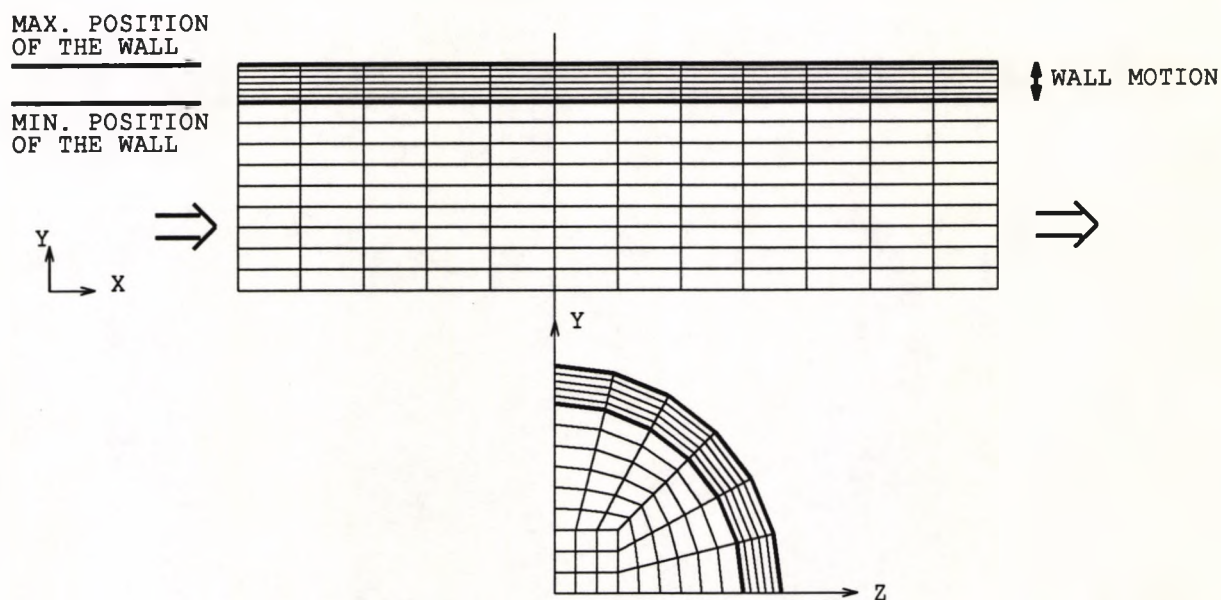


Fig. 4.13 Illustration of the moving wall treatment.

Before using this approach, grids are generated based on an estimated maximum position and the known minimum position of the wall. As illustrated in Fig.4.13, between the minimum and the estimated maximum wall positions, very fine grids are generated in order to reduce errors introduced by defining wall positions during the transient cycle. Calculations start from the minimum wall position which corresponds to the lowest pressure. At each time step, flow governing equations are solved first and pressures on the wall are evaluated and averaged at each cross-section, then the deformed vessel diameters are calculated using the pressure-diameter relationship. According to the variation of vessel diameter, wall boundaries are moved and flow equations are solved under the new boundary conditions.

This cycle is carried out until a converged solution is achieved, then calculations proceed to the next time step.

Such a treatment is coupled since the pressure used to determine the wall displacement is the one obtained from the instantaneous solution of the flow equations. The major simplifications made here are: (i) the longitudinal motion of the artery is negligible, and (ii) the radial displacement is uniform and can be expressed as a polynomial function (usually in 3rd order) of the pressure exerted by fluid on the wall. This moving wall treatment is valid provided that: (i) the motion of the wall is much slower than that of the fluid, and (ii) the grid in near wall regions is very fine. The former is generally true because typical variations of arterial diameter as a pulse passes are only about $\pm 2\%$ (Lighthill, 1975), while the latter is user controllable. The disadvantage of this treatment is that the computational mesh occupies a large amount of computer memory especially when a bifurcation geometry is concerned.

CHAPTER 5

CODE VALIDATION

5.1 INTRODUCTION

In all numerical predictive work, one question is always present, i.e., how accurate and reliable are the predictions ? To answer this, one has to examine thoroughly all the possible sources of error. In predictions obtained using CFD, there are mainly three sources of error, they are: (i) the mathematical model, (ii) the discretisation method, and (iii) the numerical algorithm. For the arterial bifurcation flow under consideration, the validity of the mathematical model was discussed in chapter 1, and since the flow is laminar for which the mathematical equations involve no empiricism, the accuracy of the predictions is expected to be in a good order. The magnitude of the discretisation error is dependent upon both the discretisation approach and the mesh density. This error can be reduced by either using a higher-order discretisation formula designed to reduce the truncation error, or refining the grid. Information on the former was provided in chapter 2, and the later is problem dependent which will be dealt with in the following numerical predictions. The errors associated with the numerical algorithm are dominated by the convergency criteria.

Apart from accuracy consideration of these kinds, it should also be born in mind that no codes are guaranteed to give reasonable and accurate results to any kinds of problems at any different levels, even within the code's capability. Therefore, external code validation for a particular problem at different levels is highly desirable. In general, code validation exercises may involve one or all of the following:

- (a) comparison with the analytical solution if one exists.
- (b) comparison with laboratory data set up specifically for validation purposes.
- (c) code to code comparison.
- (d) comparison with a wide range of application experimental data.

In this chapter, a comprehensive range of code validations are covered. Starting from the simple problem of steady flow in a rigid tube, it proceeds to complex case with the non-Newtonian viscosity, the pulsatility of the flow and the elasticity of the wall being taken into account in turn. To test the code's suitability for bifurcation flow configuration, computational results for a plane 90° bifurcation under both steady and pulsatile flow conditions were validated against reliable laboratory measurements. Moreover, comparison with an alternative code FLOW3D was also performed. This was followed by a complete set of predictions for pulsatile flow in a 3D 90° bifurcation with a Newtonian and a non-Newtonian model respectively. Effects of 3D geometry, pulsatility, and non-Newtonian viscosity were investigated individually and the results were compared with published LDA measurements of Ku and Liepsch (1986). All predictions presented in this chapter were performed with ASTEC code unless otherwise stated.

5.2 FLOW IN TUBES

5.2.1 Three-dimensional Steady Flow In a Rigid Circular Tube

With (a) Newtonian, and (b) Non-Newtonian Fluid

At the begin of this research, the ASTEC code was not ready to deal with non-Newtonian fluid flow. To test the implementation of the non-Newtonian model described in the preceding chapter, simple problems of fully developed flow in a rigid circular tube with (i) Newtonian, and (ii) non-Newtonian fluid were studied and the results were compared with analytical solutions. The tube was 8mm in diameter which is of the same order as those of large arteries, and the Reynolds number was 250 which is within the physiological flow range. The domain was divided into 18 elements in the radial direction and 4 elements in the axial direction. At the inlet of the tube in axial direction a fully developed velocity profile was prescribed, while both secondary velocity components were set equal to zero. Pressures at the

outlet was assumed to be zero. Since flow at the inlet was fully developed, the axial velocity profile at the outlet had to be the same as the prescribed inlet profile. In the Newtonian fluid case, computed velocity profile at the outlet was compared with the Hagen–Poiseuille solution given by:

$$U(r) = 2.0\bar{U} \left[1 - \left(\frac{r}{R} \right)^2 \right] \quad (5.1)$$

where r is the radial position and \bar{U} is the cross-sectional average velocity. As shown in Fig.5.1(a), an excellent agreement was achieved with the average velocity error of 0.48% and the maximum error of 0.53%.

For a non-Newtonian fluid obeying the power law $\tau = m\dot{\gamma}^n$, its fully developed velocity profile is given by:

$$U(r) = \frac{3n+1}{n+1} \bar{U} \left[1 - \left(\frac{r}{R} \right)^{\frac{n+1}{n}} \right] \quad (5.2)$$

Using a blood like fluid with $m = 0.042$ and $n = 0.61$, comparison between calculations and Eqn.(5.2) was made as shown in Fig.5.1(b). The errors occurred did not exceed 1% of the average velocity.

The velocity gradient, or shear rate, for both Newtonian and non-Newtonian fluid was also calculated and compared in Fig.5.2. As can be seen, the shear rate goes from zero at the tube axis where the fluid velocity is maximum, to a maximum at the wall, where the fluid velocity is zero. For the blood-like non-Newtonian fluid, a zero shear rate zone is formed near the tube axis and the shear rate close to the wall is higher than that of the Newtonian fluid.

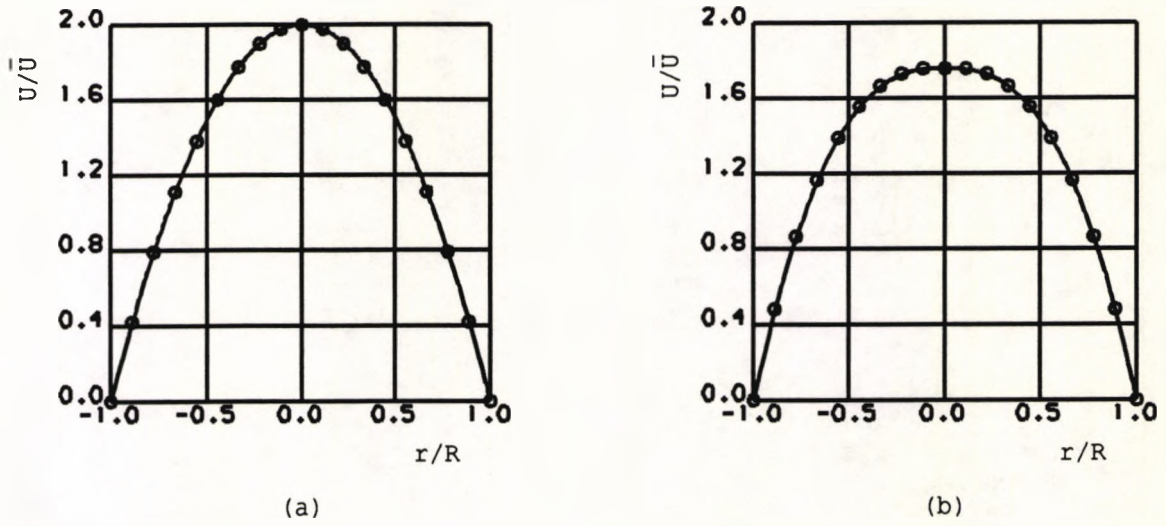


Fig. 5.1 Comparison between theoretical solution (—) and calculation (ooo) for fully developed flow in a straight tube with (a) Newtonian, and (b) non-Newtonian fluid.

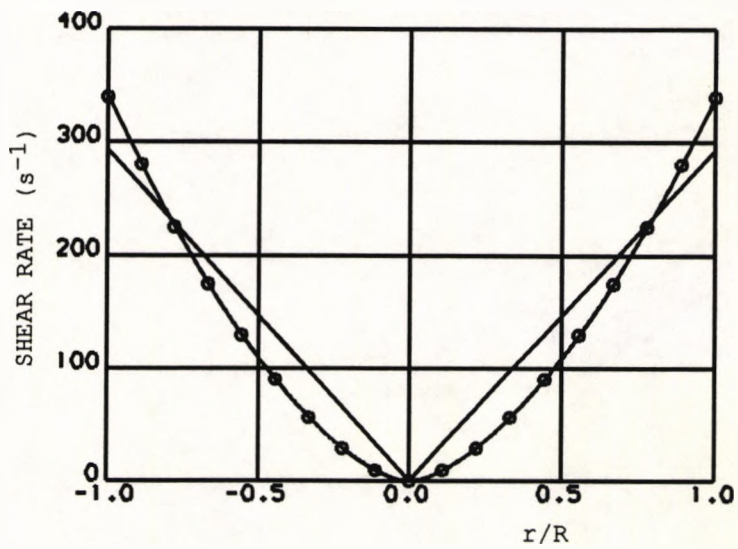


Fig. 5.2 Comparison of shear rate between a Newtonian (—) and a non-Newtonian (ooo) fluid.

5.2.2 Three-dimensional Pulsatile Flow In a Rigid Circular Tube With Newtonian Fluid

Following the steady flow prediction presented in the last section, prediction of pulsatile flow in a tube of same diameter was performed. The pulsatile flow was achieved by superimposing a sinusoidal oscillating flow on the steady flow, and the variation of pressure gradient at the inlet was given by:

$$-\frac{\partial P}{\partial x} = 232 + 3140 \cos(2\pi ft) \quad (Pa/m) \quad (5.3)$$

where f , the frequency of pulsation, was constant at 1.4HZ. The Womersley parameter, defined as $\alpha = R\sqrt{2\pi f/\nu}$ was equal to 8.18, and the average Reynolds number was 600. At the inlet of the tube pressure gradient described by Eqn.(5.3) was imposed. In ASTEC the pressure gradient boundary condition can be specified as (see Fig.5.3):

$$P^n(+)= (1-\beta)P^{n-1}(+) + \beta \left[P^n(\times) + \Delta x \left(\frac{\partial P}{\partial x} \right)^n \right] \quad (5.4)$$

where '+' stands for elements at the inlet and 'x' for elements adjacent to the inlet. Δx is the distance between the inlet and adjacent elements in x direction and β is an under-relaxation factor. The length of the tube was chosen to be 20 times its diameter because the estimated entry length, according to Lighthill (1975) $Le = (0.03Re)d$, was about $18d$. Calculation was carried out for 2 complete cycles and in each cycle forty nonuniform time-steps were used. Computed velocity profiles at the outlet of the tube were compared with the analytical solutions reported by Womersley (1955) (for details, see Appendix D). As shown in Fig.5.4, reasonable agreement is achieved. Errors occurred were not large than 3% of the time-averaged mean axial velocity. Fig.5.5 illustrates the pressure gradient, volume flow rate and wall shear rate versus time, giving an indication on their phase relationship. In this case, the phase lag of the flow rate is about 80° and that of the wall shear rate is about 40° .

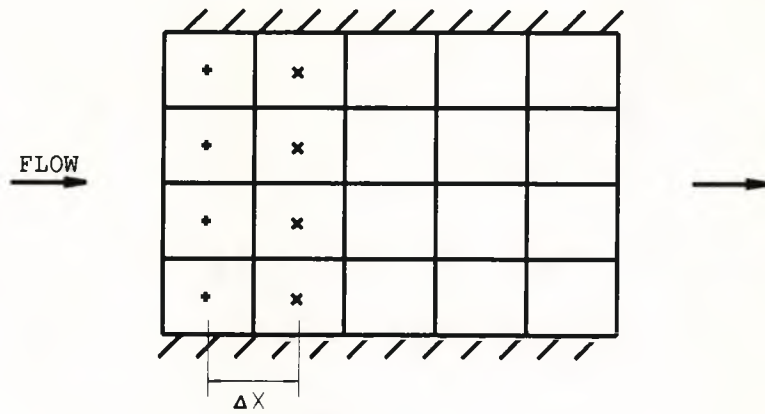


Fig. 5.3 Pressure gradient boundary condition.

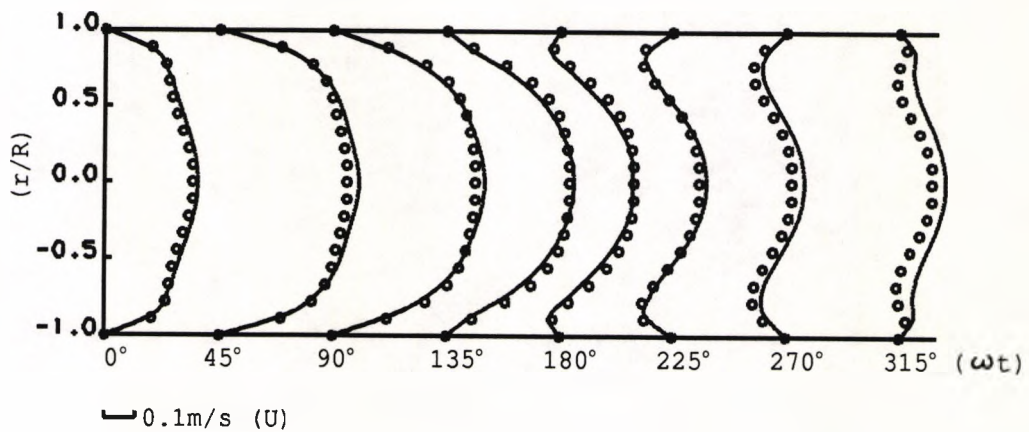


Fig. 5.4 Comparison between theoretical solution (—) and calculation (o o o) for pulsatile flow in a rigid tube over a whole cycle.

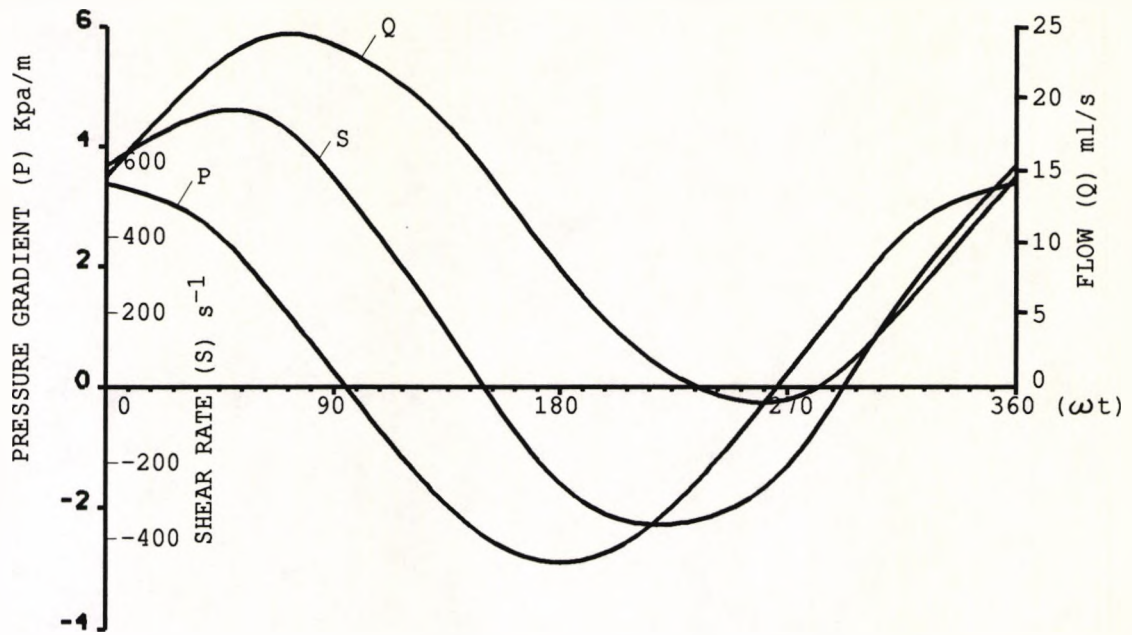


Fig. 5.5 Relation of flow (Q) and wall shear rate (S) to the pressure gradient (P).

5.2.3 Three-dimensional Pulsatile Flow In an Elastic Circular Tube With Newtonian Fluid

To make an initial investigation on the effect of wall compliance, pulsatile flow in an elastic tube was calculated using the moving wall treatment described in the last chapter. The elastic tube adopted in the calculation was the same as the one used in the theoretical and experimental study of Liepsch *et al* (1985), where the tube with an inner diameter of 8mm and a wall thickness of 1mm was made of silicone rubber (SilGel 600). The pressure-diameter curve for the silicone tube is shown in Fig.5.6. It expands approximately 2.5% in diameter during the pulsatile experiment.

The pulsatile flow conditions in the elastic tube were the same as those in the rigid case discussed in the last section. Since in the actual experiment a rigid plexiglas tube was used as the run-in tube for the silicone model, the obtained axial velocity profiles for the rigid tube were then used as the upstream boundary

condition for the elastic tube. Calculated velocity profiles were compared with the experimental data of Liepsch *et al* (1985) at 45° intervals (The measurement was taken at $r/R=0.0, 0.25, 0.5, 0.75$ and 0.9 every 22.5°). As is seen in Fig.5.7, the agreement between the calculation and the measurement is generally good. Some discrepancies can be observed: the predicted velocity profiles look fuller than the measurements during flow acceleration (between phase angles 0° and 90°), but are lower during flow deceleration (especially at phase angle 180°). Reasons for these are difficult to explain, since they may well involve in some degree the experimental errors which were reported to be 1-5% of the measurement range.

In Fig.5.8 the axial velocity profiles of the elastic model are compared with those of the rigid model. The results are presented at 45° intervals. The comparison shows that in general, there is no significant difference between the velocity profiles in the rigid and the elastic tubes. During flow acceleration velocity profiles in the elastic tube are slightly lower than those in the rigid tube. This results mainly from the cross-sectional area expansion of the elastic tube.

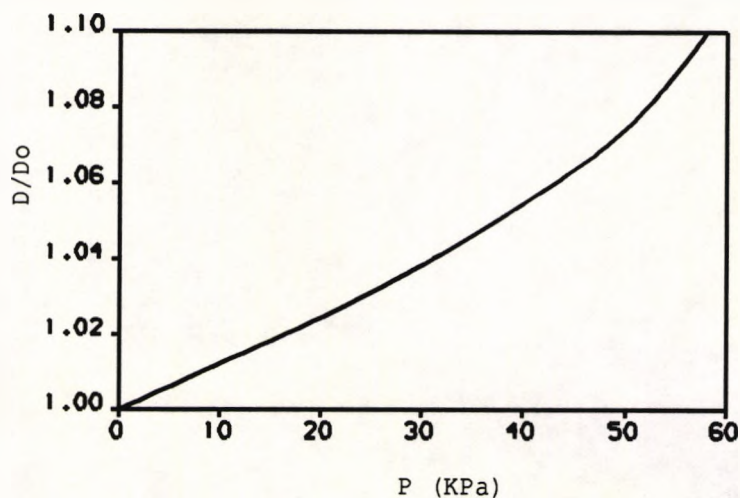


Fig. 5.6 Pressure-diameter curve for the silicone model.

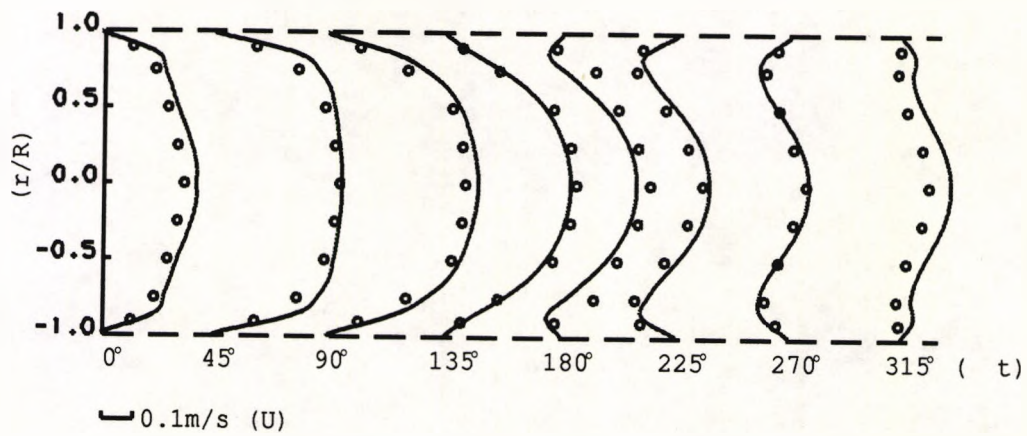


Fig. 5.7 Comparison between calculation (—) and experiment (o o o) for unsteady flow in an elastic tube.

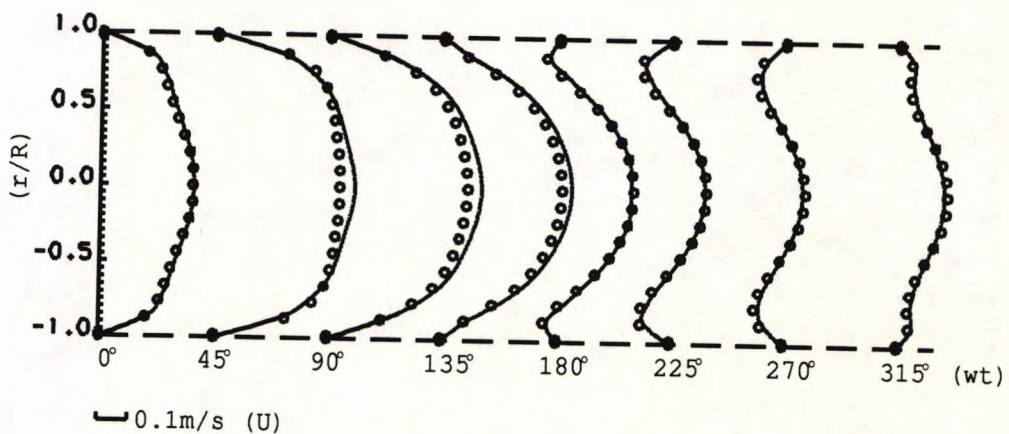


Fig. 5.8 Comparison of velocity profiles in a rigid (—) and an elastic (ooo) tube.

5.3 FLOW IN BIFURCATIONS

5.3.1 Two-Dimensional Steady Flow In A T-Bifurcation

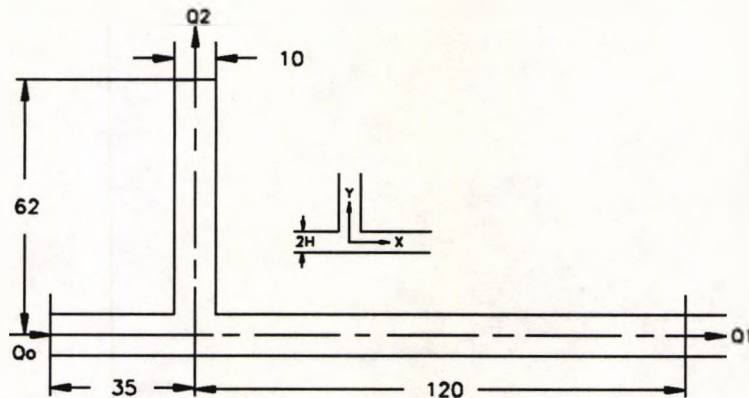
As a first step towards the modelling of arterial bifurcation flow under real physiological situation, steady flow through an idealised 2D 90° bifurcation with rigid wall was studied under various flow parameters, i.e., Reynolds number and branch to main tube flow rate ratio. Numerical results obtained were validated against published LDA measurements of Liepsch et al (1982), which were proven to be reliable.

5.3.1.1 Problem definition and grid resolution tests

For code validation purpose, the bifurcation geometry and flow conditions adopted in the experimental study were reproduced in this prediction, as shown in Fig.5.9 and Table 5.1. Prior tests were carried out for case 3 using three grid distributions, i.e., 34×22, 40×36 and 50×44, in order to determine grid dependence. Results of these calculations indicated that a 40×36 grid was sufficient with the maximum axial velocity differing by 1.2% with the finer grid and 6.1% with the coarser grid. However, to make a quantitative comparison with the measurements, the 50×44 grid was selected which was non-uniformly distributed accounting for the rapid spatial variations of flow parameters around the bifurcation region. Since ASTEC treats a two-dimensional problem as a three-dimensional one with flow restricted between two symmetric planes, the actual size of the mesh consisted of 840 elements and 1870 nodes. With this mesh a typical calculation for case 3 required 165.8 seconds on a CRAY X-MP/28.

In this simulation the fluid was distilled water with a constant density of $1000\text{Kg}/\text{m}^3$ and a dynamic viscosity of $1.02 \times 10^{-3}\text{Kg}/(\text{ms})$. For the upstream

boundary condition, a fully developed axial velocity profile and zero normal velocity were specified at the inlet. Since the x-exit was placed well downstream, the fully developed flow with specified flow partitioning was assumed there. At the y-exit pressure was assumed to be zero. No-slip condition was imposed on the rigid wall.



Case No.	Re	Q_2/Q_0
1	250	0.23
2	515	0.23
3	496	0.44
4	525	0.64
5	1130	0.23

Fig. 5.9 Bifurcation geometry.

Table 5.1 Flow parameters investigated.

5.3.1.2 Comparison of calculated and measured velocity profiles

Numerical calculations were performed for all cases listed in Table 5.1. It can be noticed that cases 1, 2 and 5 have the same branch to main tube flow rate ratio but different Reynolds number, while cases 2, 3 and 4 have roughly the same Reynolds number but different flow rate ratio. Results of these should give an clear indication of how the flow field is influenced by the two parameters (Re and Q_2/Q_0).

Figs.5.10 and 5.11 present the axial velocity profiles in the main and branch tube respectively for cases 1 to 5. It is observed that the profiles are qualitatively similar in all cases but for higher Reynolds numbers, the negative velocities at the bottom wall of the main tube are more pronounced, and the reverse flow region

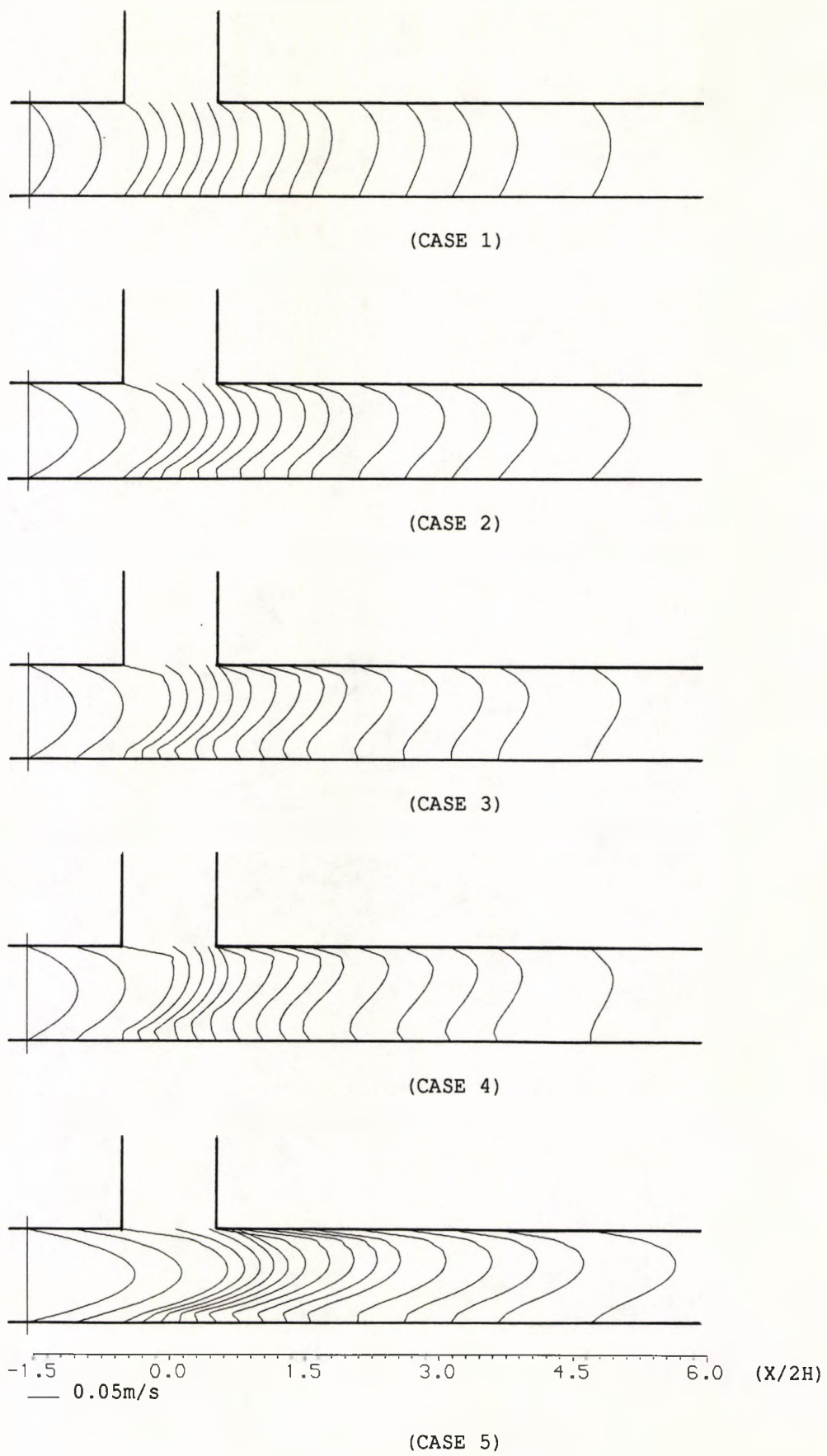


Fig. 5.10 Axial velocity profiles in the main tube.

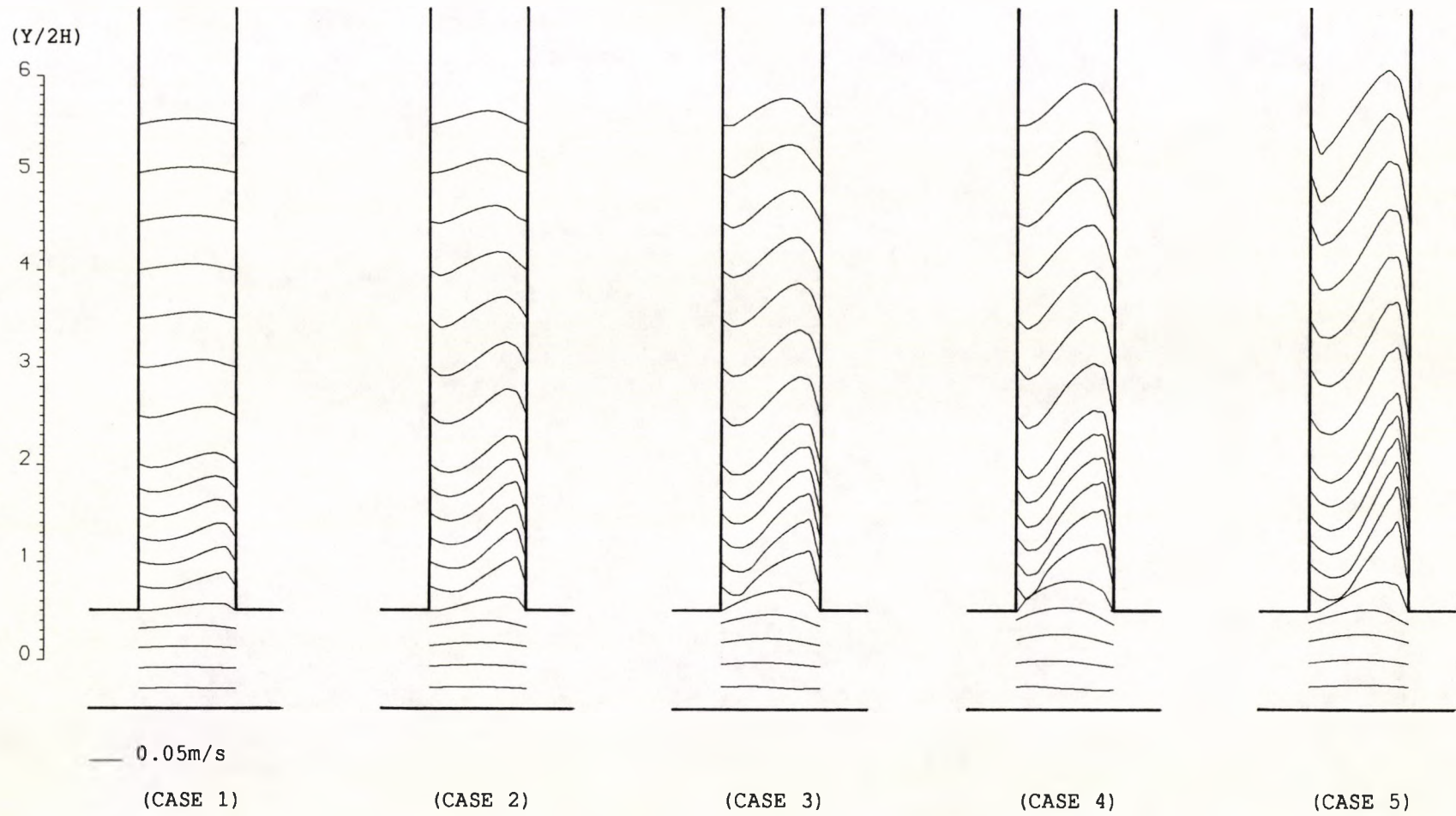


Fig. 5.11 Axial velocity profiles in the branch tube.

along the upstream wall of the branch expands in length. For the same Reynolds number, with the increase of Q_2/Q_o flow separation in the main tube after the bifurcation grows remarkably while the separation region in the branch becomes narrower and moves slightly upwards. Results of the location and size of the separation zone are summarised in Table 5.2. These results are in good qualitative agreement with the measurements.

To validate the predictive results, a quantitative comparison of calculations and measurements was performed. In Fig.5.12 the calculated axial velocity profiles are compared with the LDA measurements for case 3. It is observed that there is a very good agreement between the calculations and the measurements, especially in the main tube the axial velocity profiles were predicted quite accurately. Some differences are found in the branching tube. This may largely attribute to the three-dimensional effects of the tube used in the experiment.

A further quantitative comparison was made with an alternative code FLOW3D, as presented in Fig.5.13. It is demonstrated that the computational results of ASTEC and FLOW3D are consistent. However, their computer costs are strikingly different. For this case, the CPU time with ASTEC was about 35 times higher than with FLOW3D.

5.3.1.3 Wall shear stress

For an incompressible fluid the
shear stress is given by:

$$\tau_w = -\mu \frac{\partial u_t}{\partial n} \Big|_{wall} \quad (5.5)$$

Main Tube

Case No.	Re	Q ₂ /Q ₀	Separation Point X _s /2H	Reattachment Point X _r /2H	Maximum Width W _s /2H
1	250	0.23	no separation	no separation	0
2	515	0.23	0.30	0.95	0.15
3	496	0.44	-0.25	3.0	0.23
4	525	0.64	-0.40	4.5	0.35
5	1130	0.23	0.30	1.75	0.15

Branch

Case No.	Re	Q ₂ /Q ₀	Separation Point Y _s /2H	Reattachment Point Y _r /2H	Maximum Width W _s /2H
1	250	0.23	0.51	3.05	0.45
2	515	0.23	0.51	4.80	0.45
3	496	0.44	0.54	5.60	0.35
4	525	0.64	0.56	5.50	0.34
5	1130	0.23	0.51	>6.2	0.45

Table 5.2 Location and size of the separation region.

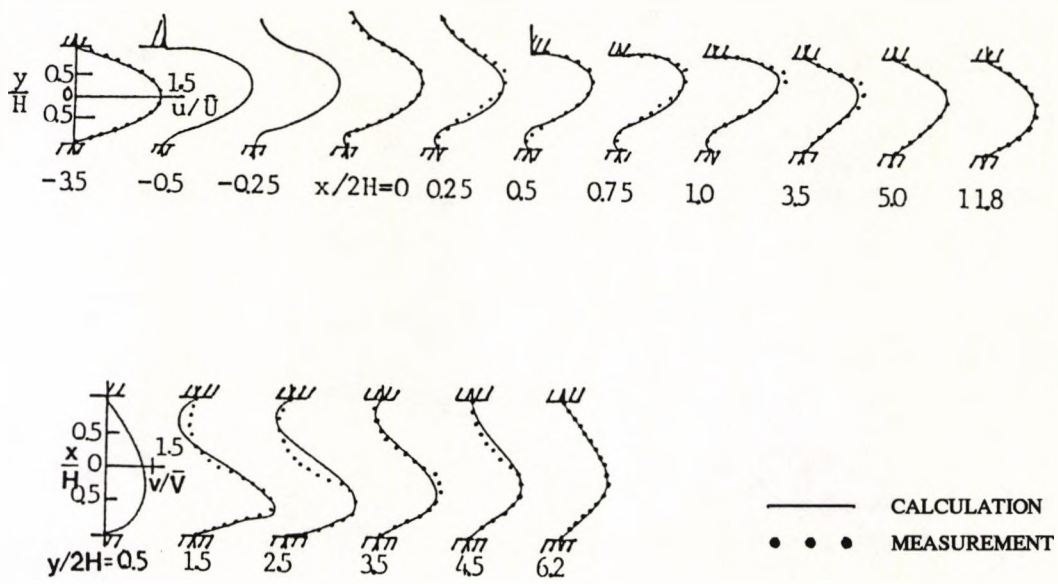


Fig. 5.12 Comparison of axial velocity profiles with the LDA measurements.

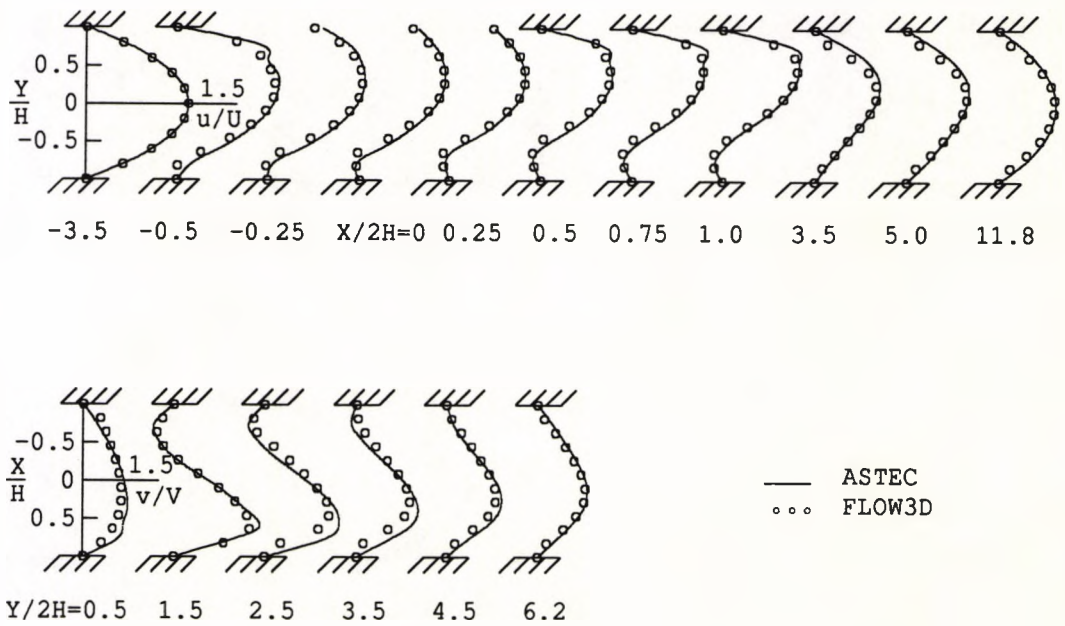


Fig. 5.13 Comparison of axial velocity profiles between ASTEC and FLOW3D.

where \mathbf{u}_t denotes the tangential velocity, \mathbf{n} is the normal unit vector on the wall. Numerical results of wall shear stress are plotted in Figs.5.14–5.17. They were non-dimensionalised in terms of the fully developed wall shear stress at the inlet for each case. Along the bottom wall of the main tube(Fig.5.14), the shear stress at upstream positions is constant indicating that the flow remains parabolic and has not been disturbed by the downstream bifurcation. Immediately after the outer corner of the bifurcation, shear stress drops abruptly reaching the minimum level which is negative except for the first case where flow does not separate. As the Reynolds number increases, the region of negative shear stress is enlarged. For a same Reynolds number, increased flow in the branch results in a decrease in wall shear. At the divider wall of the main tube(Fig.5.15), the wall shear stress is positive and the maximum value is found at $x/2H \simeq 1.0$. With the increase of Reynolds number, the value of wall shear stress rises. For a same Reynolds number, increased flow in the branch results in a decrease in wall shear downstream. At the upstream wall of the branch(Fig.5.16), the wall shear stress becomes very low with an average value well below zero. The shear stress curves intersect the zero line at two points except for the last case where there is only one intersection, indicating the extent of flow separation along the upstream wall of the branch and its dependence upon the flow parameters. The influence of Reynolds number and branch flow rate on the value of wall shear stress can be derived from this figure, which is generally the same as observed at the bottom wall of the main tube. At the divider wall of the branch(Fig.5.17), the shear stress is very high and unidirectionally positive. As the Reynolds number increases, the shear stress increases. For a same Reynolds number, increased flow in the branch results in a large increase in wall shear. When considering the bifurcation as a whole, it is found that the minimum shear stress on the upstream wall of the branch is even lower than that on the bottom wall of the main tube, while the maximum shear stress on the divider wall of the branch is about the same as that on the divider wall of the main tube for small branch flow rate, but are significantly higher for larger branch flow

rate.

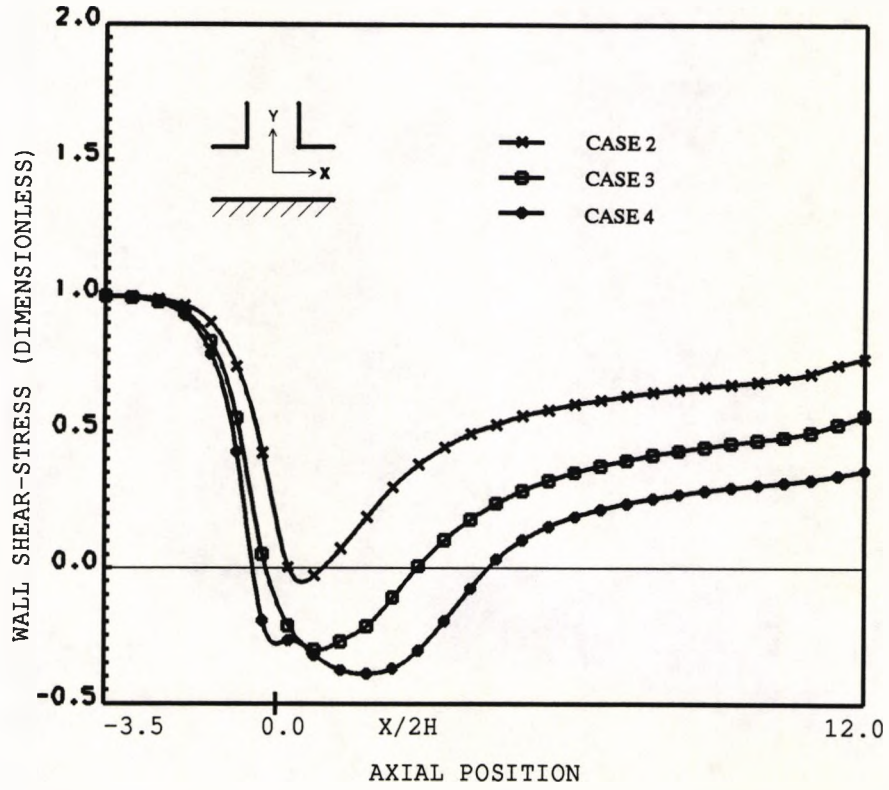
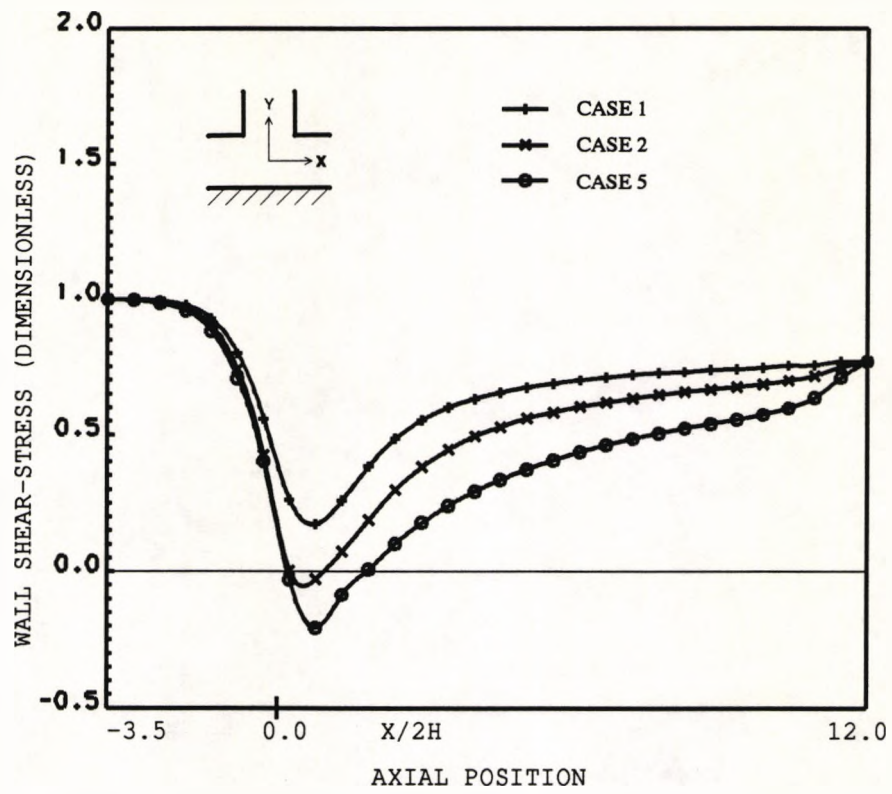


Fig. 5.14 Wall shear stress along the bottom wall of the main tube.

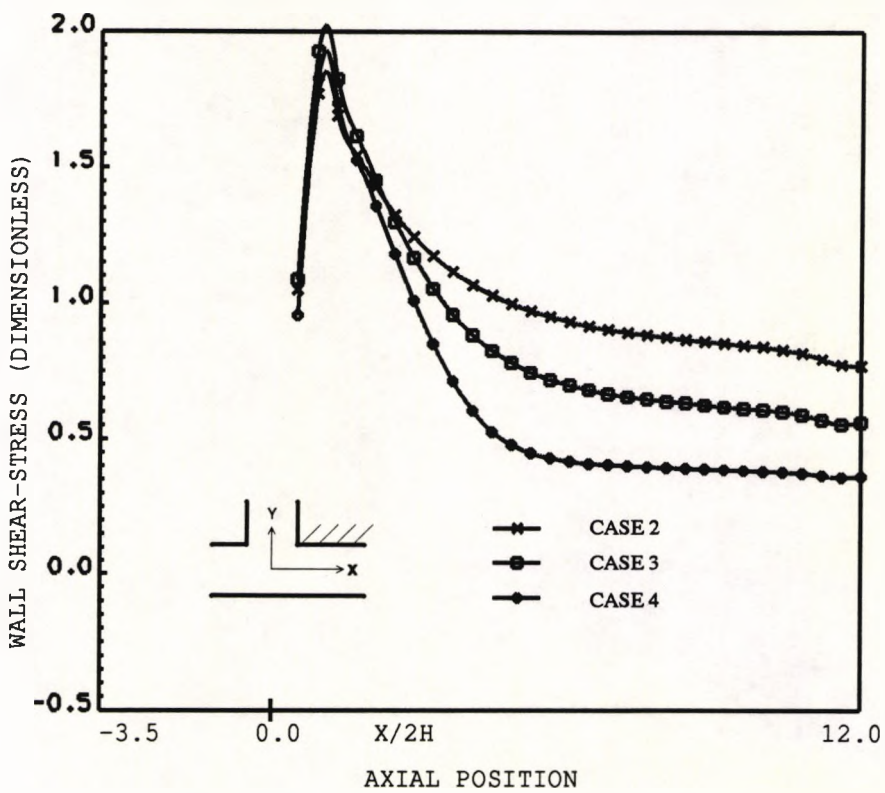
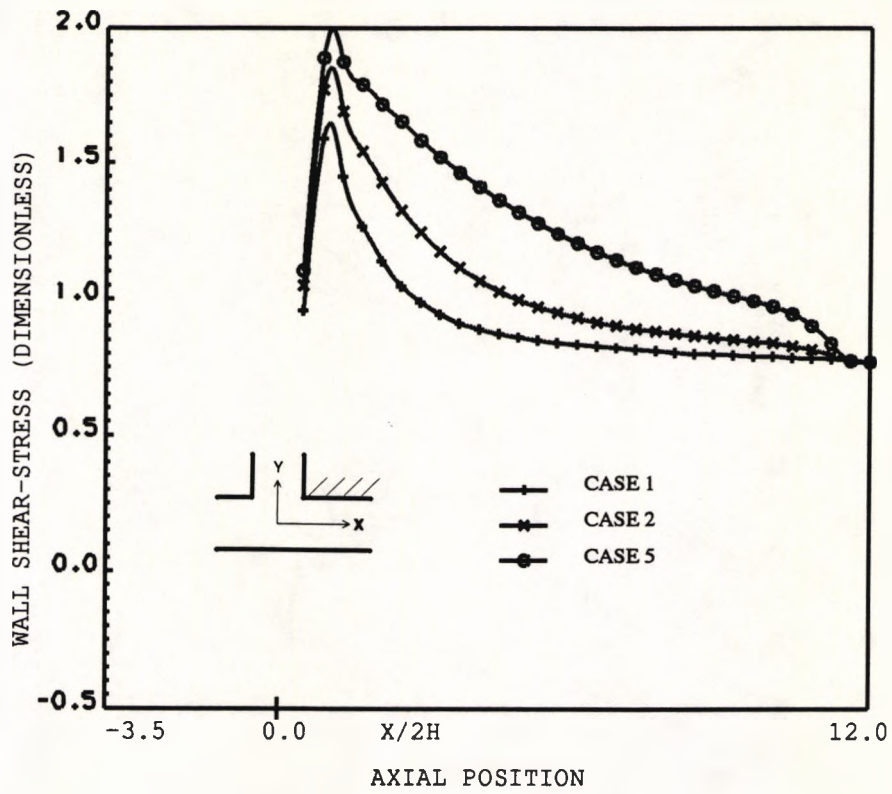


Fig. 5.15 Wall shear stress along the divider wall of the main tube.

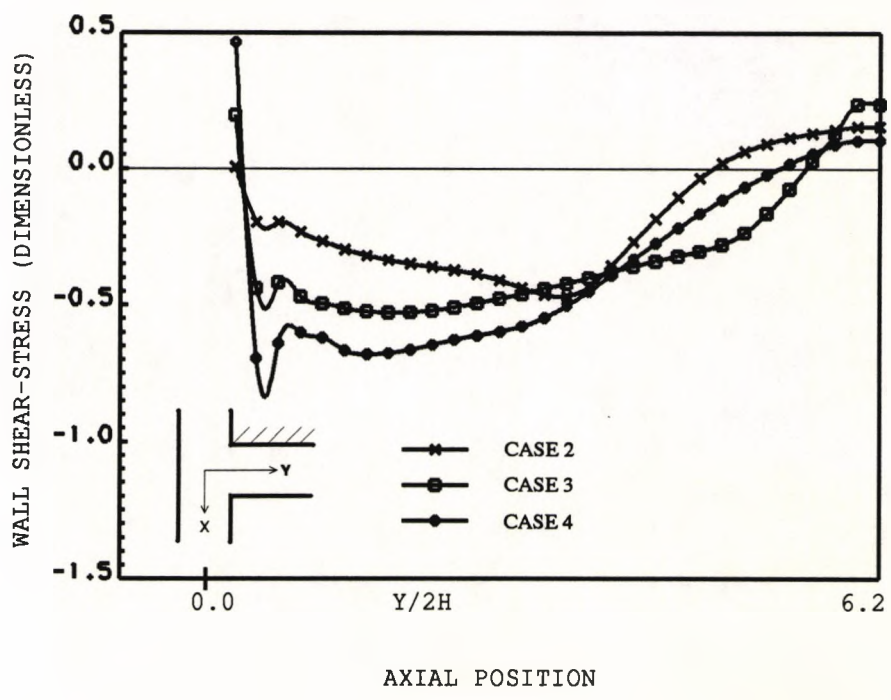
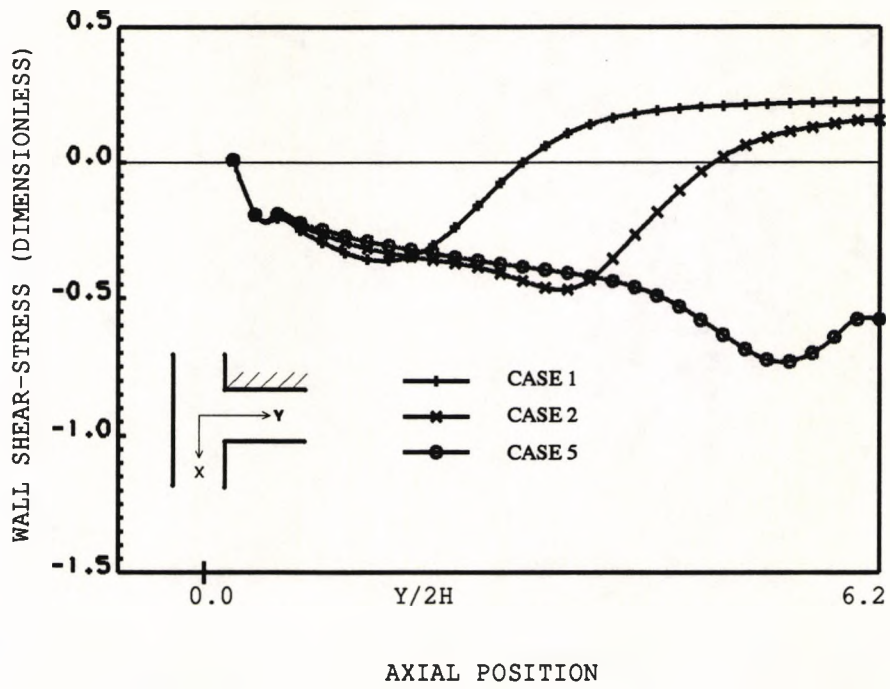


Fig. 5.16 Wall shear stress at the upstream wall of the branch.

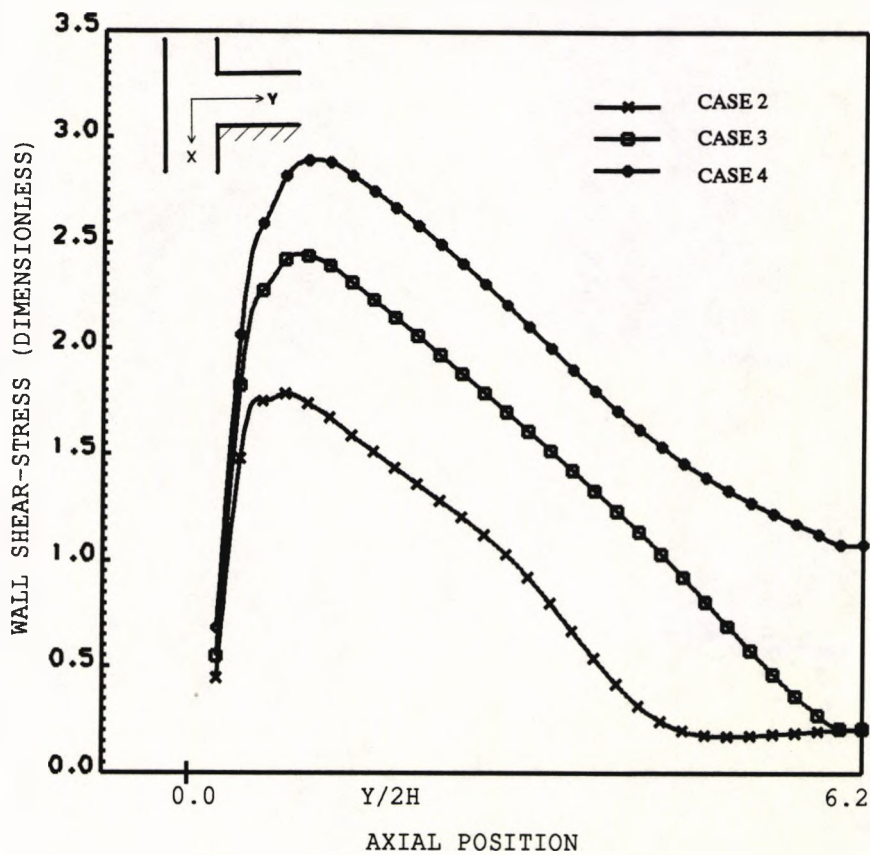
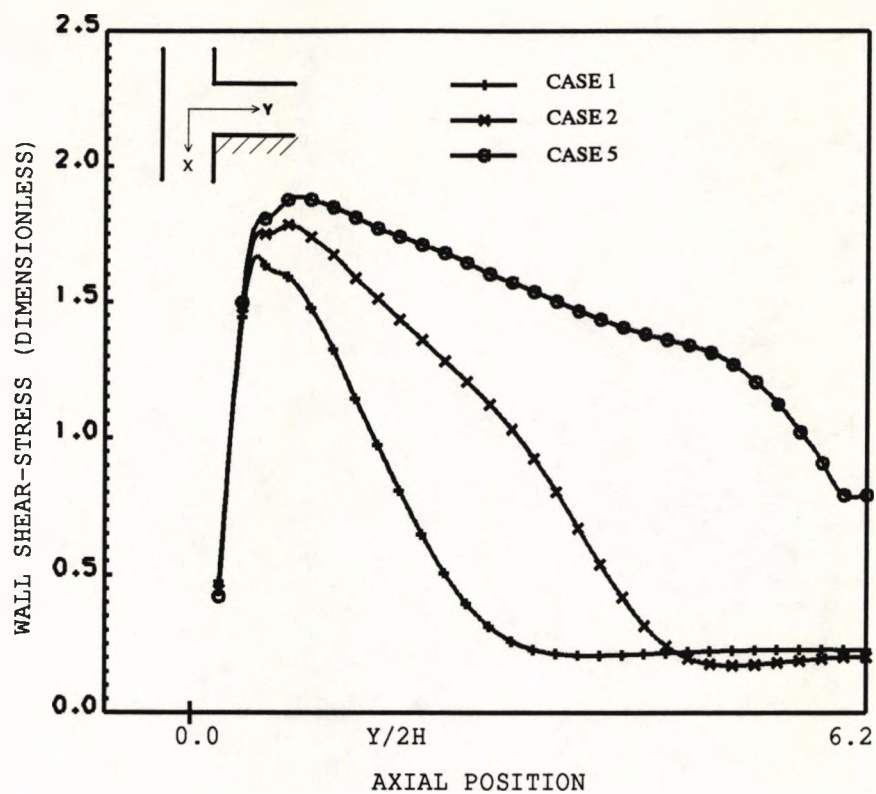


Fig. 5.17 Wall shear stress at the divider wall of the branch.

5.3.2 Two-Dimensional Pulsatile Flow In A T-Bifurcation

In the preceding section, predictions for steady flow in a T-bifurcation were validated. In this section, the pulsatility of the flow is taken into account with an intention of assessing the code's validity when applied to unsteady separating flows. The numerical results were compared with the LDA measurements reported by Khodadadi et al (1988), who extended the work of Liesch et al (1982).

5.3.2.1 Problem definition

The same bifurcation geometry as illustrated in Fig.5.9 was adopted here. The pulsatile flow was achieved by superimposing a sinusoidal oscillating flow on the steady flow and the frequency of pulsation was constant $f = 1.1Hz$. Under steady flow conditions the Reynolds number and flow rate ratio have been identified as the two controlling parameters of the present bifurcation flow. If a pulsating pressure gradient is applied at the inlet of the bifurcation, the frequency of pulsation expressed as Womersley parameter α and the amplitude of the pulsation are introduced as additional controlling factors. In this case, the average Reynolds number at the entrance of the bifurcation was 102 and the flow rate ratio (Q_2/Q_o) was kept constant at 0.7. The variation of pressure gradient at the inlet is given in Fig.5.18, which was measured using two inductive pressure sensors placed one meter apart in the inlet section of the bifurcation during the experiment. The Womersley parameter was 4.9. A glycerine water solution was the working fluid, having a density of 1150 Kg/m^3 and a dynamic viscosity of $8.4 \times 10^{-3} \text{ Kg/ms}$.

For the upstream boundary condition, the time-dependent velocity profiles obtained from the analytical solution for fully developed pulsating flow were specified at the inlet. For an inlet pressure gradient of

$$-\frac{\partial p}{\partial x} = K_{st} + K_{osc} \cos 2\pi ft \quad (5.6)$$

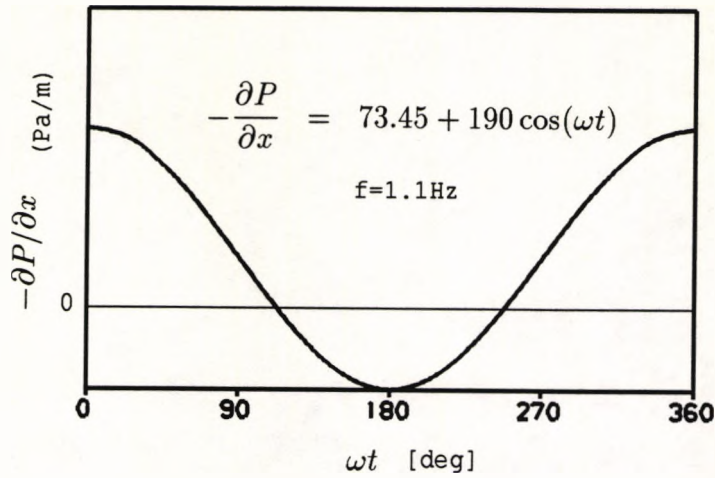


Fig. 5.18 Pulsating pressure gradient at the inlet.

the instantaneous velocity profile is given by:

$$u(y, t) = u_{st}(y) + u_{osc}(y, t) \quad (5.7)$$

$$u_{st} = \frac{K_{st}}{2\mu} H^2 \left[1 - \left(\frac{y}{H} \right)^2 \right] \quad (5.8)$$

$$u_{osc} = \frac{K_{osc}}{2\pi f} \frac{(M \sin 2\pi ft + N \cos 2\pi ft)}{\rho(A^2 + C^2)} \quad (5.9)$$

where

$$\left\{ \begin{array}{l} A = \cos \gamma H \cdot \cosh \gamma H \\ C = \sin \gamma H \cdot \sinh \gamma H \\ B = \cos \gamma y \cdot \cosh \gamma y \\ D = \sin \gamma y \cdot \sinh \gamma y \\ M = A^2 + C^2 - AB - CD \\ N = BC - AD \\ \gamma = \frac{\sqrt{2}\alpha}{2H} \end{array} \right. \quad (5.10)$$

The normal velocity component at the inlet was assumed zero and a non-slip condition was imposed on the rigid wall. At the two outlets, fully developed flow with a constant flow division ratio ($Q_1/Q_0 = 0.3$) was specified at the x-exit which was placed $12 \times 2H$ downstream, while at the y-exit zero pressure condition was assumed.

5.3.2.2 Comparison of calculated and measured velocity profiles

For the pulsatile flow defined above, calculations were performed on a 40×36 grid which was tested to be capable of providing a grid independent solution. Using a fully implicit time-differencing scheme one pulse cycle was discretised into 40 time steps which were unevenly spaced to account for steep temporal pressure gradients. The calculation was continued until a periodic solution was achieved for which about 3 cycles were needed in this case. Results at different locations of the bifurcation and different phases of the cycle were compared with the measurements. Fig.5.19 presents the comparison of axial velocity profiles in the main tube. It is observed that at the leading edge of the bifurcation ($x/2H = -0.5$) the agreement is generally good and a tendency for reverse flow is apparent for phase angles between 180° and 225° . At the trailing edge of the bifurcation ($x/2H = 0.5$) and downstream ($x/2H = 1.0$), the agreement is very good except during the early period of flow separation corresponding to phase angles between 45° and 135° , where numerical results have slightly overpredicted the reverse flow. As the flow redevelops further downstream of the separation zone ($x/2H = 10.0$), the measured and computed velocity profiles for the whole cycle are in excellent agreement.

Comparison of axial velocity profiles in the branch tube is shown in Fig.5.20. At the beginning of the branching ($y/2H = 0.5$) good agreement is observed across

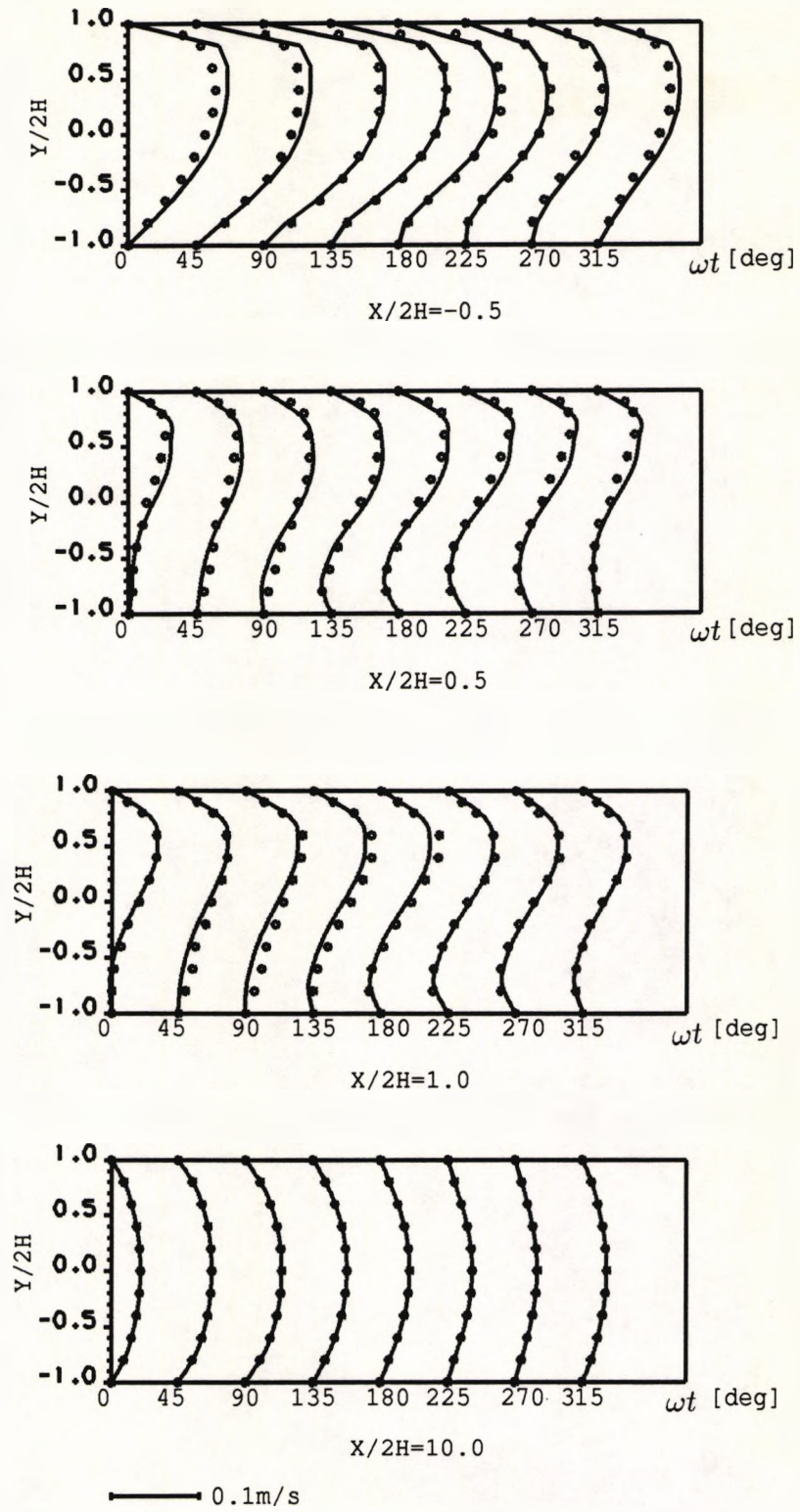


Fig. 5.19 Comparison of axial velocity profiles in the main tube.

(— calculation, ●●● measurement)

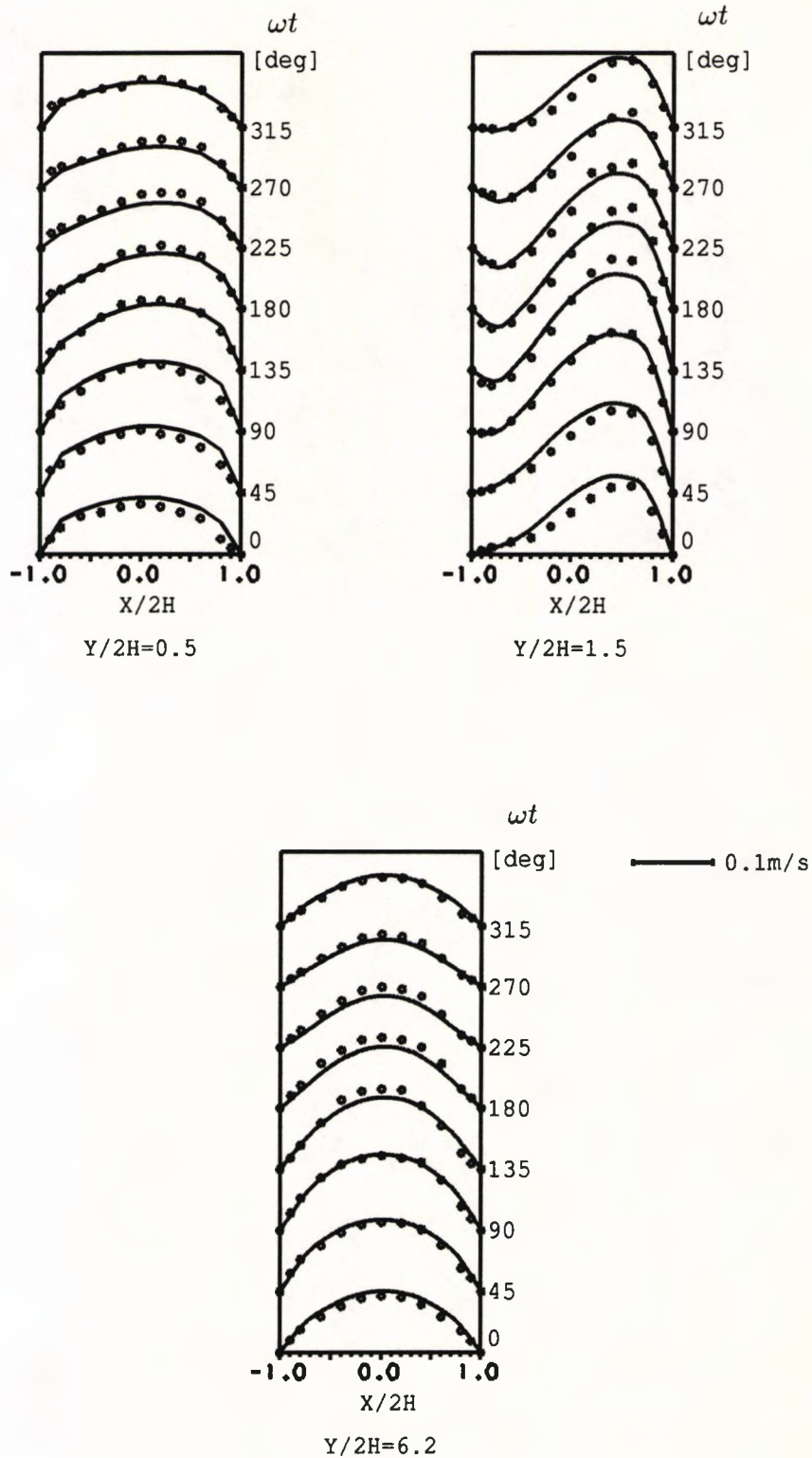


Fig. 5.20 Comparison of axial velocity profiles in the branch tube.

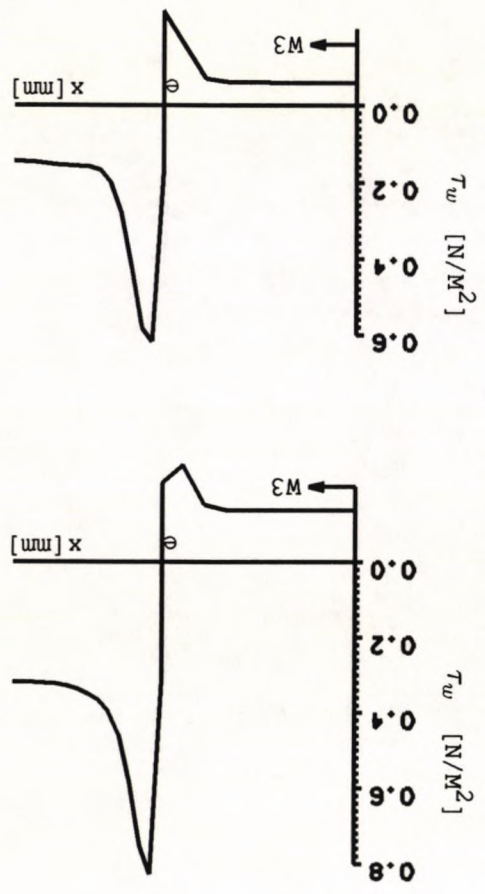
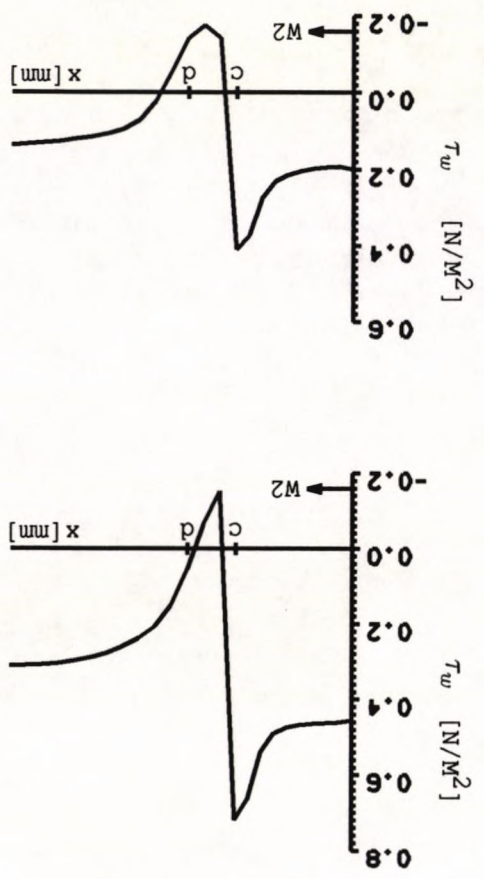
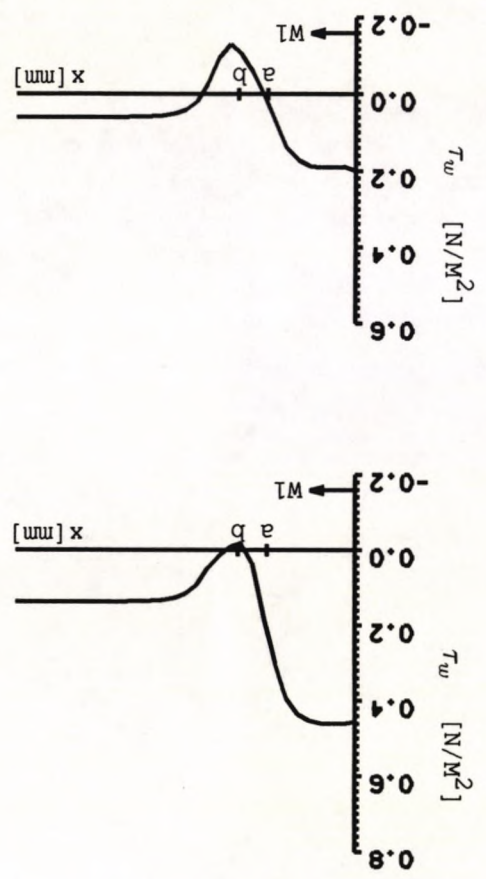
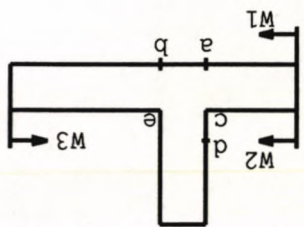
(— calculation, ●●● measurement)

the tube throughout the cycle. As the flow moves downstream at $y/2H=1.5$, which is inside the separation zone for most part of the cycle, discrepancies are noticed for phase angles between 135° and 225° . The profiles farther downstream in the branch are in excellent agreement for the whole cycle.

From these comparisons, it may be concluded that in general the pulsatile flow has been predicted very well. Small discrepancies are observed mainly for phases where flow separations exist. These may largely due to the three-dimensional effects of the bifurcating flow, and perhaps rather slightly, the theoretical upstream boundary conditions used in the prediction as well as measurement errors which were estimated to be around 5% at close wall positions ($< 1mm$) and 1% elsewhere. However, the differences found here are much less than with the numerical predictions also presented by Khodadadi et al (1988) where the separation zones were significantly exaggerated.

5.3.2.3 Wall shear stress

Wall shear stresses along the bottom wall of the main tube (W1), the upstream side walls (W2) and the dividing walls (W3) are presented in Fig.5.21 at three phase angles: 90° , 225° and 315° . Principally it shows the same feature as found in steady flow studies, i.e., in the vicinity of the leading (point marked as c) and the trailing (point marked as e) edges of the bifurcation the shear stress is high; on the bottom wall of the main tube opposite the trailing edge of the bifurcation (around points marked as a and b) and on the upstream side wall of the bifurcation (point marked as d) the shear stress is low. However, the values of the maximum and the minimum wall shear stress vary during the pulsatile cycle. It is found that the peak shear stress on the divider wall (W3) fluctuates between 0.5 and $0.9 N/m^2$ and the minimum shear stress on the bottom wall (W1) changes between -0.2 and $0.06 N/m^2$.



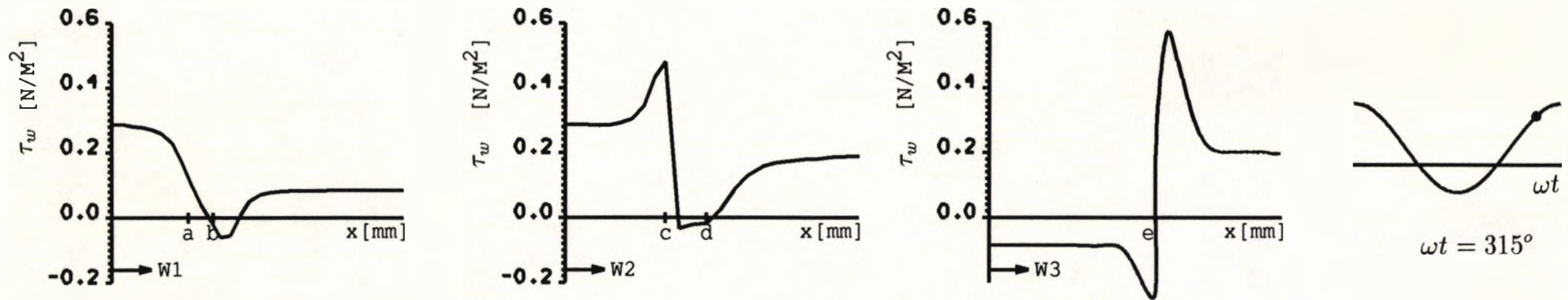


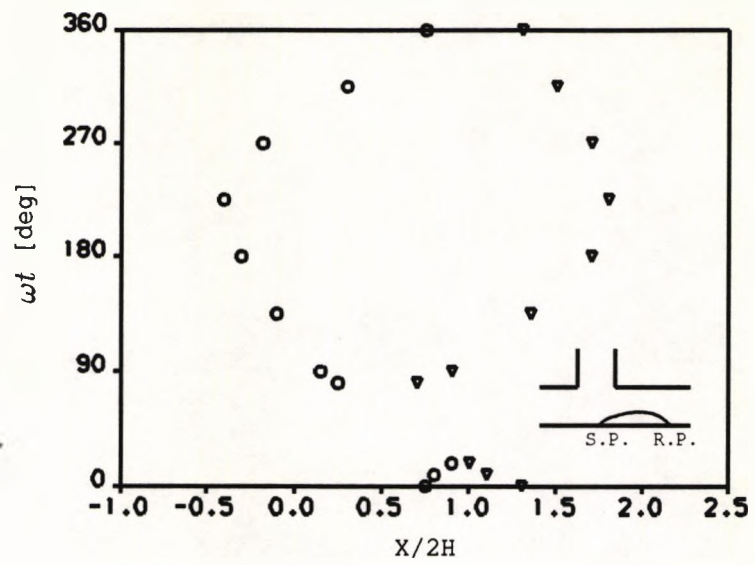
Fig. 5.21 Wall shear stress along the bottom wall (W1), the upstream side wall (W2) and the divider wall (W3) at three phase angles (90° , 225° , and 315°).

5.3.2.4 Effects of pulsation

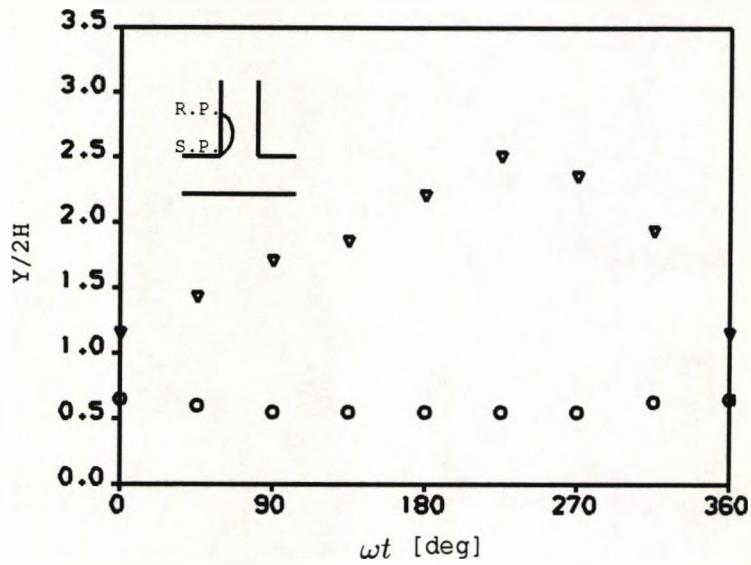
The velocity profiles discussed above show that two separation zones are established in the bifurcation. One is located on the bottom wall of the main tube opposite of the side branch and the other along the upstream wall of the branch. This finding is in conformity with the steady flow results for the same flow conditions (Khodadadi et al, 1986). The predictions also indicate that the location and extent of these separation regions vary within a cycle. In order to demonstrate the effect of the pulsating pressure gradient on the two separation zones, the estimated location of the separation and reattachment points in the main and branch tubes obtained from the numerical predictions are plotted as a function of phase angle in Figs.5.22(a) and 5.22(b) respectively. The figures show a substantial variation of these locations within a cycle as compared with the steady flow results which are summarised in Table 5.3. At zero phase angle, a small separation zone is found downstream of the bifurcation in the main tube. It diminishes gradually and has almost disappeared at around 30° . For phase angles between 30° and 50° , no flow separation is noticed in the main tube. On the other hand, separation region in the side branch exists throughout the cycle. Around phase angle 220° , the sizes of the two separation zones are largest.

Main Tube		Branch	
Separation Point $X_s/2H$	Reattachment Point $X_r/2H$	Separation Point $Y_s/2H$	Reattachment Point $Y_r/2H$
-0.11	1.46	0.55	2.10

Table. 5.3 Location of separation zone for steady flow (Khodadadi et al, 1986).



(a)



(b)

S.P. — Separation point (○)

R.P. — Reattachment point (▽)

Fig. 5.22 Temporal variation of the location and size of the separation zones in (a) main tube and (b) branch tube.

The effect of the pulsation on wall shear stress has been discussed previously. It is indicated that the maximum and minimum wall shear stresses fluctuate within a cycle. This suggests the importance of taking the pulsatile nature of the flow into account when the time varying wall shear is of special interest.

In summary, although some basic features of flow are consistent between steady and pulsatile flows, the results presented here show some major differences. First, velocity profiles upstream of the bifurcation are time varying and non-parabolic. According to Womersley theory they are intimately related to the frequency parameter (i.e. Womersley parameter) α ; larger values of α result in more blunted profiles. Second, pulsatile flow changes the location, extent and size of separation regions. During part of flow acceleration, positive flow is seen throughout the main tube behind the branch, preventing the formation of the permanent separation region existing in steady flow. During later flow deceleration, separation regions have grown remarkably larger: about 40% greater in length at the bottom wall of the main tube opposite the flow divider and 20% greater in the side branch as compared with steady flow. Third, wall shear stresses vary over the pulsatile cycle. During flow acceleration, the maximum wall shear stress in the main tube upstream of the bifurcation is approximately 25% greater than in steady flow, due in large part to the fact that the steady flow profiles are parabolic while pulsatile flow profiles vary in time.

5.3.3 Three-Dimensional Pulsatile Flow In A T-Bifurcation

Having validated numerical results for both steady and pulsatile flows in a 2D bifurcation, code validation exercises proceeded to 3D cases. The experimental data used in this section were those of Ku and Liepsch (1986), who made a systematic study on pulsatile flow in a 3D T-bifurcation with the effects of non-Newtonian viscosity and wall elasticity investigated separately. While validating the 3D predictions against laboratory measurements, the emphases of this section are to present the three-dimensional characteristics of the flow, and to investigate in detail the effect of non-Newtonian viscosity on the flow field and wall shear stress. In addition, pressure distributions in the bifurcation region were obtained and are presented in Appendix E.

5.3.3.1 Problem definition

For the 90° T-bifurcation model treated here the diameter of the main tube was 6mm and that of the branch tube was 3mm. The bifurcation had a sharp corner, this being the only difference to the experimental model in which the bifurcation edge was slightly rounded. The element division for the model bifurcation is illustrated in Fig.5.23. Since the flow is symmetric, only half of the bifurcation was considered. The applied finite element computational mesh consisted of 5992 eight-node 3D blocks and a total of 7290 nodes.

Calculations were performed under the pulsatile flow conditions reported in the experimental study, i.e., an average upstream Reynolds number of 250, a pulsatile pressure amplitude of 1400Pa/m, and a Womersley parameter of 2.3 for the sine pressure wave. The flow rate in the side branch was 50% of the entrance flow rate. For the Newtonian fluid, a 70% aqueous glycerine solution with a density of 1080Kg/m³ and a viscosity of 0.013Kg/(ms) was used. For the non-Newtonian

fluid, a separan-glycerine solution with a variable viscosity expressed in the power law as $\tau = 0.037\dot{\gamma}^{0.85}$ was employed.

Under the sinusoidal pressure gradient, fully developed velocity profiles at various phases in a long straight tube were calculated using the Womersley equations. As shown in Fig.5.24, the centerline velocities are behind the pressure pulse by about 40° . These velocity profiles were then used as the time-dependent upstream boundary condition in the main tube. For the downstream boundary condition, fully developed flow with a constant flow division ratio was prescribed at the outlet of the side branch which was 12 times its diameter long (note that Fig.5.23 does not show the whole length of this branch for the sake of clarity); zero pressure was assumed at the other outlet. A total of 40 time steps was used in one pulsatile cycle and the calculation was continued for 1.5 cycles where the error in periodicity was 1%. Each time step required about 50-70 iterations to converge; and one iteration took 4.5 seconds on a CRAY X-MP/28.

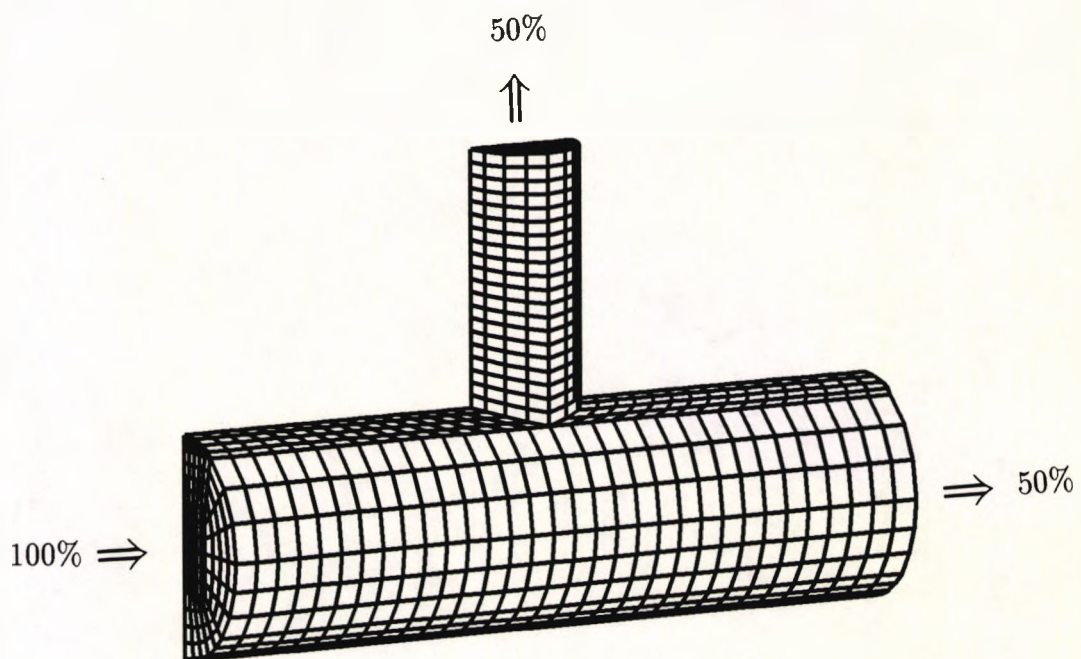


Fig. 5.23 Finite element subdivision of the 3D T-bifurcation.

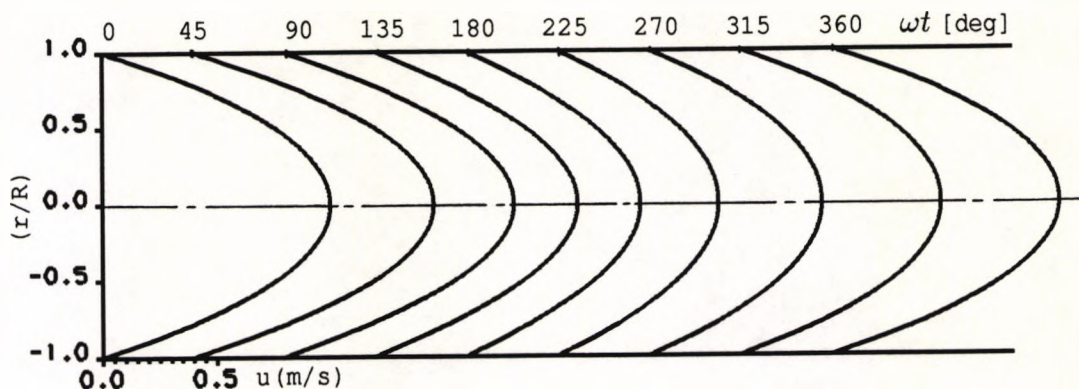


Fig. 5.24 Fully developed velocity profiles calculated using Womersley's solution.

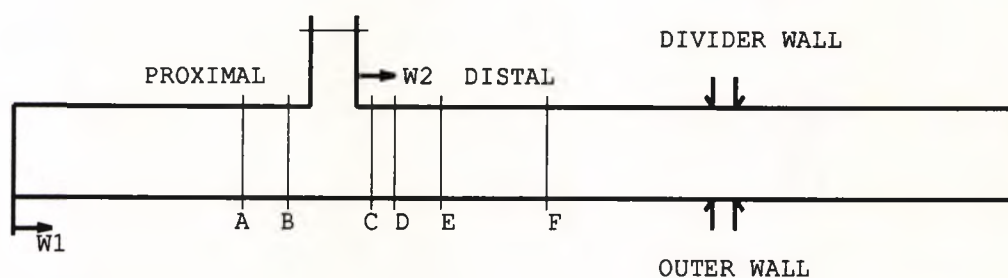
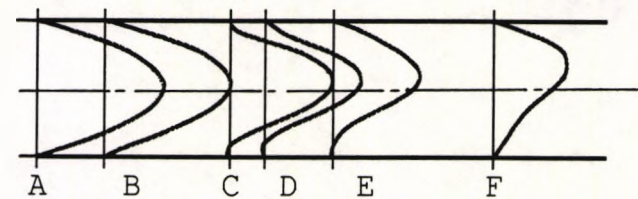
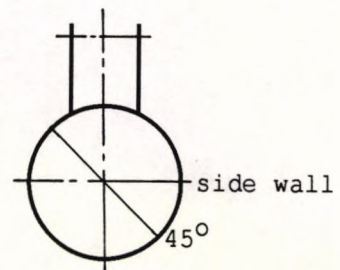
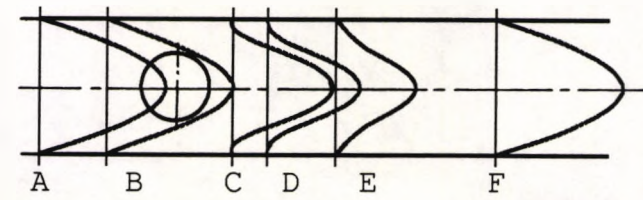
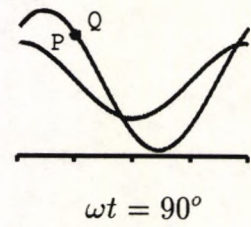
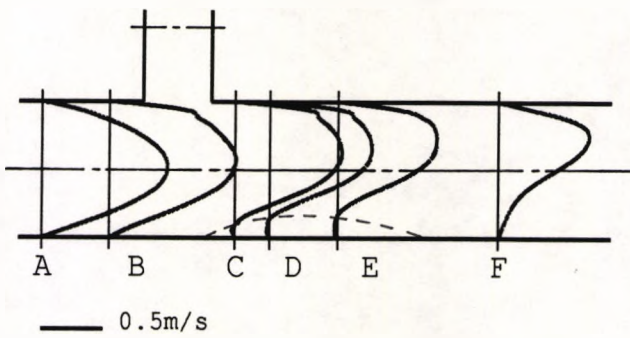
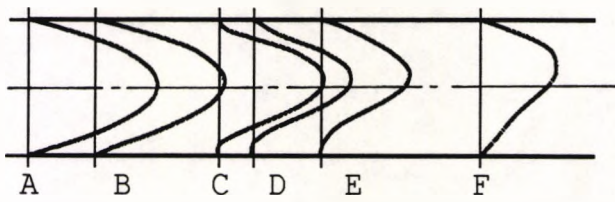
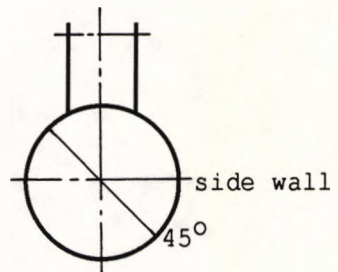
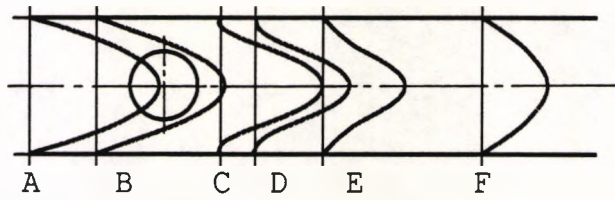
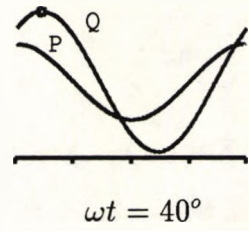
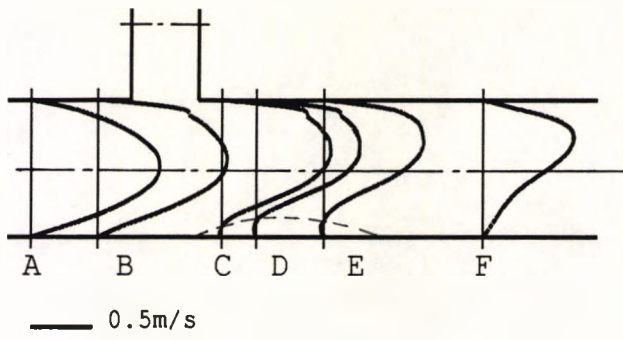


Fig. 5.25 Definition of cross sectional positions where numerical results are presented.

5.3.3.2 Description of velocity field

Fig.5.25 gives the cross-sectional positions where numerical results are presented. The diagram defines two locations proximal to the bifurcation (marked as A, B) and four locations distal to the bifurcation (marked as C, D, E, F). The axial velocity profiles at these locations in the plane of symmetry (bifurcation plane), the plane through the axis of the main tube perpendicular to that of the bifurcation, and the plane through the axis of main tube at 45° to the bifurcation plane are illustrated at specified phase angles during the pulsatile cycle in Fig.5.26.



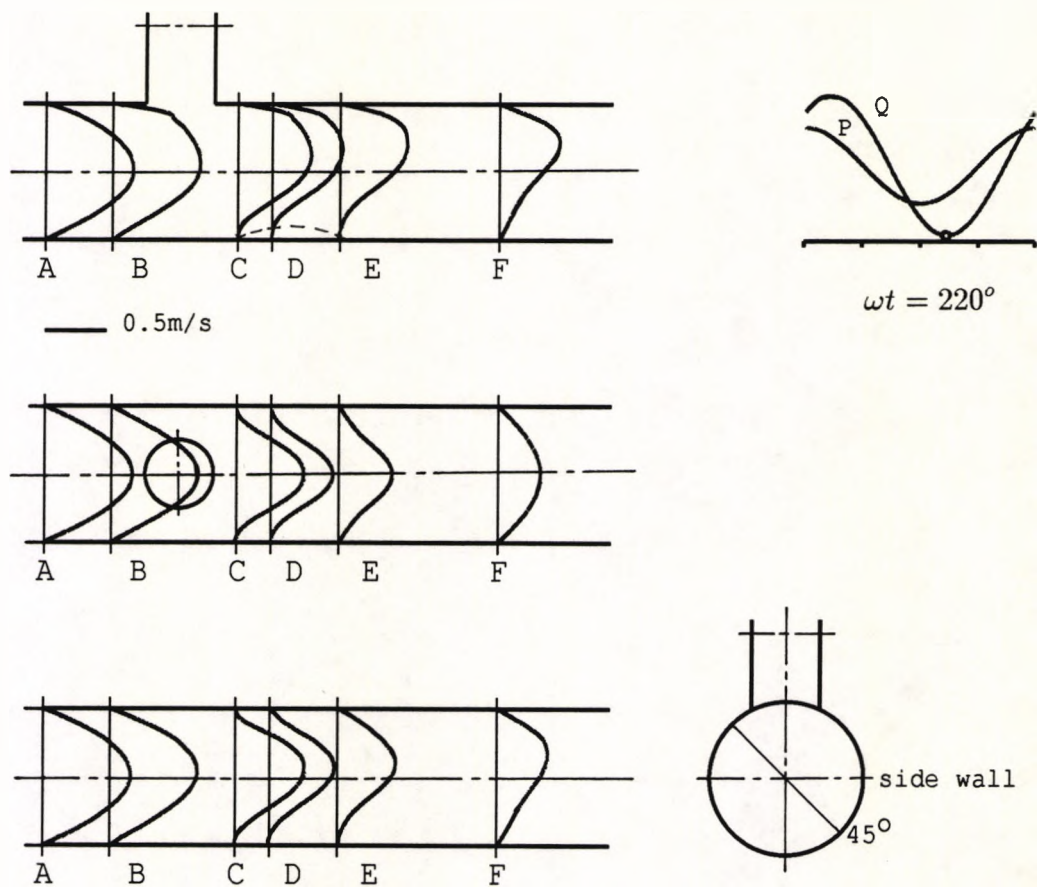


Fig. 5.26 Axial velocity profiles in the plane of symmetry and planes through the axis of the main tube at 90° and 45° to the bifurcation plane at specified phase angles.

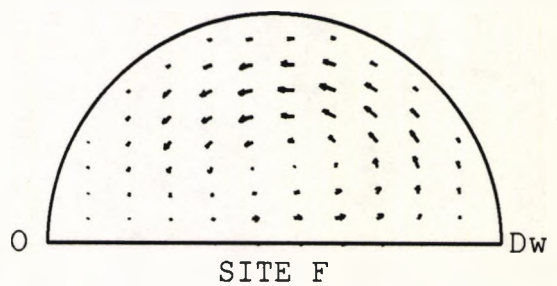
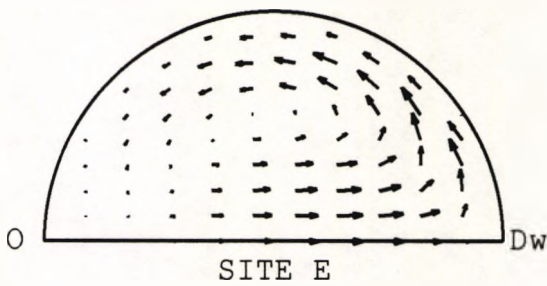
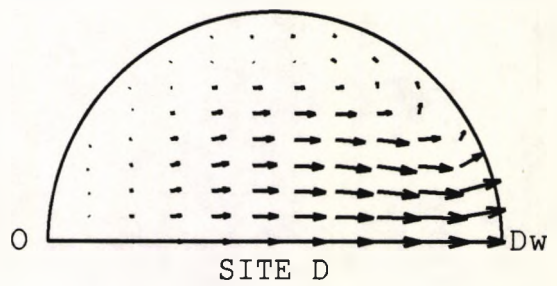
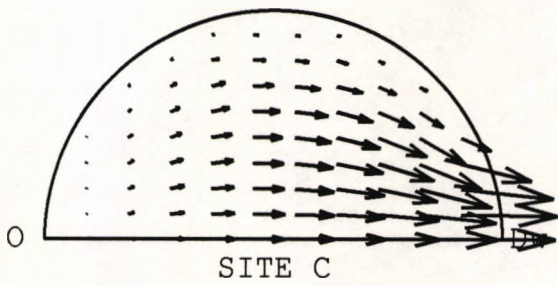
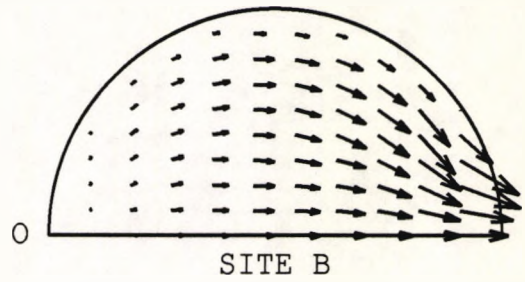
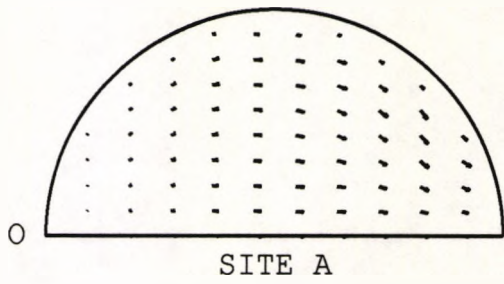
The axial velocity profiles upstream of the branching area are regular and axisymmetric over the whole cycle. Immediately after the bifurcation velocity profiles vary greatly. Near the divider wall relatively high axial velocities and steep velocity gradients can be observed. This shifting of mass flow towards the divider wall results from the branching effect. Along the outer wall, a dynamic zone of separated flow is seen. This separation zone (outlined in dashed line in the bifurcation plane) expands and contracts during the pulsatile cycle, but remains permanent throughout the cycle. At the peak flow rate ($\omega t = 40^\circ$), the maximum axial ve-

locity behind the flow divider at location D is 0.82m/s and the reverse velocities there are up to -0.021m/s . In the bifurcation plane flow separation zone is about $2.5R$ in length along the outer wall and extends up to $0.25R$ from the wall. In the plane perpendicular to that of the bifurcation, flow separation region along the side walls is very small with much reduced reverse velocities (-0.0015m/s); while in the 45° plane flow separation along the wall at the non-divide side is more obvious but still smaller than that in the bifurcation plane. At the flow deceleration phase $\omega t = 90^\circ$, flow reversal is found maximum with negative velocities reaching -0.031m/s which is about 4% of the forward directed velocity. The separation region has grown larger, occupying about $3.4R$ in length and $0.33R$ in thickness in the bifurcation plane. Along the non-divide wall in the 45° plane and the side walls in the perpendicular plane, separation zones are noticed with reduced sizes. At the minimum flow rate ($\omega t = 220^\circ$), flow separation region becomes smaller and occupies about $1.2R$ in length and $0.15R$ in thickness in the bifurcation plane. No flow separation is found in the 45° plane and the perpendicular plane.

From these results it can be noticed that under the flow condition studied here the flow separation zone is confined to a rather thin layer adjacent to the outer wall. This is mainly due to the smaller side branch used (having half of main branch diameter). Karino et al (1980) have studied experimentally the effect of branch to main tube diameter ratio and demonstrated that with decreasing side branch diameter the recirculation zone opposite the side branch became smaller and thinner.

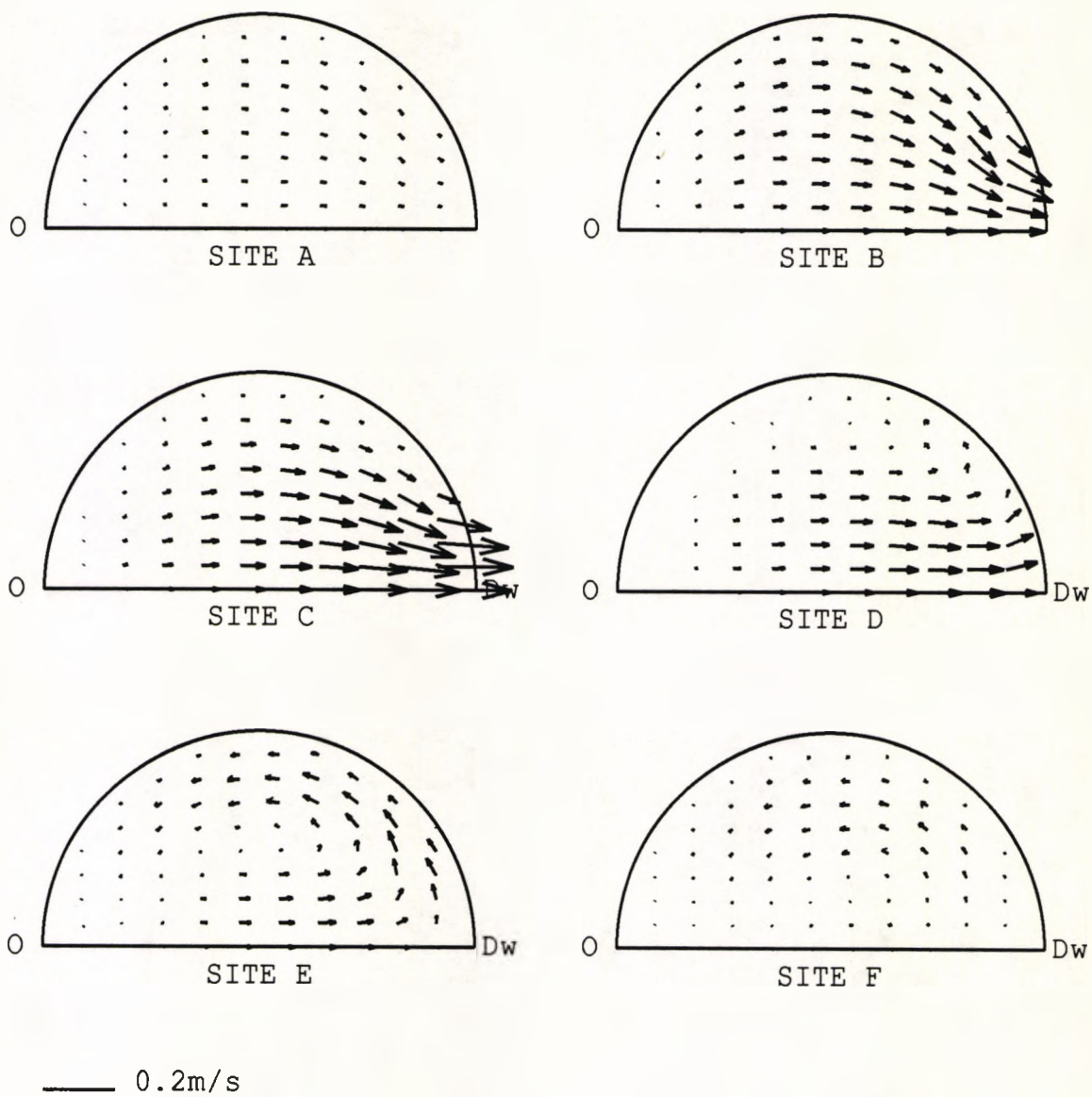
A significant feature of viscous 3D flow in a bending tube is the existence of secondary motion in cross stream planes due to the centrifugal force and the change of main flow stream direction. Secondary flow also occurs in bifurcations, since a bifurcation can be considered to be composed of two tubes bending in opposite directions. Figs.5.27 and 5.28 show the secondary velocity vector field and profiles at different cross-sections (defined in Fig.5.25) for the maximum and minimum

flow rates.



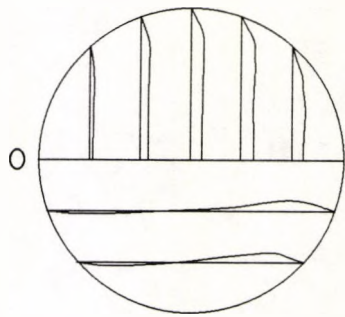
— 0.2m/s

(a) at maximum flow rate ($\omega t = 40^\circ$)

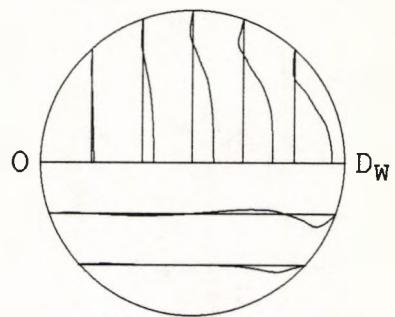


(b) at minimum flow rate ($\omega t = 220^\circ$)

Fig. 5.27 Secondary velocity vector field at different cross-sections for the maximum and minimum flow rates.

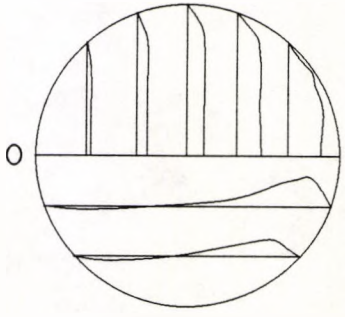


SITE A
(scaled up 2 times)

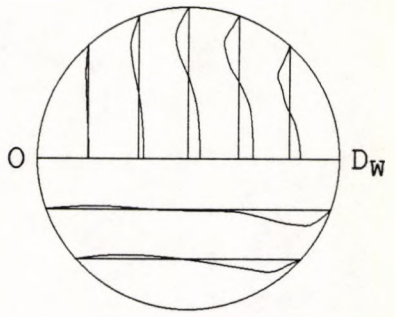


SITE D

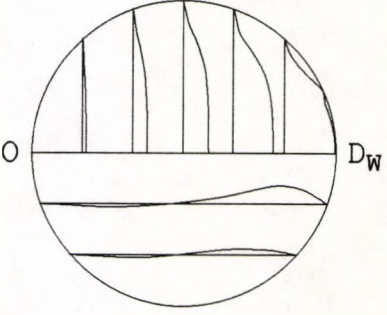
— 0.3m/s



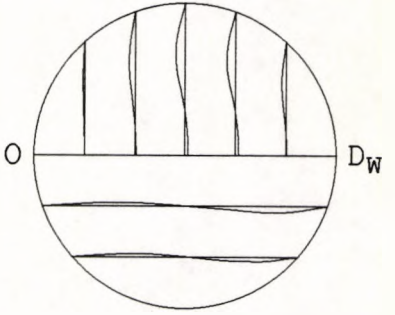
SITE B



SITE E

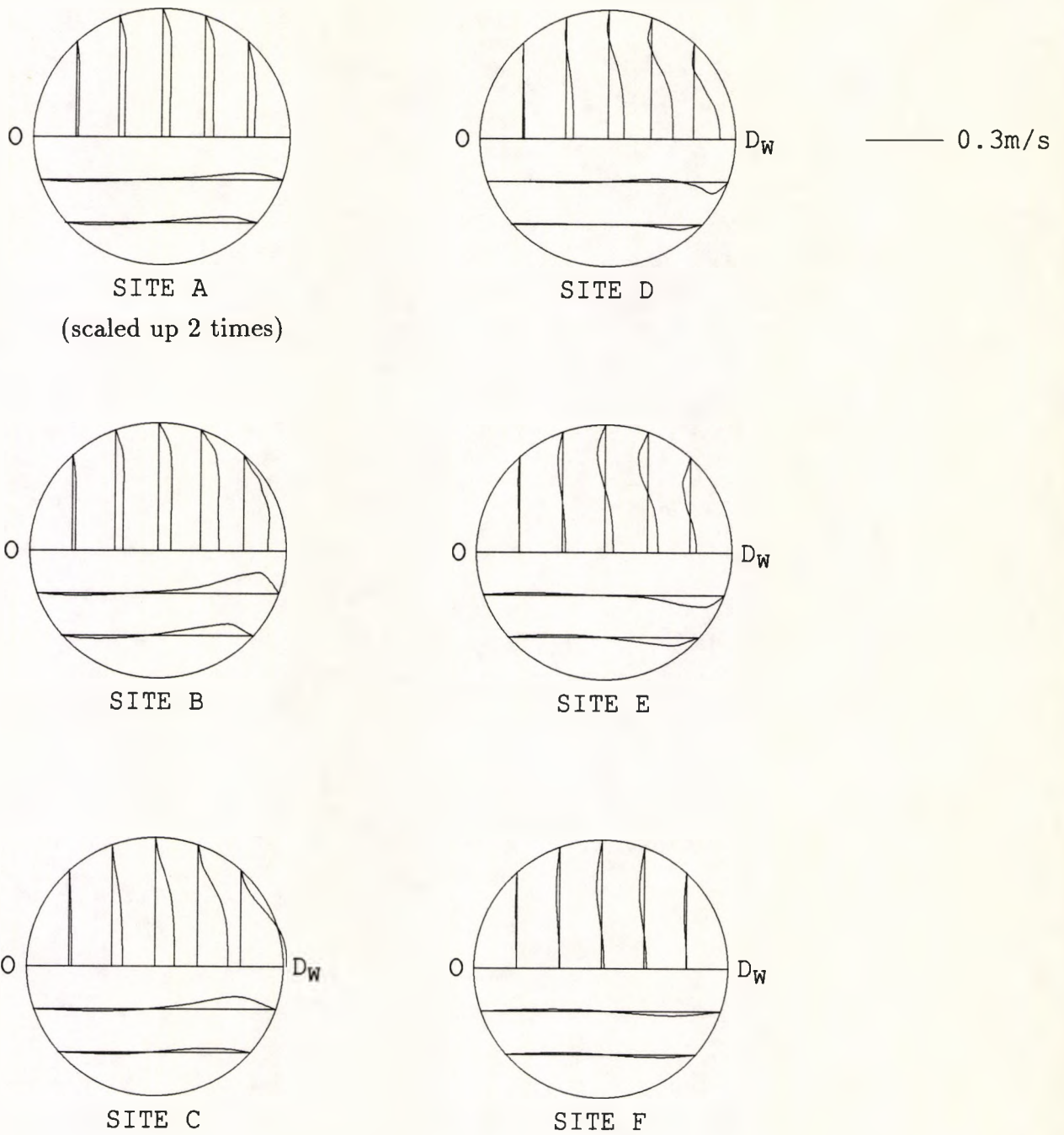


SITE C



SITE F

(a) at maximum flow rate ($\omega t = 40^\circ$)



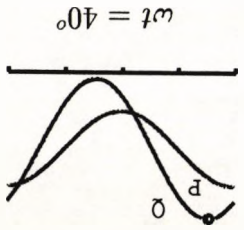
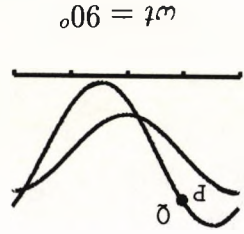
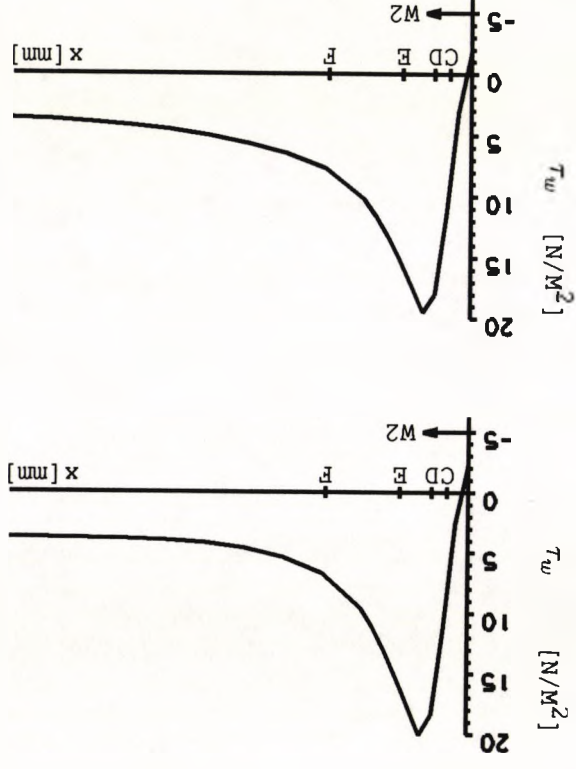
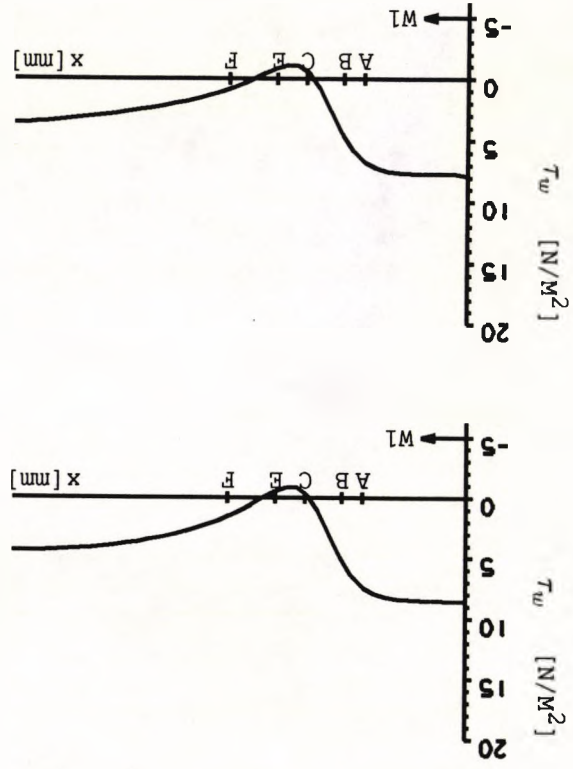
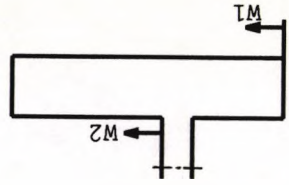
(b) at minimum flow rate ($\omega t = 220^\circ$)

Fig. 5.28 Secondary velocity profiles at different cross-sections for the maximum and minimum flow rates.

Upstream of the bifurcation at sites A and B, secondary velocity is completely directed from the outer wall towards the branching side, pointing at upstream influences due to flow branching. The secondary velocities at the branching side are higher than those at the outer wall. Near the flow divider and slightly downstream of the bifurcation at sites C and D, secondary flow is almost entirely directed towards the divider wall except in a small region near the side wall, where secondary flow is directed towards the outer wall. The highest secondary velocity is found near the flow divider at site C reaching about one third of the maximum axial velocity at the same site. Downstream of the bifurcation at site E secondary flow shows high resemblance to a Dean type vortex. Near the symmetry plane secondary velocities are directed towards the divider wall and near the side wall they point circumferentially back towards the outer wall. The highest secondary velocity at this site is observed near the side wall, but it is considerably lower than the secondary velocities observed near the flow divider at site C. Further downstream at site F secondary flow has reduced in strength as compared with the secondary flow at site E. Near the symmetry plane secondary velocities are directed towards the divider wall but are very small in magnitude; near the side wall they are directed circumferentially towards the outer wall showing some resemblance to a Dean type vortex.

5.3.3.3 Description of Wall shear stress

Fig.5.31 shows the wall shear stress along the outer wall (W1) and the divider wall (W2) at specified phase angles. At the peak flow rate ($\omega t = 40^\circ$) the wall shear stress distribution along the outer wall (W1) indicates flow separation. This is seen through the changing sign of the wall shear stress as the flow passes through the separation point and the reattachment point. Wall shear stresses at the divider wall are unidirectional and high in magnitude. The maximum wall shear stress is $20.07 N/m^2$ occurring at about one-half of a tube diameter behind the flow divider.



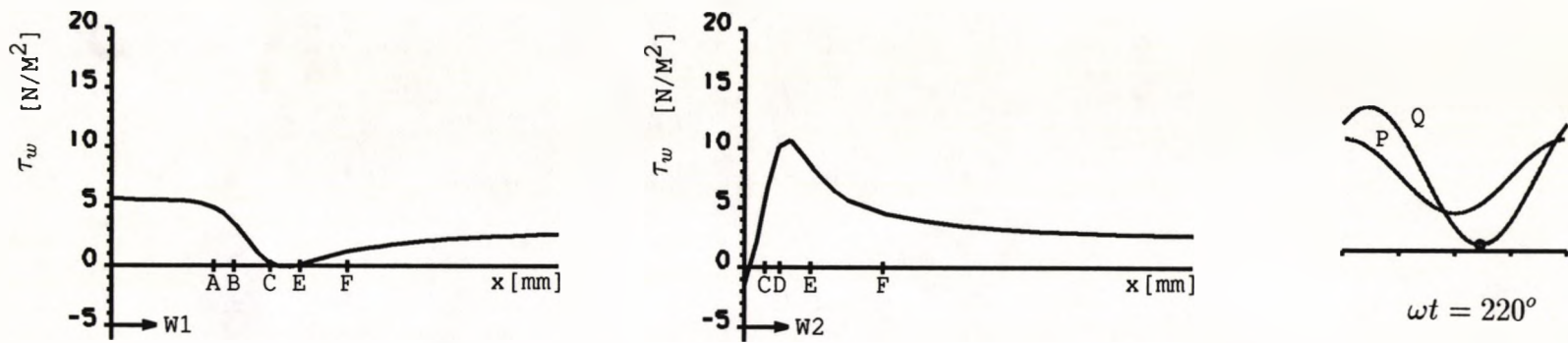


Fig. 5.29 Wall shear stress along the outer wall (W1) and the divider wall (W2) at three phase angles (40° , 90° , and 220°).

At the deceleration phase ($\omega t = 90^\circ$) wall shear stress distributions are similar to those at the peak flow rate, but with a slightly enlarged separation region and lower minimum wall shear stress which is $-1.12N/m^2$ and located between sites C and E. At the minimum flow rate the zone of flow separation is small and the minimum wall shear stress is very close to zero. The maximum wall shear stress on the divider wall is $10.66N/m^2$, which is about half of the maximum wall shear stress at the peak flow rate.

Variations of the wall shear stress at different levels of the bifurcation during the pulsatile cycle are illustrated in Fig.5.30 where the locations of A, D and F have been previously defined in Fig.5.25. At the upstream position of site A, the wall shear stress at the branching side is higher than at the outer wall, indicating the flow deviation towards the branching wall. It is noteworthy that although this skew of flow is not seen obviously in the velocity profiles presented in Fig.5.26, even a slight shift in flow would result in a relatively large difference in wall shear. The peak wall shear stress at this site is $12.69N/m^2$ and occurs on the branching wall at flow acceleration phase around $\omega t = 25^\circ$.

At site D (distal to the flow divider), the phasic variations of the shear stress on the outer and the divider walls are completely different. While the peak shear stress $\tau_w = 14.04N/m^2$ occurs on the divider wall at flow deceleration phase ($\omega t \simeq 80^\circ$), the shear stress on the outer wall is approaching the minimum level $\tau_w = -1.12N/m^2$. Low and negative shear stress on the outer wall can be observed throughout the cycle, demonstrating the existence of flow separation. During the early flow acceleration between phase angles 220° and 340° , the flow is nearly stagnant.

Downstream at site F, the shear stress on the outer wall is low in magnitude but remains positive, suggesting that no flow separation occurs at this level. The

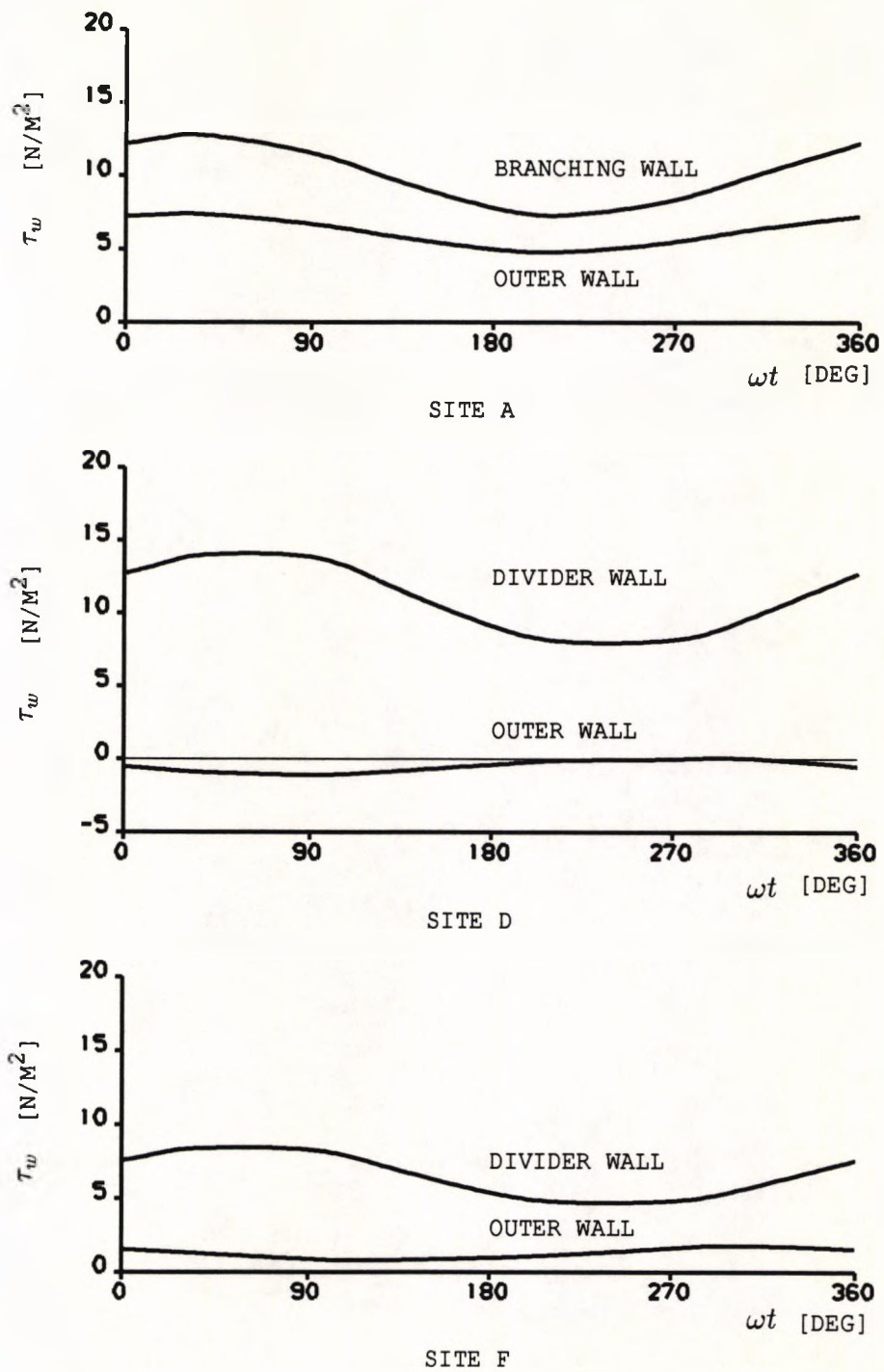


Fig. 5.30 Wall shear stress vs phase angle on the outer and the divider walls at different cross-sections of the bifurcation.

maximum shear stress on the divider wall at site F is $8.37N/m^2$; this is about 60% of the peak wall shear stress found at site D. The maximum, minimum and time-averaged shear stresses on the outer and divider walls at sites A, D and F are summarised and compared with those of a non-Newtonian fluid later in Table 5.4 (section 5.3.3.5).

5.3.3.4 Effects of three dimensionality

One of the most important three-dimensional phenomena in bifurcation flow field is the existence of secondary motion. As the fluid elements leave the parent tube and enter a branch, they are accelerated by centrifugal forces towards the flow divider side which results in secondary flows that are directed towards the divider wall in the bifurcation plane and away from it along the side wall of the branch. This phenomenon has already been seen in Figs.5.27 and 5.28, in which the highest secondary velocity is found to be about one third of the maximum axial velocity at the same cross section, suggesting the strength of the secondary motion. It is expected that this secondary flow in conjunction with the axial motion would result in helical type flow patterns in the branches as reported in the experimental studies of Bharadvaj et al (1982a) and Ku et al (1985). These flow patterns can only be seen through flow visualisations of the three-dimensional particle paths in the bifurcation. However, such flow visualisations from numerical predictive data are still very difficult to achieve at present. It is hoped to be accomplished in future studies.

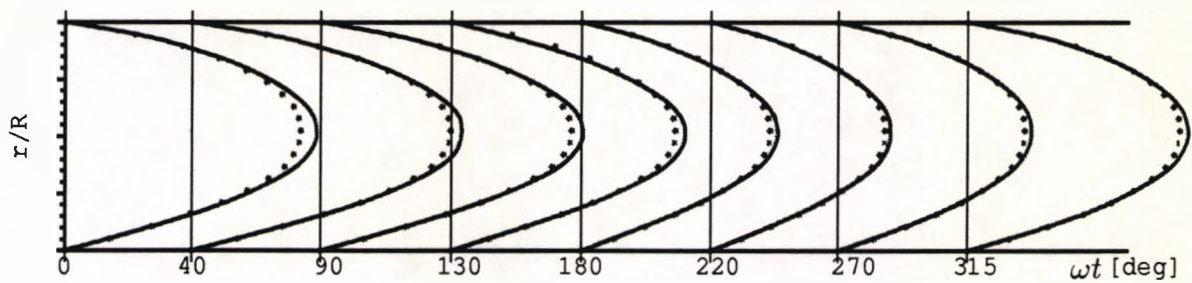
Note that the presence of the secondary circulation in bifurcation flow field not only affects the flow patterns in branches, but also causes a redistribution of axial velocity in the bifurcation plane resulting in a shift of peak velocity nearer to the divider wall and a reduction of velocity along the outer wall. These will have a direct influence on the value of the wall shear stress. Thus, in order to obtain exact and precise flow patterns and shear stress distribution in branching

arteries it becomes essential to investigate the flow in a three-dimensional geometry.

5.3.3.5 Effects of non-Newtonian viscosity

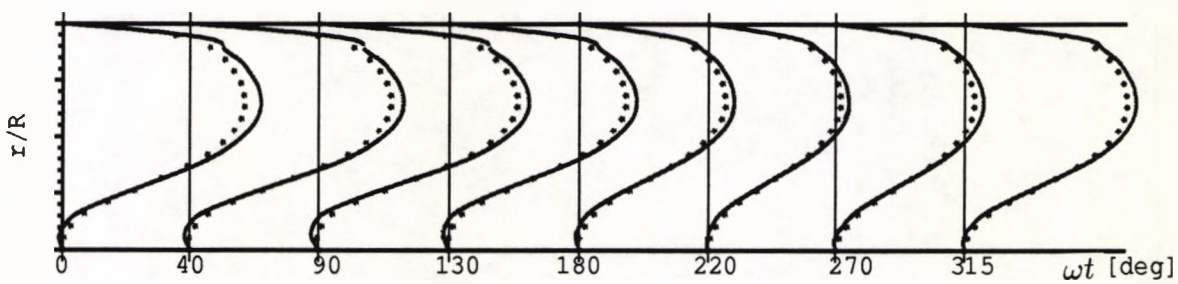
In order to investigate the effect of non-Newtonian viscosity on the flow field and distribution of wall shear stress, numerical calculations were carried out for a non-Newtonian fluid under the same pulsatile flow conditions. The employed non-Newtonian fluid has a representative viscosity of $0.013 \text{ Kg}/(\text{ms})$, which equals the viscosity of the Newtonian fluid used in the previous calculation. Comparisons of Newtonian and non-Newtonian results were made for axial velocity profiles in the plane of bifurcation and the plane perpendicular to that of the bifurcation at selected cross sections over a complete cycle, wall shear stress distributions along the outer and divider walls at specified phase angles, as well as the time varying wall shear stress at different levels of the bifurcation plane.

Fig.5.31 shows the axial velocity profiles in (a) the bifurcation plane, and (b) the perpendicular plane at sites A, D and F at different phase angles over one cycle. The Newtonian velocity profiles are drawn with solid lines, and those of the non-Newtonian with circles. In general, the shape of velocity profiles and the basic features of the flow approximately agree between the Newtonian and the non-Newtonian fluids. However, certain differences do exist. It can be observed that the non-Newtonian fluid results in blunted velocity profiles due to the shear thinning effect, and reduced reverse flow velocity and separation zone. Numerical results show that in the non-Newtonian case, flow separation occurs only during the period between late flow acceleration ($\omega t = 15^\circ$) and middle of flow deceleration ($\omega t = 160^\circ$), which occupies about 40% of the whole cycle. Furthermore, the extent of this separation zone is significantly reduced: its length along the outer wall is about one-half of that found in the Newtonian case.



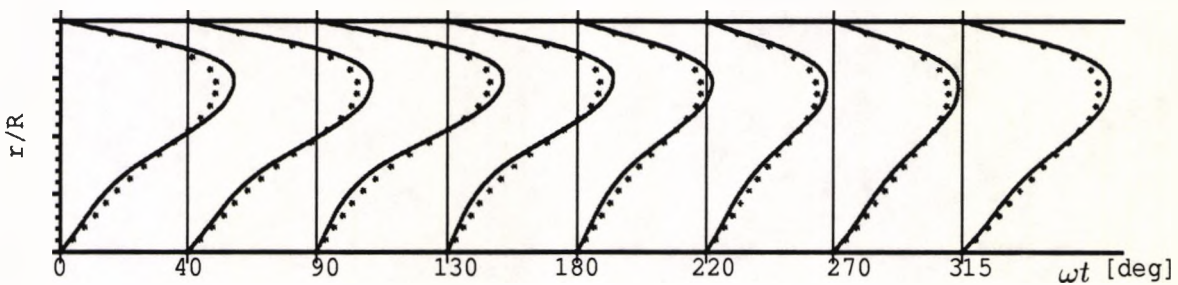
0.5m/s

SITE A



0.5m/s

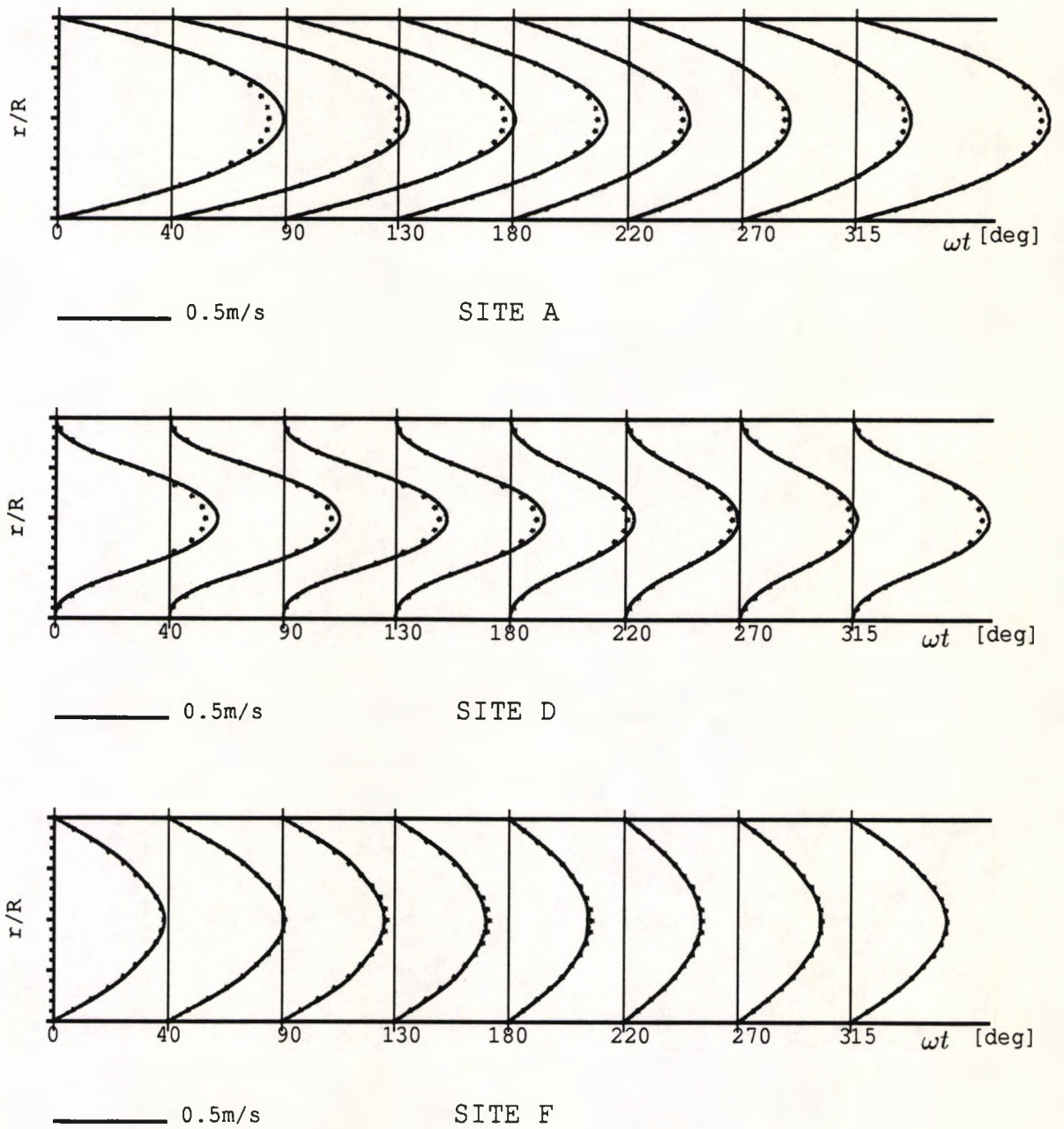
SITE D



0.5m/s

SITE F

(a) in the bifurcation plane



(b) in the perpendicular plane

Fig. 5.31 Comparison of axial velocity profiles between Newtonian (—) and non-Newtonian (•••) fluid in (a) the bifurcation plane, and (b) the perpendicular plane.

Table 5.4 gives a summary of the maximum forward flow velocities and the maximum reversed flow velocities at site D (2.5mm behind the flow divider) over one pulsatile cycle for both the Newtonian and non-Newtonian fluids. The relative difference defined as $(U_N - U_{n-N})/U_N$ is also provided. It is demonstrated that under the flow conditions studied here the difference in maximum forward flow velocities between the Newtonian and non-Newtonian fluids is relatively small (within the range of 5.5% to 8.12%), but the difference in reversed flow velocities is significant (up to 90.5%).

t (deg)	Maximum forward velocity (m/s)			Maximum reversed velocity (m/s)		
	Newtonian	non-Newtonian	$\frac{U_N - U_{n-N}}{U_N}$ (%)	Newtonian	non-Newtonian	$\frac{U_N - U_{n-N}}{U_N}$ (%)
0	0.776	0.713	8.12	-0.013	No	—
40	0.823	0.777	5.59	-0.021	-0.003	85.71
90	0.807	0.762	5.58	-0.027	-0.006	77.78
130	0.721	0.681	5.55	-0.021	-0.002	90.48
180	0.602	0.567	5.81	-0.010	No	—
220	0.551	0.520	5.63	-0.004	No	—
270	0.572	0.538	5.94	-0.002	No	—
310	0.655	0.619	5.50	-0.001	No	—

Table 5.4 Comparison of Newtonian and non-Newtonian flow: maximum forward flow velocity and maximum reversed flow velocity at site D (2.5mm behind the flow divider).

Distributions of wall shear stress along the outer wall (W1) and the divider wall (W2) are compared at the peak flow rate, flow deceleration phase and minimum flow rate in Fig.5.32, where solid line represents the wall shear stress of the Newtonian fluid, and circles represent that of the non-Newtonian fluid. The dia-

gram shows that in the non-Newtonian case the wall shear stress along the outer wall is higher (about 31% higher in average). Along the divider wall no significant difference is noticed except that the peak shear stress is slightly reduced (up to 8%) with the non-Newtonian fluid.

Fig.5.33 presents the time varying wall shear stress at different levels of the bifurcation over a complete cycle. Again, the shear stress of the Newtonian fluid is drawn as solid line, and that of the non-Newtonian fluid as solid line marked with circles. Upstream of the bifurcation at site A, the shear stress on both the outer and branching walls is higher with the non-Newtonian fluid. Distal to the bifurcation at site D and further downstream at site F, the shear stress in the non-Newtonian case is higher on the outer wall but slightly lower on the divider wall than those of the Newtonian fluid. Comparison of the maximum, minimum and time-averaged shear stress on the outer and divider walls at these sites is presented in Table 5.5.

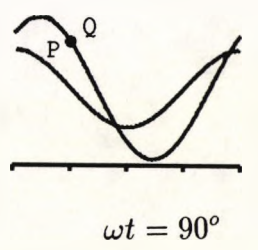
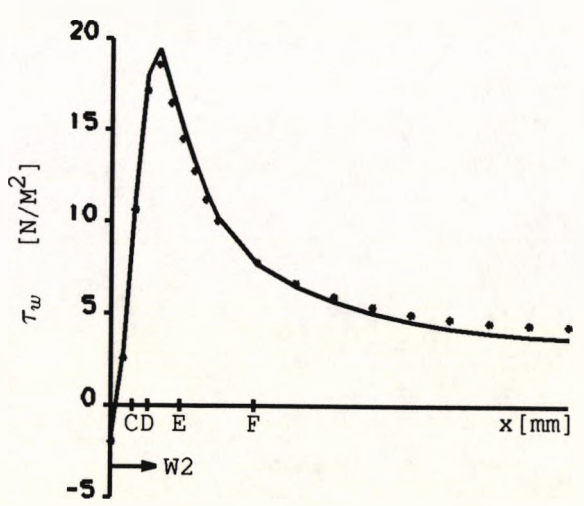
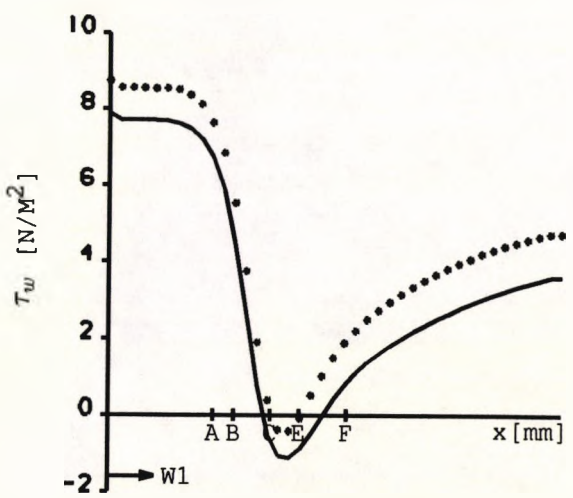
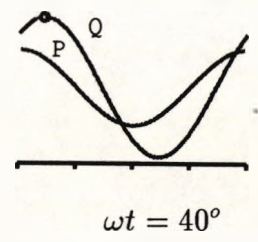
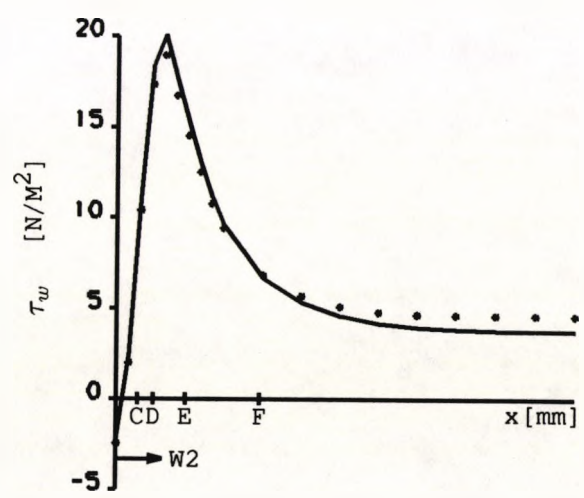
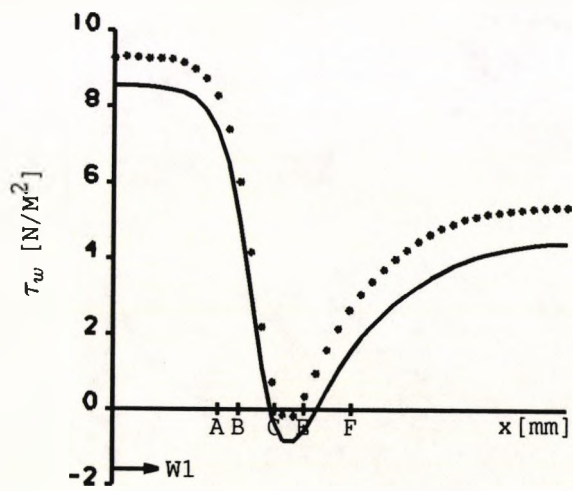
locations	Maximum τ_w (N/m ²)		Minimum τ_w (N/m ²)		Time-averaged (N/m ²)	
	Newtonian	non-Newtonian	Newtonian	non-Newtonian	Newtonian	non-Newtonian
A	7.36	8.29	4.85	5.87	6.34	7.26
D	-0.026	0.97	-1.12	-0.43	-0.65	0.30
F	1.77	2.72	0.80	1.87	1.29	2.43

(a) on the outer wall

locations	Maximum τ_w (N/m ²)		Minimum τ_w (N/m ²)		Time-averaged (N/m ²)	
	Newtonian	non-Newtonian	Newtonian	non-Newtonian	Newtonian	non-Newtonian
A	12.69	13.16	7.33	8.36	9.34	11.10
D	14.04	12.93	8.01	7.65	11.36	10.60
F	8.37	8.39	4.82	5.03	6.75	6.77

(b) on the divider wall

Table 5.5 Comparison of Newtonian and non-Newtonian flow: maximum, minimum and time-averaged shear stress on the outer and divider walls at sites A, D and F.



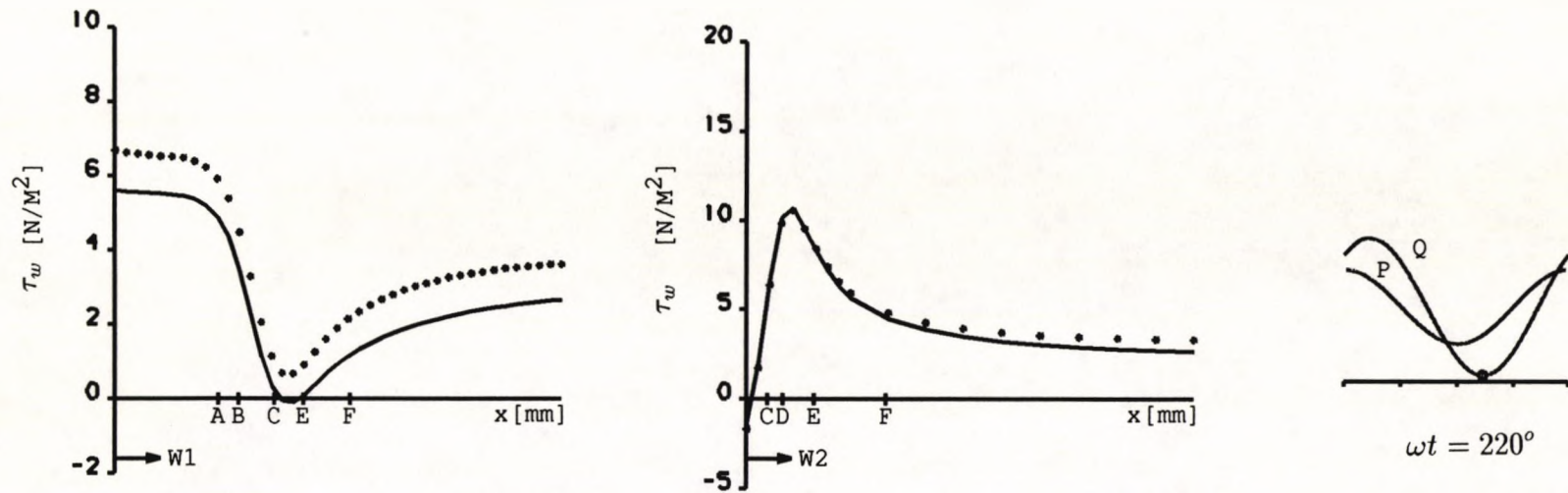


Fig.5.32 Comparison of Newtonian (—) and non-Newtonian (•••) flow: wall shear stress along the outer wall (W1) and the divider wall (W2) at three phase angles (40° , 90° and 220°).

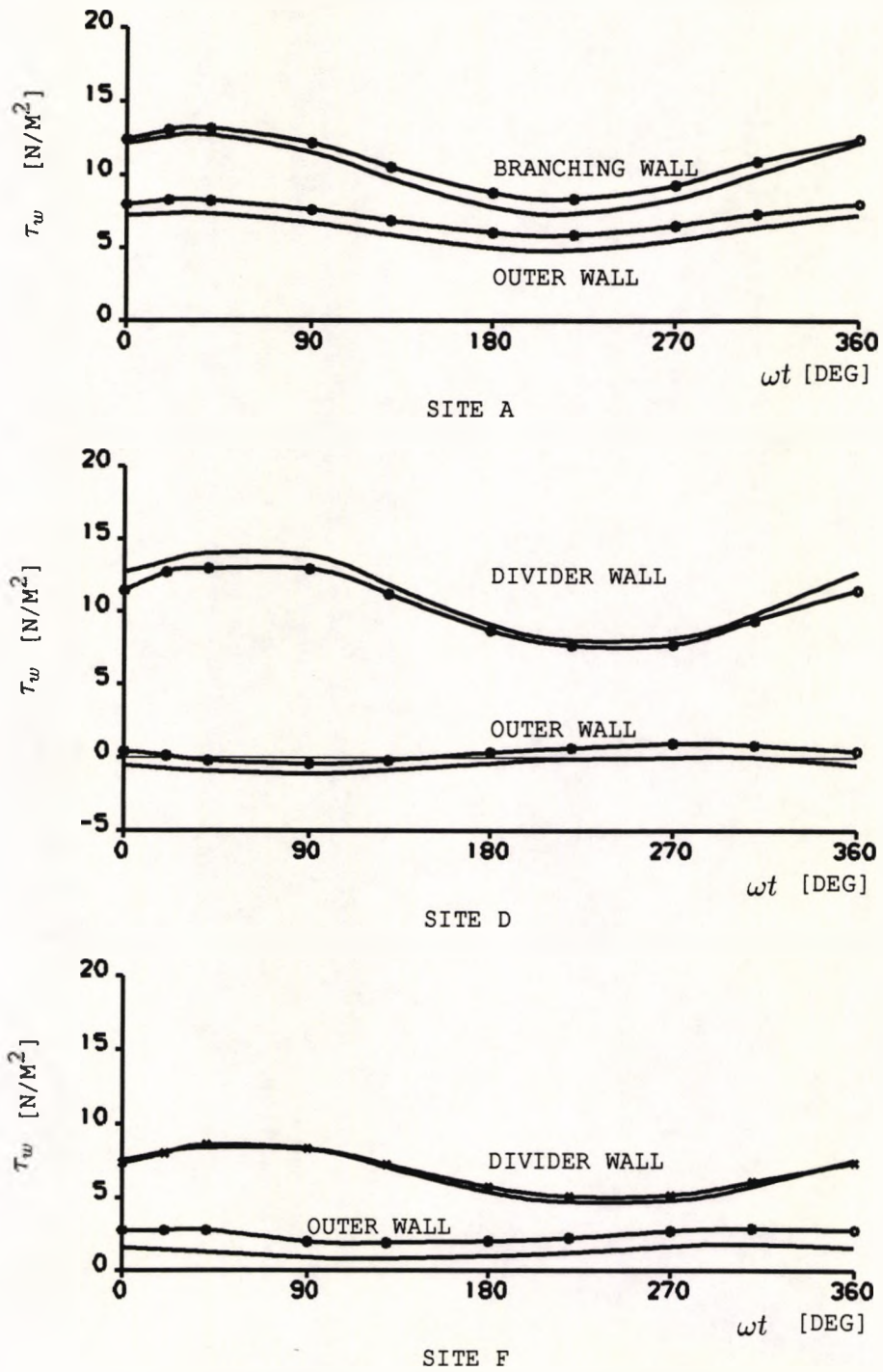
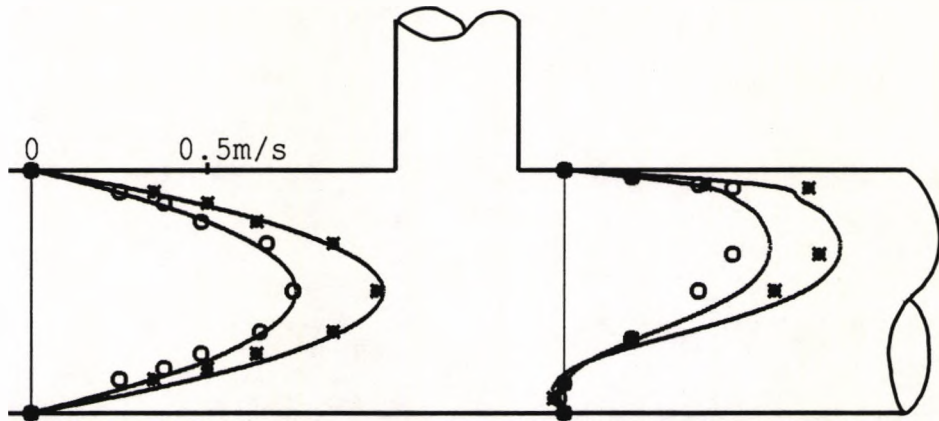


Fig. 5.33 Comparison of time varying wall shear stress between Newtonian (—) and non-Newtonian (•••) fluid.

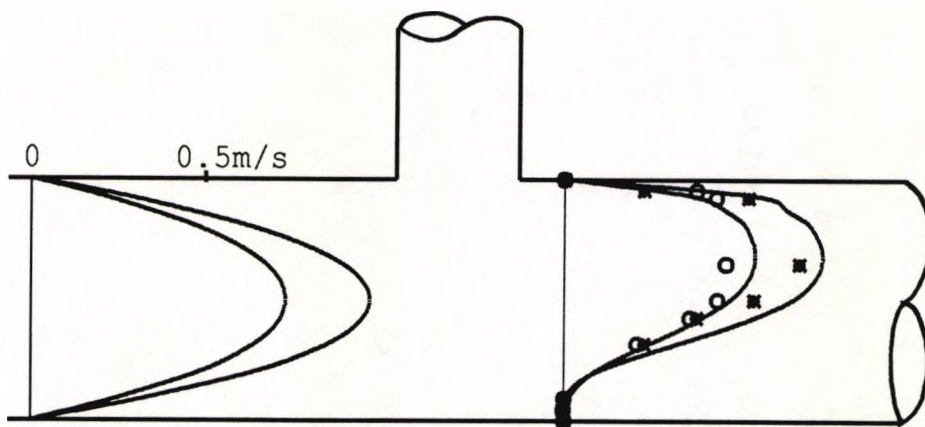
5.3.3.6 Comparison with LDA measurements of Ku and Liepsch

The comparison of the calculations and the LDA measurements is confined to axial velocity profiles in the bifurcation plane at specified phase angles since no further experimental data is available. In the experiment axial velocities were measured in the plane of the bifurcation at 25mm upstream and 2.5mm downstream of the flow divider. Comparisons of velocity profiles at these locations are shown in Figs.5.34(a) and (b) for the Newtonian and the non-Newtonian fluid respectively. Under the pulsatile flow conditions studied, upstream velocity profiles at phase angles 0° and 90° are very close to each other, so is the case for phase angles 180° and 270° . Therefore, comparison with the experiment is presented for phase angles 90° and 180° only.

In the diagram numerical predictions are drawn with solid line and experimental data with symbols (\star for $\omega t = 90^\circ$, \circ for $\omega t = 180^\circ$). It is evident that upstream velocity profiles agree very well between the calculations and the measurements with the Newtonian fluid. In the non-Newtonian case, comparison of upstream velocity profiles was not made since the experimental data was not available. Downstream in the bifurcation, some differences can be noticed. First, the predicted maximum velocities are higher than those of the measurements. Second, with the non-Newtonian fluid flow separation was found only for part of the cycle in the prediction but was shown to exist throughout the cycle in the experiment. These discrepancies may in large part ^{be} due to the bifurcation corner effect: sharp corner in the prediction and rounder corner _{in} in the experiment. Previous experimental study (Karino et al, 1979) have shown that in a rounded T-bifurcation a much larger flow recirculation zone with more rapidly circulating fluid exists along the bottom wall; these would also result in a reduced maximum velocity at cross-sections where flow recirculation is present.



(a) With the Newtonian fluid



(b) With the non-Newtonian fluid

Fig. 5.34 Comparison between calculations (—) and measurements (\star for $\omega t = 90^\circ$, \circ for $\omega t = 180^\circ$): axial velocity profiles in the bifurcation plane 25mm upstream and 2.5mm downstream of the flow divider for (a) the Newtonian fluid, and (b) the non-Newtonian fluid.

5.4 SUMMARY

It this chapter, a comprehensive range of code validation excises has been presented, and the effects of various factors investigated. Comparisons with the analytical solutions and the published LDA measurements have demonstrated that the presented predictive scheme is efficient and reliable on bifurcation flow problems. Features such as the three-dimensionality of the geometry, the pulsatility of the flow and the non-Newtonian viscosity of the fluid should all be accommodated in order to obtain exact and precise flow patterns and distribution of shear stress in arterial bifurcation models.

CHAPTER 6

PREDICTIONS OF FLOW IN 3D CANINE FEMORAL ARTERY BIFURCATIONS

6.1 INTRODUCTION

Numerical predictions presented in the previous chapter are confined to idealised bifurcation geometries under sinusoidal pulsatile flow conditions. In this chapter, numerical results for true physiological flow in 3D canine femoral bifurcations are presented and analysed. Geometries of the two bifurcation models (referred as A and B in later text) adopted in the calculations were based upon data from *in vivo* measurements of Jones et al (1990). In the predictions, blood was assumed to be (i) Newtonian and (ii) non-Newtonian obeying the power law; the vessel wall being rigid. For the upstream boundary condition, two types of physiological velocity waveform were employed. One was an averaged velocity waveform in canine arteries. Another was the *in vivo* waveform measured upstream of each bifurcation models. The presentation of the numerical results concentrates on the axial and secondary flow velocity and the pulsatile wall shear stress (in physical units). Furthermore, the effects of upstream boundary conditions and non-Newtonian viscosity on the bifurcation flow field and wall shear stress are investigated. Comparison of numerical predictions and the *in vivo* measurements is finally presented.

6.2 PROBLEM DEFINITION

6.2.1 Bifurcation Geometry

The two bifurcation models adopted here were based on data from the *in vivo* measurements (Jones et al, 1990), in which branching angles, B-mode ultrasound

images of the cross-sections of the upstream parent and both downstream daughter vessels, and the origin of both vessels were all photographed. The bifurcation geometrical data were measured from photographs. Fig.6.1 gives a schematic illustration and three-dimensional representation of the two canine ilio-femoral bifurcation models. In both models A and B, the parent and daughter vessels are straight, with the bifurcation lying in one plane which is the plane of symmetry. These assumptions are consistent with the measurements. The two models have similar configurations and differ only in vessel diameters and the parent to large daughter angle.

Fig.6.1 also illustrates the sites at which the comparison between numerical predictions and measurements is presented. In terms of the parent vessel diameter, site 1 is two diameters upstream of the flow divider in the parent artery, site 2 is at the level of flow divider in the large daughter vessel, site 3 and 4 are one and four diameters downstream respectively, and site 5 is one diameter downstream of the flow divider in the smaller daughter vessel. For convenience of comparison, they are placed at 60° to the vessel axes, since the measurements were taken at such positions.

6.2.2 Boundary Conditions

The choice of appropriate boundary conditions is often considered to be important in determining the flow field of interest. For the flow problem treated here the boundary of the flow domain comprises three types: the vessel wall, the inflow and the outflow boundaries. Since the vessel wall was assumed rigid, the no-slip condition was then valid, i.e., each velocity component was set equal to zero. At the bifurcation inlet, two types of boundary conditions were employed:

Type 1 Time-dependent velocity profiles in a straight tube calculated based on an average velocity waveform in canine arteries.

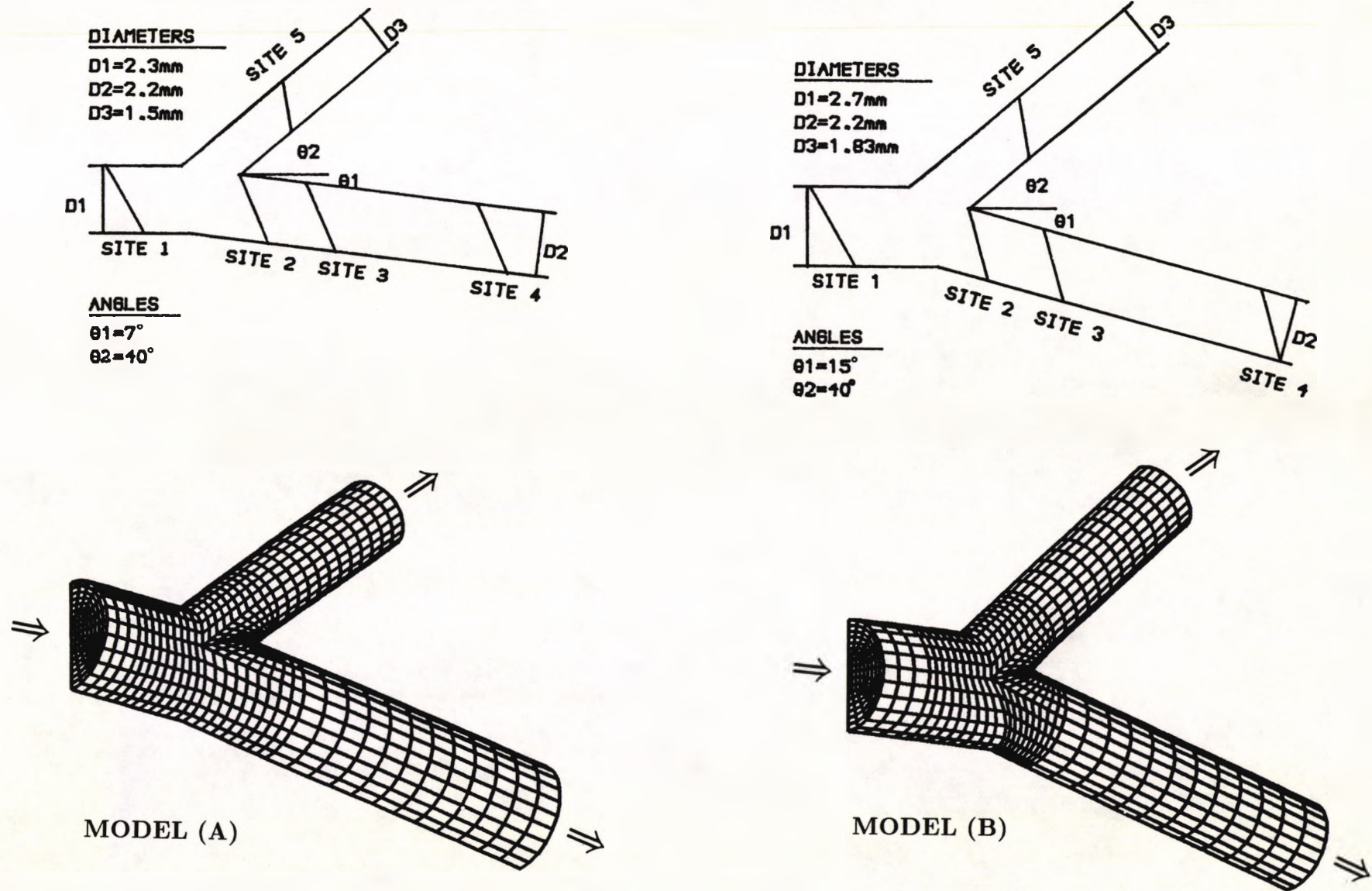


Fig. 6.1 Schematic illustration and three-dimensional representation of the two canine ilio-femoral bifurcation models.

Type 2 Instantaneous axial velocity profiles obtained from the *in vivo* measurements at site 1.

Fig.6.2 shows an average canine velocity pulse waveform under normal conditions. It was allowed to develop in a straight tube which was ten diameters long, and the corresponding calculated velocity profiles at the exit of the tube are displayed in Fig.6.3. The reason for choosing the tube to be 10 diameters in length rather than long enough to be able to generate a fully developed flow was that in the measurements the parent arteries of the two bifurcation models were found relatively straight and without branching within 8–10 diameters upstream of the bifurcation. The time-dependent axial velocity profiles shown in Fig.6.3 were prescribed at the bifurcation inlet, which is referred to as the type 1 inflow boundary condition. For the type 2 inflow boundary condition, the instantaneous axial velocity profiles obtained from the *in vivo* measurements were directly imposed. Fig.6.4 shows the measured average velocity waveforms and the axial velocity profiles at site 1 for models A and B. As can be seen, these velocity profiles are relatively symmetric. It should be mentioned that for both types of upstream boundary conditions, only axial velocities were specified, secondary velocity components at the inlet were assumed to be negligible.

At the outflow boundaries, there are generally three types of treatment: (i) to assume fully developed flow; (ii) to assume a zero condition of surface traction; and (iii) to specify a constant pressure. The first type is more restrictive as it requires the flow rate ratio between the two branches to be known a priori; also the length of the specified branch has to be large enough to permit development. The other two types are more realistic for the flow problem under consideration. Hence the constant pressure outflow condition (iii) was used. For the two bifurcations investigated, zero pressures were specified at both outlets which were placed at five diameters (in terms of parent vessel diameter) downstream from the flow divider.

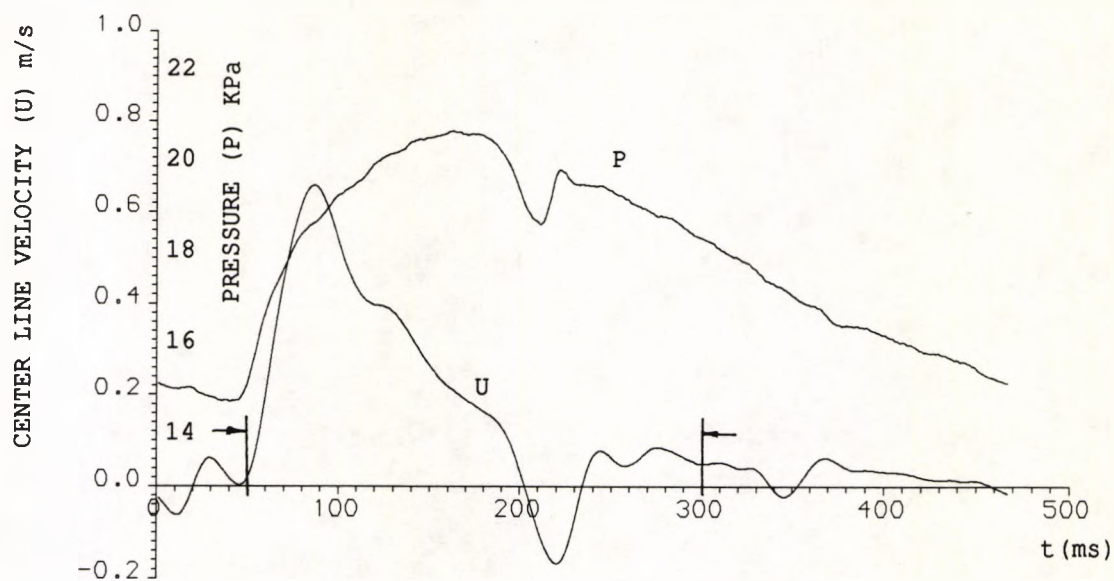


Fig. 6.2 Average canine velocity pulse waveform under normal conditions.

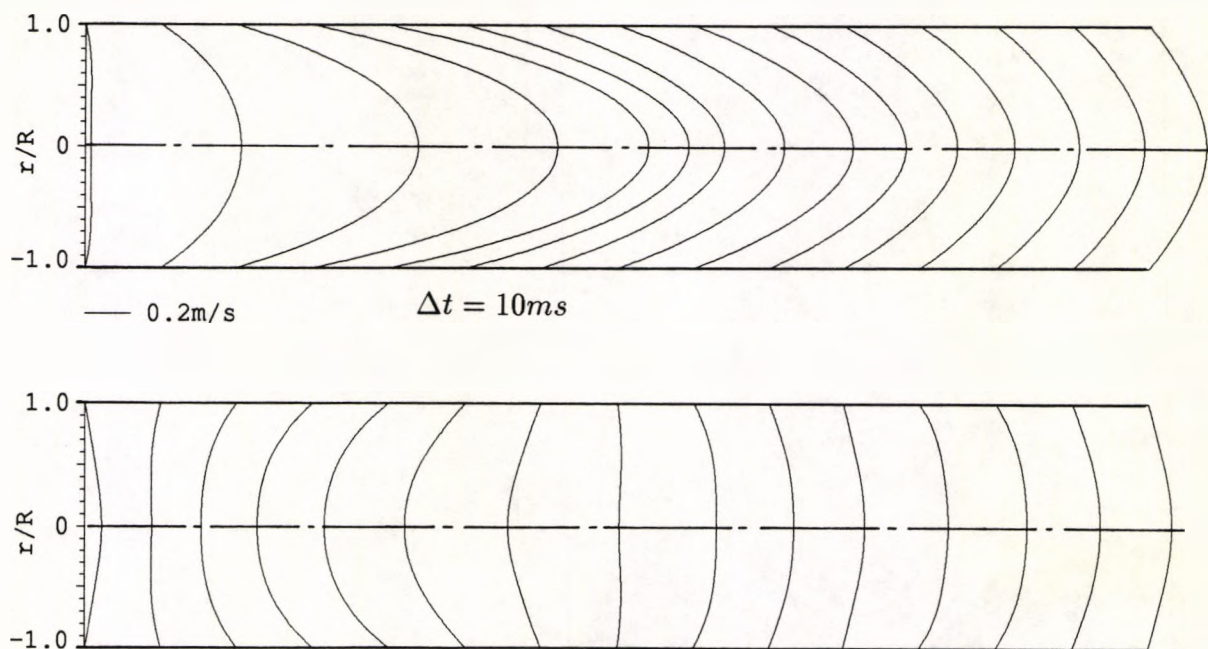
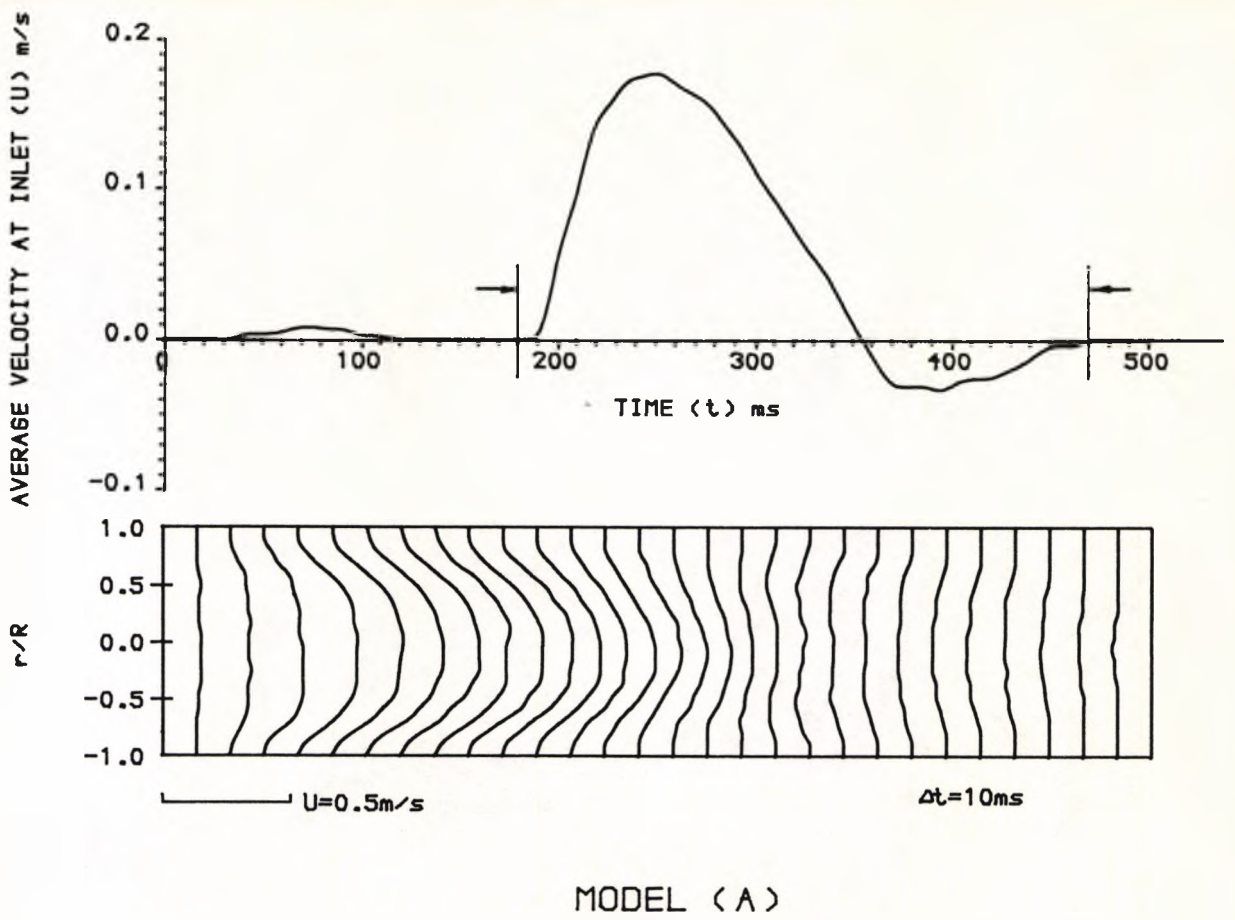
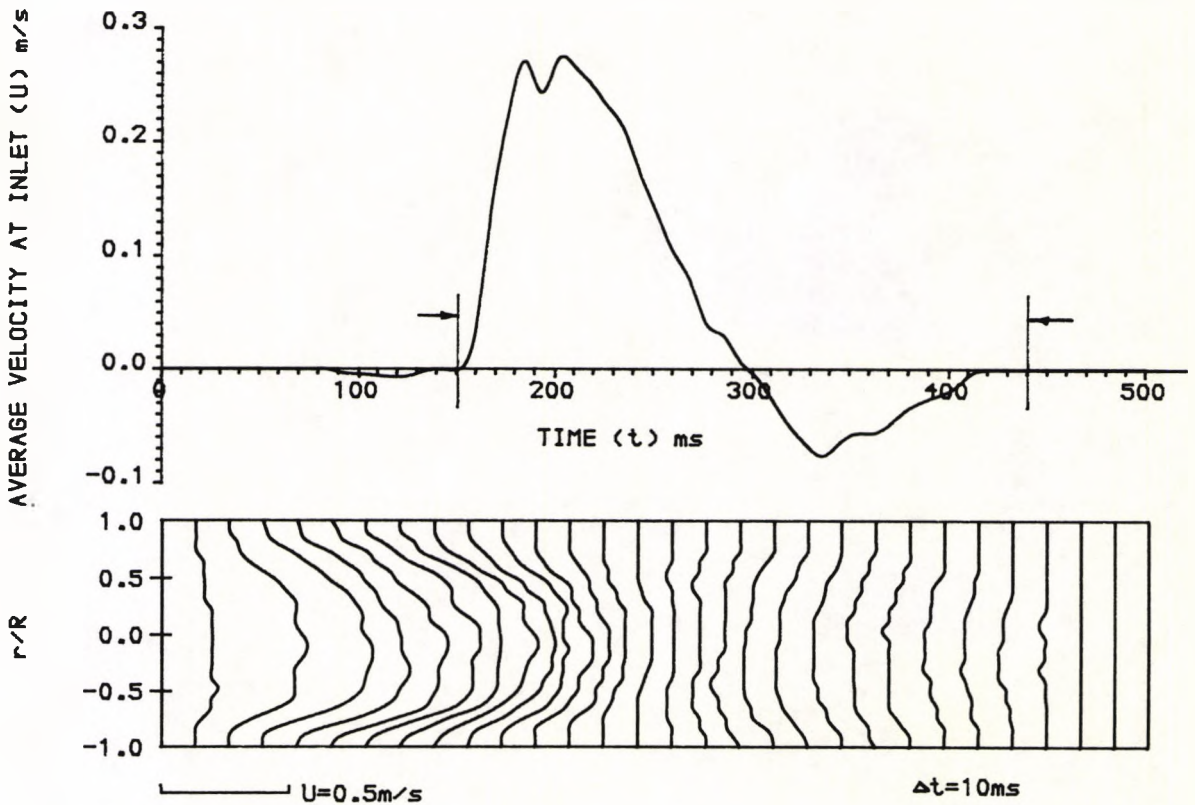


Fig. 6.3 Calculated axial velocity profiles at the exit of a straight tube 10 diameters long for the pulse period between \rightarrow \leftarrow .



MODEL (A)



MODEL (B)

Fig. 6.4 Measured average velocity waveforms and instantaneous upstream axial velocity profiles in models A and B for the pulse period between \rightarrow \leftarrow .

6.2.3 Grid Resolution Tests

In order to determine grid dependence, preliminary calculations were carried out for bifurcation model B under steady flow condition using three grid distributions, i.e, 12, 18 and 24 elements in the radial direction. Results of these calculations indicated that a grid with 18 elements in the radial direction was a good compromise between accuracy and available computer time and storage. The average velocity differences were found to be 0.19% with the finer grid and 6.17% with the coarser grid. Since in both bifurcation models a symmetry plane was assumed to exist so that simulations were confined to only half of the bifurcation. The resulting computational mesh consists of 5040 eight-node elements and a total of 6070 nodes.

6.3 NUMERICAL RESULTS

Flow predictions were conducted under three different schemes: (i) the type 1 pulsatile upstream flow condition with a Newtonian assumption for the blood, (ii) the type 2 upstream flow condition with a Newtonian assumption, and (iii) the type 2 upstream flow condition with a non-Newtonian assumption for the blood. In this section, numerical results for scheme (ii) are presented. Predictions for (i) and (iii) are presented and compared with those of scheme (ii) later in section 6.4, where effects of the upstream boundary condition and the non-Newtonian viscosity on the velocity field and wall shear stress are discussed.

When blood is taken to be homogeneous and Newtonian, its density is $1.05 \times 10^3 \text{Kg/m}^3$ and kinematic viscosity about $4 \times 10^{-6} \text{m}^2/\text{s}$ (Pedley, 1980). Under the *in vivo* pulsatile flow conditions (type 2), the average Reynolds numbers (defined as $Re = \frac{4\dot{V}}{\pi D\nu}$, where \dot{V} is the average flow rate in the parent vessel over a

whole cycle) were 92 and 108, and the Womersley parameters were 2.04 and 2.39 for bifurcation models A and B respectively. These values are in the lower physiological range, and therefore turbulent effects are unlikely.

6.3.1 Velocity Field

Velocity fields are presented for the two bifurcation models at the pulse phases of accelerated flow A_p , maximum positive flow B_p , decelerated flow C_p and maximum reverse flow D_p as defined in Fig.6.5. Figs.6.6 and 6.7 show the axial velocity profiles in the plane of the bifurcation for models A and B respectively. A three-dimensional view of the axial velocity at cross-sections perpendicular to the bifurcation plane at sites 1-5 (as defined in Fig.6.1) are presented in Figs.6.8 and 6.9 where the outer wall (the non-divider side) is seen from front.

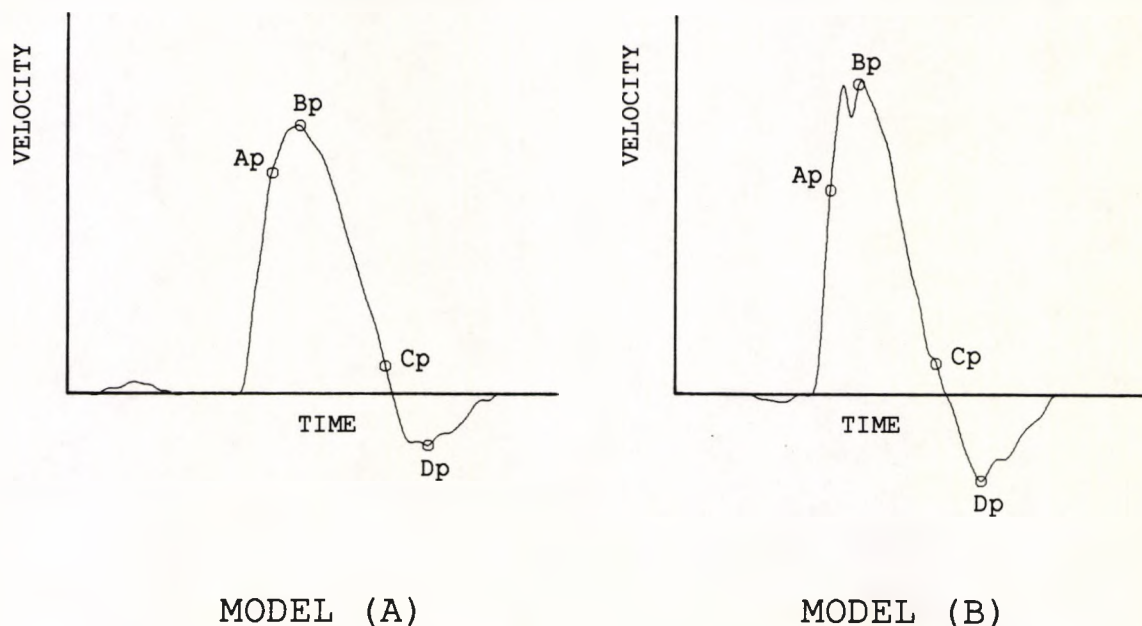


Fig. 6.5 Definition of pulse phases where numerical results are presented.

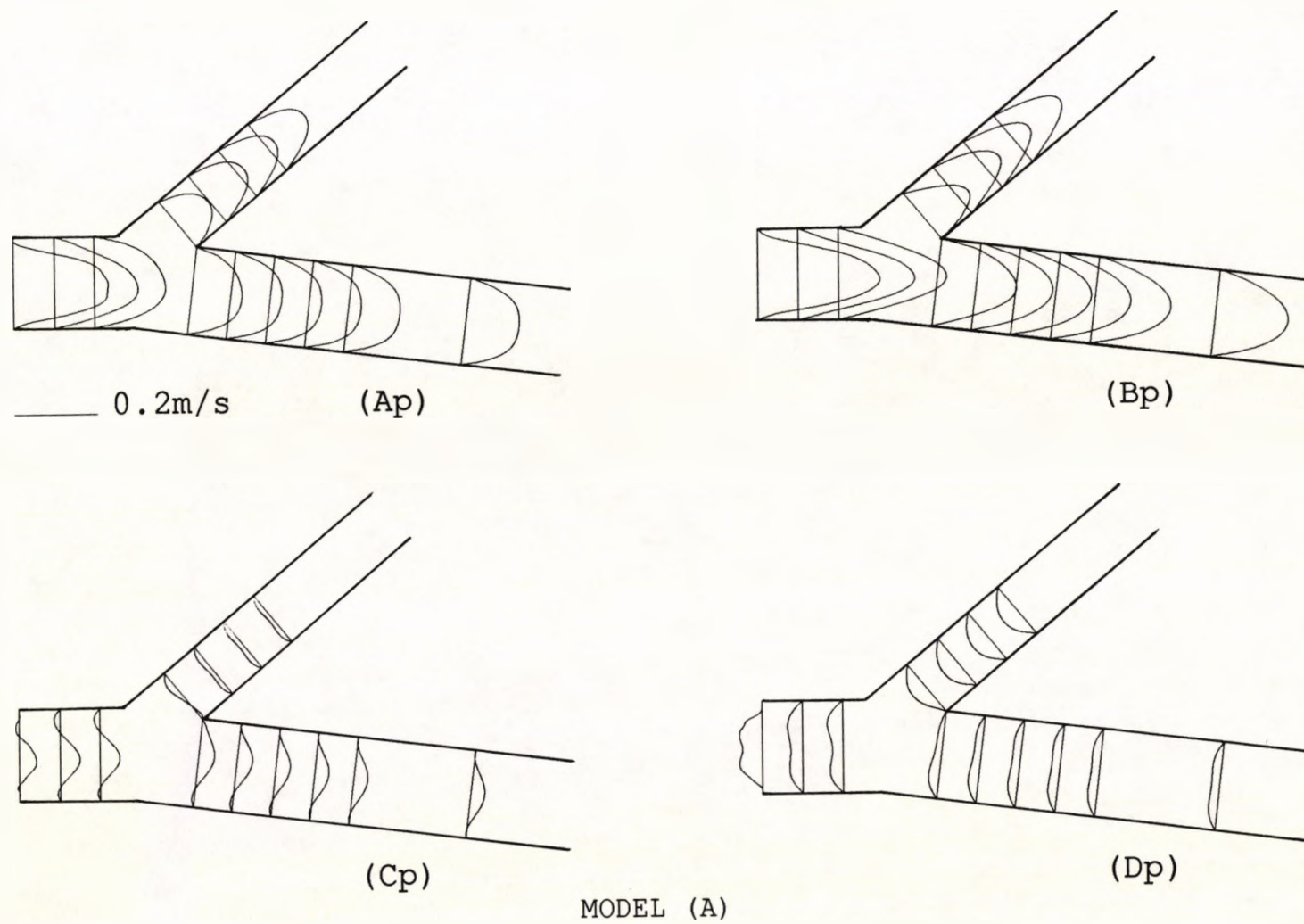


Fig. 6.6 Axial velocity profiles in the bifurcation plane of model A at four different phases Ap, Bp, Cp and Dp during a cardiac cycle.

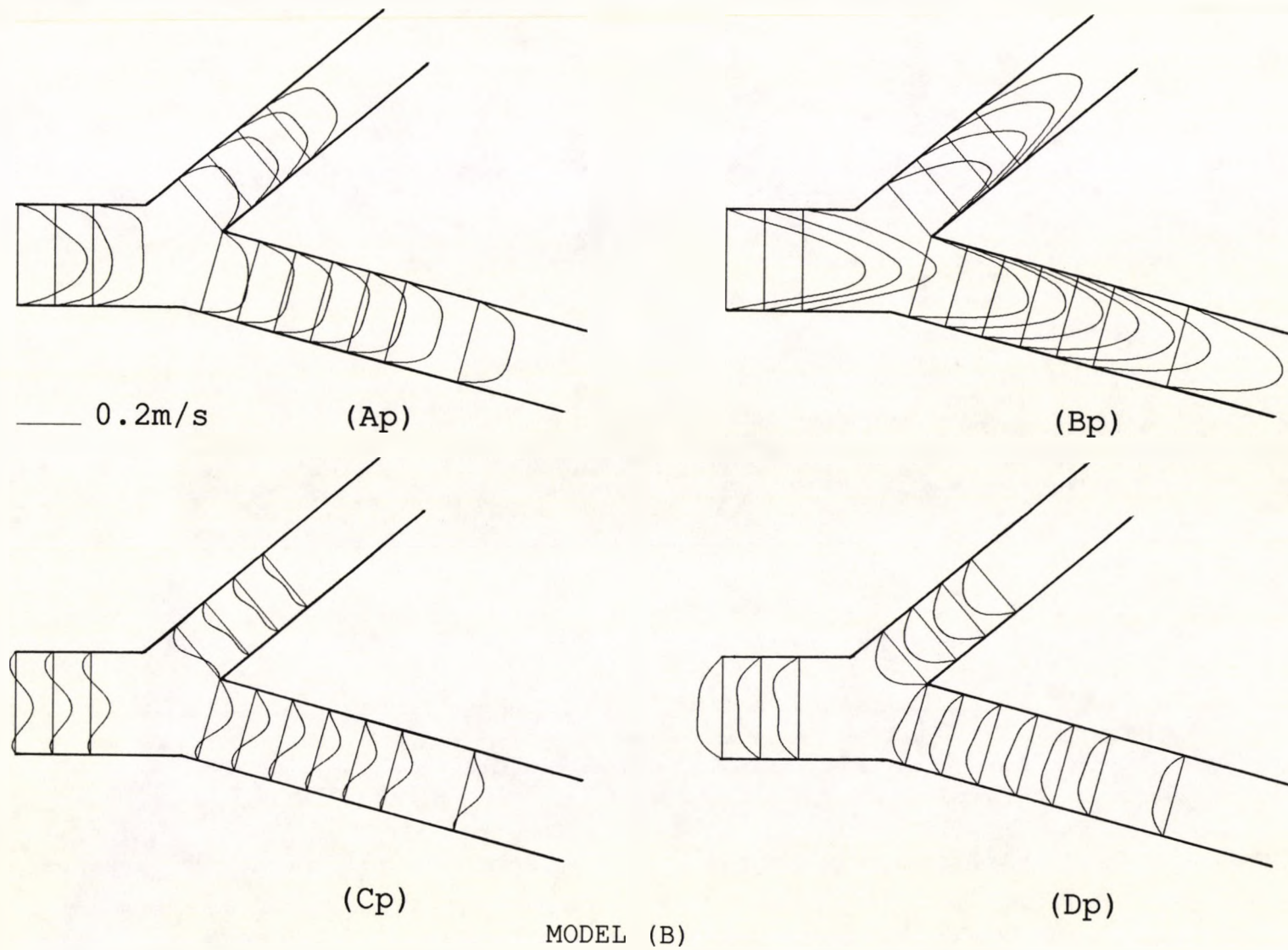
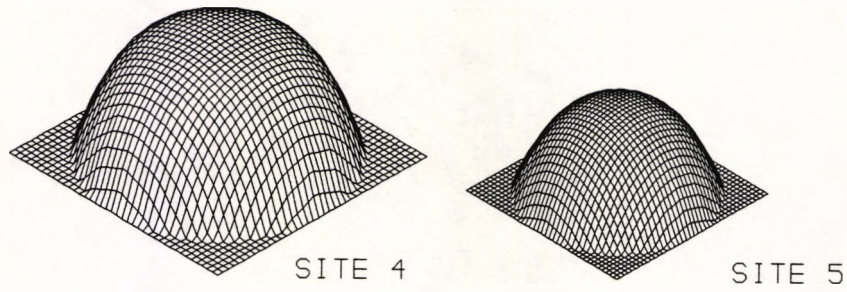
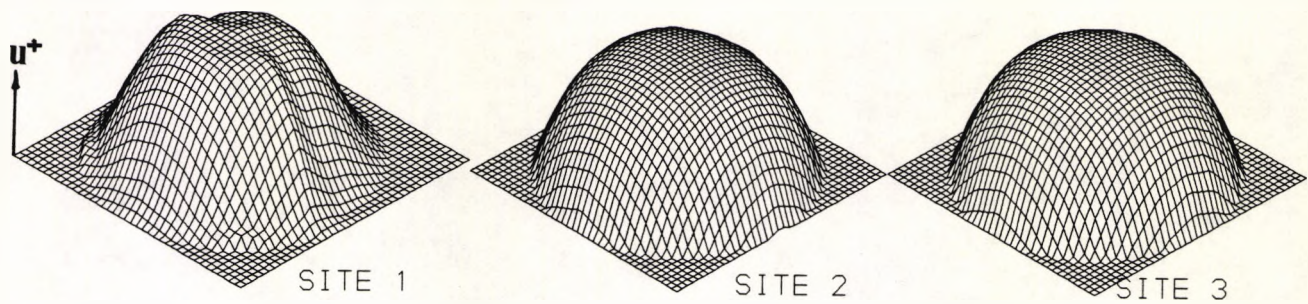
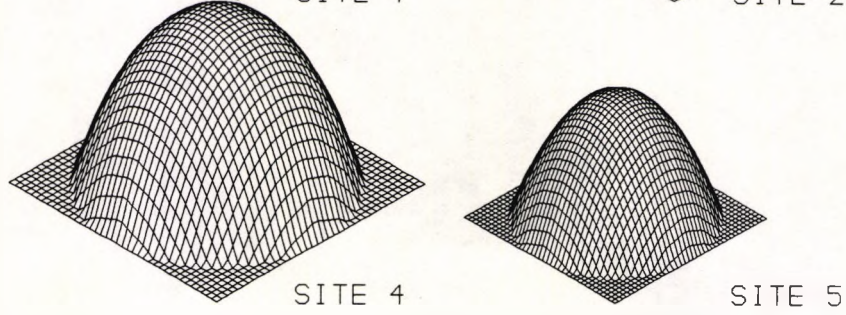
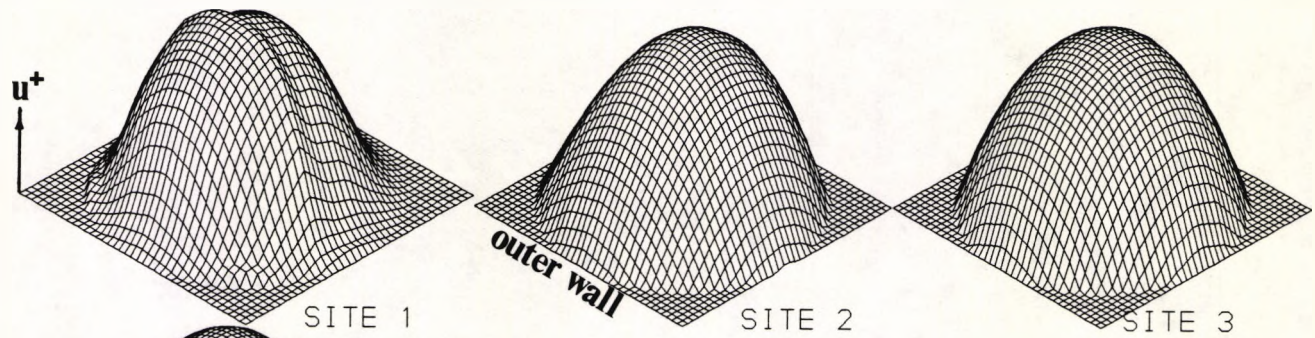


Fig. 6.7 Axial velocity profiles in the bifurcation plane of model B at four different phases Ap, Bp, Cp and Dp during a cardiac cycle.



(Ap)



(Bp)

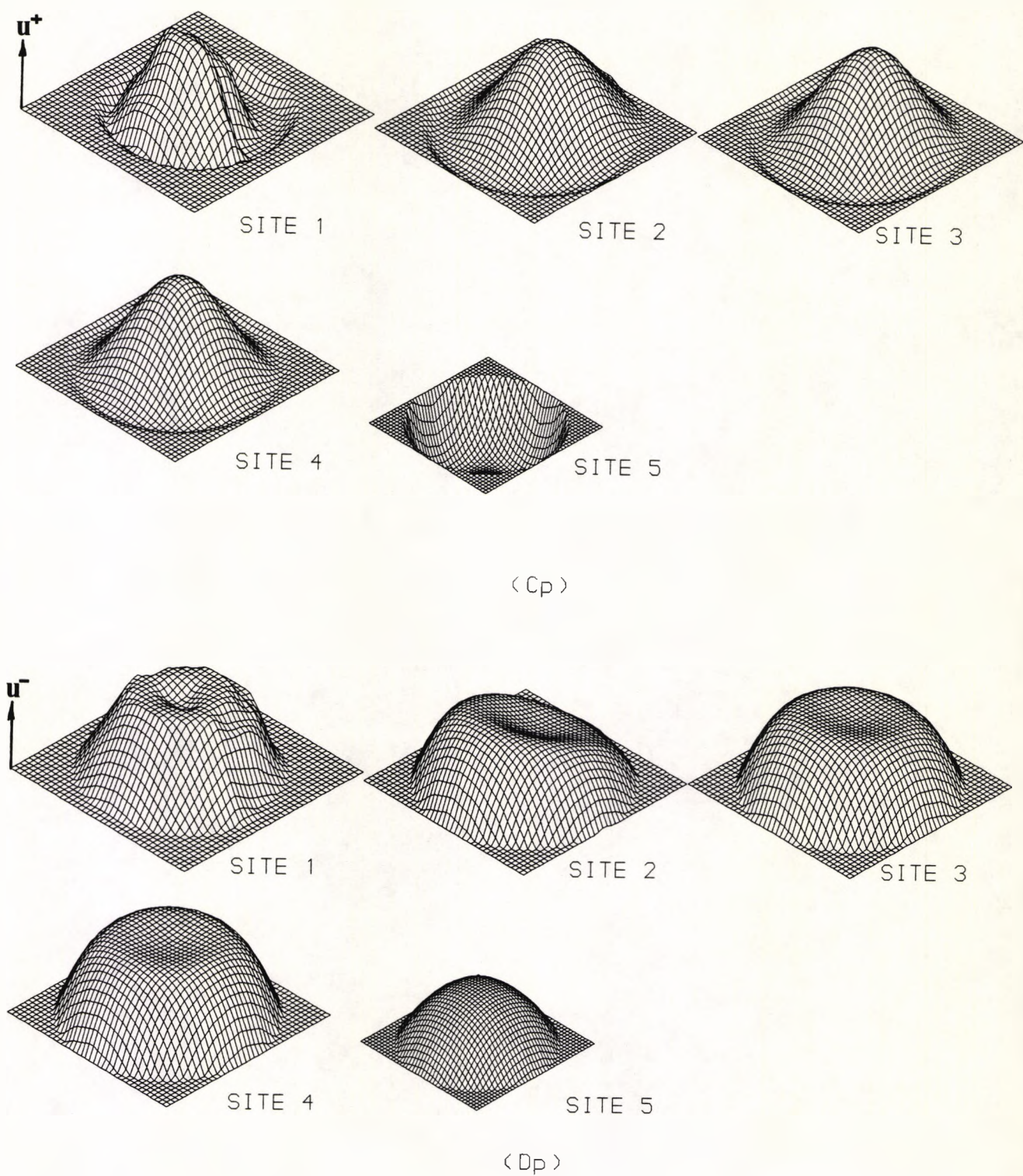
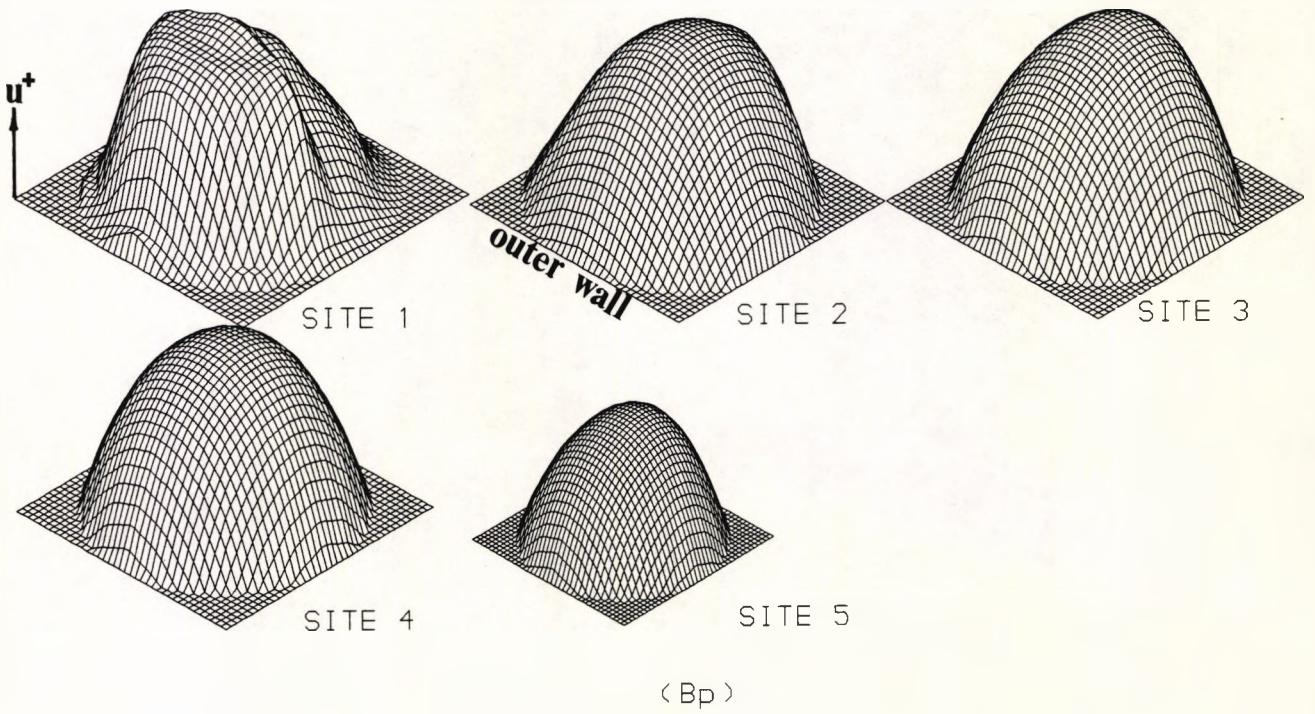
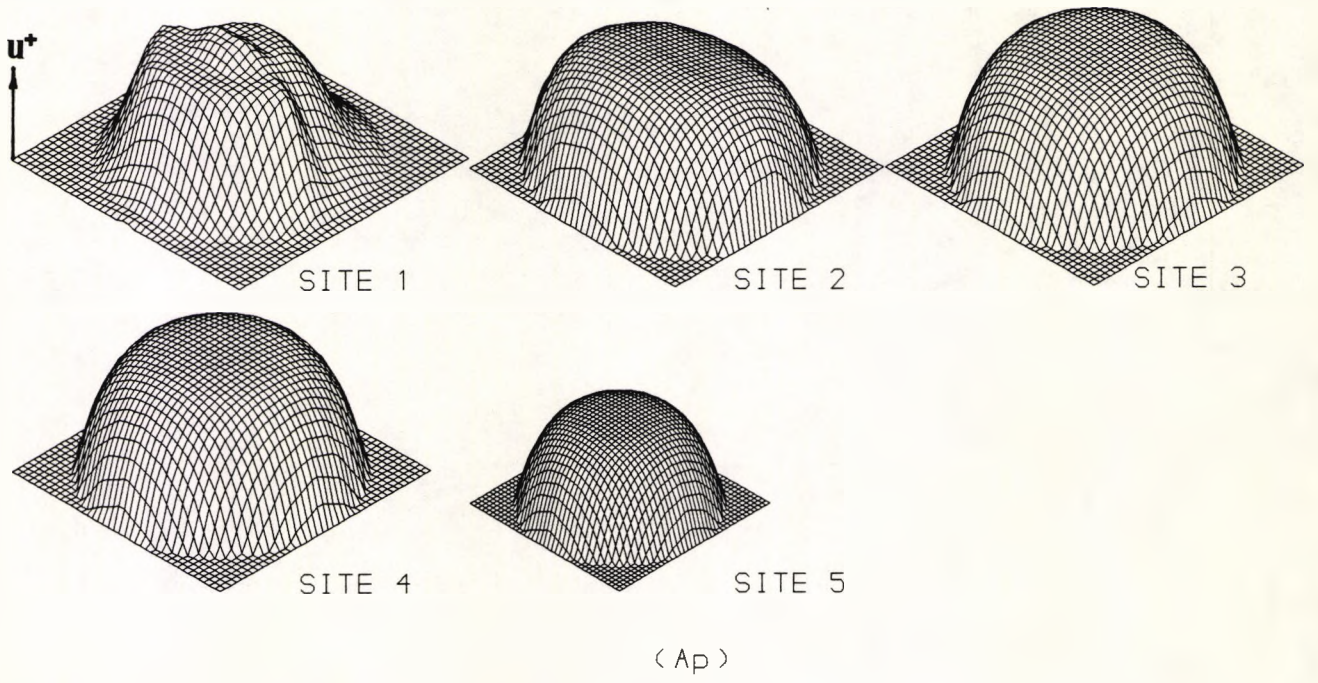


Fig. 6.8 Three-dimensional representation of axial velocity at cross-sections perpendicular to the bifurcation plane at sites 1-5 of model A during a cardiac cycle.



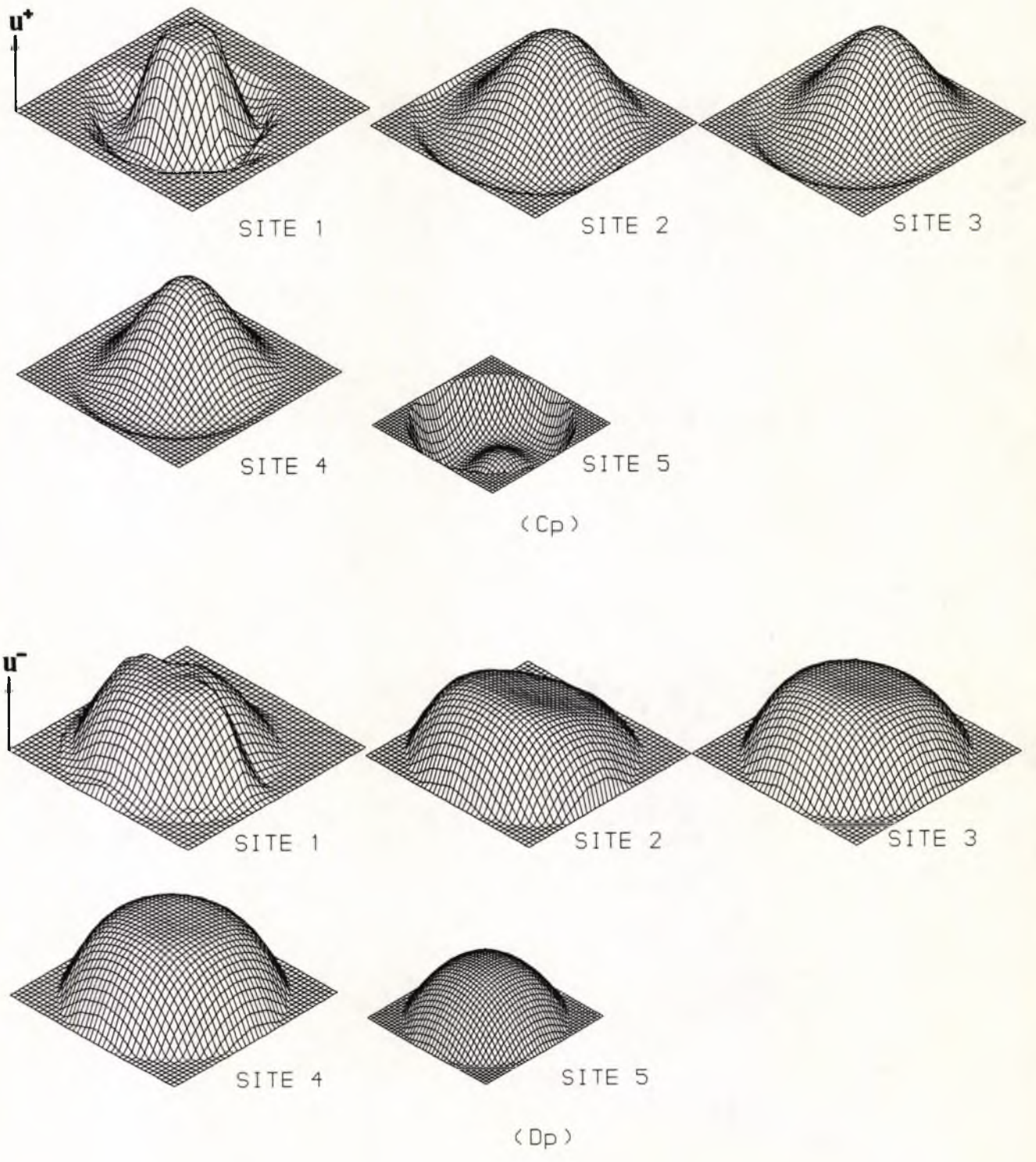


Fig. 6.9 Three-dimensional representation of axial velocity at cross-sections perpendicular to the bifurcation plane at sites 1-5 of model B during a cardiac cycle.

These plots indicate that the essential features of the flow in bifurcation models A and B are the same. In the parent vessels, velocity profiles are hardly affected by the flow branching downstream. They show a slight tendency to be skewed towards the large daughter vessel side, but otherwise rather symmetric. Reverse flow occurs during late diastole. In the two daughter vessels, velocity profiles vary with position and phase during the pulse cycle. At the level of the flow divider in the larger daughter vessels, velocity profiles are slightly deviated from the centre-line towards the non-divider side during early flow acceleration, but gradually shift back to the centre-line and shift further towards the flow divider side during flow deceleration. As the flow moves downstream, the peak velocity returns to the centre of the vessel, and near the exits velocity profiles resemble very much fully developed time-dependent long tube profiles. On the outer wall of the larger daughter vessels, flow separation is not found during flow acceleration but is noticed during late flow deceleration just before flow reversal. This suggests that in bifurcation flow regions separated flow may not always exist throughout the cycle, its presence depending largely upon some physical parameters which characterise the flow, such as Reynolds number and flow boundary conditions. This finding is consistent with previous experimental observations (Richardson and Christo et al, 1990; Cho et al, 1985). The size of this separation zone in the two models is found up to 30% of the vessel diameter extending from the outer wall on the larger daughter vessel side.

In the smaller daughter vessels, velocity profiles are rather symmetric during early flow acceleration but are soon shown to be skewed towards the flow divider side near the branching areas. During late flow deceleration, flow separation can be observed at the level of the flow divider. This separation zone occupies a maximum of 75% of the vessel diameter along the outer wall on the smaller daughter vessel side in both cases. As the flow moves downstream, however, this flow separation zone dies out rapidly and the flow is totally reversed across the vessel sections.

Near the outlets of the smaller daughter vessels, velocity profiles are fully developed.

In Figs.6.11 and 6.12 are presented secondary velocity vector fields at defined cross-sections at pulse phases of maximum positive flow A_p , decelerated flow B_p and maximum reversed flow C_p for the bifurcation models A and B respectively. The right hand side at each cross-section corresponds to the divider wall. It is seen that in the two models A and B the structure of the secondary circulation is basically the same but differs in some details. In the parent vessel at cross-section A1-A2 which is 0.2mm downstream from the entrance, secondary velocities are very small during positive flow but are relatively large and rather distorted during reverse flow. This results from the assumption of zero secondary velocity field made at the inlet. In model A where the Reynolds number is lower than that in model B, the effect of this assumption is more obvious. However, the errors introduced are shown to diminish downstream. In fact, such an approximation is analogous to the accepted procedure for a numerical experiment to test equation stability. For example, in Collins (1980), even a substantial deliberate error in axial velocity was shown rapidly to diffuse out to a negligible effect, thus demonstrating good stability in the algorithm. Nevertheless, it would be preferable to include measurements of secondary as well as axial velocities for an upstream boundary condition wherever possible.

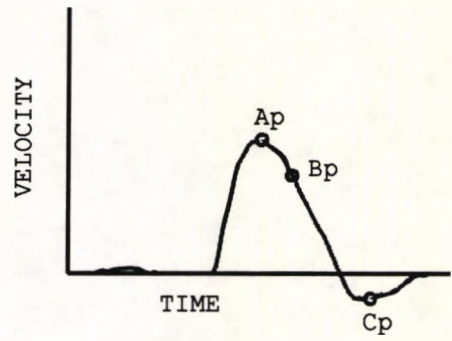
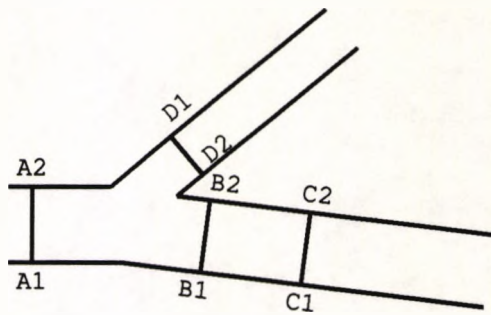
In the larger daughter vessels at cross-sections B1-B2 and C1-C2, the centrifugal force induces a secondary flow which moves in a spiral course from the divider wall to the outer wall (non divider side) along the side wall and returns back along the symmetry plane during positive flow. The secondary velocities at the level of B1-B2 are larger than those at C1-C2 in both models, but a comparison between them shows that the secondary vortices in model B are much stronger. The centre of this secondary vortex is situated near the vertical centre-line of the cross-sectional plane. It moves down towards the symmetry plane as the flow

moves downstream. In the smaller daughter vessel at cross-section D1–D2, similar secondary vortex patterns are found in model B, but no vortex motion is observed at this level in model A. During flow reversal, secondary velocities in both daughter vessels are very small.

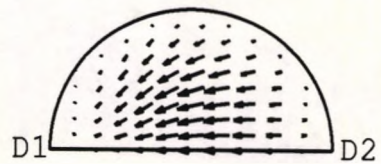
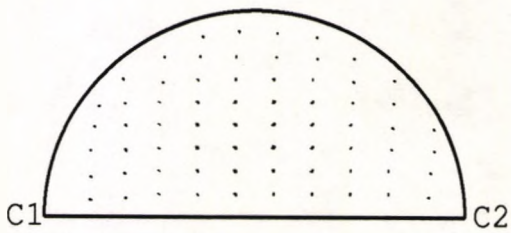
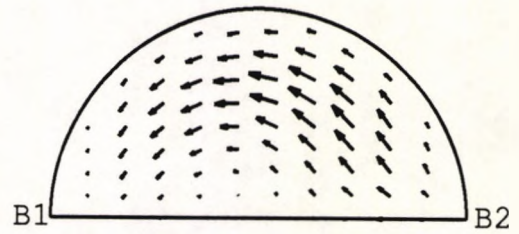
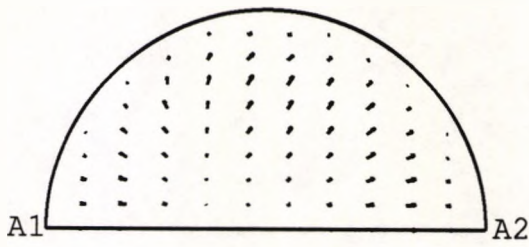
The maximum forward flow velocity, maximum reversed flow velocity and the maximum secondary flow velocity at the level of flow divider in both models A and B at defined pulse phases are summarised in Table 6.1. It shows that in the two cases studies, flow reversal and secondary motion at the level of the flow divider are more pronounced in model B, for which the secondary flow velocity at the maximum flow rate is up to 23% of the maximum axial velocity at the level of the flow divider.

		Max. forward flow velocity (m/s) U_{max}	Max. reverse flow velocity (m/s) U_{min}	Max. secondary flow velocity (m/s) V_{max}	$\left \frac{V_{max}}{U_{max}} \right $ (%)
Model A	Ap	0.1257	—	0.0045	3.6
	Bp	0.1971	—	0.0158	8.0
	Cp	0.0407	-0.0066	0.0050	12.4
	Dp	—	-0.0262	0.0006	2.3
Model B	Ap	0.1219	—	0.0235	19.3
	Bp	0.3410	-0.0127	0.0718	22.9
	Cp	0.0654	-0.0564	0.0125	19.1
	Dp	—	—	0.0053	9.4

Table 6.1 Maximum forward flow velocity, maximum reversed flow velocity and maximum secondary flow velocity at the level of flow divider in models A and B during a cardiac cycle.



MODEL (A)



— 0.02m/s

(Ap)

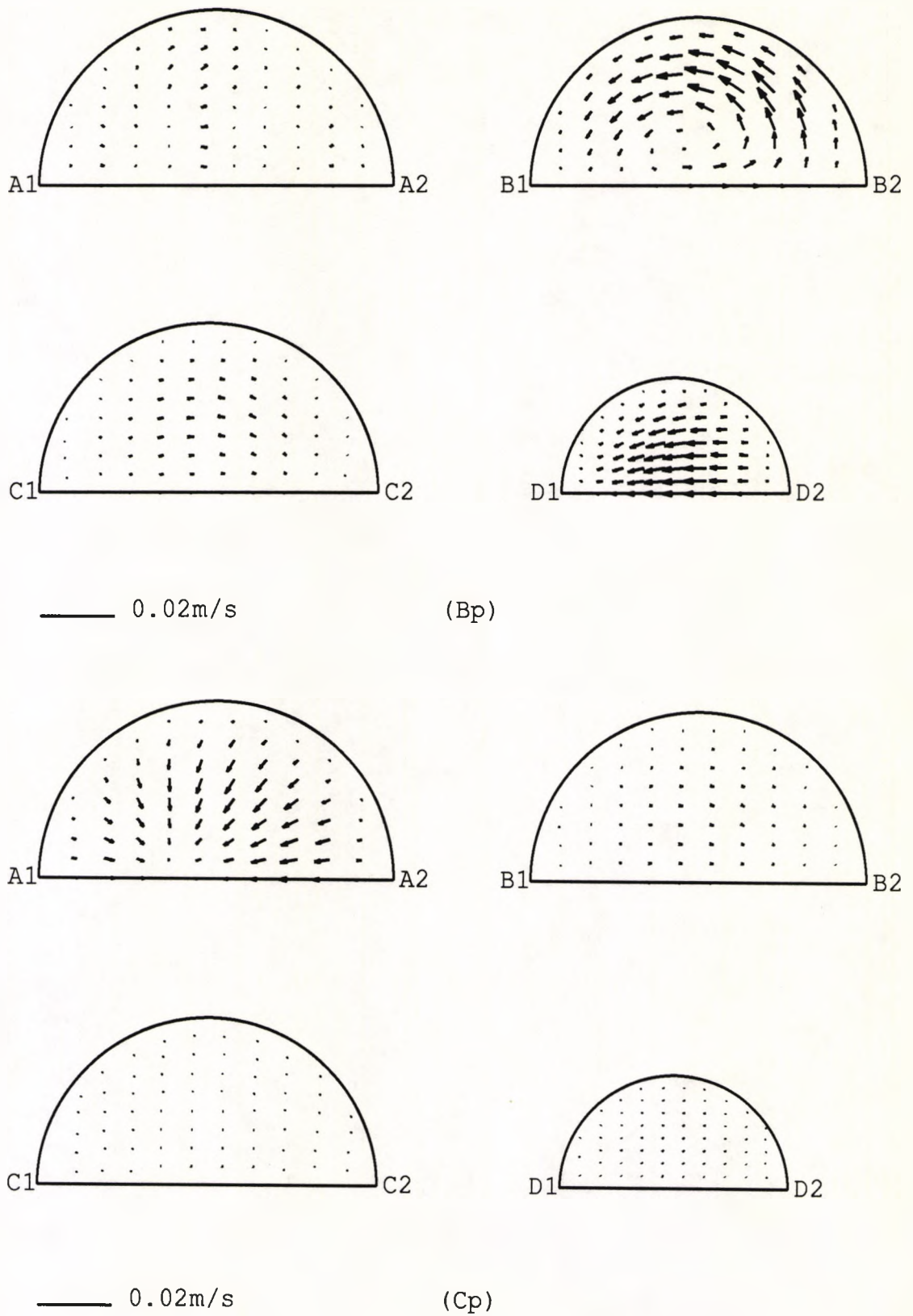
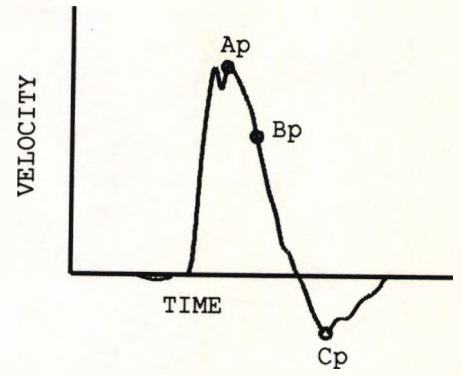
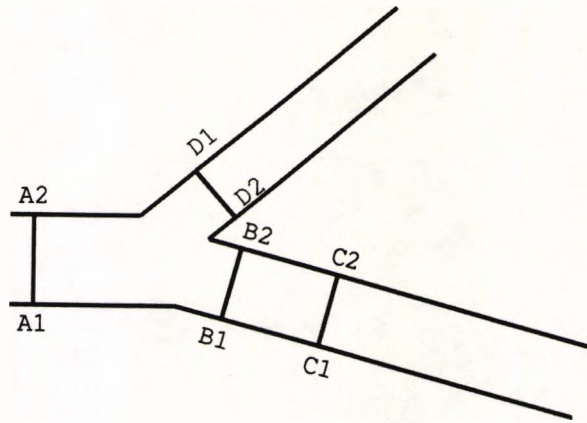
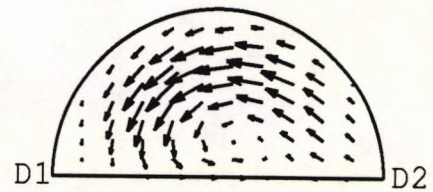
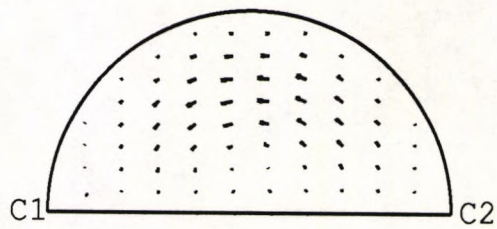
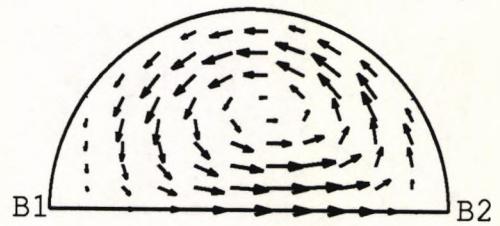
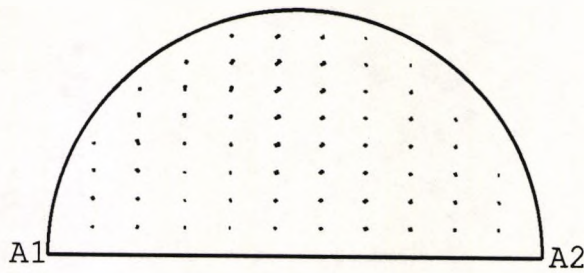


Fig. 6.10 Secondary velocity vector field at different cross-sections of bifurcation model A during a cardiac cycle.

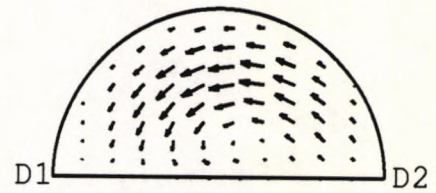
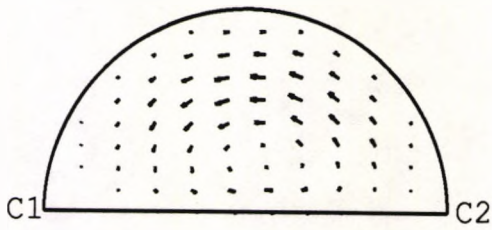
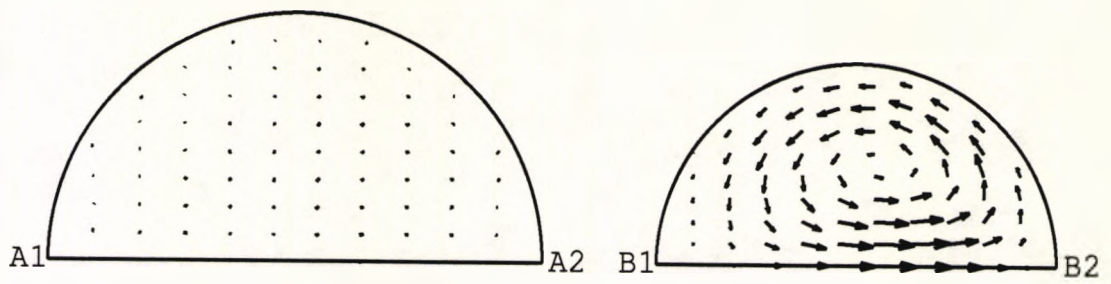


MODEL (B)

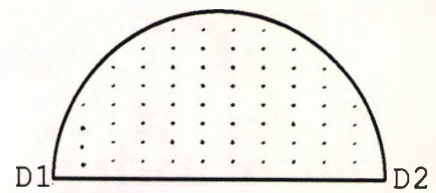
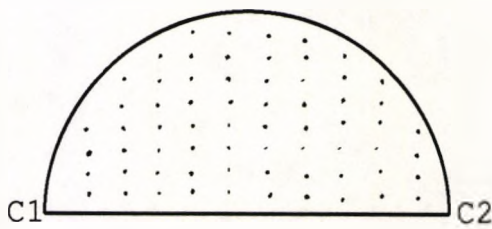
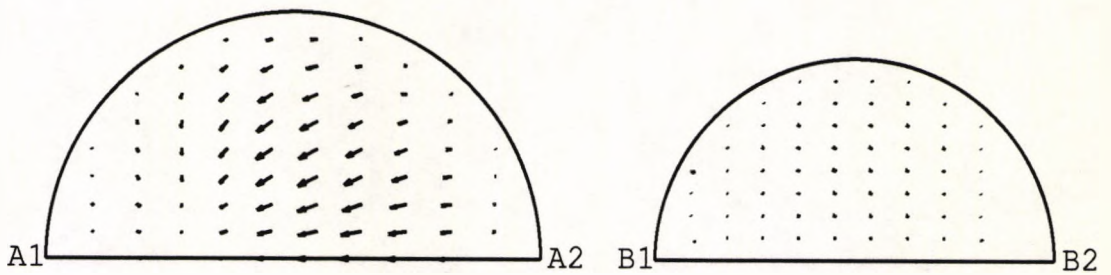


— 0.05m/s

(Ap)



— 0.05m/s (Bp)



— 0.05m/s (Cp)

Fig. 6.11 Secondary velocity vector field at different cross-sections of bifurcation model B during a cardiac cycle.

6.3.2 Wall Shear Stress

Wall shear stress is presented at different locations in the parent and larger daughter vessels in both models over a cardiac cycle. As shown in Figs.6.12 and 6.13, location 1 is one diameter above the flow divider in the parent vessel; location 2, 3 and 4 are at the divider wall of the larger daughter vessel 0.5mm, 1.5mm and 2.5mm downstream of the flow divider respectively; while locations 5,6 and 7 are at the corresponding levels at the outer wall (non-divider side).

Location 1 experiences a shear stress ranging from -0.63 to $1.92 N/m^2$ in model A and -0.98 to $3.35 N/m^2$ in model B. The peak wall shear stress occurs at the systolic acceleration phase which leads that of the peak flow rate by about $0.05t_p^*$. The wall shear stress at the divider wall (locations 2-5) is relatively high. At location 2 the maximum shear stress reaches a value of $2.21 N/m^2$ in model A and $5.03 N/m^2$ in model B occurring at the flow deceleration phase which is about $0.02t_p$ behind the phase of peak flow rate. As flow moves downstream, the value of peak wall shear stress drops.

Along the outer wall (locations 5-7) of model A, the variation of wall shear stress follows the pattern found at location 1, but with slightly reduced values. Flow separation in this model does not occur until late flow deceleration just before flow reversal. At location 5, the minimum wall shear stress is $-0.47 N/m^2$ and the time averaged mean value over the entire cycle is $0.21 N/m^2$. The outer wall of model B exhibits more reversals of wall shear stress. At location 5, the wall shear stress reaches a value of $2.92 N/m^2$ at the systolic acceleration phase, then falls and begins to shift in the negative direction at the middle of flow deceleration ($t=0.54t_p$), indicating the beginning of flow separation. Here, the minimum wall shear stress is $-0.89 N/m^2$ and the time averaged mean value is $0.20 N/m^2$. As

flow moves downstream, the value of wall shear stress rises.

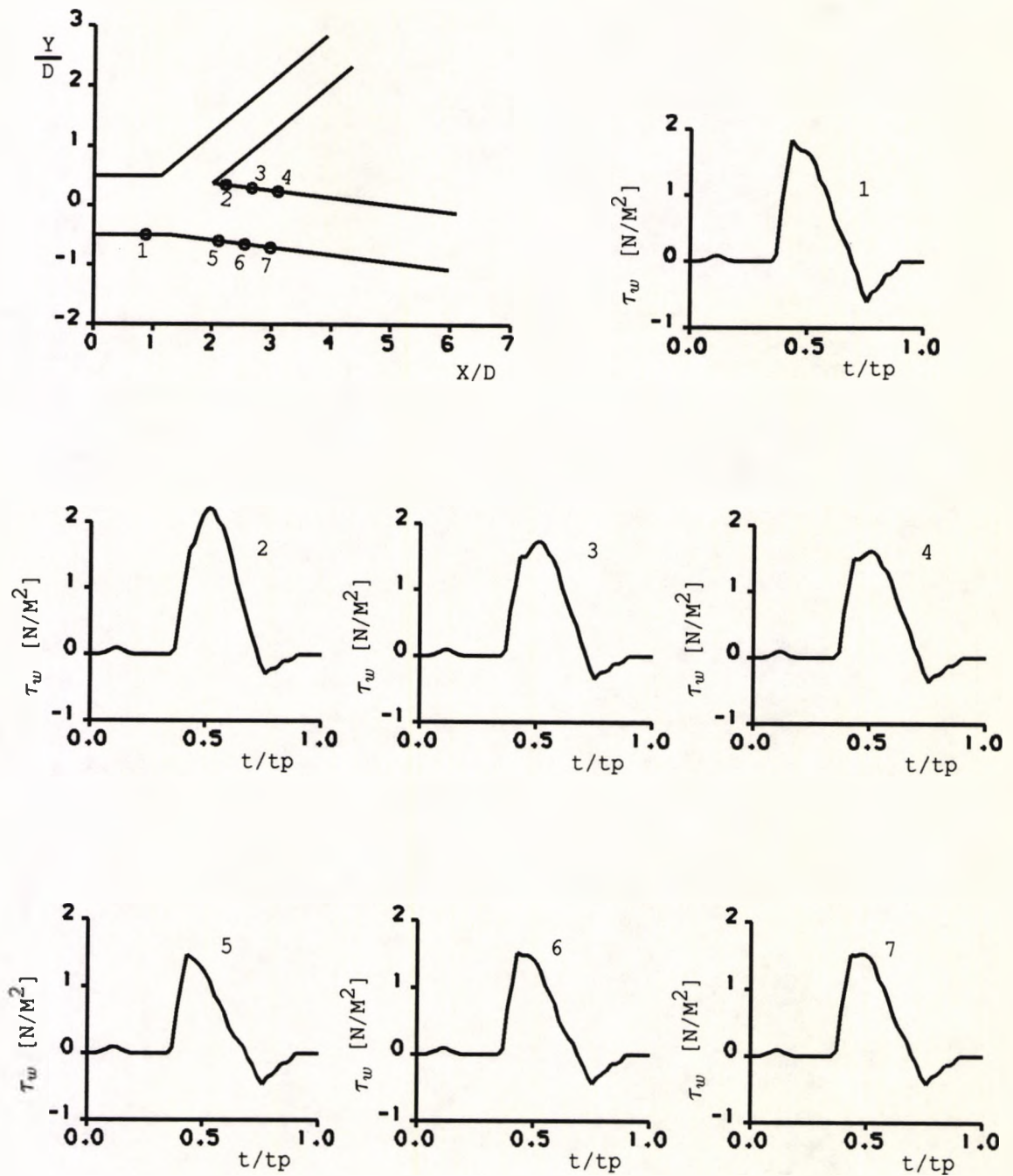


Fig. 6.12 Wall shear stress vs phase at selected sites in model A.

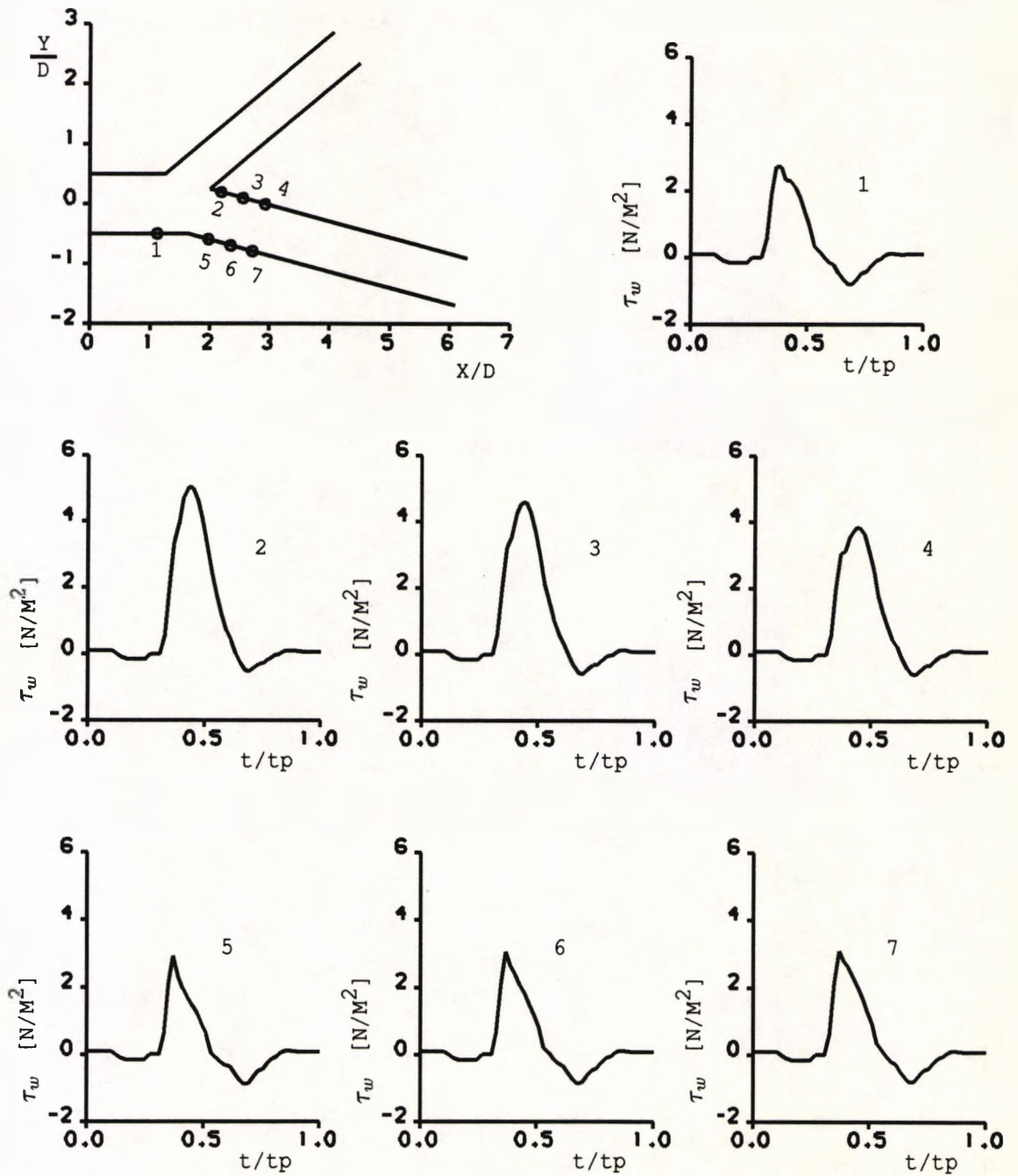


Fig. 6.13 Wall shear stress vs phase at selected sites in model B.

The maximum, minimum and the time averaged wall shear stresses at locations 1–7 in both models are listed in Table 6.2 in a later section where these values are compared with those obtained from a non-Newtonian model for the blood.

Fig.6.14 shows the shear stress along the parent–larger daughter outer wall (ooo) and the larger daughter divider wall (xxx) of model B at specified pulse phases. At the peak flow rate, the shear stress along the outer wall drops as the outer corner of the bifurcation approaches indicating a tendency of flow separation. Along the divider wall relatively high shear stress occurs with the maximum value appearing immediately after the flow divider. It then falls gradually until coinciding with the shear stress on the outer wall at about 3 diameters downstream from the flow divider. During flow deceleration, the wall shear stress along the outer wall becomes lower and turns to negative at $t=0.54t_p$. The minimum wall shear stress occurs at the level of the flow divider on the outer wall, while on the divider wall the wall shear stress is at its maximum. During the phase of peak flow reversal, wall shear stress along both the outer and the divider walls are low and negative suggesting a totally reversed flow in the parent and the larger daughter arteries.

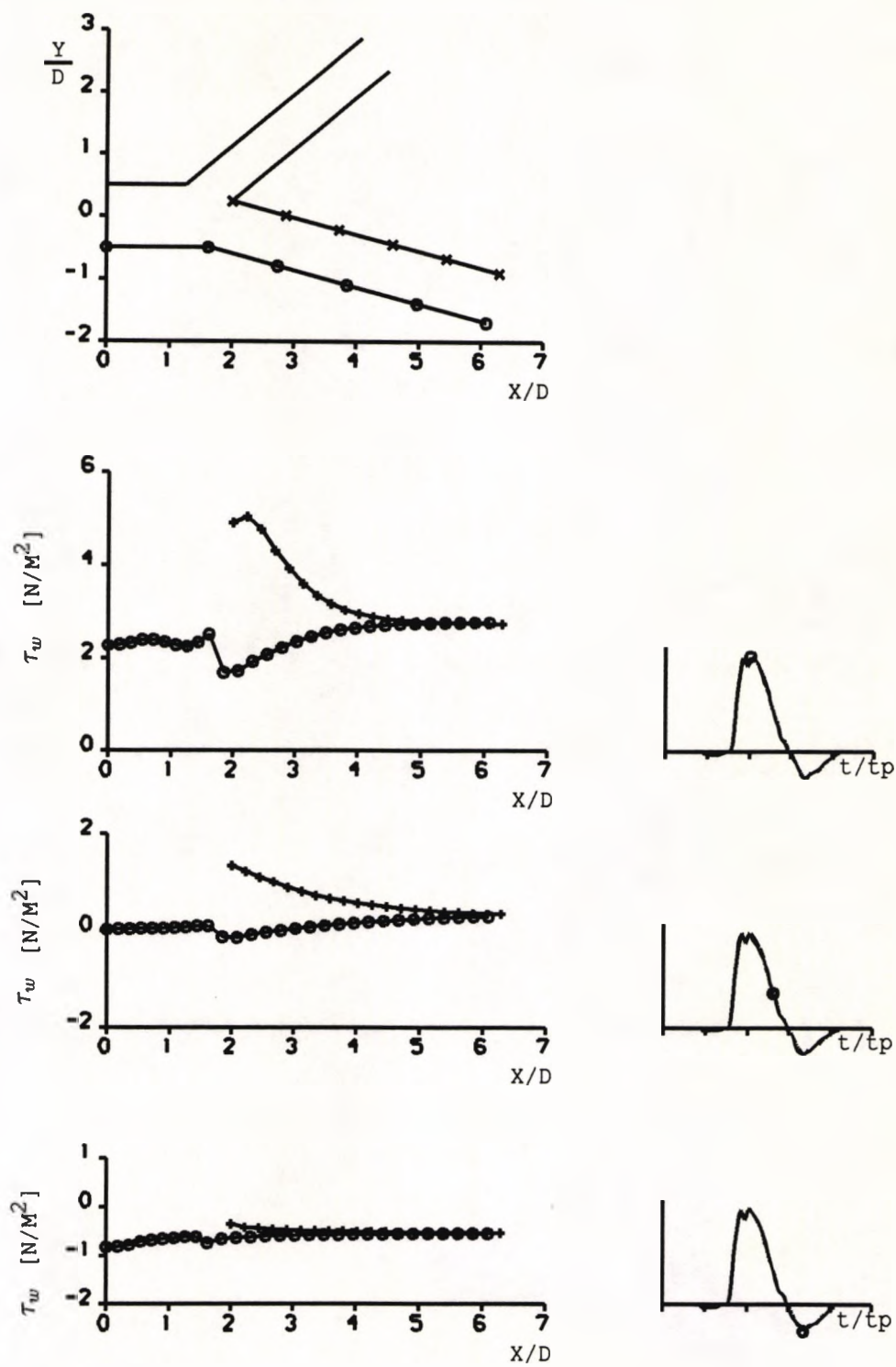


Fig. 6.14 Wall shear stress along the outer wall (ooo) and the divider wall (xxx) of model B at specified phases.

6.4 INFLUENCES OF VARIOUS FACTORS

6.4.1 Bifurcation Geometry

It is known that individual variations in the anatomy of arterial bifurcations both in human and in other mammalian species are rather astonishing. For the two canine femoral bifurcation models studies here, although the basic configuration of the two models principally agree, they differ slightly in detailed geometrical data. As seen from Fig.6.1, model A has a smaller parent vessel diameter and a smaller parent to larger daughter area ratio (1.09 for model A and 1.51 for model B), it also has a smaller parent to larger daughter angle (7° in model A and 15° in model B).

From the results of velocity field and wall shear stress presented in earlier sections, it can be observed that while the essential features of the flow are approximately the same in both models, there are at least three differences. First, the duration of reversed flow in the bifurcation outer corner area is different in the two models. As shown in Fig.6.15, the outer corner nearby area in model B experiences more flow reversals than that in model A. At location 3 in model B reversed flow occurs during approximately 40% of the entire cycle, while at the same site in model A the duration of reversed flow is about 27% of the pulse cycle. Second, as listed in Table 6.1 secondary flow is more pronounced in model B owing partially to the larger branching angle between the parent and the larger daughter vessels. Third, as a consequence of the relatively strong secondary flow, axial velocity profiles at and after the level of flow divider in model B show more skewing towards the divider wall, hence resulting in higher velocity gradient differences between outer and divider walls.

However, these differences can not be fully explained with the rather small geometrical deviation of the two models. The other fact which should not be ig-

nored is that these calculations were performed using the individual flow waveforms measured in each models. The difference in their flow waveforms must also be accounted as another reason for these.

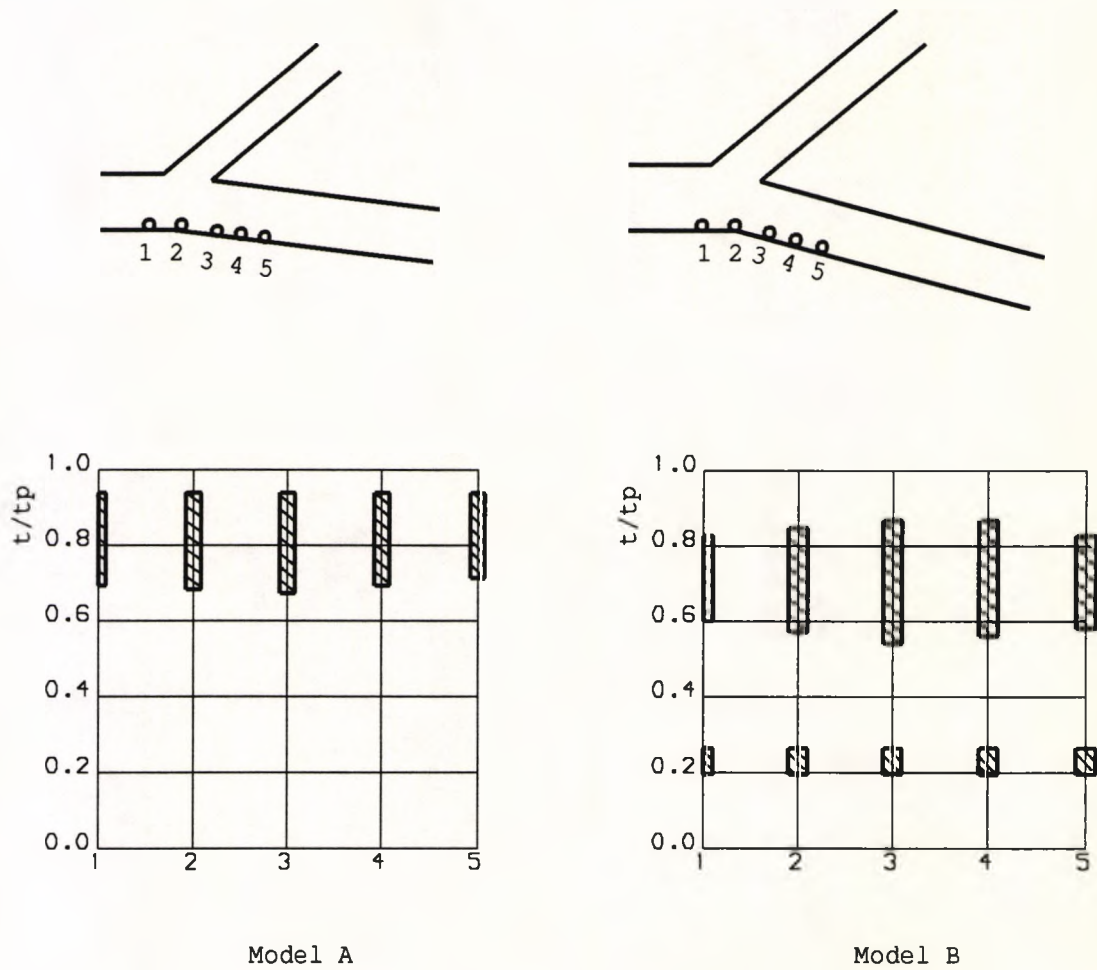


Fig. 6.15 Duration of flow reversal in the outer corner region at defined points over a cardiac cycle.

6.4.2 Upstream Flow Conditions

It was mentioned in section 6.2.2 that numerical predictions were carried out under two types of upstream flow conditions. Results presented so far have been concentrated on those obtained using the *in vivo* measured time-dependent upstream velocity profiles (type 2). It has been known that flow field and wall shear stress distribution are governed by upstream flow conditions in terms of Reynolds number, Womersley parameter and flow waveform. The effects of Reynolds number have been investigated in a T-bifurcation under steady flow conditions in last chapter. Here, the effect of flow waveform will be examined.

In Fig.6.16 dimensionless axial velocity profiles obtained using the specific *in vivo* measured flow waveform are compared with those from an averaged flow waveform in canine arteries. Due to the large amount of data involved, comparisons were only made for model A at phases of (a) flow acceleration, (b) peak flow rate and (c) maximum reversed flow. In the diagram solid lines represent results obtained from the *in vivo* measured flow waveform (type 2), open circles represent those from the averaged flow waveform (type 1). It is obvious that velocity profiles from the two different waveforms do not agree even qualitatively. Using the average flow waveform, velocity profiles are more skewed towards the divider side owing to the larger Reynolds number (about 2.8 times higher than that in the type 2). As a consequence of this, wall shear stress differences between the divider and outer walls are much greater in the case of type 1 waveform. This can be seen from Fig.6.17, where the shear stress on the divider and outer walls are compared. Since the pulse frequency and the shape of flow waveform are different, the comparison of wall shear stress is presented for the major part of flow acceleration and flow deceleration only. As shown in the figure, the peak wall shear stress on the divider wall is significantly higher, while the minimum shear stress on the outer wall is much lower when the type 1 upstream flow condition is employed. Therefore, to

obtain the exact information on flow field and wall shear stress existing in various branching ^arteries, individual flow waveform has to be used.

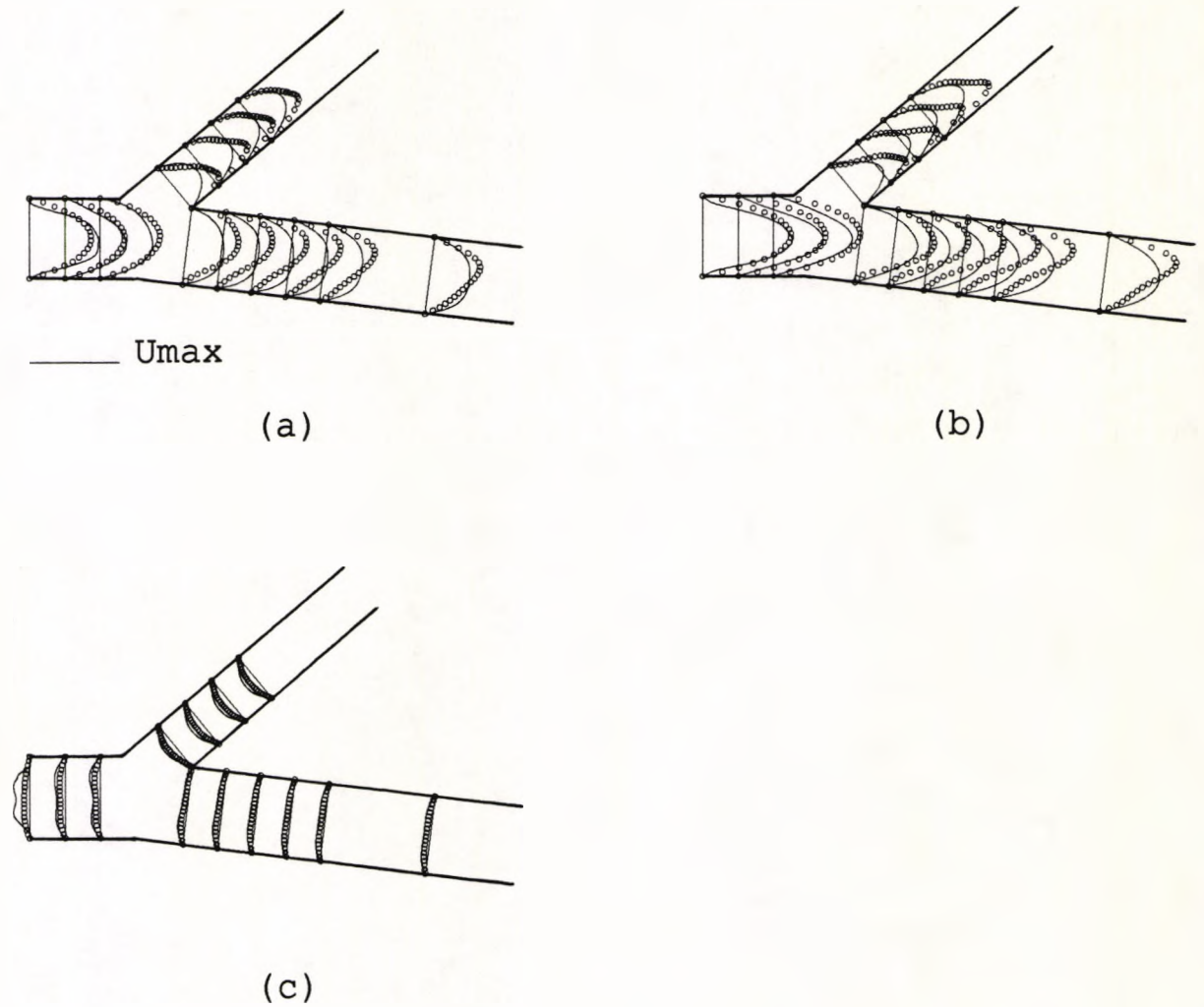
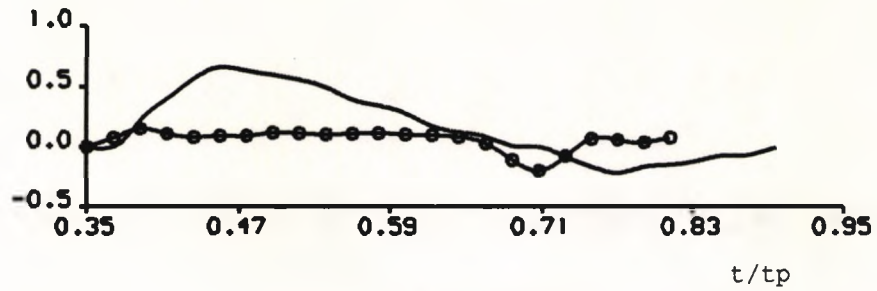
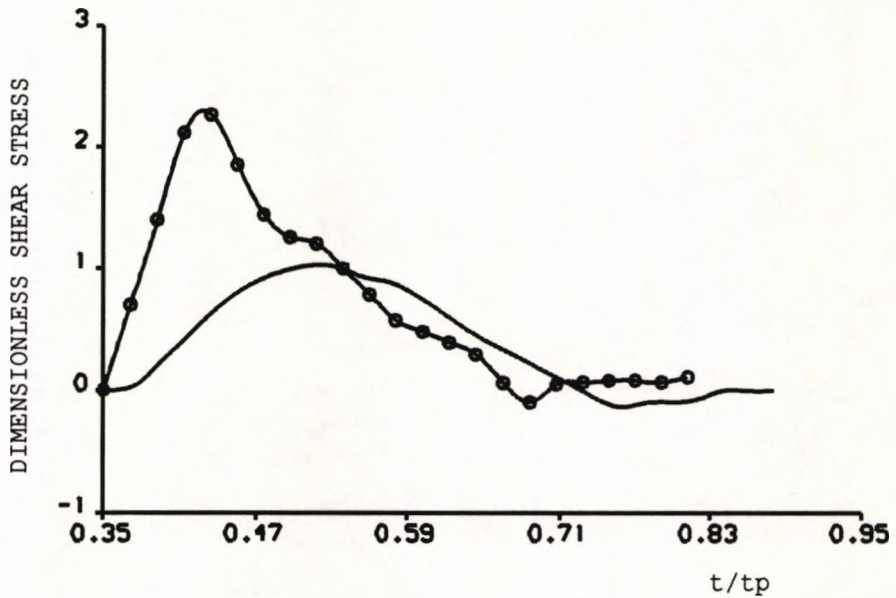


Fig. 6.16 Comparison of axial velocity profiles in the bifurcation plane of model A between type 1 (o o o) and type 2 (—) upstream flow conditions.

(U_{max} is the maximum axial velocity at the inlet.)



(a) OUTER WALL



(b) DIVIDER WALL

MODEL A

Fig. 6.17 Comparison of time varying wall shear stress between type 1 (o o o) and type 2 (—) upstream flow conditions.

(Wall shear stress was non-dimensionalised with respect to the wall shear stress of the fully developed flow at the inlet.)

6.4.3 Non-Newtonian Viscosity

In order to investigate quantitatively the non-Newtonian effects on the velocity profiles and the distribution of wall shear stress, calculations were performed with both Newtonian and non-Newtonian assumptions for the blood under the same pulsatile flow condition (*in vivo* measured upstream velocity profiles) for each bifurcation model. In the non-Newtonian case a general power law expression, $\tau = 0.042\dot{\gamma}^{0.61}$, was used (see section 4.3 for detail). In Figs.6.18 and 6.19 calculated axial velocity profiles of a Newtonian fluid are compared with those of a non-Newtonian fluid for models A and B respectively. The Newtonian velocity profiles are drawn with solid lines and those of the non-Newtonian with open circles. The comparisons show rather minor differences. In general, the velocity profiles are blunted in the non-Newtonian case due to the shear thinning behaviour of the blood. This flow phenomenon has been demonstrated by others (Moravec and Liepsch, 1983; Perktold et al, 1991). The maximum difference in axial velocity obtained is $0.026m/s$ in model A and $0.076m/s$ in model B.

Since the variation of wall shear stress is of special interest in atherogenesis, comparisons of wall shear stress between the Newtonian and the non-Newtonian fluid were made. Figs.6.20 and 6.21 show the comparisons at pulse phases of (a) flow acceleration, (b) peak flow rate, (c) flow deceleration and (d) maximum reversed flow for models A and B respectively. Solid lines represent the wall shear stress of the Newtonian fluid and circles represent that of the non-Newtonian. Surprisingly, the influence of non-Newtonian viscosity is rather different in these two cases. In model A, the positive wall shear stress is slightly higher and the negative wall shear stress is lower in the non-Newtonian case. Whereas in model B, the peak wall shear stress is reduced in a relatively large proportion with the non-Newtonian fluid. The maximum, minimum and time averaged shear stress at locations 1-7 in both models over a entire cycle are summarised in Table 6.2. It

is observed that for the non-Newtonian fluid the time averaged wall shear stress is up to 10% higher in model A but 26% lower in model B, the largest difference occurring at location 2 in model B.

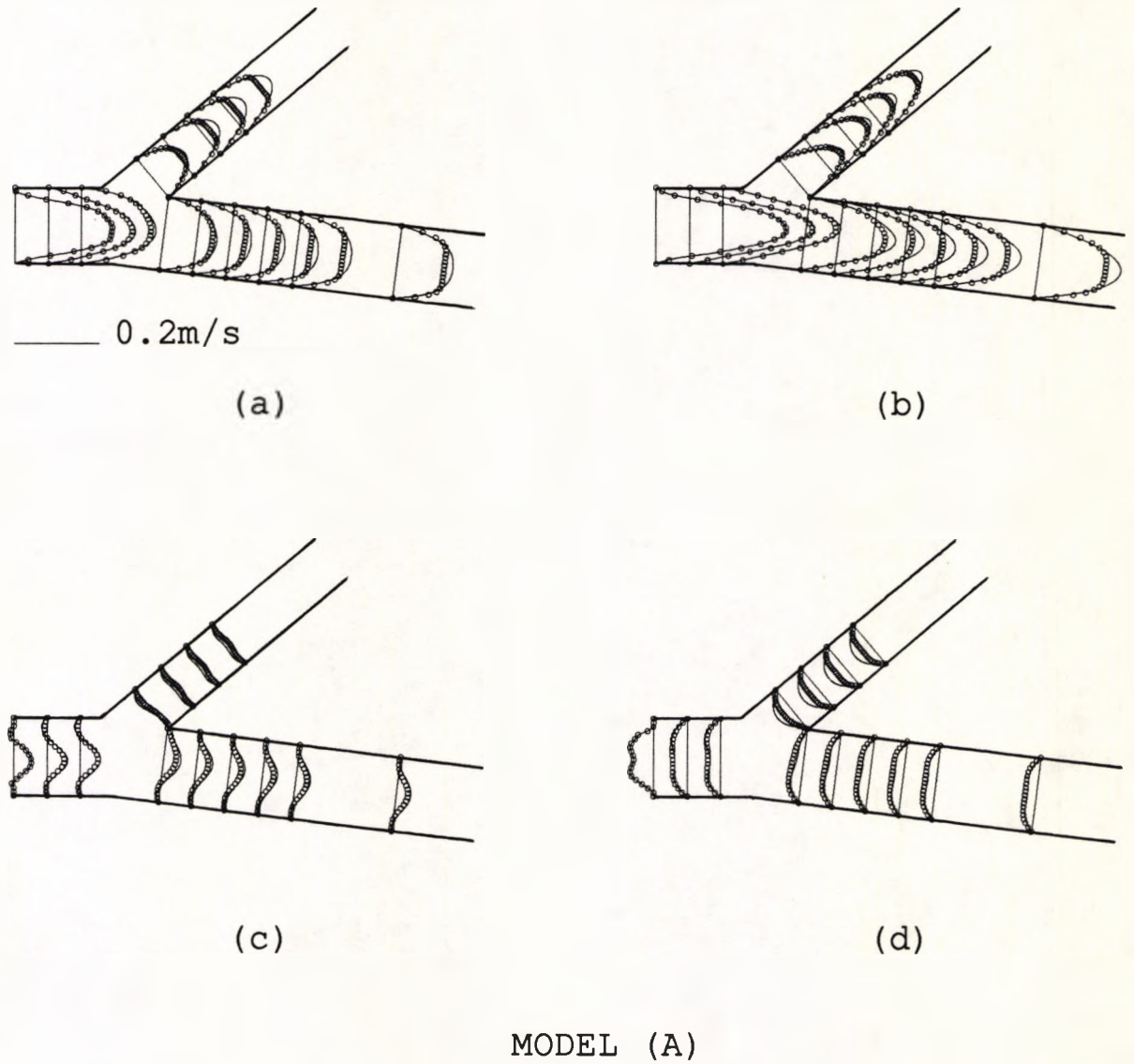
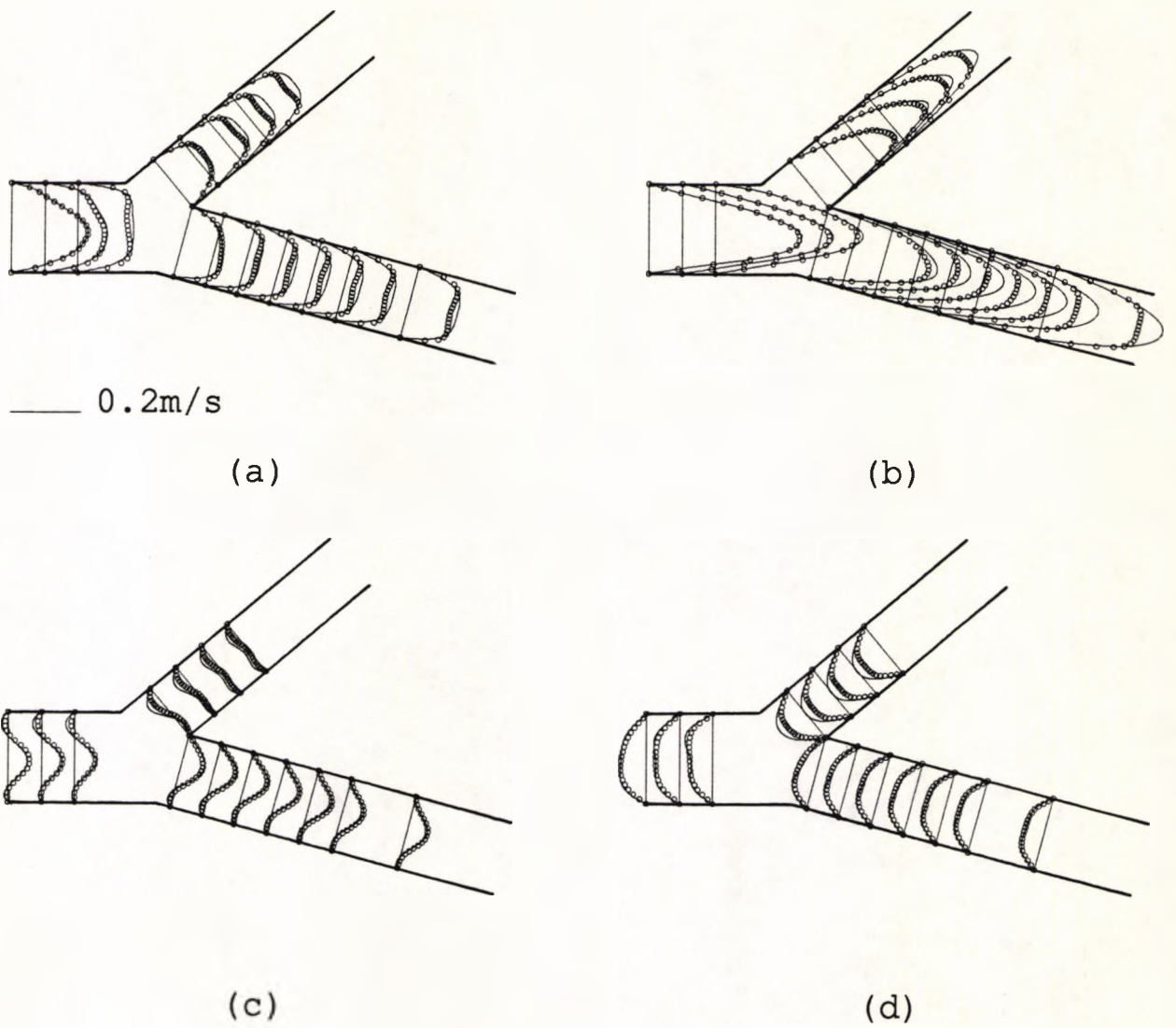


Fig. 6.18 Comparison of axial velocity profiles in the bifurcation plane of model A between Newtonian (—) and non-Newtonian (o o o) fluid.



MODEL (B)

Fig. 6.19 Comparison of axial velocity profiles in the bifurcation plane of model B between Newtonian (—) and non-Newtonian (ooo) fluid.

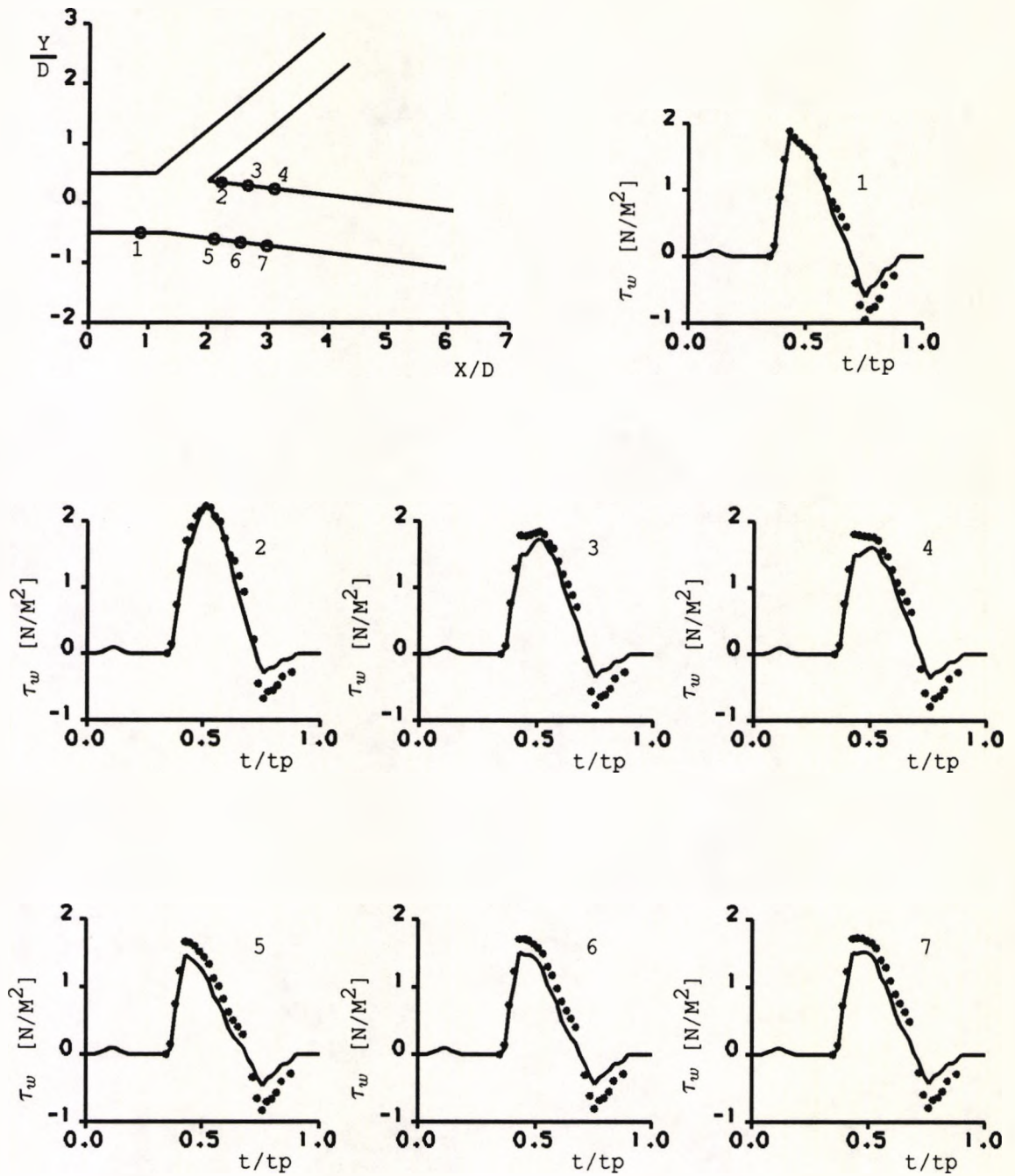


Fig. 6.20 Comparison of time varying wall shear stress between Newtonian (—) and non-Newtonian (•••) fluid at selected sites in model A.

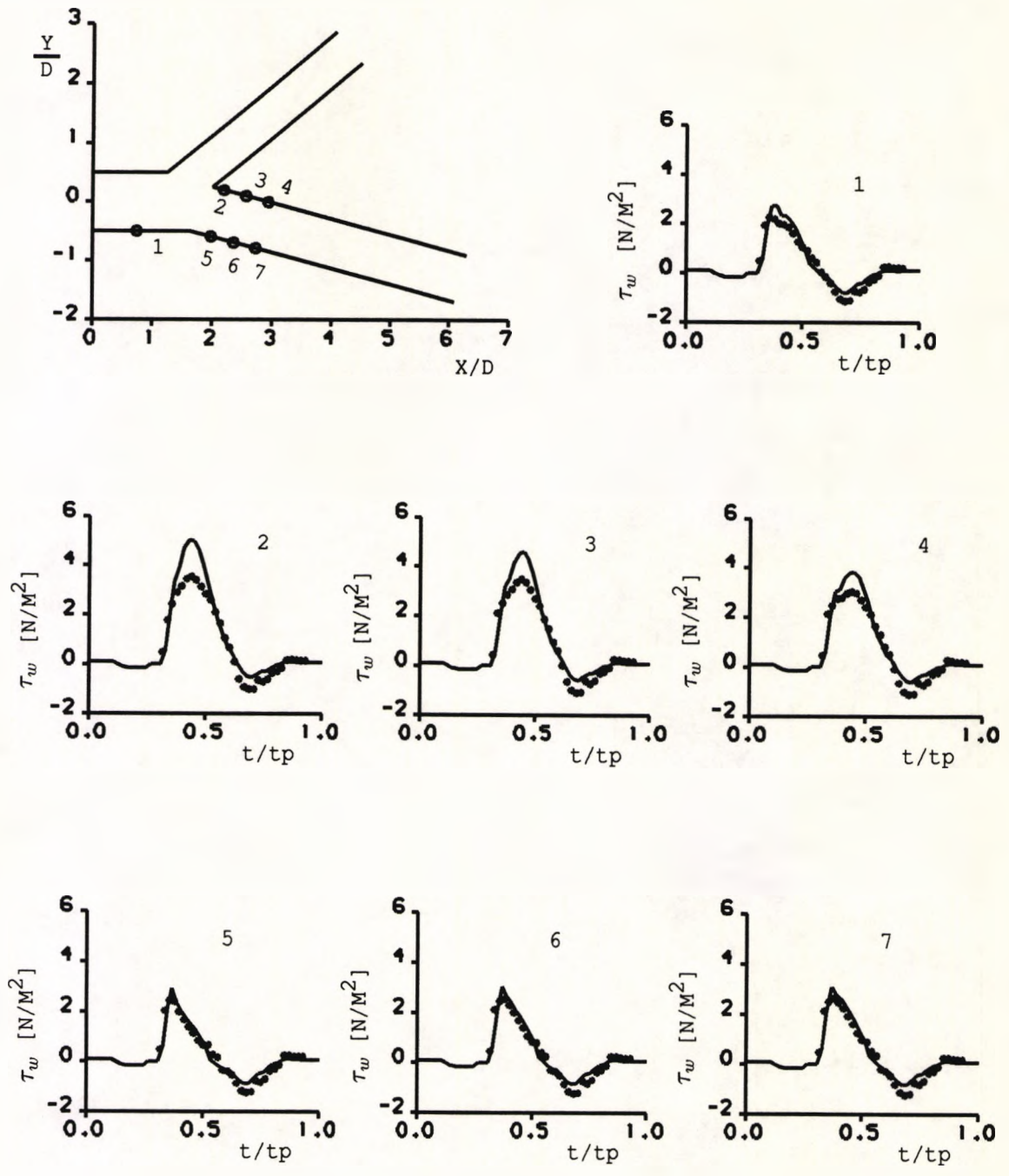


Fig. 6.21 Comparison of time varying wall shear stress between Newtonian (—) and non-Newtonian (•••) fluid at selected sites in model B.

locations	Maximum τ_w (N/m ²)		Minimum τ_w (N/m ²)		Time-averaged (N/m ²)	
	Newtonian	non-Newtonian	Newtonian	non-Newtonian	Newtonian	non-Newtonian
1(P)	1.92	1.97	-0.63	-0.99	0.29	0.29
2(D)	2.21	2.23	-0.30	-0.67	0.45	0.46
3(D)	1.74	1.85	-0.35	-0.77	0.36	0.37
4(D)	1.61	1.81	-0.37	-0.79	0.33	0.34
5(O)	1.47	1.67	-0.47	-0.83	0.21	0.24
6(O)	1.51	1.71	-0.45	-0.80	0.25	0.28
7(O)	1.52	1.73	-0.42	-0.79	0.27	0.31

(a) Model A

locations	Maximum τ_w (N/m ²)		Minimum τ_w (N/m ²)		Time-averaged (N/m ²)	
	Newtonian	non-Newtonian	Newtonian	non-Newtonian	Newtonian	non-Newtonian
1(P)	3.35	2.76	-0.98	-1.38	0.30	0.25
2(D)	5.03	3.54	-0.53	-1.01	0.83	0.61
3(D)	4.59	3.48	-0.59	-1.09	0.74	0.59
4(D)	3.83	3.03	-0.61	-1.11	0.63	0.52
5(O)	2.92	2.44	-0.89	-1.24	0.20	0.17
6(O)	3.06	2.56	-0.86	-1.24	0.27	0.22
7(O)	3.10	2.64	-0.82	-1.23	0.31	0.26

(b) Model B

- * P: parent vessel
- D: divider wall
- O: outer wall

Table 6.2 Comparison of Newtonian and non-Newtonian flow: Maximum, minimum and time-averaged wall shear stress at selected locations in models A and B over a cardiac cycle.

The somewhat opposite effects of the non-Newtonian behaviour on the wall shear stress in the two models indicate that the non-Newtonian effects are very sensitive to the flow conditions (e.g. Reynolds number) being studied. In the two models investigated here, although the time averaged Reynolds numbers do not differ greatly, the peak Reynolds numbers do (172 for model A, 304 for model B). Previous numerical studies (Appendix F, publication 6) have demonstrated that when the non-Newtonian characteristics of the blood are taken into account, the average value of wall shear stress tends to increase at low Reynolds numbers but decrease at high Reynolds numbers. Therefore, the effects of non-Newtonian viscosity on the distribution of wall shear stress can not be generalised. They must be investigated under individual flow conditions.

6.5 COMPARISON WITH IN VIVO MEASUREMENTS

To verify the computational results, quantitative comparisons between the calculations and the *in vivo* measurements were made. The predictive data used in the comparisons were those obtained from the simulation scheme (iii), i.e., under the *in vivo* measured upstream flow condition with a non-Newtonian model for the blood. When making a comparison like this, there are several aspects which must be taken into account.

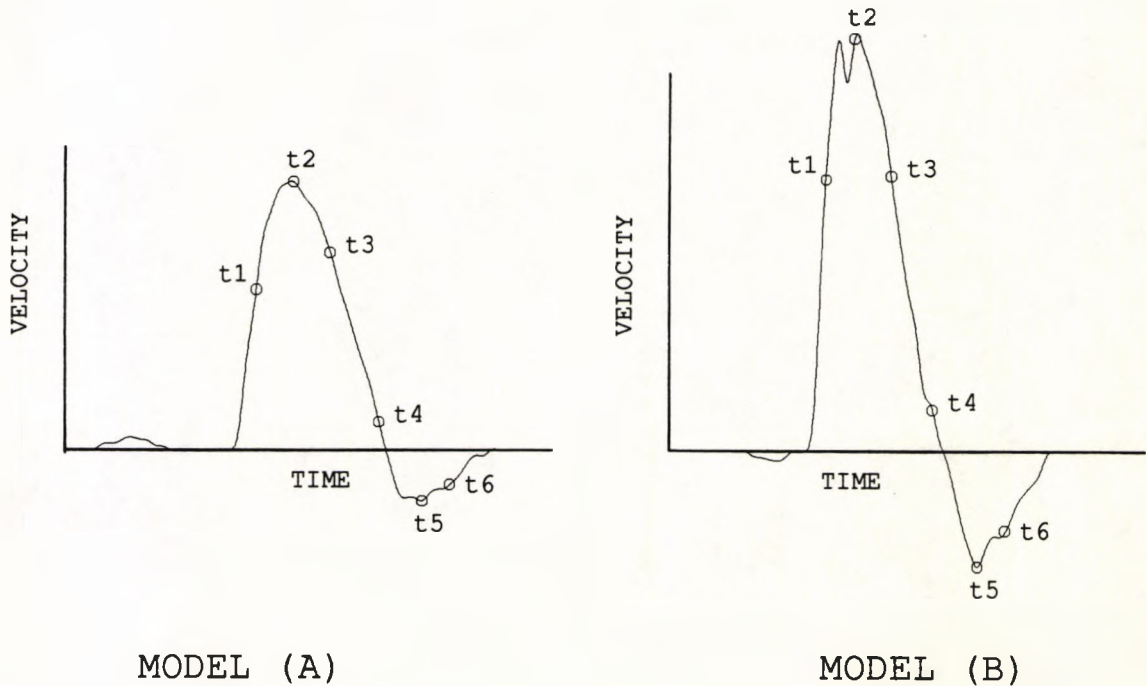
First of all, the arterial wall was treated as rigid in the predictions whereas blood vessels are viscoelastic. Although the deformable nature of the vessel is well known to be important in wave reflection and propagation, its effects on local velocity profiles are still unclear. Most of the previous studies tend to regard this as a “secondary” effect. However, recent experimental investigations (Ku and Liepsch, 1986) have found that the vessel wall compliance might have a significant effect on local bifurcation flows, especially when it is coupled with the non-Newtonian character of the blood.

Secondly, the measurements were performed by using the Doppler ultrasound device which measures the velocity components in the direction of beam (at an angle of 60° to the vessel axis), but calculates the velocity as though it is parallel to the vessel axis. This assumption is likely to give misleading results in such complex flows.

Thirdly, there are uncertainties about the velocity very close to the wall and the position of the moving wall itself in the measurements. Therefore, comparison at this stage can only be done with caution.

Figs.6.22 and 6.23 show the comparison of axial velocity profiles between predictions (—) and the *in vivo* measurements (ooo) at sites 1–5 (defined in Fig.6.1) over a cardiac cycle for models A and B respectively. In each case, the right hand side is the outer wall and the left hand side is the flow divider side. Comparisons at site 1 demonstrate a very good agreement between the calculations and the measurements in both models, indicating that using the instantaneous axial velocity profiles measured at site 1 (60° to the vessel axis) as boundary conditions at the inlet (orthogonal to the vessel axis) is reasonably accurate. This is because in parent vessels upstream of the flow divider, flow is essentially parallel to the vessel axis and the axial velocity gradients are small.

Good agreement is also observed during late diastole in both daughter vessels at all sites, except at site 5 in the smaller daughter vessel of model A where predicted velocity profiles are totally reversed during pulse phases of late flow reversal (t_5, t_6) whereas measured profiles are shown to direct forward.



(a) Definition of pulse phases where results are compared

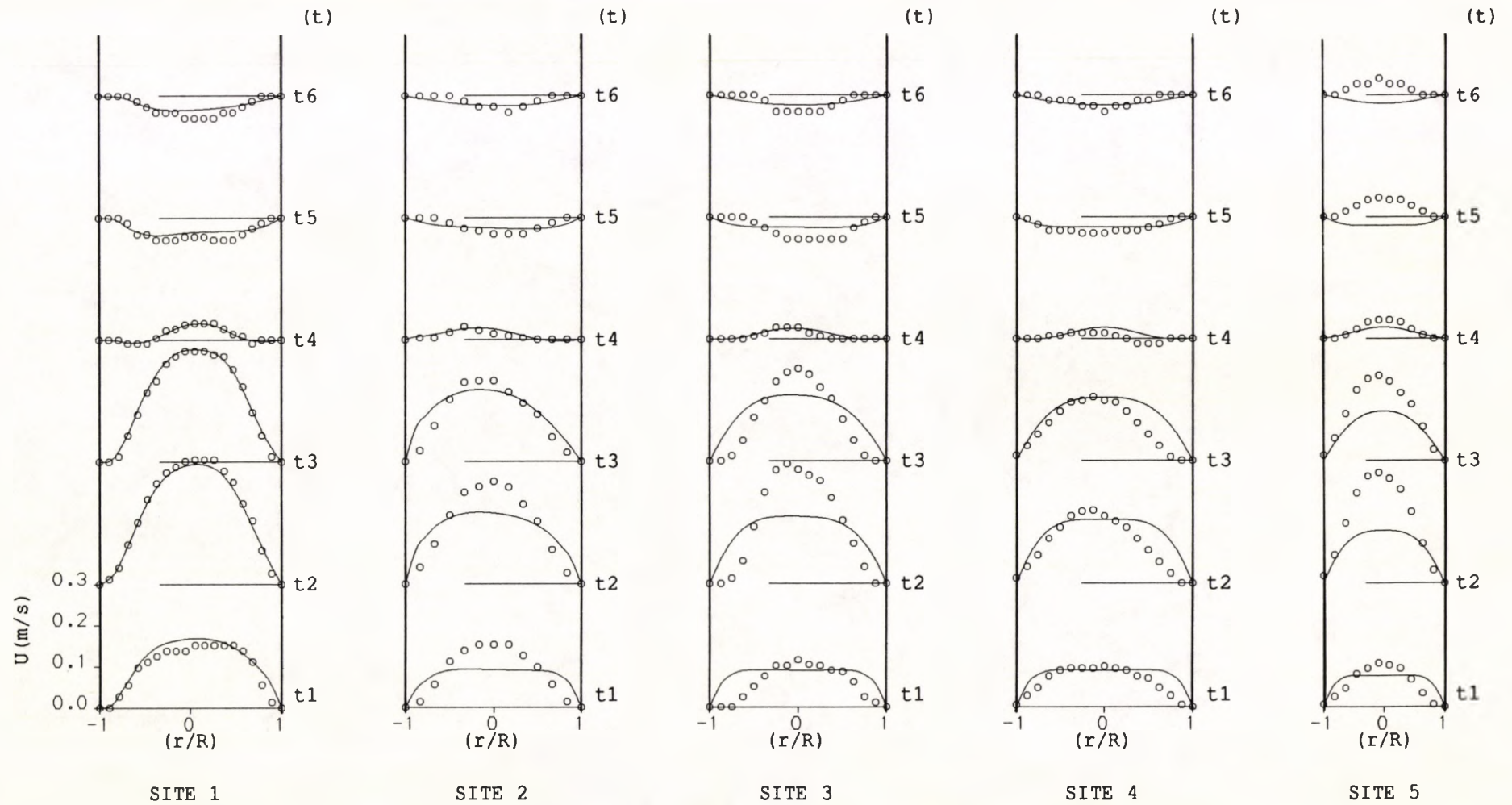


Fig. 6.22 Comparison between calculations (—) and measurements (ooo): axial velocity profiles at sites 1–5 over a cardiac cycle for model A. The right hand side is the outer wall and the left hand side is the flow divider side.

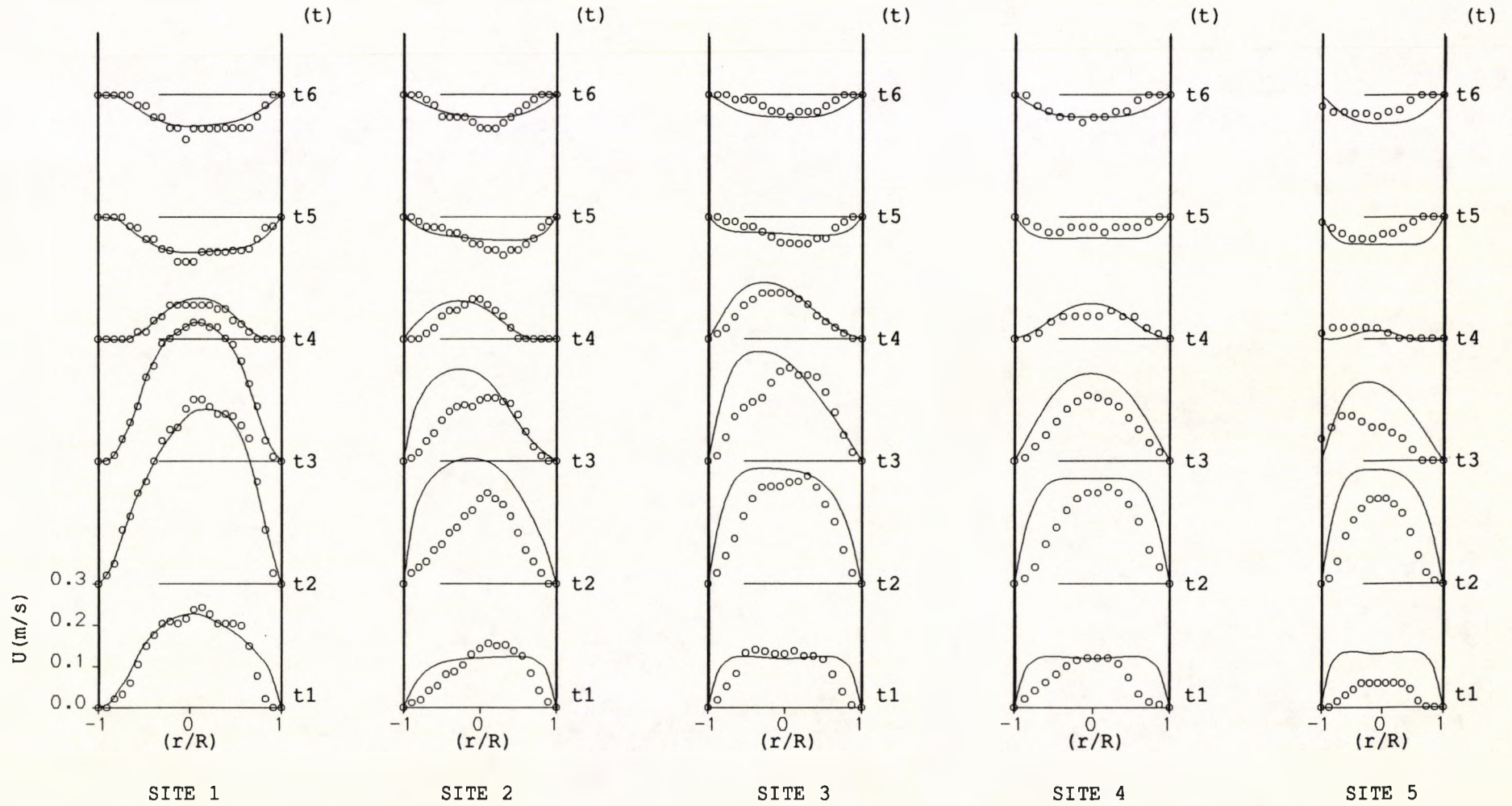


Fig. 6.23 Comparison between calculations (—) and measurements (ooo): axial velocity profiles at sites 1–5 over a cardiac cycle for model B. The right hand side is the outer wall and the left hand side is the flow divider side.

In pulse phases of flow acceleration and early flow deceleration (t_1 , t_2 , t_3), some differences are noticed in both cases. Measured velocity profiles are higher than those predicted in model A, but are somewhat lower than the numerical results in model B. These discrepancies may in large part attribute to the assumption of parallel flow made in the measurements, since the secondary motion in these bifurcations (as discussed in a previous section) is non-negligible.

Attempt was also made to compare the computed secondary velocities with the *in vivo* measurements in which the secondary velocity components normal to the axis of the vessel in the bifurcation plane were measured at the level of the flow divider. This was achieved by angulating the transducer at 90° to the axis of the larger daughter vessel, so that the secondary velocity profile directed towards the flow divider is readily measurable. Comparison of secondary velocities in the plane of the bifurcation at site 6 in model B is presented in Fig.6.24, where the left hand side corresponds to the flow divider side, and the right hand side is the outer wall, forward flow being the flow directed from the outer wall towards the flow divider. The figure shows a generally good agreement between the calculations and the measurement. Secondary velocity profiles are skewed towards the flow divider side, except during early flow acceleration they are deviated towards the outer wall. Secondary flow in the plane orthogonal to that of the bifurcation is found to be insignificant at the level of the flow divider both in the predictions and in the measurements.

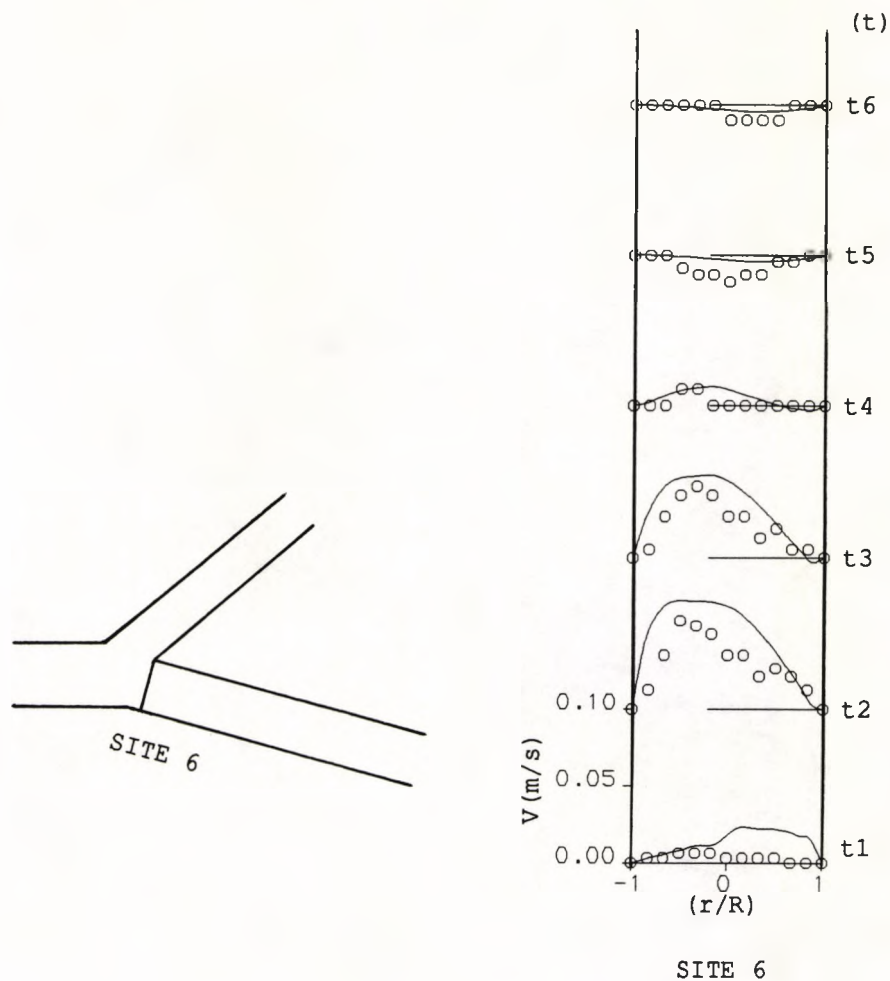


Fig. 6.24 Comparison between calculations (—) and measurements (ooo): secondary velocity profiles in the bifurcation plane at the level of the flow divider (site 6) over a cardiac cycle. The right hand side is the outer wall and the left hand side is the flow divider side.

6.6 SUMMARY

Numerical predictions of the flow and shear stress in true canine femoral bifurcations were carried out under physiological pulsatile flow conditions. The calculations were performed on a supercomputer CRAY X-MP/28, on which a complete cycle took about two and half hours (50 time steps per cycle).

Numerical results show that in the two canine femoral bifurcation models studied, the flow separation and secondary motion are rather weak in model A, hence the resulted shear stress differences between the divider and outer walls are relatively small. In model B, the duration of flow reversal occupies about 40% of the entire cycle and the secondary velocity at the level of the flow divider is up to 23% of the axial velocity at the same site. The maximum wall shear stress obtained in model B is $5.4N/m^2$ occurring near the flow divider on the divider wall, and the lowest time averaged wall shear stress is found at the outer wall of the larger daughter artery. In both cases investigated here, variations of the wall shear stress generally follow their flow waveforms in shape. No rapid oscillation in wall shear stress is found on the outer wall as shown to be present at the outer sinus of human carotid artery by others (Ku et al, 1985).

Comparisons between the Newtonian and non-Newtonian results demonstrate that, under the flow conditions studied the non-Newtonian characteristics of the blood do not have marked effect on determining general features of the flow field. However, as far as the wall shear stress is concerned, the non-Newtonian effects are significant.

Comparison between the predictions and the *in vivo* measurements show that while there is a reasonable agreement in general, local discrepancies still exist. These discrepancies may attribute to several factors, such as, the rigidity of the vessel wall in the prediction, and the assumption and uncertainties involved in the measurements. However, which of these factors is more important and to what extent the comparisons are affected by them are not known. These will be clarified by future numerical studies with the distensibility of the arterial wall being accommodated.

CHAPTER 7

CONCLUSIONS

In the present study a full analytical treatment of blood flow in general 3-D arterial bifurcations is presented. The flow in artery is assumed to be laminar and incompressible, the blood is (i) Newtonian, and (ii) non-Newtonian, the vessel wall being rigid. Under these assumptions, the three-dimensional time-dependent Navier-Stokes equations are solved using a newly developed CFD code ASTEC, which applies the finite volume method on an unstructured finite element mesh.

In order to provide accurate and reliable numerical results, code validation exercises are considered to be essential. For these, a comprehensive approach has been adopted, i.e., by means of comparison with (i) analytical solutions, (ii) experimental data, and (iii) an alternative code. A variety of bifurcation geometries and flow conditions has been treated in this study. First of all, extensive calculations have been carried out for flow in idealised 90° T-bifurcations. In the 2-D case, steady flow at five different combinations of Reynolds number and branch to main tube flow rate ratio, as well as pulsatile flow driven by a sinusoidal upstream pressure gradient have been investigated. Quantitative comparisons with the published LDA measurements (Liepsch and Moravec (1982) for steady flow, Khodadadi and Liepsch et al (1988) for pulsatile flow) have demonstrated a very good agreement between the numerical predictions and the laboratory measurements, especially in the pulsatile flow case the agreement is found to be much better than that also presented by Khodadadi and Liepsch et al (1988). Moreover, the comparison with the calculation obtained using an alternative code FLOW3D has further proved the reliability of the numerical predictions. These results also demonstrate that to obtain the exact information on flow field and wall shear stress in bifurcation regions, pulsatile flow can not be substituted by steady flow studies.

To investigate the 3-D features of the flow and the non-Newtonian effects, pulsatile flow in a 3-D T-bifurcation has been calculated for a Newtonian and a non-Newtonian fluid respectively. The numerical results demonstrate that the bifurcation flow is substantially three-dimensional; this is seen through the Dean type vortex motion found in cross-stream planes of the branches. With respect to the effect of non-Newtonian viscosity, it has been shown that under the flow conditions studied ($(Re)_{ave} = 250$, $\dot{V}_2/\dot{V}_o = 0.5$), differences between the Newtonian and the non-Newtonian flow occur mainly in the region of flow separation. With the non-Newtonian fluid, the duration of flow separation is shorter and the reversed flow is weaker. As for the wall shear stress, the maximum shear stress on the divider wall is slightly reduced (about 8%) while the minimum shear stress on the outer wall is significantly increased (about 61%) in the non-Newtonian case. Comparisons with the rather limited experimental data have demonstrated a good qualitative and a reasonable quantitative agreement.

Finally, as a first step towards providing comparable numerical results to *in vivo* measurements, blood flow in true canine femoral arterial bifurcations has been predicted under physiological flow conditions. Influences of various factors such as bifurcation geometry, flow waveform and non-Newtonian viscosity have been investigated. From the results obtained it can be concluded that the flow field and distribution of wall shear stress in branching arteries are sensitive to all these factors. To gain a quantitative understanding on the velocity field and wall shear stress, flow studies have to be carried out using the individual geometric data and flow conditions for each case. Comparisons between the predictions and the *in vivo* measurements have been made cautiously. While there is a reasonable agreement in general, local discrepancies do exist. These may attribute to the rigid wall assumption made in the predictions and the parallel flow assumption in the measurements. However, at this stage it is difficult to judge which factor is more

important. This will be clarified by future studies with the compliant nature of the arterial wall taken into account.

To incorporate the distensibility of the wall, a simplified approach has been proposed and tested in a straight elastic tube. Nevertheless, applications of this approach to bifurcation geometries seem to be impracticable due to the large amount of memory required. In future studies, the transient gridding technique (available in the latest version of FLOW3D) will be adopted to accommodate this effect.

REFERENCES AND BIBLIOGRAPHY

Abramson, D.I. ed. (1962).

Blood vessels and lymphatics. (New York: Academic Press).

Anitschkow, N. (1933).

Experimental arteriosclerosis in animals. In: Arteriosclerosis, ed. by E.V. Cowdry. (New York: Macmillan).

Anliker, M.; Rockwell, R.L. and Ogden, E. (1971).

Nonlinear analysis of flow pulses and shock waves in arteries, Part I: Derivation and properties of mathematical model, Part II: Parametric study related to clinical problems. Journal of Applied Mathematics and Physics (ZAMP) 22: 217–246(part I), 22: 563–581 (part II).

Ayorinde, O.A.; Kobayashi, A.S. and Merati, J.K. (1975).

Finite elasticity analysis of unanaesthetised and anaesthetised aorta, In: Proceedings of the Biomechanics Symposium, ASME.

Baker, D.W.; Franklin, R.F. and Ellis, R.M. (1964)

Miniature electronic instruments for medical research. Research 13: 275.

Baker, D.W. (1970).

Pulsed ultrasonic Doppler flow sensing. IEEE Trans. Sonics Ultrasonics 17: 170–185.

Bharadvaj, B.K.; Mabon, R.F. and Giddens, D.P. (1982a).

Steady flow in a model of the human carotid bifurcation. Part I - Flow visualisation. Journal of Biomechanics 15: 349–362.

Bharadvaj, B.K.; Mabon, R.F. and Giddens, D.P. (1982b).

Steady flow in a model of the human carotid bifurcation. Part II — Laser-Doppler anemometer measurements. Journal of Biomechanics 15: 363–378.

Bornstein, P. (1970).

The cross-linking of collagen and elastin and its inhibition in osteolathyrism. American Journal of Medicine 49: 429.

Burns, A.D.; Jones, I.P.; Kightley, J.R. and Wilkes, N.S. (1987).

The implementation of a finite difference method for predicting incompressible flows in complex geometries. UKAEA Report AERE CS5 204.

Burns, A.D.; Jones, I.P.; Kightley, J.R. and Wilkes, N.S. (1987).

FLOW3D Release 2: User manual, UKAEA Report, 1987.

Burns, A.D. and Wilkes, N.S. (1987).

A finite-difference method for the computation of fluid flows in complex three-dimensional geometries. UKAEA Report AERE-R 12342.

Caro, C.G.; Fitz-Gerald, J.M. and Schroter, R.C. (1971).

Atheroma and arterial wall shear: Observation, correlation and proposal of a shear dependent mass transfer mechanism for atherogenesis. Proc. Roy. Soc. Lond. B171: 109-159.

Caro, C.G.; Pedley, T.J.; Schroter, R.C. and Seed, W.A. (1978).

The mechanics of the circulation. (Oxford University Press, New York).

Caro, C.G. (1981).

Arterial fluid mechanics and atherogenesis. Recent advances in cardiovascular disease 2: 6-11.

Casson, N. (1959).

A flow equation for pigment-oil suspension of the printing ink type. In: Rheology of disperse systems, ed. by C.C. Mill, pp84-102. (Oxford: Pergamon Press).

Chen, C.J.; Naseri-Noshat, H. and Ho, K.S. (1981).

Finite-analytic numerical solution of heat transfer in two-dimensional cavity flow. Numerical Heat Transfer 4: 179-197.

Chien, S.; Usami, S.; Taylor, H.M.; Lundberg, J.L. and Gregersen, M.I. (1966).

Effects of hematocrit and plasma proteins on human blood rheology at low shear rates. Journal of Applied Physiology 21: 81-87.

Cho, Y.I.; Back, L.H. and Crawford, D.W. (1985).

Experimental investigation of branch flow ratio, angle, and Reynold number effects on the pressure and flow fields in arterial branch models. ASME Journal of Biomechanical Engineering 107: 275-267.

Ciofalo, M. and Collins, M.W. (1988).

Time-dependent numerical simulation of the starting flow of an incompressible fluid past a backward-facing step. In: Proc. AGARD Symposium Validation of CFD, Lisbon, 1988, (36)1-16.

Ciofalo, M. and Collins, M.W. (1990).

Large-eddy simulation of turbulent flow and heat transfer in plane and rib-roughened channels. (Submitted to Int. J. Num. Meth. Fluids).

Clarkson, T.B. (1963).

Atherosclerosis — spontaneous and induced. In: Advances in Lipid Research, ed. by R. Paoletti and D. Kritchersky. (New York and London: Academic Press).

Cokelet, G.R. (1972).

Biomechanics: Its foundation and objectives. Ed. by Y.C.Fung, N.Perrone and M.Anliker, (Prentice-Hall, Englewood), pp63-103.

Collins, M.W. (1980).

Finite difference analysis for developing laminar flow in circular tubes applied to forced and combined convection. Int. J. Num. Methods in Eng. 15: 381-404.

Collins, M.W. and Ciofalo, M. (1990).

Computational fluid dynamics and its application to transport processes. J. Chem. Tech. Biotechnol. 52: 5-47.

Cuvelier, C.; Segal, A. and van Steenhoven, A.A. (1986).

Finite element methods and Navier-Stokes equations. (D. Reidel Publishing Company).

Dawber, T.R.; Moore, F.E. and Mann, G.V. (1957).

Coronary heart disease in the Framingham study. American Journal of Public Health 47: (4 suppl.)

Demiray, H.J. (1972).

A note on the elasticity of soft biological tissues. Journal of Biomechanics 5: 309-311.

Deters, O.J.; Bargeron, C.B.; Mark, F.F. and Friedman, M.H. (1986).

Measurement of wall motion and wall shear in a compliant arterial cast. Journal of Biomechanical Engineering 108: 355-358.

Dinnar, U.; Enden, G. and Israeli, M. (1988).

A numerical study of flow in a three-dimensional bifurcation. Cardiovascular Systems Dynamics Society Meeting, Canada.

Duff, G.L. (1935).

Experimental cholesterol arteriosclerosis and its relationship to human arteriosclerosis. Arch Pathol. 20(18): 259.

Duguid, J.B. and Robertson, W. B. (1957).

Mechanical factors in atherosclerosis. Lanlet 1: 1205.

Duncan, D.D.; Bargeron, C.B.; Borchardt, S.E. et al (1988).

The effects of compliance on wall shear in casts of human aortic bifurcation. in Advances in Bioengineering, Ed. by Miller (ASME, New York), 39-42.

Durst, F.; Melling, A. and Whitelaw, J.H. (1988).

Principles and practice of laser-Doppler anemometry. (Academic Press: London, New York, Toronto, Sydney, San Francisco).

- Edwards, T.A. (1985).
Non-iterative 3-dimensional grid generation using parabolic partial differential equations. 23rd Aerospace Science Meeting, AIAA PAPER-85-0485.
- Eiseman, P.R. and Eriebacher, G. (1987).
Grid generation for the solution of partial differential equations. NASA contract report 178365.
- Eriksson, L.E. (1982).
Generation of boundary-conforming grids around wing-body configurations using transfinite interpolation. AIAA J. 20(10): 1313-1320.
- Euler, L (1775).
Principia pro motu sanguinis per arterias determinado, Opera Posthuma Mathematica et Physica, Petropoli, 2:814-823.
- Evens, E.A. and Fung, Y.C. (1972).
Improved measurements of the erythrocyte geometry. Microvascular Research 4: 335-347.
- Fernandez, R.C.; Witt, K.J. and Sotain, M.R. (1976).
Pulsatile flow through a bifurcation with applications to arterial disease. Journal of Biomechanics 9: 575-580.
- Feuerstein, I.A.; EL Masry, O.A. and Round, G.F. (1976).
Arterial bifurcation flows — effects of flow rate and area ratio. Can. J. Physiol. Pharmacol. 54: 795-808.
- Fishman, A.P. and Richards, D.W. (1964).
Circulation of the blood: Men and ideas. (Oxford University Press, New York).
- Fitzgerald, D.E.; Fortescue-Webb, C.M.; Ekestrom, S. and Liljeqvist, L. and Nordhus, O. (1977).
Monitoring coronary artery blood flow by Doppler shift ultrasound. Scand. J. Thor. Cardiovasc. Surg. 11: 119.
- Flaherty, J.J. and Strauts, E.J. (1969).
Ultrasonic pulse Doppler instrumentation. Proc. 8th Int. Conf. Med. Biol. Eng. 10-10.
- Forsey, C.R and Billing, C.M. (1988).
Some experiences with grid generation on curved surface using variational and optimisation techniques. In: Numerical Grid Generation Methods for Fluid Dynamics (3), ed. by K.W. Morton and M.J.Baines. (Oxford University Press).
- Forster, F.K.; Chikos, P.M. and Frazier, J.S. (1985).
Geometric modelling of the carotid bifurcation in humans : implications in ul-

trasonic Doppler and radiologic investigations. Journal of Clinical Ultrasound 13: 385-390.

Fox, J.A. and Hugh, A.E. (1966).

Localisation of atheroma : theory based on boundary layer separation. British Heart Journal 28: 388-399.

Friedman, M.H.; Hutchins, M.G.; Bargeron, C.B.; Deters, O.J. and Mark, F.F. (1981).

Correlation between intimal thickness and fluid shear in human arteries. Atherosclerosis 39: 425.

Fly, D.L. (1969).

Certain chemorheologic considerations regarding the blood vascular interface with particular reference to coronary artery disease. Circulation 40(Supp.4): 35-57.

Fry, D.L. (1972).

Localising factors in arteriosclerosis. In: Atherosclerosis and coronary heart disease, ed. by W. Likoff and B.L. Segal et al. (New York: Grune and Stratton). pp.85-104.

Fry, D.L. (1976).

Hemodynamic factors in atherogenesis. In: Cerebrovascular disease, ed. by P. Steinberg. (New York: Raven Press). pp.77-95.

Fung, Y.C. (1973).

Biorheology of soft tissues. Biorheology 10: 139-155.

Fung, Y.C. (1975).

On mathematical models of stress-strain relationship for living soft tissues. Mech. Polymeror USSR 10: 850-867.

Fung, Y.C. (1979).

Inversion of a class of nonlinear stress-strain relationship of biological soft tissues. Journal of Biomechanical Engineering, Trans. ASME 101: 23-27.

Fung, Y.C.; Fronek, K. and Patitucci, P. (1979).

Pseudoelasticity of arteries and the choice of its mathematical expressions. American Journal of Physiology 237: H620-H631.

Gessner, F.B. (1973).

Hemodynamic theories of atherogenesis. Circulation Research 33(3): 259-266.

Glass, J. and Rodi, W. (1982).

A higher order numerical scheme for scalar transport. Comp. Meth. in App. Mech. and Eng. 341: 337-358.

- Gofman, J.W. and Young, W. (1963).
The filtration concept of atherosclerosis and Serum lipids in the diagnosis of atherosclerosis. In: Atherosclerosis and its Origin, ed. by M. Sandler and G.H.Bourne. (New York and London: Academic Press).
- Gordon, P. and Scala, S.M. (1970).
Nonlinear theory of pulsatile blood flow through viscoelastic blood vessels. Proceedings of AGARD Conference on 'Fluid Dynamics of Blood Circulation and Respiratory Flow', No.65.
- Gordon, W.J. and Thiel, L.C. (1982).
Transfinite mapping and their applications to grid generation. In: Numerical Grid Generation, ed. by J.F.Thompson. (North-Holland).
- Gresho, P.A. (1984).
A modified finite element method for solving the time-dependent incompressible Navier-Stokes equations. Part I: Theory. International Journal of Mathematics in Fluids 4: 557-598.
- Gutsein, W.H. and Schneck, D.J. (1967).
In vitro boundary layer studies of blood flow in branched tubes. Journal of Atherosclerosis Research 7: 295.
- Hales, S (1733).
Statical essays. Haemastaticks II (London: Innays and Manby).
- Hassan, Y.A.; Rice, J.G. and Kim, J.H. (1983).
A stable mass-flow-weighted two-dimensional skew upwind scheme. Numerical Heat Transfer 6: 395-408.
- Harvey, W. (1628).
De Motu Cordis. Willian Fitzer, Frankfurt. Translated as "Movement of the Heart and Blood in Animals" by K.J. Franklin (1957). (Blackwell Scientific Publication, Oxford).
- Hauser, J. and Taylor, C. (1986).
Numerical grid generation in computational fluid dynamics. In: Proceedings of the International Conference held at Landshut, Germany.
- Hedberg, P.K.M. (1989).
NONDIF: A method to avoid numerical diffusion and over- and under-shoots. In: Proc. 6th Int. Conf. Num. Meth. Lam. Turb. Flow, Swansea, UK., 193-202.
- How, T.V. and Clarke, R.M. (1984).
The elastic properties of a polyurethane arterial prosthesis. Journal of Biomechanics 17: 597-608.

- Hussaini, M.Y. and Zang, T.A. (1987).
Spectral methods in fluid dynamics. Annual Review of Fluid Mechanics 19: 339–367.
- Issa, R.I. (1985).
Solution of the implicitly discretised fluid flow equations by operator–splitting. J. of Computational Physics 62: 40–65.
- Jones, C.J.H.; Lever, M.J.; Ogasawara, Y.; Parker, K.H.; Tsujioka, K.; Hiramatsu, O.; Mito, K.; Caro, C.G. and Kajiyama, F. (1990).
Blood velocity profiles at arterial bifurcations measured by high frequency pulsed Doppler ultrasound velocimetry. (to be published in American Journal of Physiology).
- Kalmanson, D.; Veyrat, C. and Chiche, P. (1970).
Venous return disturbances induced by arrhythmias. Cardiovasc. Res. 4: 279.
- Kalmanson, D.; Veyrat, C.; Derai, D. and Chiche, P. (1972).
Diagnostic value of jugular venous flow velocity trace in right heart diseases. In: Blood Flow Measurement. (Ed. V.C.Roberts, Sector Publishing Ltd.) pp57.
- Karino, T.; Kwong, H.H.M. and Goldsmith, H.L. (1979).
Particle behaviour in models of branching vessels: I. Vortices in 90° T–bifurcations. Biorheology 16: 231–248.
- Khodadadi, J.M.; Nguyen, T.M. and Vlachos, N.S. (1986).
Laminar and forced convective heat transfer in a two–dimensional 90° bifurcation. Numerical Heat Transfer 9(6): 677–695.
- Khodadadi, J.M.; Vlachos, N.S.; Liepsch, D. and Moravec, S. (1988).
LDA measurements and numerical prediction of pulsatile laminar flow in a plane 90-degree bifurcation. Journal of Biomechanics 110: 129–136.
- Kightley, J.R. and Jones, I.P. (1985).
A comparison of conjugate gradient predictions for three–dimensional problems on a CRAY–1. Comp. Phys. Comm. 37: 205–214.
- Kjaernes, M.; Svindland, A.; Walldoe, L. and Witte, S.O. (1981).
Localisation of early atherosclerotic lesions in an arterial bifurcation in human. Acta. Path. Microbiol. Scand. A(89): 35.
- Kreiss, H.O. and Olinger, J. (1971).
Comparison of accurate methods for the integration of hyperbolic equations. Report No. 36, Department of Computer Science, Uppsala University, Sweden.
- Ku, D.N. and Giddens, D.P. (1983).
Pulsatile flow in a model carotid bifurcation. Atherosclerosis 3: 31–39.

- Ku, D.N.; Giddens, D.P.; Zarins, C.K. and Glagov, S. (1985). Pulsatile Flow and atherosclerosis in the human carotid bifurcation — Positive correlation between plaque location and low and oscillating shear stress. Atherosclerosis 5(3): 293–302.
- Ku, D.N.; Giddens, D.P.; Phillips, D.J. and Strandness, D.E. (1985). Hemodynamics of the normal human carotid bifurcation : in vitro and in vivo studies. Ultrasound in Medicine and Biology 11(1): 13-26.
- Ku, D.N. and Liepsch, D. (1986). The effects of non-Newtonian viscoelasticity and wall elasticity on flow at a 90 degree bifurcation. Biorheology 23: 359–370.
- Ku, D.N. and Giddens, D.P. (1987). Laser Doppler anemometer measurements of pulsatile flow in a model carotid bifurcation. Journal of Biomechanics 20: 407–421.
- Kumar, A. (1981). A convective transport analysis using spline techniques. MSc thesis, Imperial College, London.
- Lambert, J.M. (1958). On the nonlinearities of fluid flow in nonrigid tubes. Journal of Franklin Institute 266: 83–102.
- Leonard, B.P. (1979). A stable and accurate convective modelling procedure based on quadratic upstream interpolation. Computer Methods in Applied Mechanics and Engineering 19: 59–98.
- Lewis, J.D.; Papathanaïou, C.; Yao, S.T. and Eastcott, H.H.G. (1972). Simultaneous flow and pressure measurements in intermittent claudication. Br. J. Surg. 59: 418–422.
- Liepsch, D. and Moravec, S. (1982). Measurement and calculations of laminar flow in a ninety degree bifurcation. Journal of Biomechanics 15: 473-485.
- Liepsch, D.; Moravec, S. and Zimmer, R. (1983). Pulsatile flow in distensible models of vascular branches. In: Fluid Dynamics as a Localising Factor for Atherosclerosis, ed. by G. Schettler et al (Berlin Heidelberg: Springer-Verlag).
- Liepsch, D. and Moravec, S. (1984). Pulsatile flow of non-Newtonian fluid in distensible models of human arteries. Biorheology 21: 571–586.

- Liepsch, D.; Seemann, S. and Siekmann, J. (1985).
Note on wave propagation in a thin elastic tube containing a viscous fluid. Journal of Biomechanics 18: 685–694.
- Liepsch, D. (1986).
Review article: Flow in tubes and arteries — a comparison. Biorheology 23: 395–433.
- Liepsch, D.; Poll, A. and Moravec, S. (1988).
Flow studies in true-to-scale models of human renal arteries. In: Role of Blood Flow in Atherogenesis, ed. by Yoshida et al (Tokyo: Spring-Verlag).
- Lighthill, J. (1975).
Mathematical Bio-fluid dynamics. (Society for Industrial and Applied Mathematics, Philadelphia, Pennsylvania, 19103).
- Lillington, J.N. (1981).
A vector upstream differencing scheme for problems in fluid flow involving significant source terms in steady-state linear systems. Int. J. Num. Methods in Fluids 1: 3–6.
- Lin, A. (1985).
The parameterised strongly implicit method for solving elliptic difference equations. Int. J. Num. Methods in Fluids 5: 381–391.
- Malcolm, A.D. and Roach, M.R. (1979).
Flow distribution at the apex and lateral angles of a variety of bifurcation models and their role in development and manifestations of arterial disease. Stroke 10(3): 335–343.
- Mastin, C.W. and Thompson, J.F. (1978).
Transformation of three-dimensional regions onto rectangular regions by elliptic systems. Num. Math. 29: 397–407.
- McDonald, D.A. (1952).
The occurrence of turbulent flow in the rabbit aorta. J. Physiol(Lond) 118: 340.
- McDonald, D.A. (1960).
Blood flow in arteries. (Baltimore: Williams and Wilkins Co.)
- Merrill, E.W.; Margetts, W.G., Cokelet, G.R. and Gilliland, E.R. (1965).
The Casson equation and rheology of blood near zero shear. In: Symposium of Biorheology, ed. by A.L. Copley. (New York: Interscience).
- Merrill, E.W. and Pelletier, G.A. (1967).
Viscosity of human blood: transition from Newtonian to non-Newtonian. Journal of

applied physiology 33: 178.

Miki, K. and Tagagi, T. (1984).

A domain decomposition and overlapping method for the generation of three-dimensional boundary-fitted coordinate systems. Journal of Computation Physics 53: 319-330.

Mitchell, J.R.A. and Schwartz, C.J. (1965).

Arterial Disease. (Oxford, Black Well: Scientific Publishers Ltd).

Moravec, S. and Liepsch, D. (1983).

Flow investigation in a model of a three-dimensional human artery with Newtonian and non-Newtonian fluids, Part I. Biorheology 20: 745-759.

Nakamura, M. and Sawada, J. (1987).

Numerical study on the laminar pulsatile flow of slurries. Journal of non-Newtonian fluid mechanics 22: 191-206.

Nakamura, M. and Sawada, J. (1988).

Numerical study on the flow of a non-Newtonian fluid through an axisymmetric stenosis. ASME Journal of Biomechanical Engineering 110: 137-143.

Nakamura, S. (1982).

Marching grid equations using parabolic partial differential equations. In: Numerical Grid Generation, ed. by J.F.Thompson. (North-Holland).

Nerem, R.M.; Rumberger, J.A.; Gross, D.R.; Hamlin. R.L. and Geiger, G.L. (1974).

Hot-film anemometer velocity measurements of arterial blood flow in horses. Circ. Res. 34: 193-203.

Nerem, R.M. and Levesgue, M.J. (1983).

The case for fluid dynamics as a localising factor for atherosclerosis, ed. by G.Schettler et al. (Berlin Heibelberg: Springer-Verlag). pp.26-37.

O'Brien, V.; Ehrlich, L.W. and Friedman, M.H. (1976).

Unsteady flow in a branch. Journal of Fluid Mechanics 75: 315-336.

O'Brien, V. and Ehrlich, L.W. (1977).

Simulation of unsteady flow at renal branches. Journal of Biomechanics 10: 623-631.

Olson, D.E. (1971).

Fluid mechanics relevant to respiration and flow within curved or elliptical tubes and bifurcating systems. Ph.D thesis, Imperial College, London.

Orszag, S.A. (1972).

Numerical simulation of incompressible flow within simple boundaries: I Galerkin (spectral) representation. Stud. Appl. Math. 50: 293–327.

Patankar, S.V. and Spalding, D.B. (1972).

A calculation procedure for heat, mass and momentum transfer in three-dimensional parabolic flows. Int. J. Heat and Mass Transfer 15: 1787–1806.

Patankar, S.V. (1980).

Numerical heat transfer and fluid flow. (Hemisphere publishing corporation: Washington, New York, London).

Patankar, S.V. (1981).

A calculation procedure for two-dimensional elliptic situations. Numerical Heat Transfer 4: 409–425.

Patankar, S.V. (1988).

Recent developments in computational heat transfer. ASME J. Heat Transfer 110: 1037–1045.

Patel, D.J.; Greenfield, J.C. and Fry, D.L. (1964).

In vivo pressure-length-radius relationship of certain vessels in man and dog. In: Pulsatile Blood Flow, Ed. E.O. Attinger (McGraw-Hill, New York), 293.

Patel, D.J. and Vaishnav, R.N. (1972).

The rheology of large blood vessels. In: Cardiovascular fluid dynamics, ed. by D.H. Bergel (New York: Academic), Vol.2, pp.2–65.

Peraire, J., Morgan, K. and Perio, J. (1990).

Unstructured mesh methods for CFD. Von Karman Institute for Fluid Dynamics 'Numerical Grid Generation' lecture note.

Peric, M. (1987).

Efficient semi-implicit solving algorithm for nine-diagonal coefficient matrix. Numerical Heat Transfer 11: 31–55.

Perktold, K. and Hilbert, D. (1986).

Numerical simulation of pulsatile flow in a carotid bifurcation model. Journal of Biomechanics 8: 193–199.

Perktold, K. and Peter, R.O (1990).

Numerical 3D-simulation of pulsatile wall shear stress in an arterial T-bifurcation model. Journal of Biomedical Engineering 12: 2–12.

Perktold, K. and Resch, M. (1990).

Numerical flow studies in human carotid artery bifurcations: basic discussion of the

geometric factor in atherogenesis. Journal of Biomedical Engineering 22: 111-123.

Perktold, K.; Resch, M. and Peter, R.O. (1991).

Three-dimensional numerical analysis of pulsatile flow and shear stress in the carotid artery bifurcation. Journal of Biomechanics 24: 409-420.

Peronneau, P.; Xhaard, M.; Nowicki, A.; Pellet, M., Delouche, D. and Hinglais, J. (1972).

Pulsed Doppler ultrasonic flowmeter and flow pattern analysis. In: Blood Flow Measurement. (Ed. C.Roberts, Sector Publishing Ltd. London).

Phillips, D.J.; Powers, J.E.; Eyer, M.K.; Blackshear, W.M.; Bodily, K.C.; Strandness, D.E. and Baker, D.W. (1980).

Detection of peripheral vascular disease using the duplex scanner III. Ultrasound Med. Biol. 6: 205-218.

Phillips, R.E. and Schmidt, F.W. (1984).

Multigrid techniques for the numerical solution of the diffusion equation. Num. Heat Transfer 11: 251-268.

Phillips, R.E. and Schmidt, F.W. (1985a).

Multigrid techniques for the solution of the passive scalar advection-diffusion equation. Num. Heat Transfer 8: 25-43.

Phillips, R.E. and Schmidt, F.W. (1985b).

A Multilevel-multigrid technique for recirculating flows. Num. Heat Transfer 8: 573-594.

Raithby, G.D. (1976).

Skew upstream differencing schemes for problems involving fluid flow. Computer Methods In Applied Mechanics and Engineering 9: 153-164.

Reneman, R.S.; Merode, T.v.; Hick, P. and Hoeks, A.P.G. (1985).

Flow velocity patterns in and distensibility of the carotid artery bulb in subjects of various ages. Circulation 71: 500-509.

Reneman, R.S.; Merode, T.v.; Hick, P. and Hoeks, A.P.G. (1986).

Cardiovascular applications of multi-gate pulsed Doppler systems. Ultrasound in Medicine and Biology 12: 357-370.

Reuderink, P.J. (1991).

Analysis of the flow in a 3D distensible model of the carotid artery bifurcation. Ph.D Thesis, Technische Universiteit Eindhoven.

Rhie, C.M. and Chow, W.L. (1983).

Numerical study of the turbulent flow past an airfoil with trailing edge separation. AIAA Journal 21: 1527-1532.

- Richardson, P. and Christo, J. (1990).
Flow separation opposite a side branch. In: Biofluid Mechanics, Blood Flow in Large Vessels, Ed. by D. Liepsch (Springer – Verlag), pp275-284.
- Rindt, C.C.M, Vosse, F.N.N.V.D., Steenhoven, A.A.V. and Janssen, J.D. (1987).
A numerical and experimental analysis of the flow in a two-dimensional model of the human carotid bifurcation. Journal of Biomechanics 20: 499–509.
- Rindt, C.C.M. (1989).
Analysis of the three-dimensional flow field in the carotid artery bifurcation. Ph.D thesis, Eindhoven University of Technology, Netherlands.
- Rittenhouse, E.A. and Brockenbrough, E.C. (1969).
A method for assessing the circulation distal to a femoral artery obstruction. Surg. Gynec. Obset. 129: 538–544.
- Rodkiewicz, C.M.; Sinha, P. and Kennedy, J.S. (1990).
On the application of a constitutive equation for whole human blood. ASME Journal of Biomechanical Engineering 112: 198–206.
- Ross, R. (1981).
Smooth muscle cells and atherosclerosis. In: Vascular injury and atherosclerosis, ed. by S. Moore. (New York Basel: Marcel Dekker). pp.53–77.
- Rubin, S.G. and Graves, R.A. (1975).
Viscous flow solutions with a cubic spline approximation. Comp. Fluids 3: 1–36.
- Runchal, A.K. (1987).
CONDIF: A modified central-difference scheme for convective flows. Int. J. Num. Meth. Eng. 24: 1593–1608.
- Satomura, S. (1959)
Study of flow patterns in peripheral arteries by ultrasonics. J. Acoust. Soc. Japan 15: 155.
- Schneider, G.E. and Zedan, M. (1981).
A modified strongly implicit procedure for the numerical solution of field problems. Numerical Heat Transfer 4: 1–19.
- Schultz, D.L.; Tunstall-Pedoe, D.L.; Lee, G.; Gunning, A.J. and Bellhouse, B.J. (1969).
Velocity distribution and transition in the arterial system. In: Circulatory and Respiratory Mass Transport. Ed. G.E.W. Wolstenholme and J.Knight, CIBA Symposium, J.&A. Churchill, Edinburgh.

Spalding, D.B. (1972).

A novel finite-difference formulation for differential expressions involving both first and second derivations. Int. J. for Numerical Methods in Engineering 4: 557-559.

Spalging, D.B. (1980).

Mathematical modelling of fluid mechanics, heat transfer and mass transfer processes. Imperial college, London, Mechanical Engineering Department, Report No. HTS/80/1.

Starius, G. (1977).

Construction of orthogonal curvilinear meshes by solving initial values problems. Num. Math. 28: 25-48.

Stegall, H.F.; Rushmer, R.F. and Baker, D.W. (1966)

A transcutaneous ultrasonic blood velocity meter. Journal of Applied Physiology 21: 707.

Steger, J.L. and Sorenson, R.L. (1980).

Use of hyperbolic partial differential equation to generate body-fitted coordinates. In: Numerical Grid Generation, ed. by R.E. Smith, NASA Conference Publication, CP-2166.

Stehbens, W.E. (1973).

Experimental arteriovenous fistulae in normal and cholesterol-fed rabbits. Pathology 5: 311.

Stehbens, W.E. (1975).

Flow in glass models of arterial bifurcations and berry aneurysm at low Reynolds numbers. Q. J. Expl. Physiol. 60: 181-192.

Stettler, J.C; Niederer, P. and Anliker, M. (1981).

Theoretical analysis of arterial hemodynamics including the influence of bifurcations. Part I: Mathematical model and prediction of normal pulse patterns. Part II: Critical evaluation of theoretical model and comparison with noninvasive measurements of flow patterns in normal and pathological cases. Annals of Biomedical Engineering 9: 145-175.

Stone, H.L (1968).

Iterative solution of implicit approximations of multi-dimensional partial differential equations. SIAM J. Num. Anal. 5: 530-558.

Strandness, D.E.; Schultz, R.D.; Summer, D.S. and Rushmer, R.F.(1967).

Ultrasonic flow detection. A useful technique in the evaluation of peripheral vascular disease. American Journal of Surgery 113 : 311-320.

Stubley, G.D.; Raithby, G.D. and Strong, A.B. (1980).

Proposal for a new discrete method based on an assessment of discretization errors.

Numerical Heat Transfer 4: 179–197.

Svindland, A.D. and Walloe, L. (1983).

Localisation of early atherosclerotic lesions in carotid and coronary bifurcations in human — A bifurcation of the high shear hypothesis. In: Fluid Dynamics as a Localising Factor for Atherosclerosis, ed. by G. Schettler et al. (Berlin Heidelberg: Springer – Verlag). pp.212–226.

Syed, S. & Chiappetta, L. (1985).

Finite difference methods for reducing numerical diffusion in TEACH-type calculations. AIAA paper 85–0056.

Thompson, J.F.; Thames, F.C. and Mastin, C.W. (1974).

Automatic numerical generation of body-fitted curvilinear coordinate system for field containing any number of arbitrary two-dimensional bodies. J. Comp. Physics 15: 299–319.

Thompson, J.F.; Warsi, Z.U.A. and Mastin, C.W. (1982).

Boundary-fitted coordinate systems for numerical solution of partial differential equations — a review.

Thompson, J.F. (ed.) (1982).

Numerical grid generation. (North-Holland).

Thompson, J.F. (1984).

Grid generation techniques in computational fluid dynamics. AIAA Journal 22(11): 1505–1523.

Tunstall Pedoe, D.S. (1972).

Diagnosis of aortic incompetence using directional Doppler velocity measurements — problems of quantification. In: Fluid Dynamics Measurements in the Medical and Industrial Environment. (Ed. D.J.Cockrell. University Press, Leicester), pp321.

Usab, W.J. and Murman, E.M. (1983).

Embedded mesh solution of the Euler equations using a multi-grid method. AIAA paper 83–1946, Danvers, Mass.

Van Doormal, J.P. and Raithby, G.D. (1984).

Enhancement of the SIMPLE method for predicting incompressible fluid flows. Numerical Heat Transfer 7: 147–163.

Walburn, F.J. and Schneck, D.J. (1976).

A constitutive equation for whole human blood. Biorheology 13: 201–210.

Weatherill, N.P. and Forsey, C.R. (1985).

Grid generation and flow calculation for aircraft geometries. Journal of Aircraft 22

(10): 855–860.

Weatherill, N.P. and Shaw, J.A. (1988).

Component adaptive grid generation for aircraft configurations. *AGARDOGRAPH*, ed. by H. Yoshihara, J.L. Steger and J.F. Thompson.

Wells, P.N.T. (1969).

A range-gated ultrasonic Doppler system. *Med. Biol. Eng.* 7: 641–652.

Wesley, R.L.R.; Vaishnav, R.N.; Fuchs, J.C.A.; Patel, D.J. and Greenfield, J.C. (1975).

Static linear and nonlinear elastic properties of normal and arterialised venous tissue in dog and man. *Circulation Research* 37: 509–520.

Wesolowski, S.A.; Fries, C.C.; Sabini, A.M. and Sawyer, P.N. (1965).

Significance of turbulence in hemic systems and in the distribution of the atherosclerotic lesion. *Surgery* 57: 155–162.

Whitmore, R.L. (1968).

Rheology of the circulation. Pergamon Press, Oxford.

Wilens, S.L. (1951).

The nature of diffuse intimal thickening of arteries. *American Journal of Pathology* 27: 825.

Wille, S.O. (1984).

Numerical simulation of steady flow inside a three-dimensional aortic bifurcation model. *Journal of Biomedical Engineering* 6: 49–55.

Womersley, J.R. (1955).

Method for the calculation of velocity, rate of flow and viscous drag in arteries when the pressure gradient is known. *Journal of Physiology*, 127: 553–563.

Wong, H.H. and Raithby, G.D. (1979).

Improved finite-difference methods based on a critical evaluation of the approximation errors. *Num. Heat Transfer* 2: 139–163.

Yeh, Y. and Cummins, H.Z. (1964).

Localised flow measurements with an He–Ne laser spectrometer. *Appl. Phys. Letters* 4: 176.

Young, T. (1908).

Hydraulic investigation. Subservient to an intended croonian lecture on the motion of the blood, *Philosophical Trans. of the Roy. Soc. of London* 98: 164–186.

Yu, S.Y. (1971).

Cross-linking of elastin in human atherosclerotic aortas. 1. A preliminary study. *Lab. Invest.* 25: 121.

Zarins, C.K.; Giddens, D.P.; Bharadvaj, B.K.; Sottiurai, V.S.; Mabon, R.F. and Glagov, S. (1983).

Carotid bifurcation atherosclerosis. Quantitative correlation of plaque localisation with flow velocity profiles and wall shear stress. Circulation Research 53: 502-514.

Brooks, D.E.; Goodwin, T.W. and Seaman, G.V.F. (1970).

Interactions among erythrocytes under shear. J.Appl.Physiol. 28: 171-177.

Dinnar, U. (1981).

Cardiovascular fluid dynamics. (CRC Press, Inc. Boca Raton, Florida).

Dwight, H.B. (1941, 1961).

Mathematical tables. 1st and 3rd edn. (Dover, New York).

How, T.V. and Clarke, R.M. (1984).

The elastic properties of a polyurethane arterial prosthesis. J. Biomechanics 17: 597-608.

Karino, T. and Goldsmith, H.L. (1980).

Disturbed flow in models of branching vessels. Trans. Am. Soc. Artif. Intern. Organs XXVI: 500-506.

McDonald, D.A. (1974).

Blood flow in arteries. (Edward Arnold, London).

McLachlan, N.W. (1941).

Bessel functions for engineers. (Oxford University Press).

APPENDIX A

General Form of The Stress Tensor Equation For Incompressible Non-Newtonian Fluids

It was defined in chapter 2 that the stress tensor σ_{ij} for an incompressible Newtonian fluid is given by:

$$\sigma_{ij} = -p\delta_{ij} + 2\mu S_{ij} \quad (1)$$

where μ is a constant. For non-Newtonian fluids, the relationship between the stress and strain is not the simple one given in Eqn.(1). However, for certain types of non-Newtonian fluids a relationship of the form of Eqn.(1) still applies:

$$\sigma_{ij} = -p\delta_{ij} + 2\mu_{n-N} S_{ij} \quad (2)$$

where μ_{n-N} is not a constant as μ is, but a function of the strain rate tensor S_{ij} . Since μ_{n-N} is a scalar, in order to keep Eqn.(2) tensorially correct, i.e., every term in the equation must be a tensor of the same rank, μ_{n-N} must be a scalar function of S_{ij} . In other words, it must be a function of the invariants of S_{ij} . The invariants are those special combinations of the components of S_{ij} that transform as scalars under a rotation of the coordinate system. Since S_{ij} is a symmetric tensor, it has three invariants:

$$I_1 = \sum_i S_{ii} \quad (3)$$

$$I_2 = \sum_i \sum_j S_{ij} S_{ji} \quad (4)$$

$$I_3 = \sum_i \sum_j \sum_k \epsilon_{ijk} S_{1i} S_{2j} S_{3k} \quad (5)$$

For an incompressible fluid, I_1 equals zero. In many simple flows (e.g. axial flow in a tube, cone-plate flows et al) I_3 vanishes identically, and it is commonly assumed that I_3 is not very important in other flows. Hence, it is customary to assume that μ_{n-N} is a function of I_2 only. But when $I_1 = 0$, I_2 is negative, hence it is more convenient to use

$$J_2 = 3I_1^2 - I_2 = \frac{1}{2} S_{ij} \cdot S_{ij} \quad (6)$$

Thus, μ_{n-N} is a function of J_2 and Eqn.(1) can be generalised as:

$$\sigma_{ij} = -p\delta_{ij} + 2\mu(J_2)S_{ij} \quad (7)$$

APPENDIX B

Finite Nonlinear Elastic Analysis

Consider a thin wall cylinder of mid-wall radius r and wall thickness h , subjected to a physiological loading, i.e., an internal pressure P and a longitudinal force F . By taking a longitudinal and a transversely cut segments, the circumferential stress S_θ , longitudinal stress S_z and radial stress S_r can be determined from equilibrium considerations:

$$S_\theta = P \left(\frac{r}{h} - \frac{1}{2} \right) \quad (1)$$

$$S_z = \frac{P}{2} \left(\frac{r}{h} - 1 \right) + \frac{F}{2\pi r h} \quad (2)$$

$$S_r = -\frac{P}{2} \quad (3)$$

For an incompressible material, the stresses are given by (Patel and Vaishnav, 1972):

$$S_\theta - S_r = (1 + 2a) \frac{\partial W}{\partial a} \quad (4)$$

$$S_z - S_r = (1 + 2b) \frac{\partial W}{\partial b} \quad (5)$$

where W is the strain energy function which is expressed as a polynomial function in two principal strains:

$$W = Aa^2 + Bab + Cb^2 + Da^3 + Ea^2b + Fab^2 + Gb^3 \quad (6)$$

where A, B, \dots, G are the constitutive constants; a and b are the Green-St. Venant strains in the circumferential and longitudinal directions respectively. These strains

are defined as follows:

$$a = \frac{1}{2}(\lambda_\theta^2 - 1) : \lambda_\theta = \frac{r}{R_i} \quad (7)$$

$$b = \frac{1}{2}(\lambda_z^2 - 1) : \lambda_z = \frac{l}{L_i} \quad (8)$$

where R_i and L_i are the initial undeformed mid-wall radius and length.

Substituting Eqns.(1) and (2) into (4) yields an equation relating pressure with strains and constitutive constants:

$$P = \frac{h}{r} \left\{ 6Da^3 + (4A + 3D + 4Eb)a^2 + 2(A + Bb + Eb + Fb^2)a + (Bb + Fb^2) \right\} \quad (9)$$

Similarly, by substituting Eqns.(2) and (3) into (5) an expression for longitudinal force is obtained:

$$F = 2\pi r h \left\{ (6Gb^3 + (4C + 3G + 4Fa)b^2 + 2(C + Ba + Fa + Ea^2) + Ba + Ea^2 - \frac{Pr}{2h}) \right\} \quad (10)$$

APPENDIX C

Fortran Subroutine For The Non-Newtonian Model

```
C
C*****C
C   THIS SUBROUTINE SPECIFIES THE NON--NEWTONIAN VISCOSITY   C
C   OBEYINY THE POWER LAW                                   C
C*****C
C
C   SUBROUTINE SBOUND (NOD, MTYPE, KTYPE, NOB, X, Y, Z, ALPCO, ALPREF, CPCO,
-   CPREF, ETACO, ETAREF, RHOCO, RHOREF, GAMP, PM11, PM22, PM33, PM12, PM13,
-   PM23, TL, TN, UL, UN, VL, VN, WL, WN, SL, SN, DL, DN, EL, EN, P, VBOX)
C
C   PARAMETER (KTOTM=5000)
COMMON /SPACE/ ARR(1)
COMMON /SCALAR/ NUMSCA, ISCSRC, ISCDIF, PRANS, RELSCA, CSMIN,
-   CONSCA, NUMSCD
C
COMMON/PARAMS/DELT, TIMEND, IVUP, NMAT, IDRAG, INITCO, IVCAL,
-   GX, GY, GZ, DCONV, CRIT, MTOT, KTOT, ITEMP, IPRINT, TEND, IDIFC, IPBND,
-   IDUPRT, NUMTIM, BEX, IHEAT, IRSTRT, TIME, RELPRS, DIVMAX, ITRANS,
-   RELVEL, RELTEM, CONVEL, CONTEM, CVMIN, CTMIN, ITIMAX, ISWMAX, IVRED,
-   IBLADJ, SORFV, SORFS, NSMAXV, NSMAXS, RDFACV, RDFACS, RDFACD, NTURSC
C
DIMENSION NOD (MTOT, 8), MTYPE (MTOT), KTYPE (KTOT), NOB (KTOT), X (KTOT),
-   Y (KTOT), Z (KTOT), ALPCO (NMAT), ALPREF (NMAT), CPCO (NMAT), CPREF (NMAT),
-   ETACO (NMAT), ETAREF (NMAT), RHOCO (NMAT), RHOREF (NMAT), GAMP (NMAT),
-   PM11 (NMAT), PM22 (NMAT), PM33 (NMAT), PM12 (NMAT), PM13 (NMAT),
-   PM23 (NMAT), TL (KTOT), TN (KTOT), UL (KTOT), UN (KTOT), VL (KTOT),
-   VN (KTOT), WL (KTOT), WN (KTOT), SL (KTOT, NUMSCA), SN (KTOT, NUMSCA),
-   DL (KTOT), DN (KTOT), EL (KTOT), EN (KTOT), P (KTOT)
DIMENSION VBOX (KTOT), GRADT (KTOTM, 3), DXY (KTOTM), DYZ (KTOTM),
-   DXZ (KTOTM), GAMA (KTOTM), D11 (KTOTM), D12 (KTOTM), D13 (KTOTM),
-   D21 (KTOTM), D22 (KTOTM), D23 (KTOTM), D31 (KTOTM), D32 (KTOTM),
-   D33 (KTOTM), DII (KTOTM)
C
C   SET   CONSTANTS IN THE POWER LAW RELATIONSHIP
C
C   CONST=0.042
C   AN=0.61
C   POWER=0.5*(AN-1.0)
C
C   CALL DATLOC ('VOLSUB', IVS, IDVS, IERR)
C
C   INITIALISATION
C
C   DO 1 K=1, KTOT
1   DII (K)=0.0
C
C   CALCULATE COMPONENTS OF SHEAR RATE
C
C   CALL GRADNO (UN, GRADT, NOD, ARR (IVS), X, Y, Z, VBOX, NOB)
C   DO 10 K=1, KTOT
C   D11 (K)=GRADT (K, 1)
C   D12 (K)=GRADT (K, 2)
C   D13 (K)=GRADT (K, 3)
10  CONTINUE
```

```

      CALL GRADNO (VN, GRADT, NOD, ARR (IVS) , X, Y, Z, VBOX, NOB)
      DO 20 K=1, KTOT
      D21 (K) =GRADT (K, 1)
      D22 (K) =GRADT (K, 2)
      D23 (K) =GRADT (K, 3)
20    CONTINUE
      CALL GRADNO (WN, GRADT, NOD, ARR (IVS) , X, Y, Z, VBOX, NOB)
      DO 30 K=1, KTOT
      D31 (K) =GRADT (K, 1)
      D32 (K) =GRADT (K, 2)
      D33 (K) =GRADT (K, 3)
30    CONTINUE
C
C
      DO 2 K=1, KTOT
      KT=KTYPE (K)
      DN (K) =0.09
      DXY (K) =D12 (K) +D21 (K)
      DYZ (K) =D23 (K) +D32 (K)
      DZX (K) =D31 (K) +D13 (K)
      DII (K) =2.0* (D11 (K) **2+D22 (K) **2+D33 (K) **2)
&      +DXY (K) **2+DYZ (K) **2+DZX (K) **2
C
C
C
      IF (DII (K) .LE.0.0025) DII (K) =0.0025
      IF (DII (K) .GT.1.0E+6) DII (K) =1.0E+6
C
      GAMA (K) =CONST*DII (K) **POWER/RHOREF (KT)
      EN (K) =SQRT (GAMA (K) )
2    CONTINUE
C
      RETURN
      END

```

APPENDIX D

Relationship Of Velocity, Flow Rate And Wall Shear Stress To An Oscillatory Pressure Gradient

Consider the flow of an incompressible Newtonian homogeneous fluid in a long straight circular rigid tube under a periodic pressure gradient. If the tube is sufficiently long relative to its diameter ($2R$), the radial motion of the fluid can then be neglected and its axial velocity u is independent of the distance x along the tube. The momentum equation governing such a flow becomes:

$$\frac{\partial^2 u}{\partial r^2} + \frac{1}{r} \frac{\partial u}{\partial r} - \frac{\rho}{\mu} \frac{\partial u}{\partial t} = -\frac{1}{\mu} \frac{\partial P}{\partial x} \quad (1)$$

where the oscillating pressure gradient $\frac{\partial P}{\partial x}$ may be represented by a simple harmonic motion and written in complex form:

$$-\frac{\partial P}{\partial x} = A e^{i\omega t} \quad (2)$$

where $\omega = 2\pi f$ is the angular frequency of the oscillating motion. This type of equation is a classic problem in mathematical physics. It was investigated by many authors since 1929 onwards, and its solution was applied to flow analysis in large arteries by Womersley (1955). Using the no-slip condition on the wall, its solution is given by:

$$u = \frac{A}{i\omega\rho} \left\{ 1 - \frac{J_0 \left[r\sqrt{\omega/\nu} i^{\frac{3}{2}} \right]}{J_0 \left[R\sqrt{\omega/\nu} i^{\frac{3}{2}} \right]} \right\} e^{i\omega t} \quad (3)$$

Where J_0 is a Bessel function of the first kind of order zero and complex argument. The quantity $R\sqrt{\frac{\omega}{\nu}}$ is a non-dimensional parameter which was defined as the Womersley parameter α . In a non-dimensional form with $y = r/R$, Eqn.(3)

becomes:

$$u = \frac{A}{i\omega\rho} \left\{ 1 - \frac{J_o(\alpha y i^{\frac{3}{2}})}{J_o(\alpha i^{\frac{3}{2}})} \right\} e^{i\omega t} \quad (4)$$

The numerical solution of Eqn.(4) is concerned with complex quantities and may be made by separation into real and imaginary parts. Dwight (1941, 1961) tabulated the real and imaginary parts of a Bessel function of the first kind as Ber and Bei functions; it is his tables that were used in the velocity profile calculations.

Alternatively, Eqn.(4) may be expressed in terms of modulus and phase which Womersley (1955) regarded as more tractable. This involves the substitutions:

$$J_o(\alpha y i^{\frac{3}{2}}) = M_o(\alpha y) e^{i\theta_o(y)} \quad (5)$$

$$J_o(\alpha i^{\frac{3}{2}}) = M_o(\alpha) e^{i\theta_o} \quad (6)$$

Tables of $M_o(\alpha y)$ and $\theta_o(\alpha y)$ are given by McLachlan (1941). If the real part of the pressure gradient is $M \cos(\omega t - \phi)$, the corresponding velocity is then

$$u = \frac{M}{\omega\rho} M'_o \sin(\omega t - \phi + \epsilon_o) \quad (7)$$

where

$$\left\{ \begin{array}{l} h_o = \frac{M_o(\alpha y)}{M_o(\alpha)} \\ \delta_o = \theta_o(\alpha) - \theta_o(\alpha y) \\ M'_o = \sqrt{1 + h_o^2 - 2h_o \cos \delta_o} \\ \tan \epsilon_o = \frac{h_o \sin \delta_o}{1 - h_o \cos \delta_o} \end{array} \right. \quad (8)$$

Note that Eqn.(7) can also be written as:

$$u = \frac{M}{\omega\rho} M'_o \cos \left\{ \omega t - \phi - \left(\frac{\pi}{2} - \epsilon_o \right) \right\} \quad (9)$$

Hence the phase lag of velocity behind the pressure gradient is $90^\circ - \epsilon_o$, which varies with the radial position y . Near the tube wall ($y=1$), $\epsilon_o = 90^\circ$, the temporal variation of the velocity is in phase with that of the pressure gradient; however, near the centre, it is up to 90° out of phase when α is large. This effect produces higher velocities near the wall and lower velocities near the centre for certain values of ωt . This then is the "annular effect".

By integrating Eqn.(4) across the tube, the corresponding volume flow rate is obtained:

$$Q = \frac{\pi R^2 A}{i\omega\rho} \left\{ 1 - \frac{2J_1(\alpha i^{\frac{3}{2}})}{\alpha i^{\frac{3}{2}} J_0(\alpha i^{\frac{3}{2}})} \right\} e^{i\omega t} \quad (10)$$

where J_1 is a Bessel function of order one. When the real part of the pressure gradient is $M \cos(\omega t - \phi)$, Eqn.(10) can be converted to modulus and phase form as:

$$Q = \frac{\pi R^2 M}{\omega\rho} \left\{ \sin(\omega t - \phi) - \frac{2M_1}{\alpha M_o} \sin(\omega t - \phi - \delta_{10}) \right\} \quad (11)$$

where

$$\delta_{10} = 135^\circ - \theta_1 + \theta_o \quad (12)$$

Reduced to a single-phase relationship, the volume flow rate becomes:

$$Q = \frac{\pi R^2}{\omega\rho} M M'_{10} \sin(\omega t - \phi + \epsilon_{10}) \quad (13)$$

Tables of M'_{10} and ϵ_{10} are given by Womersley (1955). It can be derived that the phase lag of flow behind the pressure is $90^\circ - \epsilon_{10}$; it tends to zero when $\alpha \rightarrow 0$, but moves very slowly towards its asymptotic values of 90° at high values of α .

Similarly, by differentiating Eqn.(4) the corresponding shear stress can be

obtained:

$$\tau = -\mu \frac{\partial u}{\partial r} = \frac{\mu}{R} \frac{M \alpha}{\omega \rho} \frac{M_1(y)}{M_o} \cos \{ \omega t - \phi - \delta_{10} \} \quad (14)$$

where

$$\delta_{10} = 135^\circ - \theta_1(y) + \theta_o \quad (15)$$

Hence, the wall shear stress is given by:

$$\tau_w = M \frac{R}{\alpha} \frac{M_1}{M_o} \cos \{ \omega t - \phi - (135^\circ - \theta_1 + \theta_o) \} \quad (16)$$

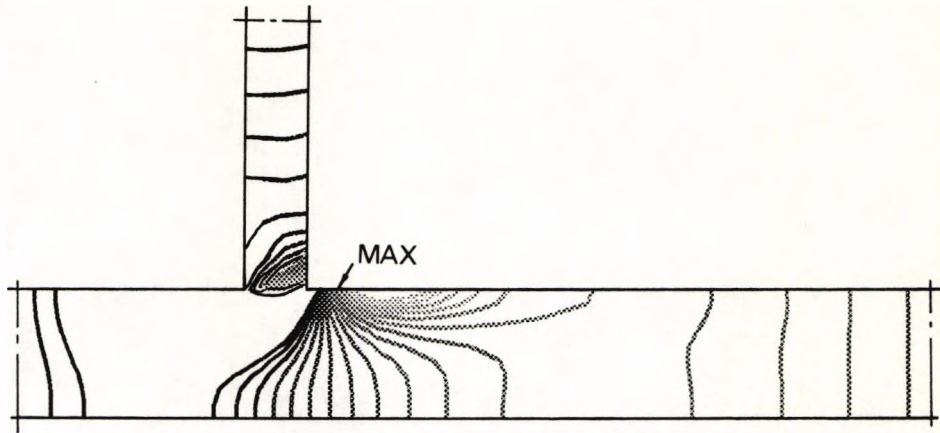
The phase lag of the wall shear stress behind the pressure gradient is up to 45° when α is large.

APPENDIX E

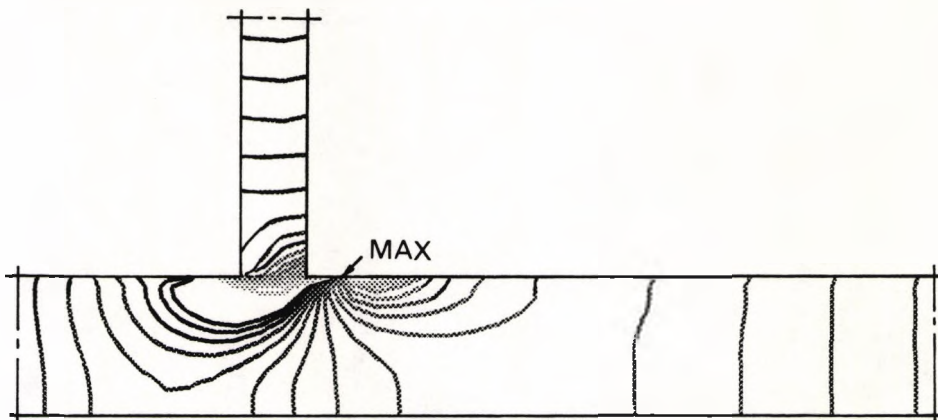
Pressure Distribution in a 3D T-bifurcation

Apart from the velocity field and variations of wall shear stress, pressure distribution in the branching region may also contribute to a better understanding of the flow phenomena occurring there. For the 3-D T-bifurcation studied in section 5.3.3, the pressure contours in the bifurcation plane are presented in Figs.E.1(a) and (b) for the maximum and minimum flow rates respectively. As indicated in the figures, the maximum pressure locations are at the corner of the flow divider and its distal positions. Pressure variations are relatively large at the immediate vicinity of the branching area owing to the flow impingment and separation. Pressure changes at the rest of the flow field due to viscous friction are rather small.

Figs.E.2(a) and (b) illustrate pressure distributions on the wall at different cross-sections (defined previously in Fig.5.25) for the maximum and minimum flow rates respectively. It is seen that proximal to the bifurcation at cross-section B, pressures on the wall at the branching side are lower than those on the outer wall. Distal to the bifurcation at cross-sections C and D, pressures on the wall at the divider side are higher than those on the outer wall. At the upstream position A and downstream positions E and F, cross-sectional pressure variations are very small.

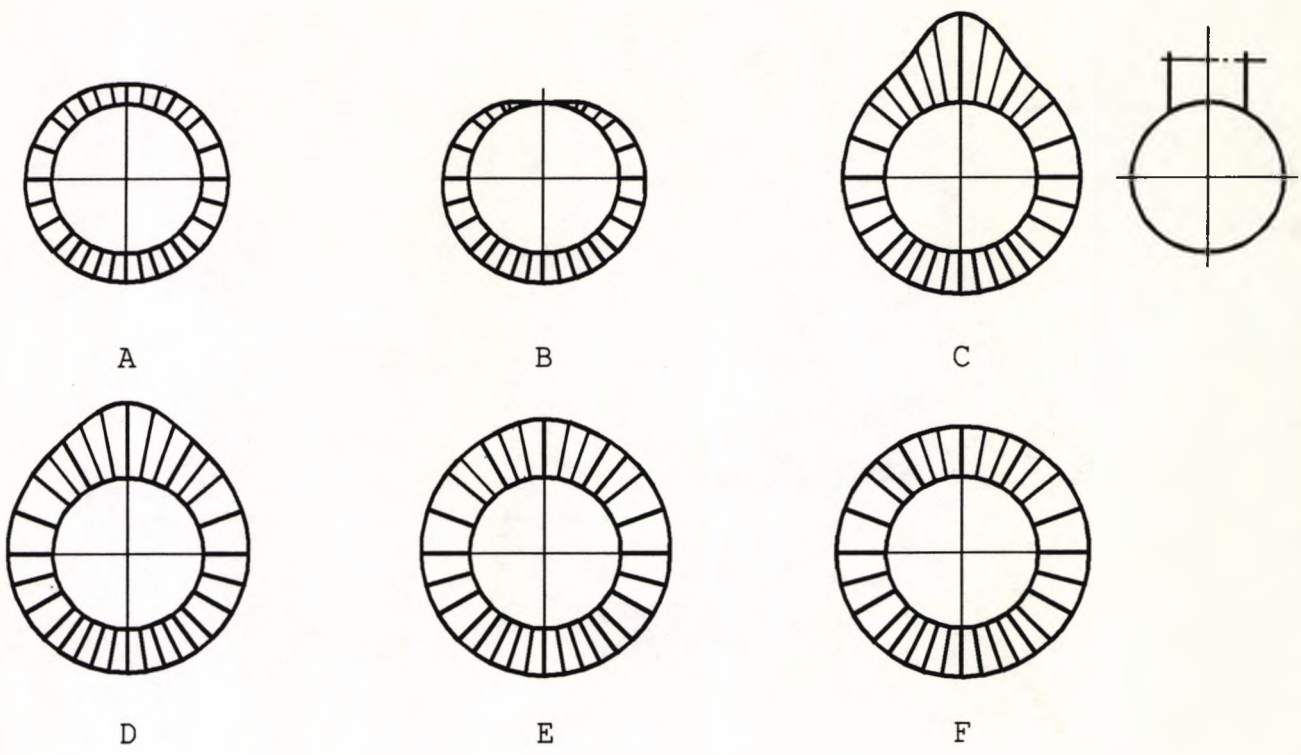


(a) at the maximum flow rate ($\omega t = 40^\circ$)

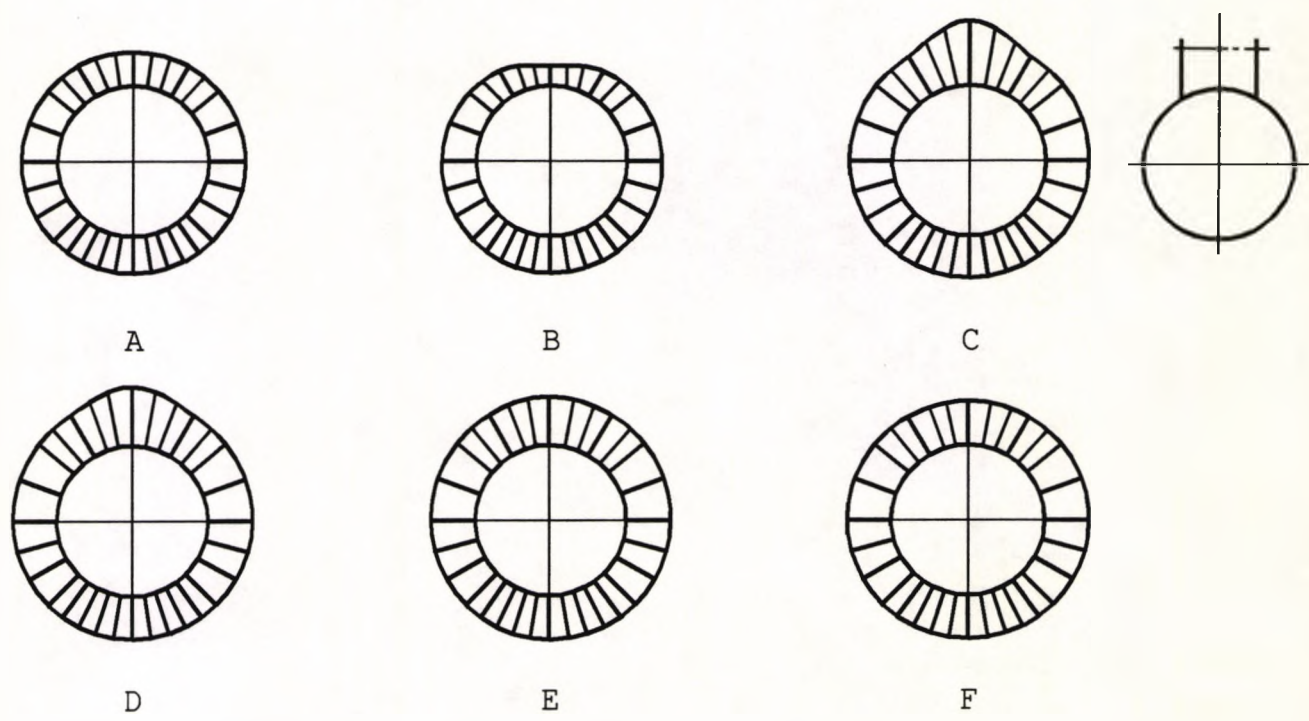


(b) at the minimum flow rate ($\omega t = 220^\circ$)

Fig. E.1 Pressure contours in the bifurcation plane of a 3D T-bifurcation for (a) the maximum, and (b) the minimum flow rates.



(a) at the maximum flow rate ($\omega t = 40^\circ$)



(b) at the minimum flow rate ($\omega t = 220^\circ$)

Fig. E.2 Pressure distributions on the wall at different cross-sections for (a) the maximum, and (b) the minimum flow rates.

APPENDIX F

PUBLISHED PAPERS

Flow Study In Canine Artery Bifurcations Using A Numerical Simulation Method.

Xu, X.Y., Collins, M.W. and Jones, C.J.H. (1992) (in the press)

ASME. J. Biomechanical Engineering.

A Review Of The Numerical Analysis Of Blood Flow In Arterial Bifurcations.

Xu, X.Y. and Collins, M.W. (1990)

Proc. Instn. Mech. Engrs. Part H: Engineering in Medicine, Vol.204, pp205–216.†

A Predictive Scheme For Flow In Arterial Bifurcations: Comparison With Laboratory Measurements.

Collins, M.W. and Xu, X.Y. (1990)

Biomechanical Transport Processes, Ed. by F.Mosora, C.Caro et al, (Plenum Press), pp125–133.†

Assessment Of The Problem Of Numerical Simulation Of Blood Flow Through Three-Dimensional Arterial Bifurcations.

Xu, X.Y. and Collins, M.W. (1989)

Biofluid Mechanics: Blood Flow In Large Vessels. Ed. by D.Liepsch (Springer-Verlag), pp455–462.

Modelling of Blood Flow In Three-Dimensional Arterial Bifurcations.

Collins, M.W. and Xu, X.Y. (1989)

ULCC Supercomputer Assisted Research Report. pp102–103.

The Effect of Non-Newtonian Viscosity On Flow And Shear-Stress At A T-Bifurcation.

Xu, X.Y. and Collins, M.W. (1992) (to be published)

The 8th International Congress of Biorheology, Beijing, August 1992.

PRESENTED PAPERS

Numerical Simulation Of Blood Flow In Arterial Bifurcation Models — Code Validation.

Xu, X.Y. and Collins, M.W. (1990)

The 43rd Meeting of The Working Party On Turbulent Flow Modelling, Harwell, February.

Grid Generation of Generalised 3-D Arterial Bifurcations.

Xu, X.Y. and Collins, M.W. (1990)

The First World Congress of Biomechanics, La Jolla, California.

Problems And Procedures in Applying Computational Fluid Dynamics To Arterial And Cardiac Flows.

Collins, M.W., Xu, X.Y., Henry, F.S. and Burns, A. (1991)

World Congress On Medical Physics And Biomedical Engineering, Kyoto, Japan.

† Included in the Appendix.

A review of the numerical analysis of blood flow in arterial bifurcations

X Y Xu, MSc and M W Collins, MA, PhD, DSc, CEng, MIMechE, MIEE, MINucE
Thermo-Fluids Engineering Research Centre, The City University, London

Arterial bifurcation flow has been of special interest for some years because of its important role in the formation of atherosclerotic plaques and thrombi. To investigate the flow phenomena analytically, four major factors need to be accommodated—the three-dimensionality of a general bifurcation, the pulsatile nature of the laminar flow, the distensibility of the arterial wall and the non-Newtonian character of the blood. In this review, both engineering and medical aspects of each factor are carefully surveyed. It is demonstrated that the latest generation of computational fluid dynamics codes can treat this problem area and that it is both feasible and desirable to investigate the effects of each independent factor.

1 INTRODUCTION

A major medical problem in the arterial system is the frequent occurrence of atherosclerosis and thrombosis in bends and bifurcations. Although the exact mechanism is unclear, a number of hypotheses have been proposed to relate haemodynamical forces to the location of atherosclerotic lesions, such as the high and low shear stress theories respectively of Fry (1) and of Caro *et al.* (2, 3). According to Fry, early atherosclerotic lesions are to be expected in regions with high shear stresses, which were found to induce endothelial injury. However, according to Caro *et al.* early lesions are more likely to develop in regions with low shear stress due to the shear-dependent mass transport mechanism for atherogenesis. Despite their apparent contradiction, one common certain point is that the local wall shear stress, and thus the local flow pattern, plays an important role. This has been further confirmed by some recent experimental studies by Fernandez *et al.* (4) and Ku *et al.* (5). Therefore, detailed analysis of flow patterns in arterial bends and bifurcations is of the utmost importance.

Considerable progress has been made in experimental studies of flow patterns in model arterial bifurcations. This work generally involved flow visualization studies by means of colouring streamlines (6) and/or the hydrogen bubble technique (7, 8), or adding particles (9) and velocity measurements by using laser Doppler anemometry and a Doppler ultrasound device (10, 11). Only a few *in vivo* measurements exist in the literature (12, 13) because of the difficulties in measuring the velocity profiles accurately in *in vivo* studies.

Efforts have been made in numerical simulation of blood flow through arterial bifurcations in recent years. The modelling of such a flow problem involves a number of novel features, such as the complex three-dimensional geometry of the bifurcation, the pulsatile nature of the flow, the distensibility of the arterial wall and the non-Newtonian characteristics of the blood. The present review attempts to take a comprehensive view of this research subject by investigating both medical and engineering aspects of each feature, thus

providing a clearly defined line of approach for further numerical research.

2 THE BIFURCATION PROBLEM

In order to simulate haemodynamic phenomena in an arterial bifurcation numerically, the geometry chosen and the grid generation become the first consideration. A brief description of recent developments in these two areas of interest to the current application is given below.

2.1 Geometry of arterial bifurcation

There is a wide range of configurations of bifurcations in the human arterial system. It has been found that almost all of them are geometrically irregular, tapered, tortured and branched in a complicated three-dimensional way (14). Also, they have rather large individual variations (15). The geometries of arterial bifurcations have been studied by a number of investigators. Because of its clinical importance, much of the work was devoted to the carotid bifurcation. Based upon a study of biplanar angiograms, Bharadvaj *et al.* (7) developed an 'average' geometry of the human adult carotid bifurcation and constructed both glass and plexiglass models. Reneman *et al.* (16, 17) used a multi-gate pulsed Doppler system to measure the relative diameter changes of the arteries during the cardiac cycle in young and old presumed healthy subjects; also the angle between the internal and common carotid artery was determined by means of a B-mode imagery. A more exhaustive study was undertaken by Forster *et al.* (18). In this study, a complete set of the common, internal and external arteries at various locations, the bifurcation angles and information on the tortuosity of the vessels is given in terms of mean values and standard deviations for a normal population, as shown in Fig. 1 and Table 1. These data can be used to improve present protocols and define limits of accuracy when utilizing ultrasonic Doppler information to assess clinically blood flow characteristics. Moreover, they are valuable in constructing a three-dimensional flow model of the carotid bifurcation.

The MS was received on 6 February 1990 and was accepted for publication on 12 November 1990.

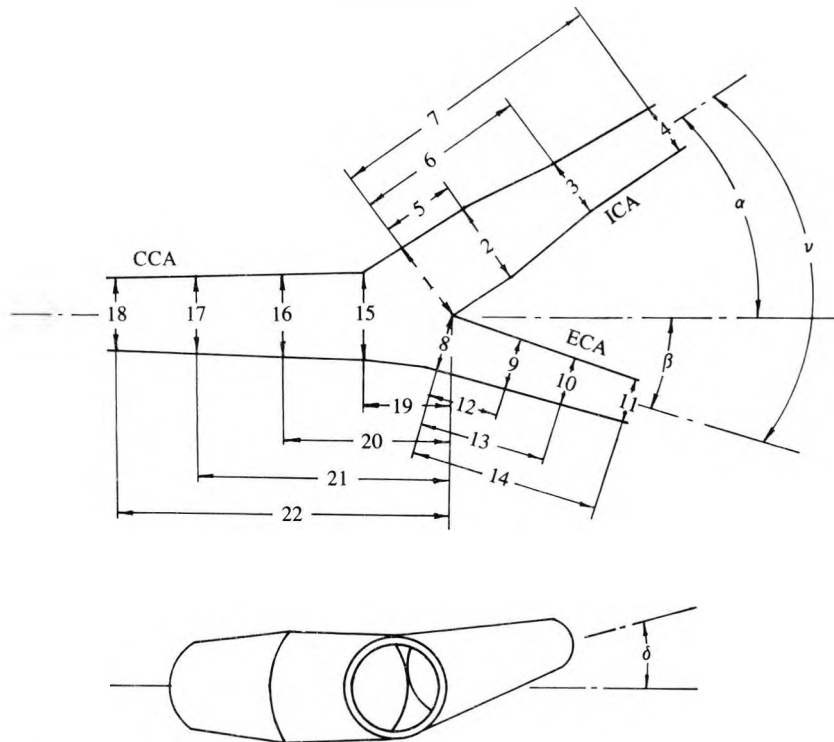


Fig. 1 Generalized geometry of carotid bifurcations. α and β are the angles from the common carotid to the internal and external carotid arteries (CCA, ICA and ECA) respectively. γ is the bifurcation angle in the plane of the ICA and ECA. δ is the angle between the ICA/CCA plane and the ECA/CCA plane

Table 1 Dimensions of a generalized carotid bifurcation [data from Forster *et al.* (18)]

Location in Fig. 1		Mean value deg	Standard deviation
Angles		33.9	13.0
		22.3	12.0
		52.6	19.5
		0.9	35.7
		Mean value mm	Coefficient of variation %
ICA	1	9.3	20.6
	2	9.4	17.5
	3	6.3	22.5
	4	5.5	13.6
	5	4.6	66.5
	6	16.7	32.7
	7	28.0	36.3
ECA	8	6.1	24.7
	9	5.0	17.8
	10	4.4	22.7
	11	4.1	24.2
	12	6.2	23.4
	13	12.6	23.2
	14	18.9	22.3
CAA	15	8.6	15.9
	16	8.1	13.6
	17	8.0	11.6
	18	7.8	12.7
	19	10.4	24.7
	20	18.8	16.9
	21	27.6	16.0
	22	36.1	16.0

2.2 Grid generation

For the application to modelling of a bifurcation the grid generation problem is crucial, since the complex boundary shapes of the bifurcation have to be represented very accurately, ensuring that no unnecessary errors are introduced. Numerical grid generation has now become a fairly common tool for use in the numerical solution of partial differential equations on arbitrarily shaped regions. Very substantial progress has been witnessed in this area in the past decade or so. A comprehensive survey of procedures and applications was given by Thompson *et al.* (19), and a number of conferences specifically in the area of numerical grid generation have been held (20, 21). Recent general surveys have been given by Thompson (22) and Eiseman and Eriebacher (23).

With the introduction of boundary-fitted curvilinear coordinate systems generated to maintain coordinate lines coincident with the boundaries, finite difference codes can be written that are applicable to general configurations without the need of special procedures at the boundaries. However, this is achieved at the expense of making the partial differential equations in the computational domain more complicated due to the non-linear coordinate transformation. Broadly speaking, numerical grid generation falls into two primary categories: algebraic methods and partial differential equation methods. A logic breakdown of these approaches is illustrated in Fig. 2.

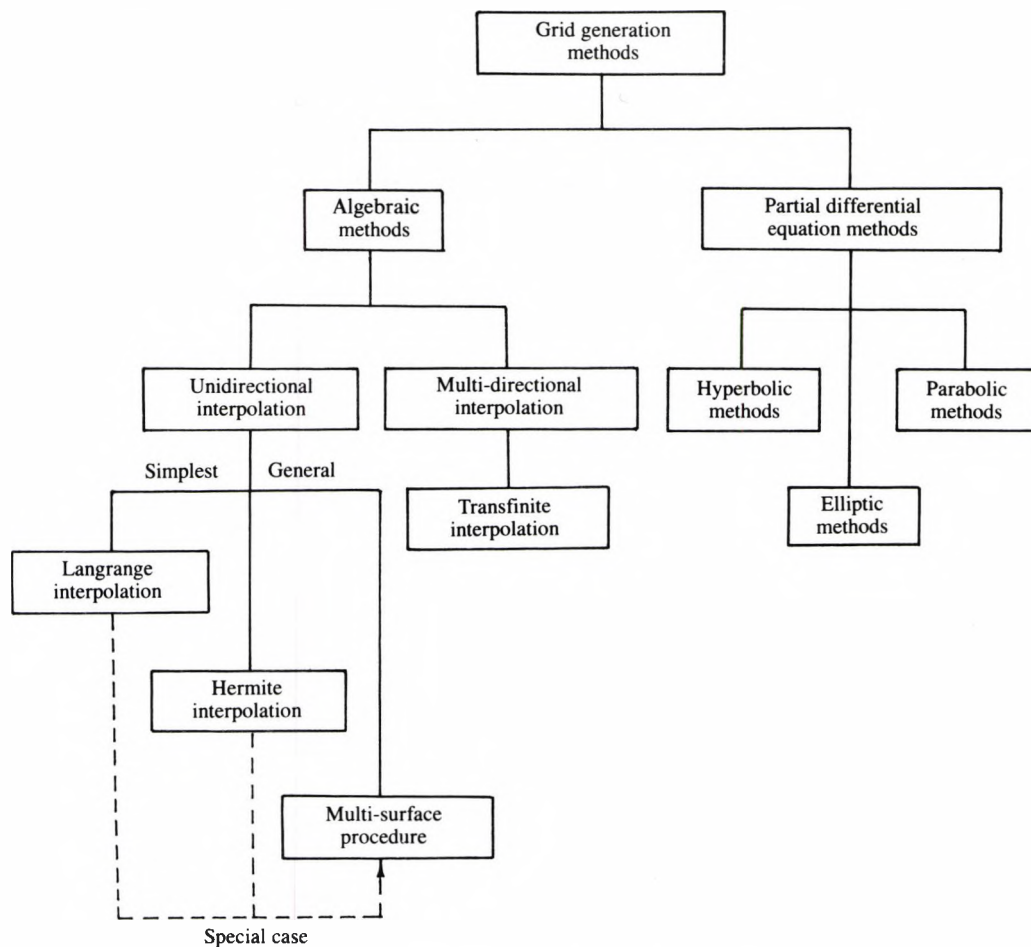


Fig. 2 Logic breakdown of grid generation methods

Algebraic methods are those in which the coordinates are determined by interpolation from the boundaries. The various interpolation methods used in algebraic grid generation can be classified as: (a) uni-directional and (b) multi-directional. The simplest uni-directional method is Lagrange interpolation and the most general one is the multi-surface procedure. The multi-directional transfinite interpolation is the most commonly used algebraic method. It was introduced by Gordon and Thiel (24) and has been used in several papers for both two-dimensional (25) and three-dimensional (26) grid generation. One of the major advantages of algebraic methods is that the generation of a mesh is performed directly and is computationally very fast. Also these techniques allow the explicit control of grid point spacing. Unfortunately, since the methods do not possess inherent smoothing properties discontinuities can arise in the mesh.

Partial differential equation systems are grid generation procedures in which the grids are the solution of a set of partial differential equations. These are further split into sub-categories entitled hyperbolic, elliptic and parabolic methods to reflect the type of partial differential equation used to generate the grids; among them the elliptic generation system is the most popular one because of its inherent smoothing properties. The application of elliptic methods can be found in Thompson *et al.* (27) and Mastin and Thompson (28). Their advantages over algebraic methods are smoothness (here meaning the continuity of geometry derivatives),

orthogonality or near-orthogonality and one-to-one guaranteed mapping. It should be stressed here that orthogonality is one of the highly desirable properties in regard to mesh generation. An orthogonal coordinate system makes the application of boundary conditions more straightforward, enables much more efficient techniques to be adopted and permits a greater degree of vectorization on supercomputers. On the other hand, severe departure from orthogonality will introduce truncation errors in difference expressions and thus reduce the accuracy of a numerical approximation. Orthogonal systems are generally applicable to any two-dimensional domain, but are difficult, or indeed impossible, to achieve in three dimensions. Therefore, it is of interest to generate grids that are nearly orthogonal, with the conditions for orthogonality being partially satisfied.

Apart from the structured meshes generated by the methods discussed above, some unstructured meshes composed of triangles or arbitrary quadrilaterals in two dimensions (and tetrahedrons or eight-node bricks in three dimensions) have also been widely used, particularly when the domain of interest is of complex shape. The techniques which are normally adopted to generate unstructured triangular meshes are either the Delaunay or the advancing front approaches, as discussed in detail by Peraire *et al.* (29). On unsaturated meshes, discretization methods which are based upon integral procedures, such as finite volume or finite element methods, are natural candidates to use. The principal advantage

Table 2 Summary of numerical research on blood flow in bifurcations

Reference	Bifurcation geometry	Type of flow	Numerical methods
O'Brien <i>et al.</i> (34)	Two-dimensional Y-type	Unsteady	Vorticity stream function
O'Brien and Ehrlich (35)	Two-dimensional T-type	Unsteady	Vorticity stream function
Liepsch and Moravec (36)	Two-dimensional T-type	Steady	Finite difference
Perktold and Hilberit (37)	Two-dimensional carotid model	Unsteady	Finite element
Rindt <i>et al.</i> (38)	Two-dimensional carotid model	Steady and unsteady	Finite element
Khodadadi <i>et al.</i> (39)	Two-dimensional T-type	Unsteady	Finite difference
Wille (40)	Three-dimensional symmetric	Steady	Finite element
Dinnar <i>et al.</i> (41)	Three-dimensional T-type	Unsteady	Finite difference
Rindt (42)	Three-dimensional carotid model	Steady	Finite element
Perktold and Peter (43)	Three-dimensional T-type	Unsteady	Finite element

of the unstructured mesh is that it provides a very powerful tool for discretizing domains of complex shape, and naturally offers the possibility of incorporating adaptivity. However, such a mesh is poorly ordered and is therefore less amenable to the use of certain algorithms and vectorized computers. In addition, it requires considerably more computer time and storage, as well as much more involved data handling procedure than does the structured mesh.

For the particular bifurcation problem concerned, the grids may be generated in two ways: (a) generating unstructured meshes and (b) segmenting the bifurcation into contiguous sub-regions, with grids being generated in each sub-region by using either algebraic or elliptic grid generation methods. The potential disadvantage of the former is the difficulty in constructing numerical finite difference schemes on unstructured grids. This difficulty is somewhat diminished by finite element formulations, which can, in a systematic fashion, generate a scheme of arbitrary order. However, the difficulty of the latter lies in the treatment of the grids at the interfaces. Some grid interfacing procedures have been developed by Miki and Takagi (30) and Steinhoff (31).

There is now a widespread availability of commercial packages for finite element and finite difference grid generation, such as the well-known TOMCAT package for two-dimensional grids (32), the Harwell finite element package TGIN (33), the interactive mesh generator SOPHIA (UKAEA) and FEMVIEW.

3 PULSATILE FLOW

The circulatory system of the human body consists of the heart muscle and two components: the pulmonary and systemic circulation systems. The systemic circulation initiated at the left ventricle is responsible for the supply of fresh blood to all the organs and tissues of the body, and thus can be considered as the feeding line of all the elements of the body. The transmission of blood through arteries is one of the most important parts of this circulation.

Blood is ejected from the left ventricle into the circulatory system by a periodic action of the heart. This added blood creates a change in pressure and results in flow of blood along the aorta and throughout the circulatory system. At any given point the pressure and velocity will change periodically, and hence the flow is pulsatile and associated with the propagation of a pressure wave. Moreover, in bends and bifurcations there are usually secondary flows. The importance of such secondary flows in the pathogenesis of atherosclerosis

has led to great interest in seeking detailed knowledge of flow fields in bifurcations. Some of the recent numerical research on this subject and the development of numerical methods and computer codes are surveyed below.

3.1 Recent numerical studies

Over the past few years, considerable progress has been made in numerical simulation of blood flow through arterial bifurcations. Some of the most important research is summarized in Table 2. In these studies the following assumptions are made: the blood is homogeneous, incompressible and Newtonian, and the flow is laminar, stationary and isothermal, the vessel wall being rigid.

Preliminary numerical studies have been performed by O'Brien *et al.* (34, 35) on two-dimensional unsteady flow through symmetric bifurcations using a vorticity stream function method. This algorithm has some attractive features and has been rather popular in two-dimensional simulations for a long time. The pressure makes no appearance, and, instead of dealing with the continuity equation and two momentum equations, only two equations need to be solved to obtain the stream function and vorticity. However, the major shortcoming of the method is that it cannot easily be extended to three-dimensional situations, for which a stream function does not exist. Thus, attention has turned to methods that use the so-called primitive variables, namely the velocity components and pressure. These procedures were adopted in most of the numerical research papers (36–43), in which the flow patterns, velocities, pressures and wall shear stresses for steady and/or unsteady flow were computed using finite difference or finite element techniques. These investigations have served to identify regions of separation and vortex motion and have provided numerical estimates of the distributions of wall shear stress and pressure which may qualitatively represent those found *in vivo*. However, it should be noted that previous numerical simulations are mostly restricted to two dimensions. Three-dimensional modelling is virtually essential, due to the absence of non-negligible three-dimensional phenomena, such as secondary flows, in a two-dimensional case. Only a few three-dimensional simulations have been performed. As an initial step, Wille (40) developed a three-dimensional mathematical model of steady flow in a symmetrical bifurcation by using the finite element method. Nevertheless, this method required too long a computational time, thus prohibiting further simulation development. Another computation scheme based on

finite difference methods was presented by Dinnar *et al.* (41). In an application to a 90° T-bifurcation of rectangular cross-section, the suggested scheme proved to be extremely efficient in comparison to the finite element method. The latest three-dimensional simulations have been performed by Rindt (42) for steady flow in a carotid bifurcation and Perktold and Peter (43) for pulsatile flow in an arterial T-bifurcation model, by using a standard Galerkin finite element method with supercomputers. To our knowledge, no numerical studies have been performed that deal with the pulsatile flow in a model of an asymmetric three-dimensional artery bifurcation with a complex geometry. This is mainly because the complexity of the geometry combined with the pulsatile nature of the flow not only creates difficulties in generating efficiently an appropriate mesh but also results in a large demand in computer storage and time. Only with a highly vectorized fluid dynamics code and a supercomputer can the solution of such a problem become practicable.

3.2 Numerical methods and available computer codes

Historically, the basic equations for fluid flow were formulated especially by Navier (1822) and Stokes (1840–50). A question then was whether they were equally applicable to laminar or turbulent flows, and this issue was resolved by Osborne Reynolds in 1895 (44). He decomposed the basic equations essentially into a time-averaged (or space-averaged) main flow and a turbulent fluctuation structure. Turbulence may be physically viewed as the motion of three-dimensional transient eddies of sizes ranging from those of a confining duct to the microscale of dissipation to thermal energy. Hence, not only are the basic equations very non-linear, requiring simultaneous satisfaction of continuity and momentum principles, but true treatment of turbulence is both three-dimensional and transient. Laminar flows, however, are amenable to assumptions of steadiness and geometrical symmetry, and up to the development of digital computers analytical solutions tended to be confined to them for cases of simple flows and geometries. Similar assumptions were held (but somewhat questionably) for the Reynolds-averaged turbulent equations.

With the advent of digital computers and finite difference methods in particular, it became possible to treat a much fuller form of the equations. Two-dimensional steady flows became standard, and a typical example of a laminar treatment (also allowing for temperature-dependent properties, non-Newtonian viscosity and viscous dissipation) was that of Collins (45–47). Because the simplifying assumptions were theoretically valid, apart from the numerical approximation and solution errors, comparisons with experiment should be good. In fact, this was generally found. Turbulent flows, however, required (a) the specification of the interaction of the 'turbulent fluctuation field' on the main field equations (a turbulence model) and (b) the validity of the 'two-dimensional steadiness' assumption. An internationally known typical turbulent computer code was that of Gosman *et al.* (48), namely TEACH-T. This utilized the SIMPLE algorithm of Spalding (see note on Table 3) to treat simultaneously the continuity and momentum principles, and the additional partial differential trans-

Table 3 Comparison of pressure-velocity coupling algorithms [from Ciofalo and Collins (61)]

Algorithm	SIMPLE	SIMPLEC	PISO	PISOC
Stopping criterion ϵ_M/M	10 ⁻³	10 ⁻³	—	—
Maximum number of iterations	100	100	1	1
RF (momentum equations)	0.1	0.1	0.01	0.01
CPU time (s)	758	424	670	620

ϵ_M Mass source residual (sum of the absolute values of net mass fluxes in/out of the control volumes) required to stop the outer iterations
 \dot{M} Total mass flowrate
 RF Residual reduction factor (ratio of final/initial residual) for stopping the linear equation iterative solvers

Notes:

- SIMPLE** The prototype of all the pressure-velocity coupling algorithms. It is essentially based on a two-step iterative cycle, in which a guessed pressure field is introduced in the momentum equations to evaluate velocities, and then a pressure-correction equation, derived by enforcing continuity under certain simplifications, is solved to obtain an improved guess.
- SIMPLEC** Proposed as an improvement to SIMPLE. It is based on a more consistent expression for the coefficients of the discretized pressure-correction equation, and has been shown to allow faster convergence for problems dominated by pressure gradients and drag forces.
- PISO, PISOC** In the PISO algorithm, an additional pressure-correction step is performed at each iteration to improve the solution of the momentum equations while maintaining continuity. The same modifications for SIMPLEC may be equally applied to PISO, yielding the PISOC algorithm.

port equations for k (turbulent kinetic energy) and ϵ (dissipation rate of k). General turbulence modelling at that time was well described by Launder and Spalding (49).

More recently, the advent of supercomputers and their parallel processing has meant that the full three-dimensional transient equations can be treated. These two features have been accompanied (as has been seen) by arbitrary grid generation methods. Hence, in principle, almost any laminar flow can be directly simulated (DS), and this can also be done for transitional and even low turbulent flows. For high turbulent flows, either conventional turbulence modelling or large eddy simulation is needed [for example see Voke and Collins (50) and Grotzbach (51)]. There are two real reservations, that of the computer storage and run-time, that is practicability and cost, and the necessity for a whole sequence of code validations. Having said this, however, such codes are ideal for the problem being considered (and other human circulation flows), as they can properly investigate pulsatility effects and even, if necessary, low turbulent effects. It must be admitted, though, that the latter would be a taxing computational exercise, with connotations of growth of small disturbances and numerical diffusion (52).

The pulsatile blood flow through a three-dimensional arterial bifurcation, then, can be described by the time-dependent three-dimensional Navier–Stokes equations. Expressed in compact tensor notation, with summation over repeated indices, the basic momentum and continuity principles may be expressed as

$$\frac{\partial}{\partial t} (\rho u_i) + \frac{\partial}{\partial x_j} (\rho u_j u_i) = \frac{\partial}{\partial x_j} \sigma_{ij} + F_{ij} \quad (1)$$

and

$$\frac{\partial \rho}{\partial t} + \frac{\partial}{\partial x_i} (\rho u_i) = 0 \quad (2)$$

where σ is a general stress and F a body force source term.

This is a general form, expressing the basis of many numerical treatments. Omitting the development for the sake of conciseness [but see Collins and Ciofalo (53)], the equations for blood of constant density in a Cartesian coordinate system may be written as:

Momentum equations:

$$\frac{\partial u}{\partial t} + \frac{1}{\rho} \frac{\partial p}{\partial x} - \nu \left(\frac{\partial^2 u}{\partial x^2} + \frac{\partial^2 u}{\partial y^2} + \frac{\partial^2 u}{\partial z^2} \right) + u \frac{\partial u}{\partial x} + v \frac{\partial u}{\partial y} + w \frac{\partial u}{\partial z} = 0 \quad (3)$$

$$\frac{\partial v}{\partial t} + \frac{1}{\rho} \frac{\partial p}{\partial y} - \nu \left(\frac{\partial^2 v}{\partial x^2} + \frac{\partial^2 v}{\partial y^2} + \frac{\partial^2 v}{\partial z^2} \right) + u \frac{\partial v}{\partial x} + v \frac{\partial v}{\partial y} + w \frac{\partial v}{\partial z} = 0 \quad (4)$$

$$\frac{\partial w}{\partial t} + \frac{1}{\rho} \frac{\partial p}{\partial z} - \nu \left(\frac{\partial^2 w}{\partial x^2} + \frac{\partial^2 w}{\partial y^2} + \frac{\partial^2 w}{\partial z^2} \right) + u \frac{\partial w}{\partial x} + v \frac{\partial w}{\partial y} + w \frac{\partial w}{\partial z} = 0 \quad (5)$$

Continuity equation:

$$\frac{\partial u}{\partial x} + \frac{\partial v}{\partial y} + \frac{\partial w}{\partial z} = 0 \quad (6)$$

where u , v and w are the velocity components in the x , y and z directions respectively. The pressure is p , ρ is the density of the fluids and ν is the kinematic viscosity. To solve numerically such equations is an arduous task in computational fluid dynamics, especially when the flow field of interest is of a complex geometry. Generally speaking, two approaches can be made to treat this problem, those using (a) finite element and (b) finite difference methods.

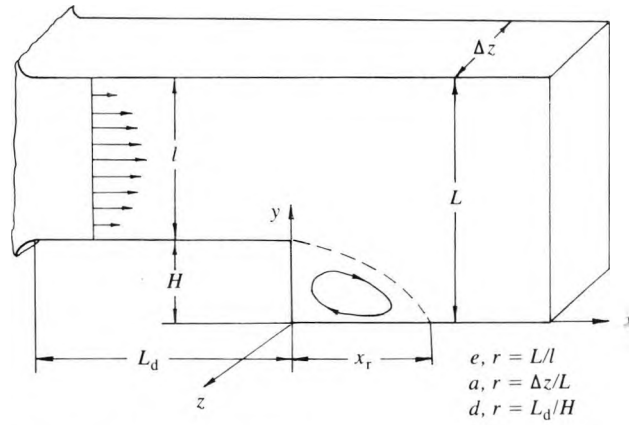
Finite element methods subdivide the calculation domain into elements, and over each element approximate the dependent variables by a 'shape function' or profile assumption. The discretization equations are usually derived by the use of a variational principle or a weighted residual method (such as the Galerkin method). The major advantage of finite element methods is their geometrical flexibility, so that complex geometries can be modelled with relative ease. However, these methods are sophisticated and computationally very expensive for three-dimensional problems due to the large system of algebraic equations involved. On the other hand, finite difference methods are less complicated and less expensive in their use of computer storage and time, but are less amenable to geometrically complex problems.

To overcome these inherent problems, tremendous efforts have been made. Both finite element and finite difference methods have been improved to a certain extent. Gresho (54) has modified the finite element method for solving the time-dependent incompressible Navier-Stokes equations, but the computer code produced was still more expensive than the standard finite difference codes. FLOW3D, recently developed at AERE, Harwell, is a good example of a flow modelling

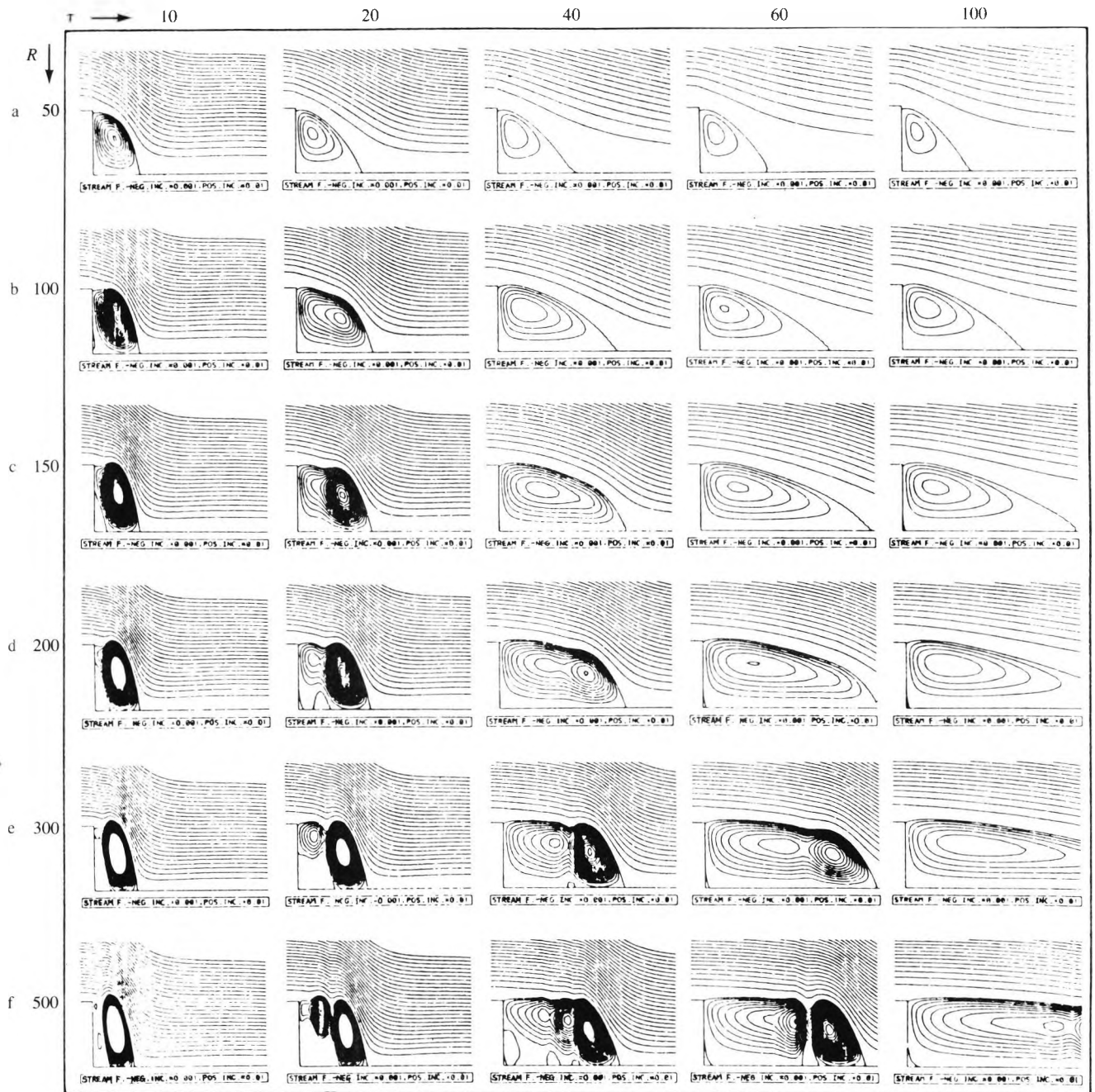
code using finite difference methods. It has three-dimensional time-dependent capability and uses non-orthogonal body-fitted coordinates. One of the key features of FLOW3D is its poly-algorithm structure, whereby options are available for the user to specify different solution algorithms, that is SIMPLE (55), SIMPLEC (56), PISO (57) and PISOC, and different linear algebra solvers, that is line relaxation, Stones' method and ICCG (58). The code's architecture and general characteristics are described by Burns *et al.* (59). Details of the computational treatment of the equations, with emphasis on non-orthogonal grids, are given by Burns and Wilkes (60). This software is being continually tested and refined through applications to both simple test problems and challenging practical engineering problems. Extensive studies of the transient laminar flow over a complex back-step arrangement via this code have been carried out by Ciofalo and Collins (61). In this work the influences of boundary and initial conditions, differencing schemes, time stepping, pressure-velocity coupling algorithms and other parameters are discussed in detail. Conciseness permits reporting here just one of these features, that of the above coupling algorithm. The investigation is summarized as Table 3 [Table III of reference (61)]. SIMPLE has already been mentioned and the others are derivatives. SIMPLEC was concluded to be the best alternative, both from time aspects and accuracy. PISO and PISOC have resulted in errors in certain circumstances. In our application, we will be investigating (probably) time-dependent flow structures, and Fig. 3 [taken from reference (61)] gives an example of two-dimensional effects. Figure 3a defines the geometry, while Fig. 3b gives attractive stream function plots for a variety of Reynolds numbers and times.

One of the major aims of improving finite difference codes is to extend their use to cases of complex geometries. FLOW3D has this capability by using body-fitted coordinates. A small-angle bifurcation problem can be solved by introducing a splitter plate as a solid region in computation space. Further, a general bifurcation can be treated by using multiple-block structured grids (which has just been implemented in Release 3). Hence, FLOW3D should be considered as having a near-future good capability to model a general arterial bifurcation flow.

Another engineering code is ASTEC, recently developed at UKAEA (62). In this code, finite difference methods have been applied on a finite element mesh which makes it a unique fluid flow code combining the economy of the former with the geometrical flexibility of the latter. The element required by ASTEC are arbitrary quadrilaterals in a two-dimensional case and eight-node blocks in three dimensions. Although each element must have eight nodes, note that there is no restriction regarding the number of elements to which a particular node belongs. The conservation equations are described in integral form and are solved numerically by applying them to individual nodal control volumes. In ASTEC, the volume integrals are approximated by assuming that the mean value of the variable over the control volume equals the nodal value. However, the pressure gradient term is converted to a surface integral of pressure using Gauss's divergence theorem. The surface integrals are evaluated by summing over the faces of the control surface, and on each face the pres-



(a) Geometry and nomenclature



(b) Streamline evolution for various Reynolds numbers (R) and times (R is based on free-stream velocity and step height H , τ is non-dimensional time $\equiv t u_0/H$, where u_0 is impulsive starting velocity and t dimensional time)

Fig. 3 Two-dimensional transient predictions for a backward-facing step, using a modern CFD code [from Ciofalo and Collins (61)]

Table 4 Main characteristics of FLOW3D and ASTEC

Capabilities	FLOW3D	ASTEC
(1) Type of flow		
Laminar/turbulent	Y/Y	Y/Y
Steady/transient	Y/Y	Y/Y
Incompressible/compressible	Y/Y	Y/Y
Non-buoyant/buoyant	Y/Y	Y/Y
Isothermal/non-isothermal	Y/Y	Y/Y
Newtonian/non-Newtonian	Y/Y	Y/Y
(2) Grid	Body-fitted Adaptive grids	Finite element
Numerical methods	FLOW3D	ASTEC
Pressure/velocity coupling algorithms	SIMPLE, SIMPLEC, PISO, PISOC	SIMPLE
Space-differencing schemes	Central (CD), upwind (UW), hybrid upwind (HU), second-order upwind (HUW), third-order upwind (QUICK)	HU, Skew upwind, reduced skew upwind
Linearized equation solvers	Line relaxation (LRLX), preconditioned conjugate gradients (ICCG), Stone's strongly implicit method (SIP) etc.	ICCG
Time-differencing schemes	Crank Nicolson, fully implicit	Fully implicit

sure and the advective and diffusive fluxes are approximated in terms of nodal values of the variables. The pressure on the face is simply assumed to be the mean of the pressures at the two nodes whose control volumes are separated by the face. To minimize the false diffusion errors associated with the advection terms, a skew upwind scheme is employed. A special interpolation procedure of Rhie and Chow (63) is used to avoid pressure checkerboarding. The procedure for solving the discrete equations is iterative and based on the SIMPLE method. A preconditioned conjugate gradient algorithm is used to calculate the pressure corrections. The time differencing is fully implicit, so that there is no Courant stability restriction to the time step.

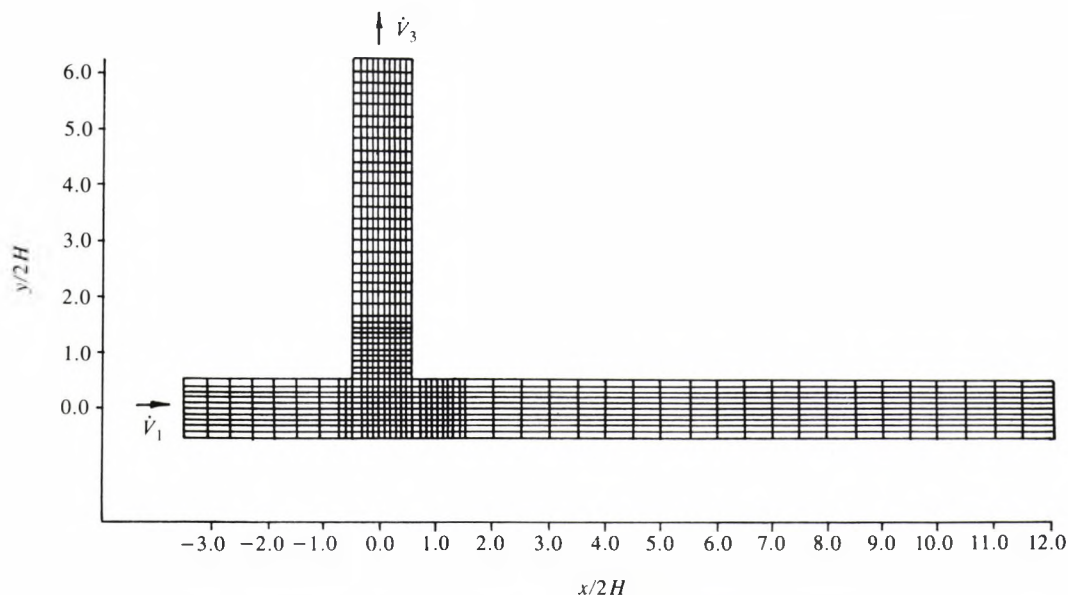
FLOW3D and ASTEC have very similar capabilities, which together with the employed numerical methods are summarized in Table 4. However, by using a finite element mesh of eight-node blocks, ASTEC provides much greater geometrical flexibility than FLOW3D does. The ASTEC code, again, appears to be of high potential to model flows through a realistic arterial bifurcation.

A further alternative is the commercial code PHOENIX from CHAM (concentration heat and momentum). CHAM is considering a T-junction bifurcation problem to assess predictions comparable to those from FLOW3D or ASTEC (D. B. Spalding, unpublished personal communication, 1989).

To make the solution of large three-dimensional problems sufficiently fast, a high degree of vectorization is essential to obtain best performance from present-day supercomputers. Both FLOW3D and AZTEC have been tailored for the supercomputer CRAY in the sense that the program is written so that the CRAY compiler CFT77 will produce a highly vectorized code.

3.3 Validations of the computer codes

With the new generation of computer codes careful validation exercises should be carried out, and in an engineering context this is discussed extensively by Collins and Ciofalo (53). For the current medical application, the LDA measurements of Liepsch and Moravec (36)

**Fig. 4** Bifurcation geometry and mesh division (channel height $2H = 10$ mm)

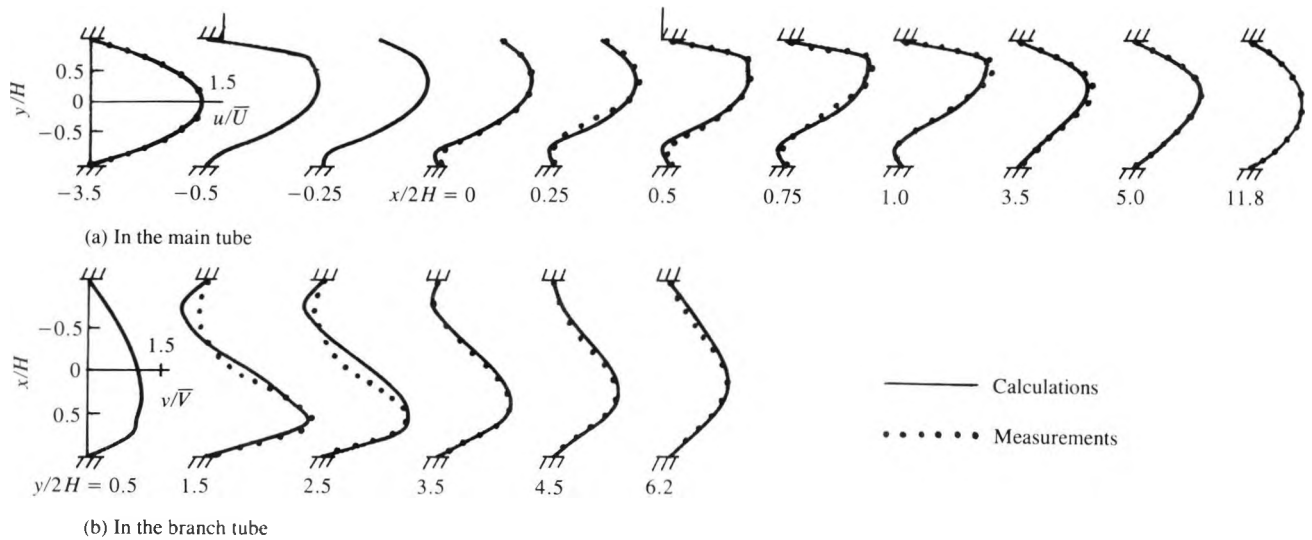


Fig. 5 Comparison between calculations of ASTEC and the LDA measurement of Liepsch and Moravic (36) for a Reynolds number of 496 and a branch-main tube flowrate ratio of 0.44 (positions are indicated in Fig. 4)

were felt to be ideal. For both FLOW3D and ASTEC simple tests were carried out on a two-dimensional steady laminar flow in a T-bifurcation for Reynolds numbers ranging from 250 to 1100. Figure 4 shows the bifurcation geometry and element division used in the calculations. A quantitative comparison of the calculated and measured results for a Reynolds number of 496 and a branch-main tube flowrate ratio of 0.44 is presented in Fig. 5, while in Fig. 6 the computational results of ASTEC are compared with those of FLOW3D for the same test case. It is observed that the computational results of ASTEC and FLOW3D are consistent, and show very good agreement with measurement.

The presented results are for the case of steady flow of a Newtonian fluid in a rigid two-dimensional T-junction only. So far, code validations have also been performed on pulsatile flow in a two-dimensional T-

junction, both steady and pulsatile flow in a three-dimensional T-junction with a circular cross-section and steady flow of a non-Newtonian fluid in a rigid tube. Because of the limitation of space, these results are not presented here, part of them being published in Collins and Xu (64). To date, all the work is laminar.

4 VESSEL WALL DISTENSIBILITY

Blood vessel walls are viscoelastic inhomogeneous multi-layered tissues. They are composed mainly of connective tissues and smooth muscle. Experimental results have shown that the blood vessel wall exhibits non-linear viscoelastic properties, and the vessel diameter may change by some 10 per cent depending on age.

In most of the previous work, distensibility of the arterial wall was regarded as a 'second-order' effect on

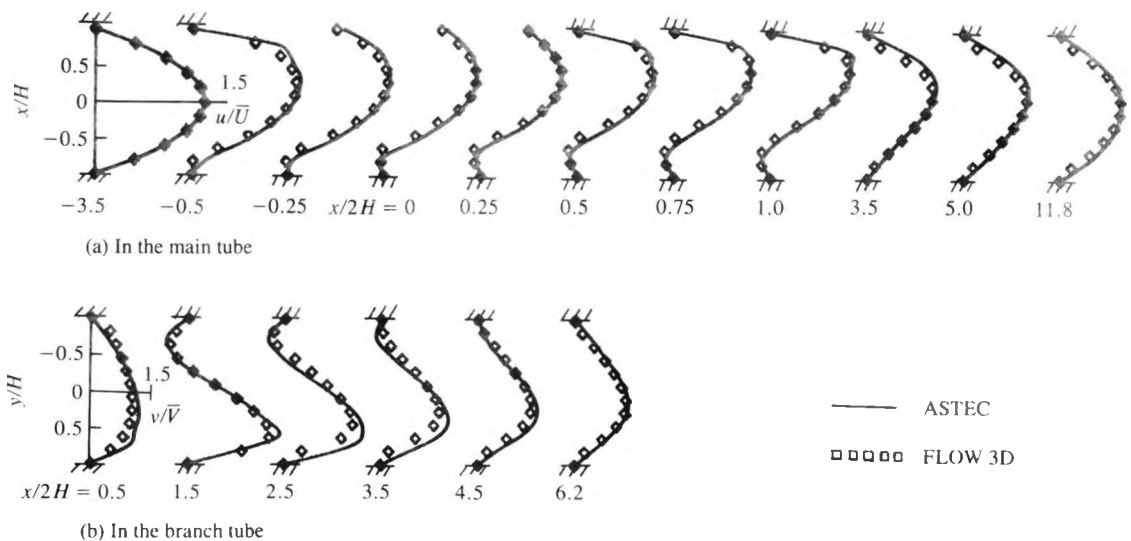


Fig. 6 Comparison between calculations of ASTEC and calculations of FLOW3D for a Reynolds number of 496 and a branch-main tube flowrate ratio of 0.44 (positions are indicated in Fig. 4)

arterial bifurcation flow and was generally neglected. Even so, it is well known that distensibility is an important factor in pulsed-wave propagation. A recent experimental study performed by Ku and Liepsch (65) has shown the differences between rigid and elastic wall behaviour during pulsatile flow. The experiment was carried out with (a) a rigid glass model and (b) an elastic silicon rubber model in pulsatile flow. When dealing with the elastic silicon model obvious reductions in negative velocities and the size of secondary flow regions were observed. This demonstrated the fact that wall elasticity may well be an important factor in the understanding of bifurcation flows. A proper mathematical model of the mechanical behaviour of the arterial wall is essential to the investigation of their effects on arterial flow. Many different descriptions have been derived with various assumptions of arterial wall behaviour, such as membrane, thick shell, elastic, visco-elastic, linear or non-linear. These models have been extensively studied and applied in linear theories of Womersley (66) and McDonald (67) and non-linear theories of Anliket *et al.* (68). However, all these analyses are restricted to one-dimensional flow.

A two-dimensional wall motion (in radial and axial directions) based on the membrane theory of thin elastic shells has been recently applied by Liepsch (69) in an investigation of the propagation of pressure waves through a straight thin-walled elastic tube. This study has shown that theoretical velocity profiles in elastic tubes, obtained from measured pressure gradient waveforms via linear theory, agree well with measured profiles. It may be considered as a starting point for further research in the field. In fact, in the City University Research Centre a research programme is being commenced to survey and develop a mathematical model of the arterial wall.

An important issue to accommodate the wall distensibility in numerical modelling of an arterial bifurcation flow is the problem of moving boundaries, which requires the coordinate system to be time dependent because the boundaries move, either of themselves or in response to influences of the physical problem. The simplest procedure is to regenerate the coordinate system at each time step using the new boundary locations, or other factors from the physical solution at the previous time step. The solution for the new coordinates at each time step thus is done separately from the physical solution at that step. Alternatively, the equations for the coordinate system can be added to the system of physical solution equations and the entire set of equations solved simultaneously at each time step. For the particular problem concerned, the motion of the coordinate system is caused by deformation of the arterial wall. The driving forces that deform the arterial wall include the pressure and shear stress exerted by the blood. As an initial step, deformation of the arterial wall can be simplified as circumferential extensions only. By evaluating the normal pressure on the wall and moving it along the normal vector to a 'force-free' position, the new boundary locations at each time step will then be determined. The incorporation of the moving grid into the solution algorithm, in general, is the same regardless of the reason for grid movement. Several examples of grids following boundary motions are cited by Thompson *et al.* (19). Since the time derivative of the Jacobian

for the coordinate transformation from physical to computational domain is introduced, more computations are necessary.

5 NON-NEWTONIAN EFFECTS

Blood is a suspension of formed elements in plasma. These formed elements are the red cells, white cells and platelets, in which red cells are by far the most numerous and completely dominate the mechanical properties. Extensive work has been done on the determination of the mechanical properties of blood, particularly the value of blood viscosity and its dependence on shear rate. Although all the issues about the viscous behaviour of blood components have still not been resolved, it is well accepted that blood can be considered as Newtonian at high shear rates but non-Newtonian at low shear rates.

In most of the previous studies pure Newtonian behaviour of blood was assumed, since the non-Newtonian behaviour of blood, like wall distensibility, was regarded widely as a 'second-order' effect on arterial bifurcation flow. The non-Newtonian effects have been much less extensively studied than the other factors. Currently, however, attention is being paid to them, and they may have some significance in the parts of the bifurcation of greatest interest.

Moravec and Liepsch (70) studied the differences in flow behaviour of Newtonian and non-Newtonian fluids in a simplified three-dimensional model of the human renal artery bifurcation by using a laser Doppler anemometer. In this study, substantial differences were found in the flow behaviour of the Newtonian and non-Newtonian fluids, especially in zones of flow separation and secondary flow. Another experimental work performed by Ku and Liepsch (65) also revealed this fact. All these results tend to indicate that non-Newtonian flow behaviour cannot be neglected, even in large blood vessels. It is, therefore, necessary to accommodate this factor in numerical studies. Both of the computer codes assessed above are capable of treating a non-Newtonian fluid flow.

6 CONCLUSION

Blood flow through an arterial bifurcation is laminar but substantially three-dimensional, containing vortices and secondary flows. This problem involves many complicating factors, such as three-dimensional geometries, pulsatility, wall distensibility and non-Newtonian visco-elasticity. The best line of approach to deal with such a complex problem is to isolate each character and study it separately. This rationale was also followed by Ku and Liepsch (65), in order to specify the relative effects of each.

Two examples of the latest generation of computer codes, FLOW3D and ASTEC, have been assessed in detail, and are capable of treating this problem area. The computed results for steady flow in a plane T-bifurcation have been validated by comparison with published LDA measurements; the comparison is very satisfactory. Three-dimensional predictions have also been performed and some of the results have been published (64).

It is intended to investigate the effects of non-Newtonian viscosity and flexible wall in a three-dimensional T-bifurcation model, which should be the same as the one employed by Ku and Liepsch (65); this will complete the code validation exercise. Then it will be possible to progress to *in vivo* bifurcation flow predictions, some of which have already been made (71).

A parallel research programme to investigate mathematical models of the arterial wall is also in progress.

The review presented here is abridged from an earlier internal report by the authors (72). For a more thorough and in-depth discussion of computational fluid dynamics work, the reader is referred to the review by Collins and Ciofalo (53).

ACKNOWLEDGEMENTS

The authors gratefully acknowledge the support of a British Heart Foundation Research Grant for this programme of work.

REFERENCES

- 1 Fry, D. L. Haemodynamic forces in atherogenesis. In *Cerebrovascular disease*, 1976, pp. 77–95 (Raven Press, New York).
- 2 Caro, C. G., Fitz-Gerald, J. M. and Schroter, R. C. Atheroma and arterial wall shear. Observation, correlation and proposal of a shear dependent mass transfer mechanism for atherogenesis. *Proc. R. Soc. Lond.*, 1971, **B171**, 109–159.
- 3 Caro, C. G. Arterial fluid mechanics and atherogenesis. *Recent Advances in Cardiovascular Disease*, 1981, **2**, 6–11.
- 4 Fernandez, R. C., Witt, K. J. and Botain, M. R. Pulsatile flow through a bifurcation with applications to arterial disease. *J. Biomech.*, 1976, **9**, 575–580.
- 5 Ku, D. N., Giddens, D. P., Zarins, C. K. and Glagov, S. Pulsatile flow and atherosclerosis in the human carotid bifurcation. *Arteriosclerosis*, 1985, **5**(3), 293–302.
- 6 Stehbens, W. E. Flow in glass models of arterial bifurcations and berry aneurysm at low Reynolds numbers. *Q. J. Expl. Physiol.*, 1975, **60**, 181–192.
- 7 Bharadvaj, B. K., Mabon, R. F. and Giddens, D. P. Steady flow in a model of the human carotid bifurcation. Part I—Flow visualisation. *J. Biomech.*, 1982, **15**, 349–362.
- 8 Ku, D. N. and Giddens, D. P. Pulsatile flow in a model carotid bifurcation. *Arteriosclerosis*, 1983, **3**(1), 31–39.
- 9 Karino, T., Kwong, H.M. and Goldsmith, H.L. Particle flow behaviour in models of branching vessels; I. Vortices in 90° T-junctions. *Biorheol.*, 1979, **16**, 231–248.
- 10 Bharadvaj, B. K., Mabon, R. F. and Giddens, D. P. Steady flow in a model of the human carotid bifurcation. Part II—Laser-Doppler anemometer measurements. *J. Biomech.*, 1982, **15**, 363–378.
- 11 Lutz, R. T., Hsu, L., Menamat, A., Zrubek, J. and Edwards, K. Comparison of steady and pulsatile flow in a double branching arterial model. *J. Biomech.*, 1984, **18**, 753–759.
- 12 Ku, D. N. and Giddens, D. P. Haemodynamics of the normal human carotid bifurcation: *in vitro* and *in vivo* studies. *Ultrasound in Med. Biol.*, 1985, **11**(1), 13–26.
- 13 Jones, C. J. H., Lever, M. J., Ogasawara, Y., Parker, K. H., Tsujioka, K., Hiramatsu, O., Caro, C. G. and Kajiyama, F. Velocity profiles at an arterial bifurcation: measurement using high frequency multichannel Doppler ultrasound (to be published).
- 14 Pedley, T. J. *The fluid mechanics of large blood vessels*, 1980 (Cambridge University Press).
- 15 Lippert, H. and Pabst, R. *Arterial variations in man*, 1985 (J. F. Bergmann Verlag, Munchen).
- 16 Reneman, R. S., Merode, T., Van, H. P. and Hoeks, A. P. G. Flow velocity patterns in and distensibility of the carotid artery bulb in subjects of various ages. *Circulation*, 1985, **71**, 500–509.
- 17 Renaman, R. S., Merodes, T., Van, H. P. and Hoeks, A. P. G. Cardiovascular applications of multi-gate pulsed Doppler systems. *Ultrasound in Med. Biol.*, 1986, **12**, 357–370.
- 18 Forster, F. K., Chikos, P. M. and Frazier, J. S. Geometric modelling of the carotid bifurcation in humans: implications in ultrasonic Doppler and radiologic investigations. *J. Clin. Ultrasound*, 1985, **13**, 385–390.
- 19 Thompson, J. F., Warsi, Z. U. A. and Mastin, C. W. Boundary-fitted coordinate systems for numerical solution of partial difference equations—a review. *J. Comput. Physics*, 1982, **47**, 1–108.
- 20 Thompson, J. F. *Numerical grid generation*, 1982 (North-Holland).
- 21 Hauser, J. and Taylor, C. Numerical grid generation in computational fluid dynamics. Proceedings of the International Conference held at Landshut, 1986, Germany.
- 22 Thompson, J. F. Grid generation techniques in computational fluid dynamics. *AIAA J.*, 1984, **22**(11), 1505–1523.
- 23 Eiseman, P. R. and Eriebacher, G. Grid generation for the solution of partial differential equations. NASA contractor report 178365, 1987.
- 24 Gordon, W. J. and Thiel, L. C. Transfinite mapping and their applications to grid generation. In *Numerical grid generation* (Ed. J. F. Thompson), 1982 (North-Holland).
- 25 Usab, W. J. and Murman, E. M. Embedded mesh solution of the Euler equations using a multiple-grid method. AIAA papers, 1983.
- 26 Erikson, L. E. Generation of boundary-conforming grids around wing-body configurations using transfinite interpolation. *AIAA J.*, 1982, **20**(10), 1313–1320.
- 27 Thompson, J. F., Thames, F. C. and Mastin, C. W. Automatic numerical generation of body-fitted curvilinear system for field containing any number of arbitrary two-dimensional bodies. *J. Comput. Physics*, 1974, **15**, 299–319.
- 28 Mastin, C. W. and Thompson, J. F. Transformation of three-dimensional regions onto rectangular regions by elliptic systems. *Numer. Math.*, 1978, **29**, 397–407.
- 29 Peraire, J., Morgan, K. and Peiro, J. Unstructured mesh methods for CFD. Von Karman Institute for Fluid Dynamics 'Numerical grid generation' lecture note, 1990.
- 30 Miki, K. and Takagi, T. A domain decomposition and overlapping method for the generation of three-dimensional boundary-fitted coordinate systems. *J. Comput. Physics*, 1984, **53**, 319–330.
- 31 Steinhoff, J. Blending method for grid generation. *J. Comput. Physics*, 1986, **65**, 370–385.
- 32 Thompson, J. F., Thames, F. C. and Mastin, C. W. TOMCAT—a code for numerical generation of boundary-fitted curvilinear coordinate systems on fields containing any number of arbitrary two-dimensional bodies. *J. Comput. Physics*, 1977, **24**, 274–302.
- 33 Winters, K. H. and Jackson, C. P. A guide to finite-element grid generation using TGIN (release 1). AERE-R 11530, 1984.
- 34 O'Brien, V., Ehrlich, L. W. and Friendman, M. H. Unsteady flow in a branch. *J. Fluid Mech.*, 1976, **75**, 315–336.
- 35 O'Brien, V. and Ehrlich, L. M. Simulation of unsteady flow at renal branches. *J. Biomech.*, 1977, **10**, 623–631.
- 36 Liepsch, D. and Moravec, S. Measurement and calculations of laminar flow in a ninety degree bifurcation. *J. Biomech.*, 1982, **15**, 473–585.
- 37 Perktold, K. and Hilberit, D. Numerical simulation of pulsatile flow in a carotid bifurcation model. *J. Biomech.*, 1986, **8**, 193–199.
- 38 Rindt, C. C. M., Vosse, F. N. N. V. D., Steenhoven, A. A. V. and Janssen, J. D. A numerical and experimental analysis of the flow in a two-dimensional model of the human carotid bifurcation. *J. Biomech.*, 1987, **20**, 499–509.
- 39 Khodadadi, J. M., Vlachos, N. S., Liepsch, D. and Moravec, S. LDA measurements and numerical prediction of pulsatile laminar flow in a plane 90-degree bifurcation. *J. Biomech. Engng.*, 1988, **110**, 129–136.
- 40 Wille, S. O. Numerical simulation of steady flow inside a three-dimensional aortic bifurcation model. *J. Biomed. Engng*, 1984, **6**, 49–55.
- 41 Dinnar, U., Enden, G. and Israeli, M. A numerical study of flow in a three dimensional bifurcation. Cardiovascular Systems Dynamics Society Meeting, 1988, Canada.
- 42 Rindt, C. C. M. Analysis of the three-dimensional flow field in the carotid artery bifurcation. PhD thesis, 1989, Eindhoven University of Technology, The Netherlands.
- 43 Perktold, K. and Peter, R. Numerical 3D-simulation of pulsatile wall shear stress in an arterial T-bifurcation model. *J. Biomed. Engng*, 1990, **12**, 2–12.
- 44 Reynolds, O. On the dynamical theory of incompressible viscous fluids and the determination of the criterion. *Phil. Trans. Proc. R. Soc.*, 1895, **A186**, 123–164.
- 45 Collins, M. W., Allen, P. H. G. and Szpiro, O. Computational methods for entry length heat transfer by combined laminar convection in vertical tubes. *Proc. Instn. Mech. Engrs*, 1977, **191**, 19–30.

- 46 Allen, P. H. G., Collins, M. W. and Szpiro, O. The influence of temperature dependence of thermophysical properties on the prediction accuracy in laminar mixed-convection heat transfer in vertical tubes. Proceedings of Sixth International Conference on *Heat transfer*, Toronto, 1978.
- 47 Collins, M. W. A finite difference analysis of non-Newtonian fluids in circular tubes. Proceedings of Third International Conference on *Numerical methods in thermal problems*, Seattle, 1983, pp. 540–550.
- 48 Gosman, A. D., Khalile, E. and Whiterlaw, J. H. The calculation of two-dimensional turbulent recirculating flows. Proceedings of Symposium on *Turbulent shear flows*, Pennsylvania State University, Pa., 1977.
- 49 Launder, B. E. and Spalding, D. B. The numerical computation of turbulent flows. *Comput. Meth. Appl. Mech. Engng*, 1974, 3, 269–289.
- 50 Voke, P. R. and Collins, M. W. Large-eddy simulation retrospect and prospect. *Physico-Chemical Hydrodynamics*, 1981, 4(2), 119–161.
- 51 Grotzbach, G. Simulation of turbulent flow and heat transfer for selected problems of nuclear thermal-hydraulics. International Conference on *Supercomputing in nuclear applications*, Mito, Japan, March 1990.
- 52 Voke, P. R. and Collins, M. W. Large-eddy simulations of turbulent flow in plain and distorted channels. AERE Harwell Report HTFS RS 551, 1984, Annual Research Symposium, University of Warwick.
- 53 Collins, M. W. and Ciofalo, M. Computational fluid dynamics and its application to transport processes (submitted to *Journal of Chemical Technology and Biotechnology*).
- 54 Gresho, P. A modified finite element method for solving the time-dependent incompressible Navier–Stokes equations. Part I: Theory *Int. J. Numer. Math. in Fluids*, 1984, 4, 557–598.
- 55 Patankar, S. V. *Numerical heat transfer and fluid flow*, 1983 (Hemisphere).
- 56 Van Doormal, J. P. and Raithby, G. D. Enhancement of the SIMPLE method for predicting incompressible fluid flows. *Numer. Heat Transfer*, 1984, 7, 147–163.
- 57 Issa, R. I. Solution of the implicitly discretised fluid flow equations by operator-splitting. *J. Comput. Physics*, 1986, 62, 40–65.
- 58 Kightley, J. R. The conjugate gradient method applied to turbulent flow calculations. Proceedings of the Sixth GAMM Conference on *Numerical methods in fluid mechanics*, Gottingen, 1985.
- 59 Burns, A. D., Jones, I. P., Kightley, J. R. and Wilkes, N. S. FLOW3D, release 2: user manual. UKAEA report, 1987 (AERE Harwell).
- 60 Burns, A. D. and Wilkes, N. S. A. Finite difference method for the computation of fluid flows in complex 3D geometries. UKAEA report, 1987 (AERE, Harwell).
- 61 Ciofalo, M. and Collins, M. W. Time-dependent numerical simulation of the starting flow of an incompressible fluid past a downstream facing step. Proceedings of AGARD Conference on *Validation of computing fluid dynamics*, NATO, Lisbon, 1988.
- 62 Lonsdale, R. An algorithm for solving thermal-hydraulic equations in complex geometry. The ASTEC Code, UKAEA report, 1988 (Dounreay).
- 63 Rhie, C. M. and Chow, W. L. A numerical study of the turbulent flow past an airfoil with trailing edge separation. *AIAA J.*, 1983, 21, 1525–1532.
- 64 Collins, M. W. and Xu, X. Y. A predictive scheme for flow in arterial bifurcations: comparison with laboratory measurements. In *Biomechanical transport processes*, NATO workshop, Corsica, 1989.
- 65 Ku, D. and Liepsch, D. The effects of non-Newtonian visco-elasticity and wall elasticity on flow at a 90 degree bifurcation. *Biorheol.*, 1986, 23, 359–370.
- 66 Womersley, J. R. Oscillatory flow in arteries: the constrained elastic tube as a model of arterial flow and pulse transmission. *Physics in Med. Biol.*, 1958, 2, 178–187.
- 67 McDonald, D. A. *Blood flow in arteries*, 1960 (Williams and Wilkins, Baltimore).
- 68 Anliket, M., Rockwell, R. L. and Ogden, E. Nonlinear analysis of flow pulses and shock waves in arteries. Part I: Derivation and properties of mathematical model. Part II: Parameters study related to clinical problems. *J. Appl. Math. Phys. (ZAMO)*, 1971, 22, 217–246 (Part I), 563–581 (Part II).
- 69 Liepsch, D. Note on wave propagation in a thin elastic tube containing a viscous fluid. *J. Biomech.*, 1985, 18, 685–694.
- 70 Moravec, S. and Liepsch, D. Flow investigation in a model of a three-dimensional human artery with Newtonian and non-Newtonian fluids. Part I. *Biorheol.*, 1983, 20, 745–759.
- 71 Collins, M. W. and Xu, X. Y. Flow studies in canine artery bifurcation using a numerical simulation method (submitted to *ASME Journal of Biomechanical Engineering*, 1990).
- 72 Xu, X. Y. and Collins, M. W. The problem of numerical analysis of blood flow in arterial bifurcation—a review. Internal report, The City University, 1989.

A PREDICTIVE SCHEME FOR FLOW IN ARTERIAL BIFURCATIONS :
COMPARISON WITH LABORATORY MEASUREMENTS

M. W. Collins and X. Y. Xu

Thermo-Fluids Engineering Research Centre
The City University
London, U.K.

ABSTRACT

This is an initial study of overall prediction exercise to simulate blood flow through three-dimensional arterial bifurcations, ASTEC code is used with finite element grid definition and finite difference solution methods. Results are compared with laboratory measurements of Ku and Liepsch for T-junctions. Comparison is excellent for two-dimensional steady flow tests, and very good for three-dimensional pulsatile flows.

INTRODUCTION

It is a well known fact that atherosclerosis and thrombosis occur predominantly in arterial bends and bifurcations. Although the exact mechanism is not yet well understood, more recent studies (Zarins et al., 1983; Ku et al., 1985) have confirmed Caro's observation (Caro et al., 1971) that atherosclerotic lesions develop more frequently in regions with low shear stresses and with recirculation. Therefore, detailed insight into the flow phenomena occurring in bifurcations possibly contributes to a better understanding of the mechanism underlying the formation of atherosclerotic plaques and thrombi.

Extensive studies have been performed on flow in arterial bifurcations and branches. O'Brien et al. (1977) made a prediction of unsteady laminar flow through a two-dimensional T-junction based on a Vorticity-Stream function formulation. Detailed measurements and numerical calculations of steady flow in a plane 90 degree bifurcation were presented by Liepsch et al. (1982). The extension to the study of pulsatile flow was reported by Khodadadi et al. (1988). To investigate the effects of non-Newtonian behaviour and wall flexibility, Ku and Liepsch (1986) performed LDA measurements on flow at a three-dimensional T-bifurcation. An excellent review of previous research into the details of flow behaviour in model bifurcations has been made by Liepsch (1986).

The present study is an initial step of the overall prediction exercise which aims to simulate arterial bifurcation flows under real

physiological conditions. For convenience of comparison with published measurements, the idealised T-bifurcation models are adopted and the validation of the numerical results is provided. All calculations presented were performed using ASTEC (developed at UKAEA), a fluid flow code applying finite volume solution methods to a finite element mesh (Lonsdale, 1988). As assessed by Xu and Collins (1989), the unique combination of great geometrical flexibility and high efficiency makes ASTEC a well-suited code for the current application.

NUMERICAL METHODS

The numerical predictions are based upon the system of time-dependent Navier-Stokes and continuity equations for viscous, incompressible Newtonian fluid flow in a three-dimensional geometry with rigid walls. These equations can be written in the integral form

$$\int \vec{u} \cdot d\vec{A} = 0 \quad (1)$$

$$\rho \frac{\partial}{\partial t} \int \vec{u} \, dV = -\rho \int \vec{u}\vec{u} \cdot d\vec{A} - \int \nabla P dV + \mu \int \nabla^2 \vec{u} \cdot d\vec{A} \quad (2)$$

Where $\vec{u} = (u, v, w)^T$ is fluid velocity, $d\vec{A}$ and dV represent elements of control area and control volume respectively, and P is pressure. Together with appropriate initial and boundary conditions, equations (1) and (2) are uniquely solvable for velocity components and pressure.

The procedure for solving the discrete equations is iterative and based on the SIMPLE method as inferred by Patankar and Spalding (1972). A preconditioned conjugate gradient algorithm is used to calculate the pressure corrections. To minimise the false diffusion errors associated with the advection term, a vector upwinding scheme is employed. The time differencing is fully implicit, so that there is no Courant stability restriction to the timestep.

To make solution of large three-dimensional problems sufficiently fast, a high degree of vectorization is essential to obtain best performance from present-day supercomputers. ASTEC has been tailored for the supercomputer CRAY in the sense that the programme is written so that the CRAY compiler CFT 77 will produce a highly vectorised code.

RESULTS AND DISCUSSION

Steady Flow in a Two-dimensional T-bifurcation

Particularly with a new code such as ASTEC careful validation exercises should be carried out. For these, the experimental data of Ku and Liepsch were felt to be ideal. To ensure that ASTEC is suitable for the current application, a simple test was carried out on a two-dimensional laminar flow in a T-bifurcation for Reynolds numbers ranging from 250 to 1100. Figure 1 shows the bifurcation geometry and element division used in the calculation. Since ASTEC is a three-dimensional code, the two-dimensional problem was solved on the three-dimensional mesh of one element thick with flow restricted between two symmetric planes. The mesh consists of 840 elements and 1870 nodes. With this mesh a typical calculation for a Reynolds number of 496 and a flow rate ratio \dot{V}_3/\dot{V}_1 of 0.44 required 165.8 seconds on a CRAY X-MP/28.

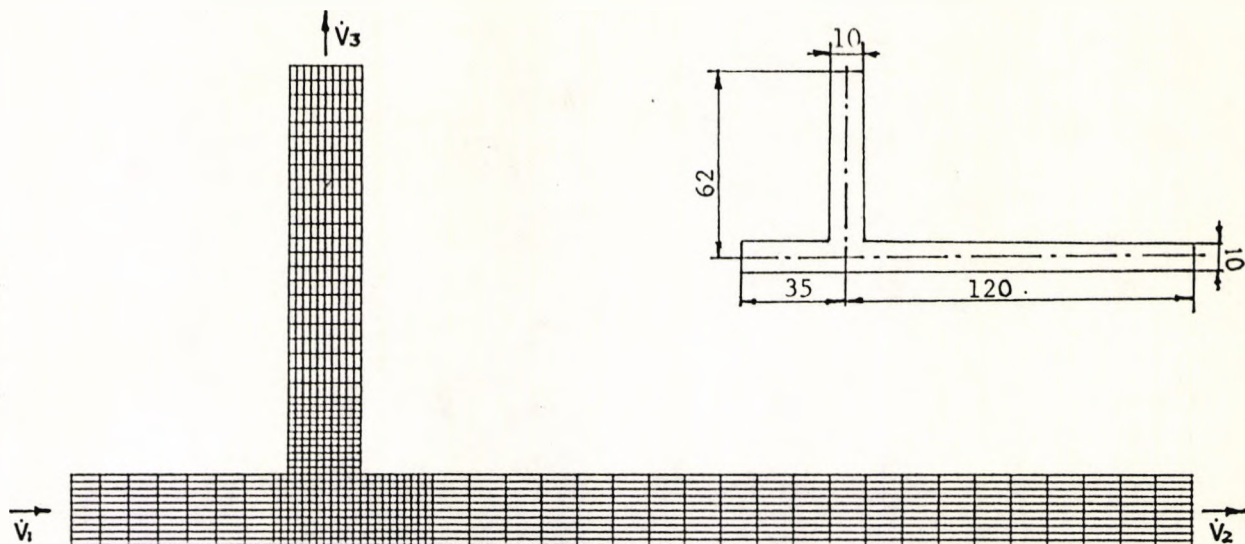


Fig. 1. Bifurcation geometry and mesh division.

In this simulation the density of the fluid is 1000Kg/m^3 , and the dynamic viscosity is $1.02 \times 10^{-3} \text{ Kg/(ms)}$. At the inlet plane a fully developed axial velocity profile and zero normal velocities are specified. Since the two outlets are well downstream, a fully developed axial velocity profile with specified flow rate has been assumed at one outlet, and zero pressure is assumed at the other. No-slip conditions are imposed on the rigid walls.

Figures 2 and 3 present the velocity vectors in the main and branching tubes respectively, for a Reynolds number of 496 and a flow rate ratio of 0.44. It is seen that the velocity profiles are parabolic at the inlet and outlet regions. Before the bifurcation, the velocity profiles are almost unchanged until about 10mm upstream from the branching. Behind the bifurcation in the main tube, the velocity profiles are skewed towards the upper wall. A reverse flow region of about 20mm in length exists at the bottom wall. The flow farther downstream of the bifurcation becomes fully developed. In the branching tube, the reverse flow region along the upstream wall is more pronounced than in the main tube. The region of reverse flow is about 43mm in height which corresponds to 4.3 times the diameter of the tube.

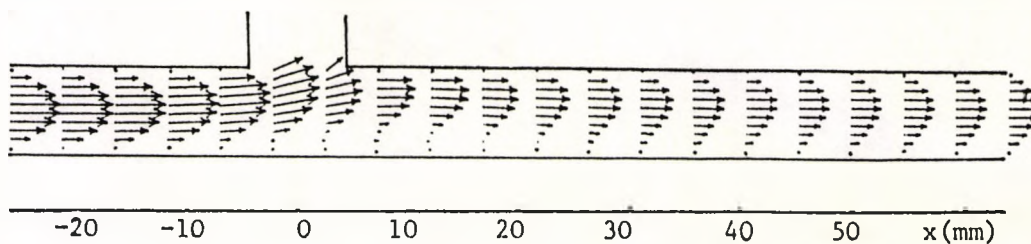


Fig. 2. Velocity vectors in the main tube ($Re=496$, $\dot{V}_3/\dot{V}_1=0.44$).

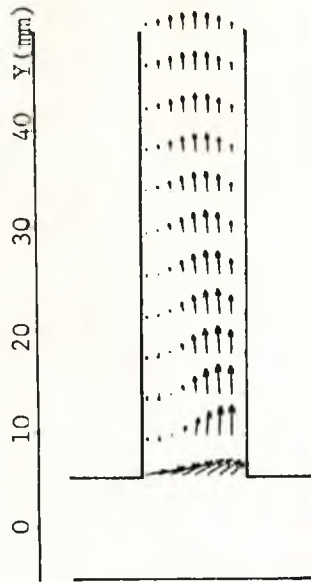


Fig. 3. Velocity vectors in the branching tube ($Re=496$, $\dot{V}_3/\dot{V}_1=0.44$).

To examine the accuracy of the calculations, a quantitative comparison of the calculated and measured results has been performed. In Figure 4 the calculated axial velocity profiles are compared with LDA measurements obtained by Liepsch et al. (1982). It is observed that there is a very good agreement between the calculations and the measurements; especially in the main tube the axial velocity profiles are predicted quite accurately. Some differences are found in the branching tube. This may be due to the three-dimensional effects of the tube used in the experiments. The differences are, in fact, rather less than with numerical predictions also presented by Liepsch et al.

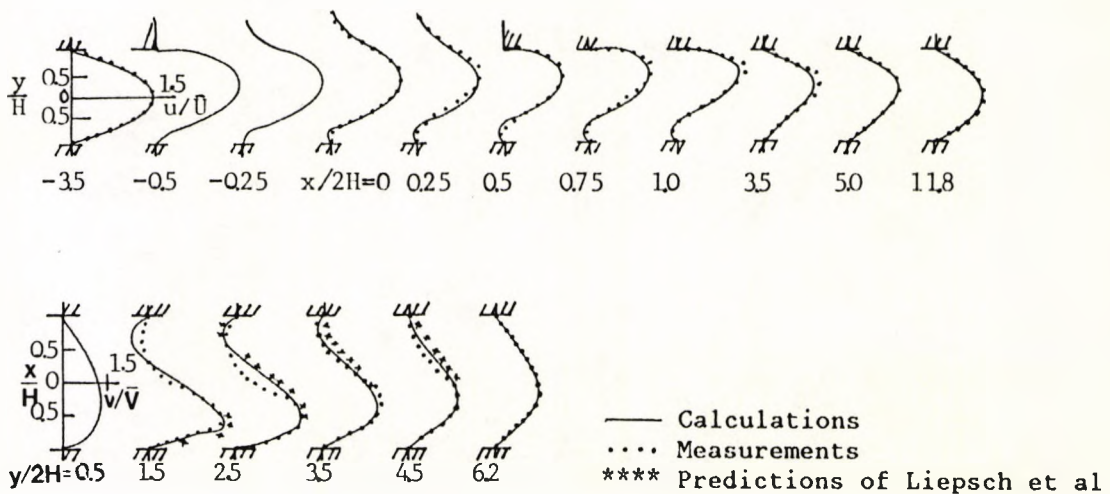


Fig. 4. Comparison between calculations and the LDA measurements of Liepsch et al. (1982). ($Re=496$, $\dot{V}_3/\dot{V}_1=0.44$)

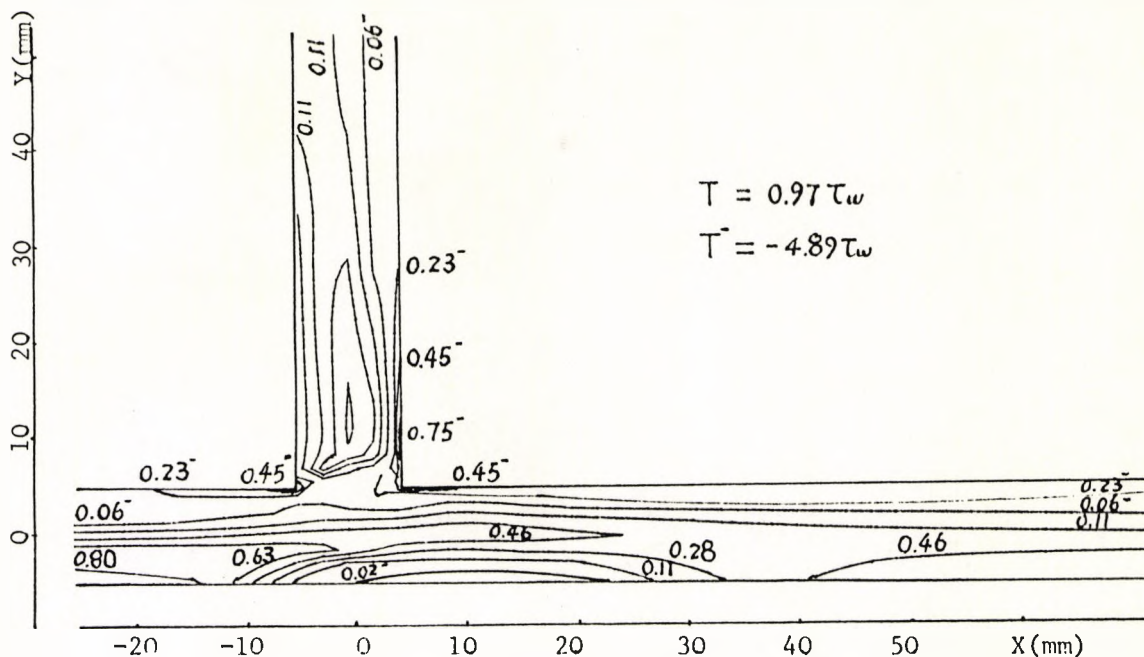


Fig. 5. Shear-stress contours ($Re=496$, $\dot{V}_3/\dot{V}_1=0.44$).

The shear-stress contours for a Reynolds number of 496 and a flow rate ratio \dot{V}_3/\dot{V}_1 of 0.44 are shown in Figure 5. For convenience of comparison, the shear-stress contours are plotted as a percentage of their maximum and minimum values respectively. These values are given in terms of the fully developed wall shear-stress at the inlet. Figure 5 shows that there are two zones of low shear-stress formed, one is opposite the branching near the bottom wall of the main tube, with another along the upstream wall of the branching tube. In the region of the divider wall of the branching tube, a high shear-stress zone is formed. The same happens along the upper wall of the main tube around the corner area. Again, the agreement between the predicted shear-stress contours and those presented by Liepsch et al.(1982) is very good.

Steady Flow in a Three-dimensional T-bifurcation

A three-dimensional prediction was performed on steady flow through a T-bifurcation with circular cross-section at an average upstream Reynolds number of 250 and a flow division ratio of 50:50. In this bifurcation, the diameter of the main tube is 6mm and the diameter of the side branch is 3mm. The element division for the model bifurcation is illustrated in Figure 6. Since the flow is symmetric, only half of the bifurcation was considered. The mesh used in the calculation consists of 5360 elements and 6526 nodes. A 70% aqueous glycerine solution with a density of 1180Kg/m^3 and a viscosity of 0.013Kg/(ms) was used in the simulation. The boundary conditions were the same as those applied to the two-dimensional case.

The calculation had a 'cold' start, which means that the initial guess of all variables was zero. When the convergence criterion for the maximum change of velocity components of two successive iterations was less than 1.0×10^{-4} , a converged solution was obtained in 335 seconds on a CRAY X-MP/28.

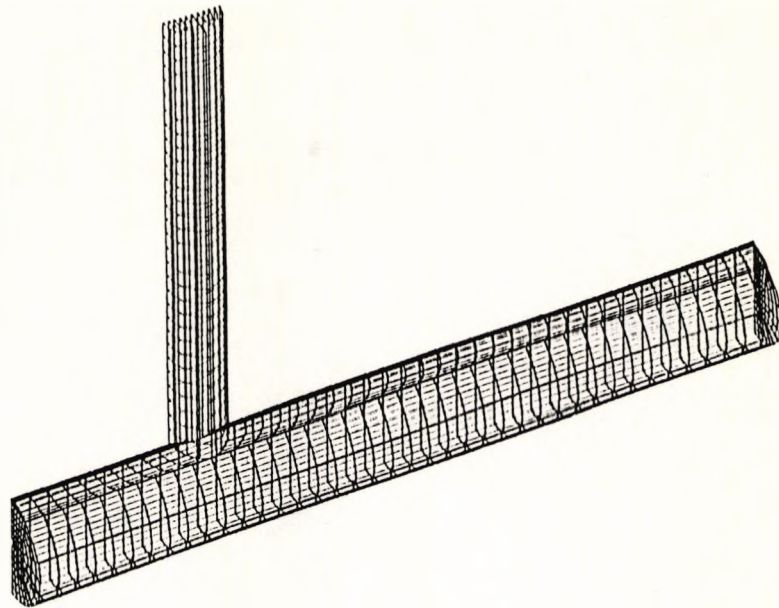


Fig. 6. Finite element mesh used in the calculation.

Figure 7 presents the axial velocity profiles in the symmetry plane. At the inlet and outlet regions, the axial velocity profiles hardly differ from parabolic ones. After the flow divider, maximum axial velocities are shifted towards the divider wall, which is primarily caused by the flow branching. A region with negative axial velocities could be seen at the bottom wall, with negative velocities reaching approximately 2cm/sec.

Figure 9 demonstrates the secondary flow at the cross-sections given in Figure 8. It is observed that secondary flow at the entrance of the main tube (A) is completely directed from the outer wall towards the branching side. At the flow divider site in the main tube (B), secondary flow is almost entirely directed towards the divider wall, where the highest secondary velocities are found. Downstream in the main tube (C) secondary flow shows high resemblance to a Dean type vortex. Near the symmetry plane secondary velocities are directed towards the divider wall and near the side wall they point circumferentially back towards the non-divider wall. At both sites in the branch tube (D and E), secondary velocities are directed towards the divider wall near the symmetry plane and circumferentially back near the side wall.

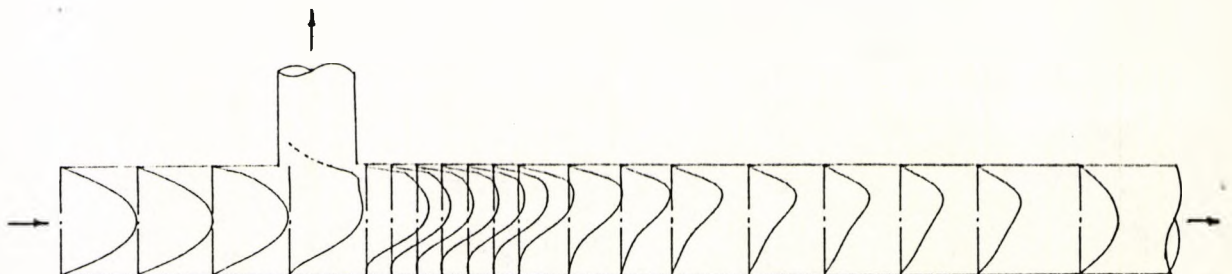


Fig. 7. Axial velocity profiles in the symmetry plane.

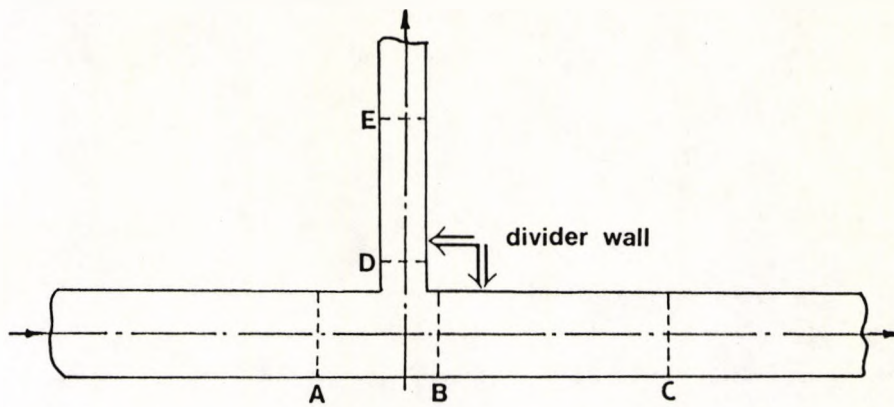


Fig. 8. Cross-sections where secondary flow are presented.

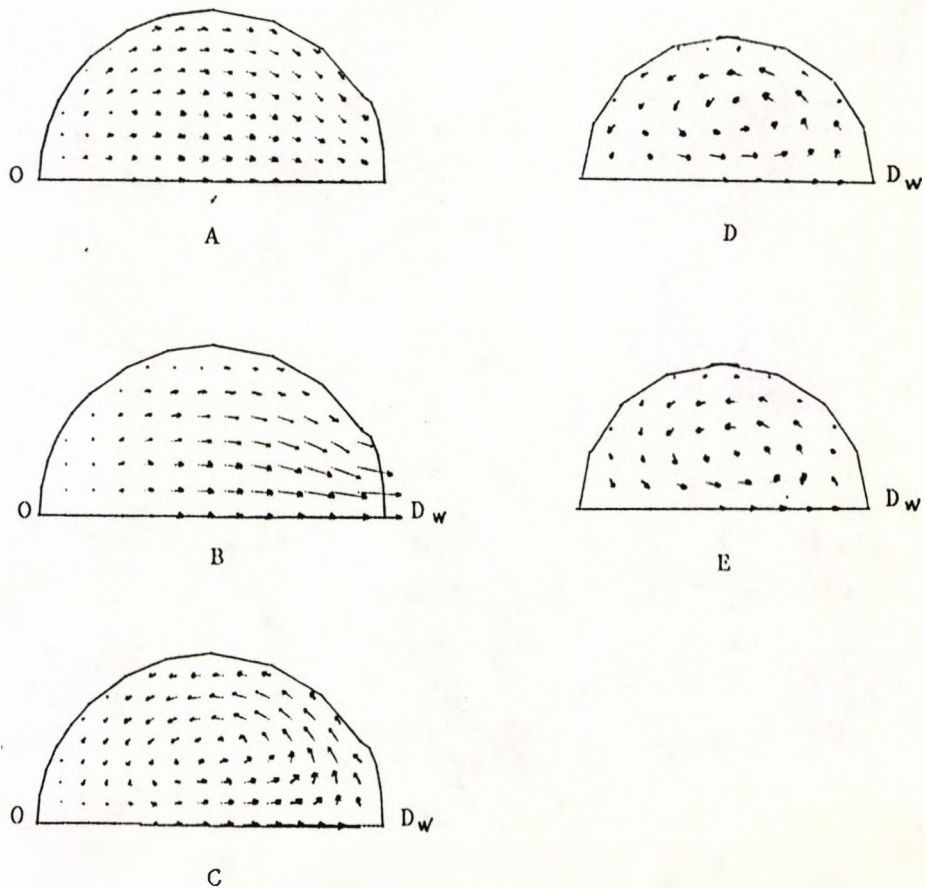


Fig. 9. Secondary flow in the main and the branching tube.
(O : outer wall, D_w: divider wall)

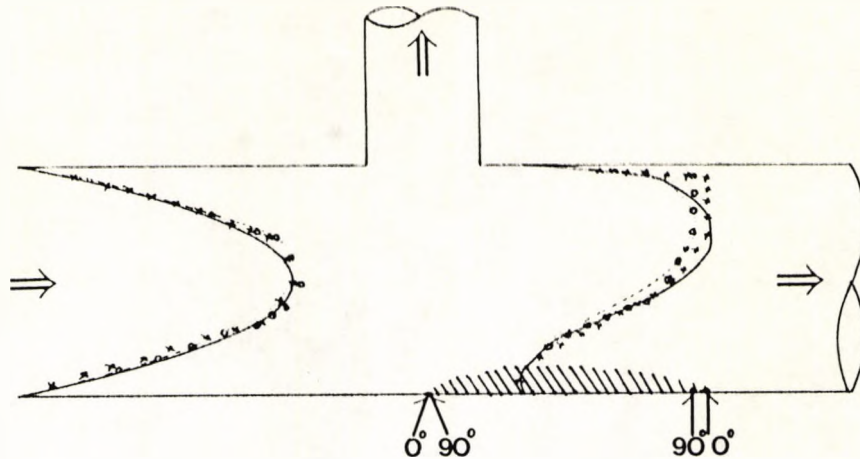


Fig. 10. Calculated (—,....) and measured (....,.....) axial velocity profiles at 0 and 90 degrees in the symmetry plane 20mm upstream and 2.5mm downstream from the branch. |||| shows the limits of predicted reverse flow region for phase 0° and 90° .

Pulsatile Flow in a Three-dimensional T-bifurcation

Following the steady flow prediction presented in the previous section, a preliminary prediction of pulsatile flow in the same three-dimensional T-bifurcation was performed. The flow conditions reported in the experimental study of Ku and Liepsch (1986) were reproduced in this prediction, i.e. an average main tube Reynolds number of 250, an average upstream pressure gradient of 4000pa/m, a pulsatile pressure amplitude of 1000pa/m, and a Womersley parameter of 2.3 for the sine wave input. Therefore, with 0° of phase representing the peak pressure, the pressure gradient at the inlet plane can be given by

$$-\frac{\partial P}{\partial x} = 4000 + 1000 \cos \omega t \quad (3)$$

By imposing the inlet pressure gradient as one of the boundary conditions, the calculation was carried out from 0° of phase with the converged solution of the steady flow case as its initial guess. Thirty-six time steps in a cycle were used. The calculation for a quarter of a cycle took 15 minutes on a CRAY X-MP/28.

Figure 10 illustrates the velocity profiles at 0 and 90 degrees in the symmetry plane 20mm upstream and 2.5mm downstream from the branch. Similar to the steady velocity profiles, the pulsatile profiles in the main tube 2.5mm downstream of the bifurcation are skewed towards the flow divider wall. A reverse flow region could always be seen at the bottom wall of the main tube throughout the cycle, although the extent of this region varies within the cycle. A most pleasing effect is the prediction in the right sense of the slight experimental increase and reduction going from 0° to 90° phase of the velocity profiles upstream and downstream of the bifurcation. These predictive results, then, are consistent with the laboratory measurements of Ku and Liepsch (1986).

CONCLUSION

From the results presented above, the following conclusions can be drawn :

1. A predictive scheme for flow in two- and three-dimensional bifurcations is presented. Calculations for steady flow in a plane T-bifurcation, both steady and pulsatile flow in a three-dimensional T-bifurcation have been performed.
2. The computed results for steady flow in a plane T-bifurcation have been validated. Comparison of the calculations and the published LDA measurement is very satisfactory.
3. The presented predictive scheme has been proved to be efficient and reliable on three-dimensional problems.
4. It is intended to complete the pulsatile flow exercise for the entire 360° cycle, and to investigate the effects of non-Newtonian viscosity and flexible wall. Then it will be possible to progress to in vivo bifurcation flow prediction.

ACKNOWLEDGMENTS

We gratefully acknowledge the support of a British Heart Foundation Research Grant for this programme of work.

REFERENCES

- Caro, C. G., Fitz-Gerald, J. M., and Schroter, R. C., 1971, Atheroma and arterial wall shear, Proc. Roy. Soc. London B, 177:109.
- Khodadadi, J. M., Vlachos, N. S., Liepsch, D., and Moravec, S., 1988, LDA measurements and numerical prediction of pulsatile laminar flow in a plane 90-degree bifurcation, J. Biomechanics, 15:7:473.
- Ku, D., Giddens, D., Zarins, C., 1985, Pulsatile flow and atherosclerosis in the human carotid bifurcation. Arteriosclerosis, 5:293.
- Ku, D., and Liepsch, D., 1986, The effects of non-Newtonian viscoelasticity and wall elasticity on flow at a 90° bifurcation, Biorheology, 23:359.
- Liepsch, D., 1986, Review article: Flow in tubes and arteries - a comparison, Biorheology, 23:395.
- Liepsch, D., Moravec, S., Rastogi, A. K., and Vlachos, N. S., 1982, Measurement and calculations of laminar flow in a ninety degree bifurcation, J. Biomechanics, 15:No.7:473.
- Lonsdale, R. D., 1988, An algorithm for solving thermalhydraulic equations in complex geometries: the ASTEC code. in: UKAEA Report.
- O'Brien, V., Ehrlich, L. W., 1977, Simulation of unsteady flow at renal branches. J. Biomechanics, 10:623.
- Patankar, S. V., Spalding, D. B., 1972, A calculation procedure for heat, mass and momentum transfer in three-dimensional parabolicflows, Int'l J. Heat Mass Transfer, 15:1787.
- Xu, X. Y., and Collins, M. W., 1989, Assessment of the problem of numerical simulation of blood flow through three-dimensional bifurcations, in: Proc. Int'l. Symposium on Biofluid Mechanics and Biorheology, 671.
- Zarins, C. K., Giddens, D. P., and Bharadvaj, B. K., 1983, Carotid bifurcations atherosclerosis: Quantitative correlation of plaque localization with flow velocity profiles and wall shear stress Circ.Res., 53:502.